UNIVERSITÀ DEGLI STUDI DI PADOVA

Dipartimento di Fisica e Astronomia ''G. Galilei''

CORSO DI DOTTORATO DI RICERCA IN ASTRONOMIA
CICLO XXXIV

SEARCH AND CHARACTERIZATION
OF MULTIPLANETARY SYSTEMS
USING GROUND AND SPACE-BASED DATA

Tesi redatta con il contributo finanziario
della Fondazione CARIPARO

Coordinatore: Prof. Giovanni Carraro
Supervisore: Prof. Giampaolo Piotto
Co-supervisori: Dott. Luca Borsato
　　　　　　　　Prof. Luca Malavolta

Dottoranda:
Gaia Lacedelli

Abstract

Planets in multiplanetary systems, being formed in the same protoplanetary disk and evolved in the same environment, offer a unique opportunity for comparative planetology. The study of well-characterized systems allow us to investigate the formation and evolution processes, by constraining theory and helping to discriminate among competing models, which should be able to reproduce the observed properties and trends of the planetary population. To better understand exoplanets and exoplanetary system complexity, it is essential to build a robust sample of well-characterized multiplanetary systems. Currently, ultra-precise photometers and high-resolution spectrographs can be used to infer accurate planetary radii and masses, needed to determine the average density and to provide clues on the inner bulk composition, which is fundamental to obtain a complete characterization of a system in combination with the orbital architecture.

This thesis is motivated by improving our knowledge of multiplanetary systems. On one side, we focused on the precise characterization of a new multiplanetary system orbiting the late-G dwarf star TOI-561. This star was initially observed by the *TESS* mission, which identified the presence of three transiting candidates. We followed-up the system with the HARPS-N spectrograph collecting 82 high-resolution radial velocities (RVs). We determined that TOI-561 is old, metal-poor, and alpha-enhanced. Moreover, belonging to the thick-disk, TOI-561 is one of the few stars of this Galactic population that hosts a multiplanetary system. From the RV analysis we discovered two additional external planets. However, RVs could not confirm the outermost *TESS* candidate, which would also make the system dynamically unstable. We demonstrated that the two transits initially associated with this candidate are instead due to single transits of the two planets discovered using RVs. On the basis of our observational data, we proposed a final configuration with four transiting planets, namely an ultra-short period (USP) super-Earth (TOI-561 b) and three mini-Neptunes (TOI-561 c, d, and e). The unusual density of TOI-561 b, which is the lowest density USP planet known to date, and the interesting (and debated) system configuration called for follow-up studies. We therefore collected a second season of 62 HARPS-N RVs, which we combined with previous previous HARPS-N data and published HIRES RVs. Moreover, we collected ultra-high precision photometric data with *CHEOPS*, observing various transits of TOI-561 b and c, and one transit of the previously single-transiting planet TOI-561 d. Our global analysis, including also new *TESS* observations, confirmed the four-planet configuration, as well as the low density of TOI-561 b, which, given the low stellar metallicity, is effectively consistent with the general bulk density-stellar metallicity trend. The precise masses and radii obtained for the four planets allowed us to conduct interior structure and atmospheric escape modelling. According to our model, planet b has basically no

gas envelope, and it could host a certain amount of water. In contrast, TOI-561 c, d, and e likely retained an H/He envelope, in addition to a possibly large water layer. The inferred planetary compositions suggest different atmospheric evolutionary paths, with planets b and c having experienced significant gas loss, and planets d and e showing an atmospheric content consistent with the original one. Finally, we identified an additional (fifth) long-period signal (~ 470 d) in the RVs, which could be due to either an external planetary companion or to stellar magnetic activity. Further insights into this system will come from additional *TESS*, *CHEOPS* and HARPS-N follow-up planned for the coming year.

In our efforts to improve exoplanet characterization, in the second part of the thesis we focused on the development of a new tool for the characterization of interacting multiplanetary systems showing transit time variations (TTVs). In presence of mutual gravitational interactions, the most consistent way to analyze photometric and spectroscopic data is through the photodynamical approach, which combines photometric and dynamical analysis to simultaneously determine the mass and radius of both the star and planets accounting for the gravitational dynamic interactions via an N-body simulation. We implemented our `Python` version of a photodynamical code, using the the `batman` package for transit modelling, the orbital integrator `rebound` for N-body integration, and determining the best combination of the orbital parameters using a Bayesian analysis. We started testing the code on the well-known four-planet system WASP-47, obtaining promising results. We also used some of the code functionalities to perform new dynamical analysis of multiplanetary systems such as TOI-836 and Kepler-37. Once completed, optimized, and definitely validated, we will publicly release the code, which will be an important tool for the understanding and characterisation of known and newly-detected multiplanetary systems showing TTVs.

Riassunto

Gli esopianeti orbitanti in sistemi planetari multipli, essendosi formati ed evoluti all' interno dello stesso disco protoplanetario, offrono un'opportunità unica per condurre analisi comparative e per indagare i processi di formazione ed evoluzione planetaria. Lo studio dei sistemi multipli può infatti aiutare a delineare e testare nuove teorie e modelli, che devono essere in grado di riprodurre le caratteristiche dei sistemi osservati. Per questo, è essenziale avere a disposizione un campione significativo di sistemi multipli caratterizzati con precisione. Oggi, grazie alla presenza di strumenti tecnologicamente sempre più avanzati, abbiamo la possibilità di determinare con precisione raggio e massa, e quindi la densità media, di un numero crescente di esopianeti. La misura della densità permette di stimare la composizione interna di un esopianeta, ed è quindi un dato fondamentale per ottenere una visione completa di un sistema, insieme alla determinazione della configurazione orbitale.

La necessità di ampliare la nostra conoscenza dei sistemi planetari multipli è il fondamento su cui si basa questa tesi, che si sviluppa su due diversi fronti. Da un lato, ci siamo concentrati sulla caraterizzazione dettagliata di un nuovo sistema planetario multiplo orbitante la stella TOI-561. Questa stella è stata osservata inizialmente dalla missione spaziale *TESS*, la quale ha identificato nella curva di luce tre candidati pianeti transitanti. Abbiamo quindi osservato la stella con lo spettroscopio ad alta risoluzione HARPS-N, ottenendo 82 velocità radiali (RV). Dalla nostra analisi stellare TOI-561 è risultata essere una stella vecchia, meno metallica del Sole, e con sovrabbondanza di elementi α. Per di più, è una delle poche stelle appartenti alla popolazione galattica di ''*thick-disk*'' ad ospitare un sistema planetario multiplo. Dall'analisi delle RV abbiamo determinato la presenza di due nuovi pianeti esterni, mentre non è stato possibile identificare il segnale del terzo candidato indicato da *TESS*, che per di più avrebbe reso il sistema dinamicamente instabile. Abbiamo quindi dimostrato che i due transiti inizialmente associati a questo candidato erano piuttosto due transiti singoli dei due pianeti identificati nelle RV. La nostra configurazione finale proposta prevede quindi la presenza di quattro pianeti transitanti, di cui una super-Terra con periodo ultra breve (TOI-561 b) e tre mini-Nettuni (TOI-561 c, d, e). Data la peculiarità di TOI-561 b, avente la densità più bassa tra tutti i pianeti noti a periodo ultra breve, e l'interessante (e dibattuta) architettura, abbiamo deciso di studiare più approfonditamente il sistema con nuovi dati. Abbiamo osservato nuovamente TOI-561 con HARPS-N, ottenendo 62 punti addizionali. Inoltre, abbiamo osservato la stella con il telescopio spaziale *CHEOPS*, ottenendo fotometria ad altissima precisione per svariati transiti di TOI-561 b e TOI-561 c ed osservando un secondo transito di TOI-561 d, che presentava solamente un transito nella curva di luce *TESS*. La nostra nuova analisi, effettuata includendo anche nuove osservazioni *TESS* e alcune osservazioni pubbliche dello spettroscopio HIRES, ha confermato la configuazione a quattro pianeti, così come il primato di TOI-561 b per la minor densità. Grazie alla precisione ottenuta nelle misure di raggio e massa dei quattro pianeti, abbiamo potuto modellare la loro struttura interna e la loro evoluzione atmosferica. Secondo il nostro modello, il pianeta b non presenta alcun inviluppo gassoso, ma potrebbe ospitare una certa quantità di acqua al suo interno. Al contrario, TOI-561 c, d, ed e hanno probabilmente conservato un inviluppo di H/He, oltre ad un possibile strato di acqua. Sulla base della loro composizione, i pianeti sembrano aver avuto storie evolutive differenti per

quanto riguarda il contenuto di gas, con i due pianeti interni che ne hanno perso una notevole quantità, mentre i due esterni che hanno conservato buona parte del gas presente originariamente. Infine, abbiamo identificato nelle RV un quinto segnale a lungo periodo ($\sim$ 470 d), che potrebbe essere dovuto sia alla presenza di un pianeta esterno sia ad attività magnetica stellare. Il sistema TOI-561 verrà analizzato ancora più in dettaglio grazie ai dati *TESS*, *CHEOPS* e HARPS-N in previsione per l'anno in corso.

A scopo di migliorare il processo di caratterizzazione planetaria, nella seconda parte della tesi ci siamo concentrati sullo sviluppo di un software per l'analisi e la caratterizzazione di sistemi multipli con pianeti che interagiscono gravitazionalmente e che quindi mostrano variazioni dei tempi di transito (TTV). In questo caso, l'approccio più coerente ed informativo per analizzare dati fotometrici e spettroscopici è il cosiddetto metodo fotodinamico. Esso permette di combinare analisi fotometrica e dinamica per determinare simultaneamente raggio e massa della stella e dei pianeti, tenendo conto delle interazioni gravitazionali mutue grazie ad una simulazione ad N-corpi. Abbiamo implementato la nostra versione in `Python` di un codice fotodinamico, usando il software `batman` per l'analisi fotometrica, l'integratore numerico `rebound` per l'integrazione ad N-corpi e utilizzando metodi Bayesiani per ottenere la miglior combinazione dei parametri orbitali del sistema. Abbiamo iniziato a testare il codice sul noto sistema a quattro pianeti WASP-47, ottenendo risultati promettenti. Abbiamo anche utilizzato alcune funzionalità del codice fotodinamico per effettuare nuove analisi dinamiche di sistemi planetari multipli, in particolare TOI-836 e Kepler-37. Una volta terminato, ottimizzato e validato in maniera definitiva, renderemo il codice pubblicamente usufruibile, in modo che diventi un importante strumento per la caratterizzazione di sistemi planetari multipli interagenti, sia noti sia ancora da scoprire.

Contents

Contents

List of Figures

List of Figures

List of Tables

Introduction

Exoplanetology is currently one of the most thriving fields in astrophysics. Dedicated surveys and missions, both observing from ground and space, led in only three decades to an exponential growth in the number of confirmed exoplanets – now more than 4500 – and provided an even bigger number of candidates that still await confirmation, with many others to be revealed with current and future facilities.

The most important lesson that we learned from the study of exoplanets is that they are intriguingly different, both one from the other, and from what we expected based on the knowledge of the planets in our own Solar System, with some of them turning out to be more exotic than anything we could have expected. This astonishing diversity also applies to the architectures of the ~ 820 multiplanetary systems discovered to date, challenging the formation and evolutionary theories. The more we learn about exoplanets and exoplanetary systems, the more we understand the theories behind the formation of our own Solar System, and therefore also on how the Earth formed, with the delicate conditions needed to host life.

To help putting some order on our understanding of exoplanets and exoplanet system complexity, and build the comprehensive framework comprising planetary formation and evolution processes, it is essential to construct a substantial sample of well-characterized multiplanetary systems. In particular, for a first inner bulk characterization of the planets in a given system, planetary masses and radii are key quantities for the determination of the average densities, needed to understand the planetary internal structure. The knowledge of the planets composition, combined with the study of the orbital configuration, gives important information of the processes occurred in the system history, and it allows for comparative planetology. Such an in-depth characterization is only possible by combining data and information coming from different observing techniques (i.e. radius from transit photometry, and mass from radial velocity analysis), and exploiting synergies between various instruments, which can provide a multifaceted view of the same system.

In this context, this thesis aims to contribute to the construction of a robust sample of well-characterized multiplanetary systems, with two distinct projects. On one side, it focuses on the confirmation and in-depth characterization of a new multiplanetary system, using state-of-the-art facilities and data analysis tools. On the other side, it encompasses the development of a new tool to analyze transiting, interacting multiplanetary systems in the most coherent and comprehensive way. This so-called ''photodynamical''

approach is necessary to obtain an accurate determination of the planetary properties of dynamically active systems, which are becoming a substantial subsample of the known observed systems.

A brief introduction on the main observing techniques, facilities, and general context relevant to this work is presented in Chapter 1, while Chapter 2 describes the primary methods and techniques employed in the analyses we performed in this thesis work. Chapter 3 presents a first characterization of the TOI-561 multiplanetary system, discovered by the *TESS* space telescope, and that we followed-up with the HARPS-N spectrograph. A more in-depth view of this system is provided in Chapter 4, including our investigation on the actual system configuration and on the planetary internal structure modelling enabled by an additional HARPS-N radial velocity campaign and by ultra-precise photometric observations that we collected using the *CHEOPS* space telescope. Finally, Chapter 5 introduces our implementation of a photodynamical code, which couples photometric analysis with N-body integration to account for mutual gravitational interactions of multiplanetary systems and to obtain an accurate determination of the planetary properties.

Chapter 1

Exoplanets

1.1 Overview

Over the centuries, mankind has always speculated about the existence of planetary systems other than our own, and wondered about the presence of life elsewhere in the Universe. In the last three decades, starting in 1995 with the discovery of the first exoplanet orbiting a star different from the Sun (Mayor & Queloz, 1995), we finally began answering those questions, and since then the exoplanetary science has experienced an exponential growth. With the rising number of discovered exoplanets (more than 4500 are known to date), it became increasingly clear that exoplanets do not necessarily reflect the expectations we had based on the knowledge of our own Solar System. Instead, they show a wide and unforeseen diversity, with Jupiter-like planets having periods of just a couple of days, planets in highly inclined or eccentric orbits, tidally locked planets, planets with molten silicates at their surface (the so-called ''lava worlds''), and much more. This variety makes difficult to classify exoplanets in a unique, universally-accepted way, but we can identify some indicative radius classes:

- Earths, or terrestrial planets ($R < 1.25\ R_\oplus$)

- super-Earths ($1.25\ R_\oplus < R < 2\ R_\oplus$)

- Neptunes ($2\ R_\oplus < R < 6\ R_\oplus$)

- Jupiters ($6\ R_\oplus < R < 15\ R_\oplus$)

Along the lines of the exoplanetary diversity, we immediately note that there is a category of planets, the so-called super-Earths, which have no direct solar-system analogues. However, recent surveys such as *Kepler* (see Section 1.3.2) showed that they are among the most common planets observed in the near Universe (e.g. Batalha et al. 2013). These planets have masses spanning from roughly 2 to 10 $M_\oplus$, and their average densities can be explained by a broad variety of different bulk compositions, from water-dominated planets to rocky cores surrounded by a thick gas layer. Given also the absence of a solar-system counterpart, this category pose a big challenge in planetary formation theories. In this
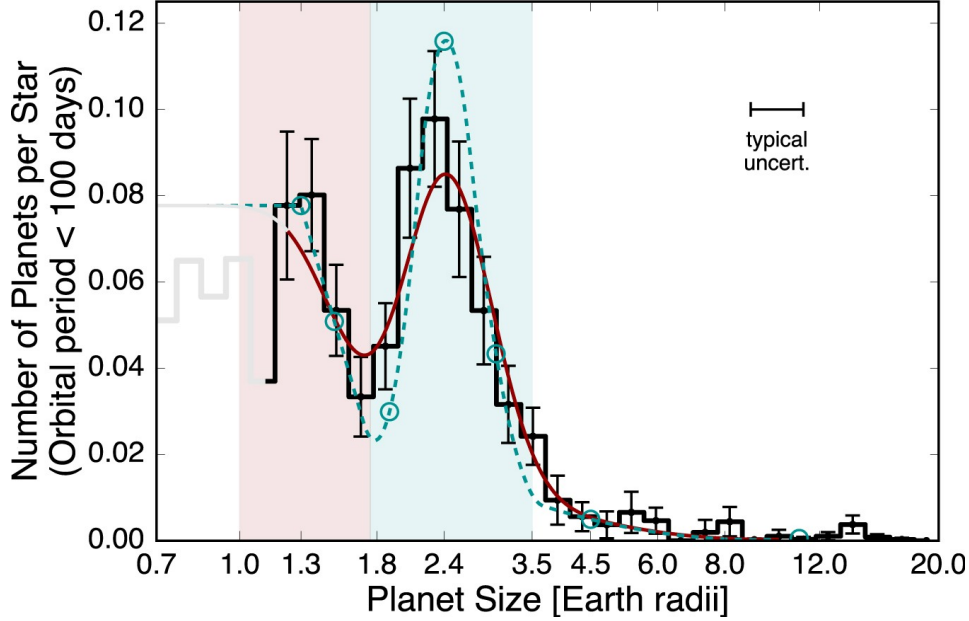
Figure 1.1 The bimodal radius distribution of planets around Sun-like stars, with a gap at about $\sim 1.8\ R_{\oplus}$. The shaded areas highlight the regime of super-Earth (light red) and sub-Neptunes (light cyan). From Fulton et al. (2017).

regard, current investigations on the relation among super-Earths and the sub-class of mini- (or sub-) Neptunes, i.e. planets with $R < 4\ R_{\oplus}$ and $M < 10\ R_{\oplus}$ are ongoing. Mini-Neptunes have a mass range that partially overlaps with the one of super-Earths, but these planets have very low bulk densities, therefore implying the presence of a significant H/He envelope. Looking at the observed radius distribution (Figure 1.1), a paucity of planets around $1.8\ R_{\oplus}$ emerges, i.e. the so-called ''radius gap'', with planets below the gap being mainly rocky and planets above the gap hosting a relevant gaseous envelope (Fulton et al., 2017). This suggests the presence of a transition between the super-Earth and sub-Neptune populations. One of the explanations suggested by current theories is that the radius gap could result from processes of photoevaporation or core-powered mass-loss, which imply the loss of the gaseous envelope and leave as a result a rocky core (e.g. Owen & Wu 2013, Lopez & Fortney 2014, Owen & Wu 2017, Lopez & Rice 2018, Ginzburg et al. 2018, Gupta & Schlichting 2019).

This is only an example of the challenges we are facing while investigating the fascinating field of exoplanetology. Working towards a comprehensive view and characterization of the exoplanet population, alongside the elaboration of theoretical frameworks aimed at explaining the composition, formation and evolution of the observed exoplanets, new discovery methods and precise instrumentation have been developed, as described in the next sections.
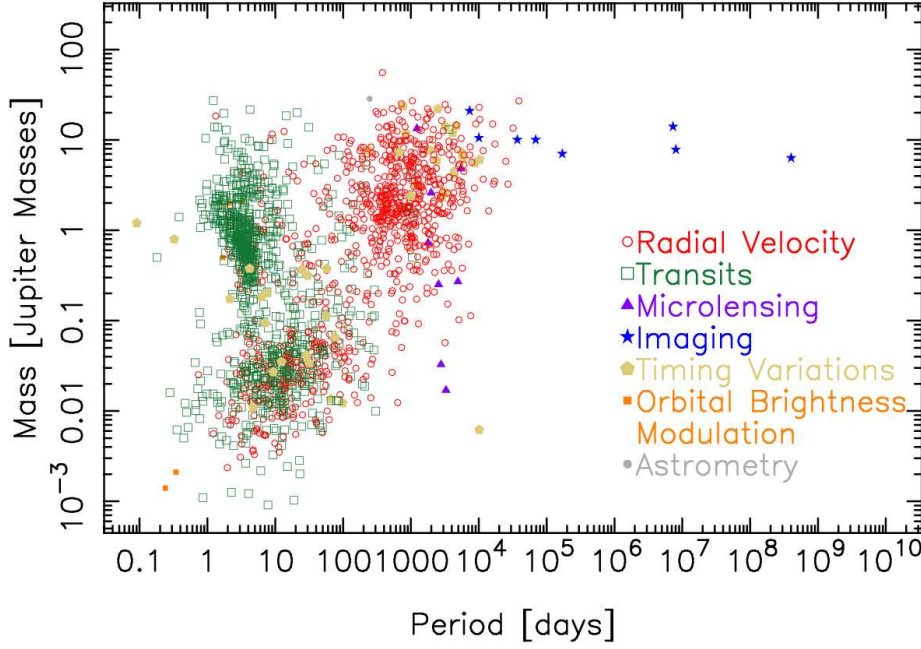
Figure 1.2 Mass-period distribution of confirmed exoplanets as of 23 November 2021. Different colours and symbols represent different discovery techniques. Credits: https://exoplanetarchive.ipac.caltech.edu/exoplanetplots/.

1.2 Observational methods

Being so faint with respect to their host stars, and having short angular separations, exoplanets are difficult to detect. Most of the discovery techniques rely on indirect measurements of time-varying signals (transit detection, radial velocities, transit timing variation, microlensing, astrometry), and only a couple of them can provide a direct measure of spatially-resolved signals (high contrast imaging, interferometry). So far, the most fruitful techniques that have been used to discover exoplanets are the transit method and the radial velocity technique. As shown in Figure 1.2, the two techniques account together for more than the 95% of the discovered exoplanets.

A short description of the three main discovery techniques employed in this thesis, i.e. radial velocities, transit photometry, and transit time variations, is reported in the following sections.

1.2.1 Radial Velocities

The radial velocity (RV) technique, used in the past century to study stellar binaries and stellar kinematics, is one of the first used for exoplanetary discoveries. It is indeed the technique that allowed for the discovery of 51 Pegasi b, the first exoplanet orbiting a main-sequence star, leading in 2019 to the assignment of the Nobel Prize in Physics to Michel Mayor e Didier Queloz.

This indirect method is based on the detection of the reflex motion caused on the host star by the presence of an orbiting planet. The motion of the star around the barycenter of the star-planet system results in a Doppler shift of the stellar lines. The RV (Doppler) measurement describes the projected motion

along the line-of-sight of the host star. Following Lovis & Fischer (2010), this can be expressed as

$$v_\mathrm{r} = \gamma + K \left[\cos(\omega + v) + e \cos(\omega)\right] \qquad (1.1)$$

where γ is the motion of the barycenter of the system, ω is the argument of pericenter, v is the true anomaly, e is the orbital eccentricity, and K is the RV semi-amplitude. In practical units, K can be written as

$$K = \frac{28.4329\,\mathrm{m\,s^{-1}}}{\sqrt{(1 - e^2)}} \left(\frac{P}{\mathrm{yr}}\right)^{-1/3} \frac{M_\mathrm{p} \sin(i)}{M_\mathrm{J}} \left(\frac{M_\star + M_\mathrm{p}}{M_\odot}\right)^{-2/3} \qquad (1.2)$$

with P and i indicating the orbital period and inclination, and M_p, $M_\star$ being the mass of the planet and the star, respectively. Usually, M_p is negligible with respect to $M_\star$, and if $M_\star$ is known, i.e. obtained combining spectroscopic analysis, photometry, parallax, and evolutionary models, we can infer the so-called ''minimum'', or projected, mass $M_\mathrm{p} \sin(i)$. It is not possible to directly measure the planetary mass, since RV analysis alone cannot give information on the inclination of the orbiting body, which could be either a small-mass planet on a nearly edge-on orbit, or a more massive planet on an highly-inclined orbit. This degeneracy can be solved if a measurement of the inclination is available, i.e. if the planet is transiting and the inclination is known from photometry (see Section 1.2.2).

The semi-amplitude induced by a planetary companion is usually very small. For example, Jupiter causes on the Sun a variation of $K \simeq 13\ \mathrm{m\,s^{-1}}$, while the Earth of only $K \simeq 10\ \mathrm{cm\,s^{-1}}$. In addition to the intrinsic difficulty of measuring such a small semi-amplitude, observing campaigns spanning several years are needed to appropriately sample the orbit of long-period planets, and to unambiguosly determine the nature of the RV signal, which could be also caused by aliasing or by stellar activity. Stellar activity (see Section 1.4.2), which includes phenomena like magneto-convection (granulation and super-granulation), pulsations, faculae/plage, starspots, and flares, can indeed induce RV variations that mimic a planetary signal, being most of the activity signals periodic or quasi-periodic. Moreover, activity prevents the detection of very small planetary signals. In fact, state-of-the-art spectrographs are moving towards a systematic accuracy of few tens of $\mathrm{cm\,s^{-1}}$ (see Section 1.3.1), but the RV variation induced by stellar activity is usually much higher. The development of techniques that mitigate stellar effects is a current prolific and rapidly evolving field, with different approaches, i.e. Gaussian Process regression (Dumusque, 2018; Lanza et al., 2018; Rajpaul et al., 2021; Wise et al., 2018), Deep Learning algorithms (de Beurs et al., 2020), post-processing corrections (Cretignier et al., 2021), which are leading to promising results.

1.2.2 Transit photometry

The first transit of an exoplanet was observed few years later than the discovery of 51 Peg b, as a result of the photometric monitoring of the RV-discovered planet HD-209458 (Charbonneau et al., 2000; Henry et al., 2000). With the launch of dedicated space-mission like *CoRoT* (Baglin et al., 2006) and *Kepler* (Borucki et al., 2010), this technique soon became the most productive in terms of discoveries, with many thousand of detected exoplanets and exoplanetary system candidates.
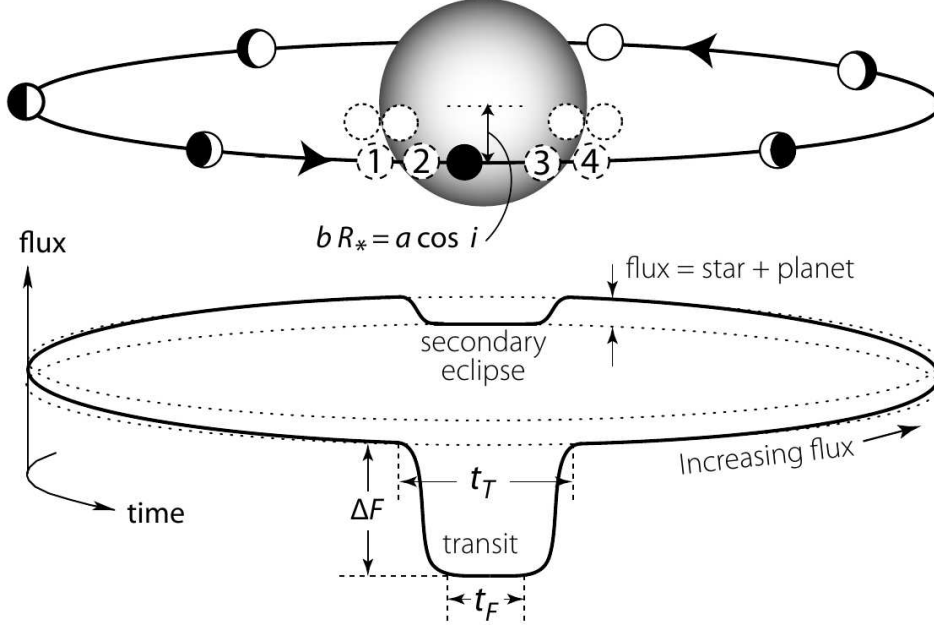
Figure 1.3 Sketch of an exoplanetary transit. The dashed, numbered circles show the four contact points. Parameters are described in the main text. Credits: M. Perryman, *The Exoplanet Handbook*, 2nd edition, Figure 6.26.

A transit (or primary eclipse) occurs when a planet passes in front of its host star, blocking part of the stellar light and causing a flux drop. An occultation (or secondary eclipse) occurs when the planet passes behind the stellar disk (Figure 1.3). After the transit, the bright side of the planet comes into view, and it produces a constant increase in the total flux, which drops again during the secondary eclipse. The extended, geometric formulation of a transit light curve (LC) is reported in Mandel & Agol (2002).

When the flux drop is maximum, i.e. when the planet is perfectly aligned with the center of the star, we have the central time of transit, or transit time (T_0). The flux variation (ΔF), or transit depth, is proportional to the ratio between the projected area covered by the planet and the stellar disk. In the simple case of circular orbits it can be expressed as:

$$\frac{\Delta F}{F} = \left(\frac{R_{\mathrm{p}}}{R_{\star}} \right)^2 . \tag{1.3}$$

As a reference, Jupiter has a transit depth of $\frac{\Delta F}{F} \simeq 10000$ ppm, while the Earth of $\frac{\Delta F}{F} \simeq 84$ ppm. The total transit duration (t_{T}) is the difference between the contact points 1 and 4 (Figure 1.3), while the full transit duration (t_{F}) is defined as the difference between contact points 2 and 3, being the end of the transit ingress and the beginning of the transit egress, respectively. The equation of both transit durations as a function of the Keplerian elements can be found in Winn (2010) and Kipping (2010). The determination of the contact times is affected by the limb-darkening (LD) effect. LD is related to the

temperature gradient from the stellar core to the atmosphere. In the center of the disk, we observe radiation coming from deeper, hotter regions (reached at optical depth $\tau = 2/3$), while at the disk edges, or limbs, we observe radiation coming from cooler, more superficial regions, since the line of sight enters the stellar photosphere at a steeper inclination. Therefore, a smaller ΔF is observed near the edge, and a deeper one at the center. This translates into less distinct contact points (in particular 2 and 3), and in the typical rounded bottom at the center of the transit.

Another parameter that influences the transit duration is the so-called impact parameter (b), which quantifies the difference between the centers of the planetary and stellar disks at the transit time. For circular orbits, the impact parameter can be approximated as:

$$b = \frac{a}{R_\star} \cos(i).$$ (1.4)

As shown in Figure 1.4, transit shape and duration change at varying impact parameter:

- $b = 0$: the planet passes exactly in the center of the stellar disk. The inclination is $90°$, and the transit duration is maximum.

- $0 < b < 1$: the planet crosses the disk between the disk center and the edges. The duration is shorter, and the transit changes towards a V-shape as b approaches 1.

- $b = 1$: the planet disk is not completely into the stellar disk. This configuration is called ''grazing transit''. In this case, the contact points 2 and 3 are not defined, and $t_T = t_F$.

- $b > 1$: the planet is not transiting at all.

From the study of a transit we can directly infer the planetary radius R_p, the inclination of the orbit and the semi-major axis (once the stellar radius $R_\star$ is known and well-constrained), as well as a precise orbital period, P, if more than one transit is observed. The measurement of the planetary radius is particularly important. If the mass can also be estimated, then average density follows, allowing for a first estimation of the inner bulk composition. This allows us to distinguish between gaseous and rocky planets, and provides a first clue about the habitability. Radius, mass and density are also important to investigate the formation and evolution processes, linking the observed planetary properties to population synthesis models and theoretical evolutionary frameworks (Morbidelli et al., 2012).

1.2.3 Transit Time Variations

A single planet on a Keplerian orbit transits at regular time intervals dictated by its orbital period P. In this case, the mid-transit time is described with a linear ephemeris:

$$T_{lin} = T_{ref} + P \times E \,,$$ (1.5)

where E is an integer transit number called ''epoch'', and T_{ref} is the transit time at $E = 0$. However, if one or more additional planets are present in the system, they gravitationally perturb the orbit of the
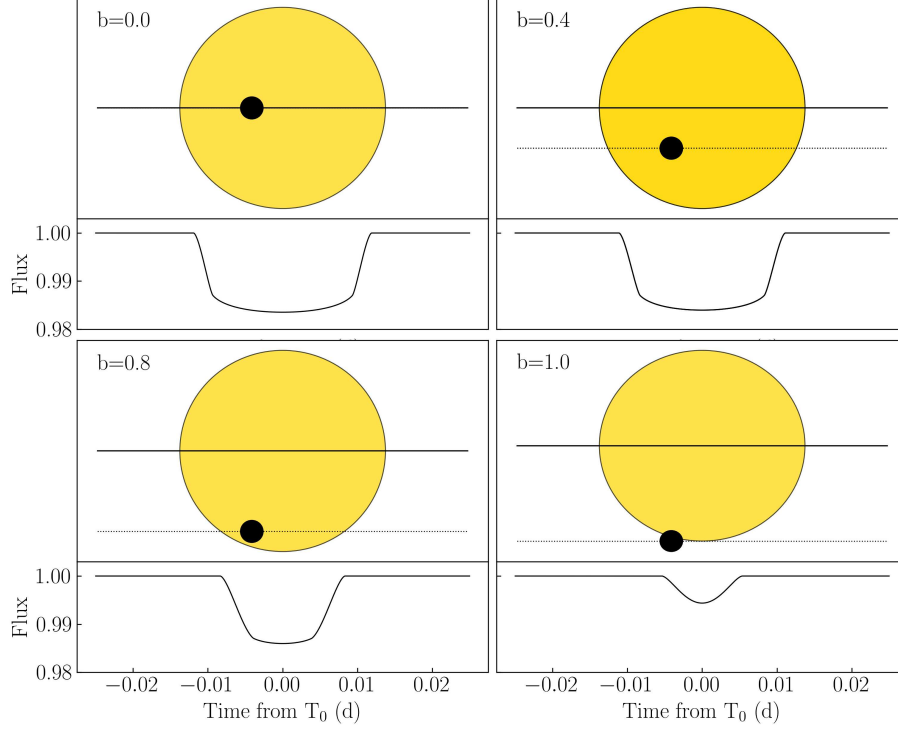
Figure 1.4 Examples of exoplanetary transits at varying impact parameter.

transiting planet, causing timing deviation with respect to a strictly Keplerian orbit. The variation of the mid-transit times with respect to the linear ephemeris of a purely Keplerian orbit are the base of the so-called Transit Time Variations (TTVs) technique (Agol et al., 2005; Holman & Murray, 2005). In the last decade, this technique proved to be an excellent method for the discovery and characterisation of multiplanetary systems (see e.g. Holman et al. 2010, Lissauer et al. 2011b, Borsato et al. 2014, Becker et al. 2015, Gillon et al. 2017, Freudenthal et al. 2019, Leleu et al. 2021b), with more than 250 known systems showing significant TTVs (Holczer et al., 2016; Kane et al., 2019).

The TTV signal is usually represented in the $O-C$ diagram (O minus C; Sterken 2005), where O are the observed transit times and C are the linear transit times (Eq. 1.5). Figure 1.5 shows an explanatory example. The TTV signal ($O-C$) of a given planet mainly depends on the perturber's mass, period, and eccentricity (Agol et al., 2005). In presence of, or close to, mean-motion resonances (MMRs)[1] the amplitude of the TTV signal is highly amplified, allowing for the detection of vary small mass

---

[1]A MMR occurs when planetary orbits are dynamically coupled, exerting regular, periodic gravitational influence on each other (Perryman, 2014, Sec. 2.6). The presence of a MMR is pointed out if the orbital periods are related by commensurabilities of the form $P_1/P_2 \simeq j/k$, with 1, 2 referring to the inner and outer planes, respectively, and j and k are small integers. The order of the resonance is given by $|j-k|$.
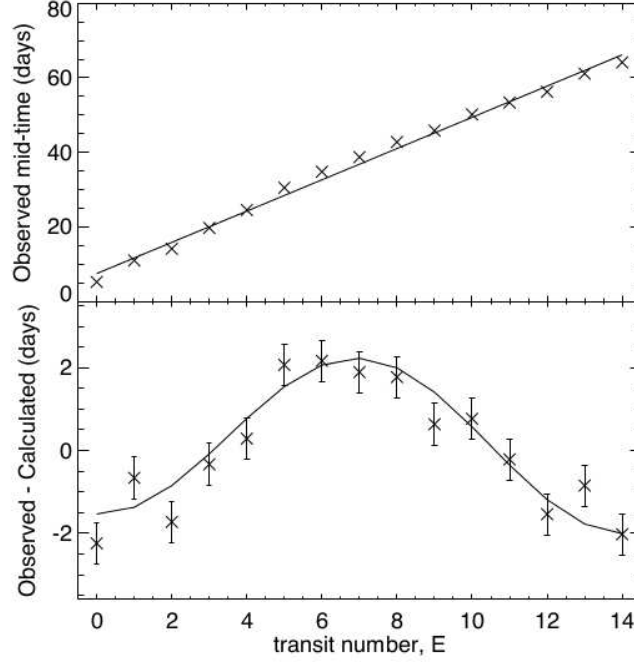
Figure 1.5 Explanatory model of the TTVs of the WASP-47 system (Becker et al., 2015), with a greatly exaggerated perturbation. *Top panel*: measured transit times, with over-imposed a least-squares linear fit. *Bottom panel*: $O - C$ diagram, corresponding to the residuals of the previous fit. The solid line represents a sinusoidal fit. From Agol & Fabrycky (2018).

planets. Moreover, Lithwick et al. (2012) showed that, in case of two planets in a near-first order MMR, the phase of the signal is predictable and the mutual gravitational interactions cause an anti-correlated signal among the two planets (see Figure 1.6) on a periodic timescale called ''super-period'' (P_{TTV}). The TTV super-period depends on the separation from the closest resonance, and it has the expression (Lithwick et al., 2012):

$$P_{\text{TTV}} = \frac{1}{|j/P_2 - k/P_1|} . \tag{1.6}$$

The TTV technique has been successfully applied to various areas of exoplanetary science. It has been used to confirm candidates in multiplanetary systems (through the detection of anti-correlated signals; see e.g. Holman et al. 2010, Lissauer et al. 2011a, Steffen et al. 2012b, Xie 2013), and to discover previously unknown planets, both transiting and non-transiting (e.g. Ballard et al. 2011, Fabrycky et al. 2012, Millholland et al. 2016, Malavolta et al. 2017a, Masuda 2017, Zhu et al. 2018), leading to a more complete view of system architectures and properties. For example, using TTVs to investigate the population of non-transiting systems offers a promising way of determining the frequency of non-coplanar systems and investigate their formation mechanisms (Xie et al. 2014, Lai & Pu 2017, Spalding & Millholland 2020, Masuda et al. 2020). Through the study of TTVs, planetary masses (and orbital parameters) of interacting planets can be constrained (e.g. Nesvorný et al. 2013, Ofir et al. 2014, Gillon
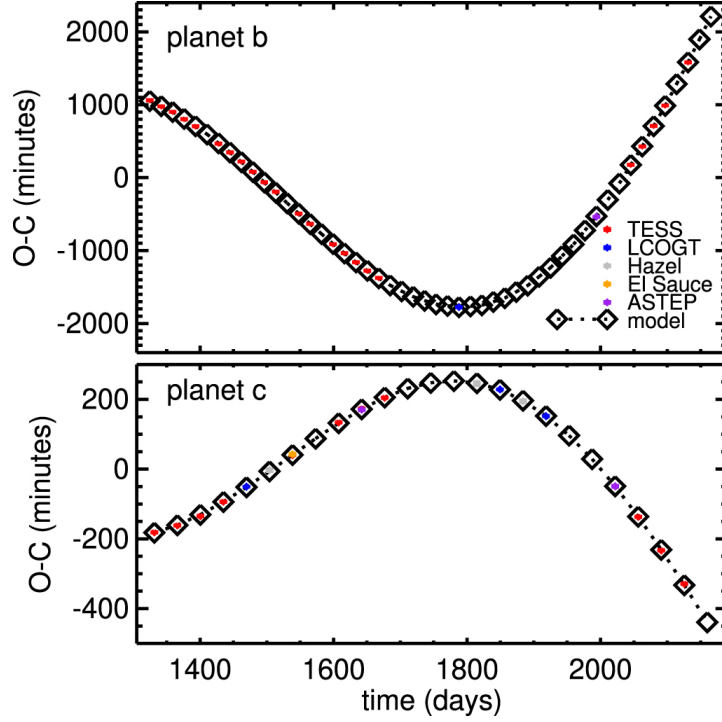
Figure 1.6 Observed anti-correlated TTV signals of the TOI-216 planets (coloured dots), with over-plotted the best-fitting model (diamonds, dotted line). From (Dawson et al., 2021).

et al. 2017), leading to average planetary densities determination and, consequently, allowing us to perform bulk inner structure modelling (e.g. Grimm et al. 2018, Agol et al. 2021). TTVs can also place limits on the presence of companions of hot Jupiters (Steffen et al. 2012a, Wu et al. 2018), and they can be used to investigate the presence of more specific accompanying objects, such as satellites (exomoons, Kipping 2009a,b; Lewis 2013) or Trojans (Ford & Gaudi 2006, Madhusudhan & Winn 2009). Moreover, the study of dynamically interacting systems can put constraints on formation and migration scenarios, e.g. resonant chain captures (Delisle, 2017), divergent encounters (Batygin & Morbidelli, 2013), etc.

1.3 Current and future missions

A selection of the main current and near-term discovery facilities for each detection method (chronologically ordered) is presented here, with a more detailed focus on the instruments directly employed in this thesis, which are HARPS-N, *TESS* and *CHEOPS*.

1.3.1 Radial Velocity facilities

HIRES

The High Resolution Echelle Spectrometer (HIRES, Vogt et al. 1994) is installed at the Keck-I 10-m telescope on Mauna Kea, Hawaii. It has a resolving power of about $25000 - 85000$ in the spectral range $300 - 1000$ nm. The wavelength calibration is made through an iodine absorption cell.

HARPS

The High Accuracy Radial Velocity Planet Searcher (HARPS, Mayor et al. 2003) is mounted at the ESO 3.6-m telescope in La Silla (Chile), and it is built to obtain a long-term RV accuracy of the order of 1 m s^{-1} (attained for spectral type later than G and for non-rotating stars, i.e. $v \sin i < 2$ km s^{-1}). It is an echelle spectrograph contained in a vacuum vessel, thermally stable within a few mK, to avoid spectral drift due to temperature and air pressure variations, and it is fed by two fibres, which collect the star light and record simultaneously a calibration reference spectrum or the background sky. It has a resolving power of 115000 and it covers the spectral range from 378 to 691 nm.

HARPS-N

HARPS-north (HARPS-N, Cosentino et al. 2012, 2014) is the northern twin of HARPS, and it is mounted at the 3.6-m Telescopio Nazionale Galileo (TNG) in the Roque de Los Muchachos Observatory (La Palma, Canary Islands). Its location in the Northern hemisphere was chosen to allow for synergies with the *Kepler* spacecraft (see Section 1.3.2), in particular for RV confirmation and follow-up of *Kepler* transiting candidates. It covers the same wavelength range of HARPS, with a resolving power of 115000. It is currently the best instrument in the Northern hemisphere for the discovery and characterization of exoplanets, down to Earth-size ones. Thanks to its high stability (with a global short-term precision of 0.3 m s^{-1}, and a long-term precision better than 0.6 m s^{-1}), it can achieve an accuracy better than 1 m s^{-1} in the RV measurements. The HARPS-N Project is a collaboration between the Astronomical Observatory of the Geneva University (lead), the CfA in Cambridge, the Universities of St. Andrews and Edinburgh, the Queens University of Belfast, and the TNG-INAF Observatory. Since its first light in 2012, it achieved major results in many different areas of exoplanetary science, including atmospheric analysis (e.g. Pino et al. 2020, Fossati et al. 2021), study of young planets (e.g. Malavolta et al. 2016, Damasso et al. 2020, Carleo et al. 2021), detection of Rossiter-McLaughlin effect (e.g. Esposito et al. 2017, Mancini et al. 2018, Rainer et al. 2021), and characterization of small-mass planets (e.g. Pepe et al. 2013, Bonomo et al. 2014, Buchhave et al. 2016, Haywood et al. 2018, Malavolta et al. 2018, Mortier et al. 2018, Rice et al. 2019, Rajpaul et al. 2021).

ESPRESSO

The Echelle SPectrograph for Rocky Exoplanets and Stable Spectroscopic Observations (ESPRESSO, Pepe et al. 2021) is an ultra-stable fibre-fed echelle high-resolution spectrograph mounted at the ESO

Very Large Telescope (VLT). It observes in the optical range (380–788 nm) with a resolving power of 70000, 140000 and 190000 in the Medium-, High-, and Ultra-High Resolution modes, respectively. ESPRESSO is the state-of-the-art spectrograph in the optical range, and it is built to reach an RV precision of 10 cm s^{-1} over a time-span of 10 years, aiming at detecting Earth twins in the habitable zone of solar-like stars.

EXPRES

The EXtreme PREcision Spectrometer (EXPRES, Jurgenson et al. 2016) is an optical fiber-fed echelle instrument installed at the 4.3-m Lowell Observatory Discovery Channel Telescope (DCT) in Arizona. It covers the wavelength range $380 - 780$ nm, and it has typical resolving power of 137500, with a maximum resolution of $R \sim 150000$ in some regions of the detector, as confirmed by its performance verification (Blackman et al., 2020). Like ESPRESSO, it is built with the aim of detecting Earth-like planets around Sun-like stars. To achieve this purpose, EXPRES is designed to reach an instrumental precision of 15 cm s^{-1}.

NEID

NEID (Schwab et al., 2016) is a recently commissioned high-resolution fiber-fed spectrograph mounted at the 3.5-m WIYN Telescope at Kitt Peak National Observatory in Arizona. It covers a wavelength range from 380 to 930 nm using a single detector, and it has a resolving power of $R \sim 100000$. NEID has a bottom-up error budget yielding an estimate of 27 cm s^{-1} single-measurement instrumental precision (Halverson et al., 2016), and, as the other extremely-precise RV facilities, it aims at detecting Earth-like planets in the habitable zones of nearby, bright G, K, and M dwarfs.

MAROON-X

The M-dwarf Advanced Radial velocity Observer Of Neighboring eXoplanets (MAROON-X, Seifahrt et al. 2018) is double-channel optical (blue: $500 - 670$ nm, red: $650 - 920$ nm) spectrograph with a resolving power $R = 85000$. It is mounted at the 8.1-m Gemini-North telescope, and it is built with the aim of detecting Earth-size planets in the habitable zones of mid- to late-M dwarfs. It is designed to deliver 1 m s^{-1} RV precision for M dwarfs down to and beyond $V = 16$ mag.

HARPS3

HARPS3 (Thompson et al., 2016) will be a fibre-fed, high resolution, high stability, echelle spectrograph to be installed on an upgraded and robotized 2.5-m Isaac Newton Telescope (INT) in La Palma (Canary Islands). It is being built as part of the Terra Hunting Experiment, a future 10-year RV measurement programme to discover Earth-like exoplanets. The design will be a close-copy of the very successful HARPS and HARPS-N instruments ($R = 115000$, wavelength range: $380 - 690$ nm), with

some innovations, i.e. a customised fibre adapter, a new continuous flow cryostat, detailed characterisation of the CCD, an optimised integrated polarimeter, and the instrument integrated into a robotic operation.

In addition to the above-mentioned optical spectrographs, more and more instruments are being developed to accomplish multi-wavelength observations. In fact, by coupling optical and near-IR observations it is possible to extend the M-dwarf exoplanet surveys, while at the same time providing strong constraints on wavelength-dependent noise sources, such as star spots. In this context, few representative instruments are:

- **CARMENES** (Quirrenbach et al., 2014), mounted at the 3.5-m telescope at the Calar Alto Observatory (Spain). It consists of two separated spectrographs covering the wavelength ranges $520 - 960$ nm and $960 - 1710$ nm, with resolution $R = 80000 - 100000$. It performs high-accuracy RV measurements (~ 1 m s^{-1}) with long-term stability.

- **GIARPS** (Claudi et al., 2017), installed at the TNG in La Palma. It targets the simultaneous use of the HARPS–N (optical) and GIANO–B (infrared, Oliva et al. 2012) spectrographs to achieve high-resolution spectroscopy over the wavelength range 380–2450 nm in a single exposure.

- **NIRPS** (Near Infra Red Planet Searcher, Bouchy et al. 2017), a high-resolution ($R = 100000$) infrared spectrograph ($970 - 1810$ nm) that will operated simultaneously with the optical spectrograph HARPS in La Silla. Its first light is foreseen in 2022 (Bouchy, 2021).

1.3.2 Transit-search missions

Ground-based surveys

To maximize the area of sky monitoring, survey searching for transiting planets from the ground have significantly benefited from the development of automated telescopes and telescope networks. A selection of the main ground-based facilities is reported here.

HATNet

The Hungarian Automated Telescope net (HATNet, Bakos 2018) is one of the most fruitful ground-based projects, and it comprises six telescopes in the Northern hemisphere (four at the Whipple Observatory in Arizona and two at Mauna Kea; Bakos et al. 2002, 2004) and further six telescopes located in three Southern sites: (1) Las Campanas, Chile (2) Siding Spring, Australia, (3) HESS γ-ray site, Namibia (Bakos et al., 2009, 2013). The telescopes can achieve a photometric precision of about $3 - 10$ mmag at $I \sim 8 - 11$ mag.

SuperWASP

Together with HATNet, the SuperWASP (Super Wide-Angle Search for Planets, Pollacco et al. 2006, Collier Cameron et al. 2009) survey has been responsible for the majority of transiting planets discovered from the ground. It consists in two robotic observatories (employing wide-field camera arrays) operating in both hemispheres of the sky, i.e. SuperWASP-North, located amongst the Isaac Newton Group (ING) of telescopes in La Palma, and SuperWASP-South in the South African Astronomical Observatory (SAAO). After pipeline processing, the typical long-term photometric root mean square (RMS) for a non-variable star is of about 4 mmag and 10 mmag for $V = 9.5$ mag and $V = 12$ mag, respectively.

LCOGT

The Las Cumbres Observatory Global Telescope (LCOGT, Brown et al. 2013) is a world-wide network of telescopes devoted to time-domain astronomy, including a total of 42 telescopes with apertures spanning from 40 cm to 2 m. The telescopes are located in seven sites[2], and they can work together as a single instrument. Even though not specifically designed as an exoplanet-search survey, LCOGT proved to be particularly suited for follow-up of planetary candidates from space telescopes such as *TESS* (e.g. Davis et al. 2020, Rodriguez et al. 2021, Burt et al. 2021, Shporer et al. 2021)[3].

NGTS

The Next-Generation Transit Survey (NGTS, Wheatley et al. 2017) is a wide-field survey that employs 12 robotic 20-cm telescopes located at the ESO Paranal Observatory (Chile) to search for transiting planets around bright K and early-M star, with a photometric accuracy of 1 mmag at $V = 13$ mag. In addition to searching for new planets, NGTS is also suited to perform ground-based follow-up of exoplanet candidates from space telescopes such as *TESS* (e.g. Armstrong et al. 2020, Hobson et al. 2021, Leleu et al. 2021a)[3] and, in future, *PLATO*.

Space missions

Kepler/K2

The NASA *Kepler* satellite (Borucki et al., 2010) has transformed the field of exoplanet research, both for its huge contribution to the number of discovered transiting exoplanets (counted in thousands), and for the deep insights into the diversity and richness of planetary architecture and into a broad range of physical planetary phenomena (see Section 6 of Perryman 2018). The 0.95-m telescope, launched in 2009, monitored more than 150000 stars (8–16 mag) a single field of 115 deg^2 for four years, observing

---

[2] https://lco.global/observatory/sites/.

[3] These are some representative examples, but many other *TESS* candidates have been followed-up/confirmed using NGST and LCOGT data. See the complete list of *TESS* confirmed planets (https://tess.mit.edu/publications/) for a more complete overview.

both in long-cadence mode ($\sim$ 30 min per image) and short-cadence mode ($\sim$ 1 min per image). It achieved a photometric accuracy of 30–40 ppm for 12 mag stars with data binned in 6.5-h intervals, and of $\sim$ 700 ppm h^{-1} over the 11–16 mag range. With several years of data, *Kepler* is capable of detecting signals down to several ppm, depending on orbital period.

After the end of the prime mission in 2013 due to the failure of a second reaction wheel, a revised phase began in 2014 under the name of *K2*. The *K2* mission observed 19 fields (or ''campaigns'') near the ecliptic plane for about 80 days each, and it ended in 2018 when the spacecraft run out of fuel. Despite the large systematics introduced by the pointing drift, it obtained a photometric precision of 80 ppm in 6-h intervals at $V = 12$ mag, within a factor of two of the main mission (Howell et al., 2014).

TESS

The *Transiting Exoplanet Survey Satellite* (*TESS*, Ricker et al. 2014) is a NASA all-sky survey devoted to search for transiting planets around bright ($V \leq 12$ mag) and nearby stars. The primary goal of *TESS* is to discover planets smaller than Neptune that transit stars bright enough to enable follow-up spectroscopic observations (which was not always possible with *Kepler* targets, being often too faint) that can provide planet masses and atmospheric compositions. *TESS* observes from an elliptical high Earth orbit (HEO) in a 2:1 lunar-resonant configuration with an orbital period of $\sim$ 13.7 days. At the orbit perigee, science operations are interrupted for no more than 16 h to downlink data. *TESS* has four identical, highly optimized, wide-field, red-optical (600 to 1000 nm) cameras with an effective pupil diameter of 10-cm that together can monitor a 24° $\times$ 96° strip of the sky, called ''sector''. Each sector is monitored for 27 days (comprising two *TESS* orbits interrupted by the downlink time).

Launched in 2018, during its primary 2-year mission *TESS* observed a total of 26 sectors, 13 in the Southern and 13 in the Northern ecliptic hemisphere, with sector overlap at the ecliptic poles to provide additional sensitivity toward smaller and longer-period exoplanets (Figure 1.7). *TESS* achieved a photometric precision of 230 ppm in 1-h intervals on a 10 mag star, well within the the mission requirements. It delivered both short-cadence light curves (2-min exposures) of specifically targeted stars, and 30-min full-frame images (FFIs) of the entire field of view. Since 2020, *TESS* entered its first mission extension, lasting slightly more than 2 years. During Year 3 of the mission (July 2020-July 2021, 13 sectors), the Southern ecliptic hemisphere has been re-observed. During Year 4+ (July 2021-September 2022; 16 sectors), parts of the Northern ecliptic hemisphere will be re-observed, and a 240° swath of the ecliptic will be observed for the first time, including the locations of the *K2* campaign fields. In the extended mission, a new 20-s cadence data mode has been introduced, and the FFI cadence has changed to 10 m. Since the beginning of the science operations, *TESS* discovered more than 170 exoplanets, while $>$ 5000 planetary candidates, denoted as *TESS* Objects of Interest (TOIs), are still awaiting confirmation.

CHEOPS

The *CHaracterizing ExOplanet Satellite* (*CHEOPS*, Benz et al. 2021) is the first ESA small-class mission dedicated to the study of bright, nearby stars that are already known to host exoplanets, exploiting
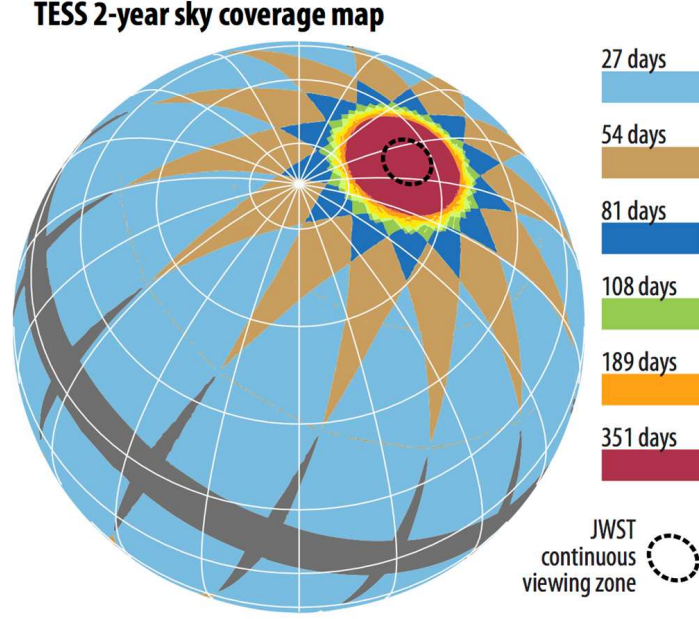
Figure 1.7 *TESS* sky coverage map of the 2-year primary mission. Each sector is highlighted in light blue, and the different colours represent the total duration each sky region is observed. Credit: MIT/NASA.

ultra-high precision photometric observations. *CHEOPS* is a partnership between ESA and Switzerland, with a dedicated Consortium led by the University of Bern, and with important contributions from 10 other ESA-member States. Launched in December 2018, *CHEOPS* is operating in a Sun-synchronous, low Earth orbit (LEO) at ∼ 700 km altitude. *CHEOPS* is a 33.5-cm on-axis telescope observing on a wide wavelength band from 400 to 1100 nm. In-orbit performance studies demonstrated that *CHEOPS* achieves a noise level of ∼ 15 ppm per 6-h intervals for $V = 9$ mag stars, corresponding to the transit of an Earth-sized planet orbiting a G5 dwarf ($R_\star \simeq 0.9\ R_\odot$) in a 60-d orbit detected with a SNR > 10, and of 75 ppm per 3-h intervals for $V = 12$ mag stars, corresponding to a Neptune-sized planet around a K dwarf ($R_\star \sim 0.7 R_\odot$) with a period of 13 days detected with SNR = 30 (Benz et al., 2021). To obtain high photometric performances by mitigating the effect of pointing jitter and imperfect flat-field correction, avoiding at the same time saturation for bright star, *CHEOPS*'s PSF has been purposely defocused (Figure 1.8).

The main science goal of *CHEOPS* is to allow for a better understanding of planet formation and evolution, by setting new constraints on planetary structures thanks to accurate knowledge of radii and masses. To achieve this, during the 3.5 years of its primary mission, *CHEOPS* will focus on different science topics, mainly:

- Determine the mass-radius relation of planets, focusing on objects with small radii, rare objects (extreme in density, unusual radius, etc.), and planets in multiplanetary systems. Synergies with the *TESS* mission are naturally entailed.

- Exploring system architectures and migration scenarios using TTVs .
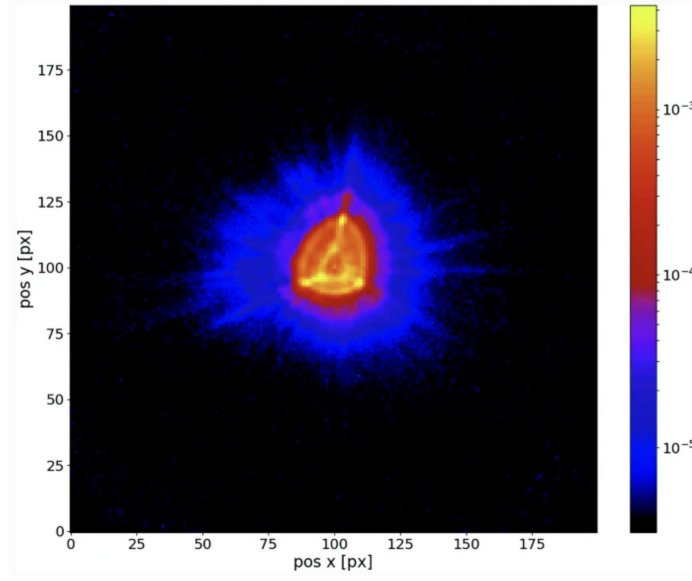
Figure 1.8 *CHEOPS*'s PSF flux distribution as measured during the in-orbit commissioning. Due to the on-purpose defocus, 90% of the PSF flux is comprised in 16 pixels. From Benz et al. (2021).

- Study in details dust clumps in edge-on debris disks around young stars.

- Probe the atmosphere of known hot Jupiters to study the physical mechanisms and efficiency of the energy transport from dayside to nightside.

- Investigate unusual features in photometry, i.e. due to dynamical effects (tidal dissipation, ellipsoidal deformation due to tidal distortions), or to the presence of moon and rings.

PLATO

After *TESS* and *CHEOPS*, the next mission dedicated to the study of transiting planets is *Planetary Transits and Oscillations of stars* (*PLATO*, Rauer et al. 2014). *PLATO* is an ESA M-class mission planned for launch by end 2026, which aims at detecting and characterise exoplanets transiting bright ($V \leq 11$ mag) and nearby stars. *PLATO* is expected to discover thousands of planets, with an emphasis on Earth- and super-Earth planets in the habitable zone of solar-like stars, accessible thanks to *PLATO*'s long uninterrupted observations (Nascimbeni et al., 2021). Through parallel asteroseismology, *PLATO* also aims to characterise planetary radii at $\sim 2\%$ precision, masses at $\lesssim 10\%$ precision, and ages at $\sim 10\%$ precision. The *PLATO* optical design consists in 26 telescopes of 20-cm each (24 with 25-s cadence, and 2 with 2.5-s cadence), optimized for a single $450 - 1000$ nm band pass, providing a wide field of view (~ 2000 deg^2) and a large magnitude range (4–16 mag). *PLATO* will be operated from the Lagrange point L2.

In addition to the above mentioned missions, specifically dedicated to the study of transit photometry, two other missions worth mentioning are *JWST* and *ARIEL*.

With its 6.5-m primary mirror, the *James Webb Space Telescope* (*JWST*, Gardner et al. 2006) will address a huge variety of galactic and extra-galactic topics. The satellite has been successfully launched on 25 December 2021, and it is now on route towards L2. Regarding exoplanetary science, it will provide high signal-to-noise light curves and spectra of transiting planets. *JWST* should provide light curves of the primary and secondary eclipses of planets down to $\sim 1\ R_{\oplus}$ (and below), and it could be able to detect H_2O, CH_4, CO (and eventually PH_3) in gas giants (Wang et al., 2017).

The *Atmospheric Remote-sensing Infrared Exoplanet Large-survey* (*ARIEL*, Pascale et al. 2018), is an ESA M-class mission planned for launch by 2029. With its 1-m telescope, *ARIEL* will observe a sample of ~ 1000 planets simultaneously in visible and infrared wavelengths to study what exoplanets are made of, and how they formed and evolved (Tinetti et al., 2018). It is the first mission specifically dedicated to measuring the chemical composition and thermal structures of hundreds of transiting exoplanets.

1.4 Host stars

The knowledge of fundamental properties of exoplanet host stars is of paramount importance in the context of exoplanet characterization, since accurate absolute stellar quantities such as luminosity, mass, and radius are relevant to any interpretation of the relative values derived from transit and RVs measurements. Moreover, the knowledge of exoplanet host stars provides clues for a deeper understanding of the conditions and dependencies relevant to planet formation and evolution. In fact, the host star metallicity enters into the planetary formation models, as well as age and rotation enter detailed system evolution modelling.

1.4.1 Host star properties

The properties of exoplanet host stars are derived from a combination of astrometric, photometric, and spectroscopic observations, interpreted predominantly within the context of stellar evolutionary models.

Spectroscopic analyses provide robust estimates of some basic stellar quantities. Through the study of the equivalent width of absorption lines, the main quantities influencing the relative line strengths and line profiles can be derived, namely effective temperature (T_{eff}), surface gravity ($\log g$), microturbulence velocity (ξ), and metallicity ([Fe/H]), where [Fe/H] is the log number abundance of Fe/H relative to the solar value[4]. This analysis usually employs atmospheric models, often assuming a plane-parallel geometry (e.g. Kurucz 1993) under the assumption of local thermodynamic equilibrium (LTE), and basic atomic data, mainly the line oscillator strengths (e.g. Luck & Heiter 2005, Sousa et al. 2007, Santos et al. 2013, Mortier et al. 2013). To perform this kind of analysis, a medium/high spectral resolution is required ($R \sim 50 - 70000$), with a spectral range covering most of the optical spectrum at high SNR (several hundred per resolution element). A second, different approach is based on the spectrum-matching technique, which consists in fitting directly the observed spectra with synthetic ones calculated

---

[4]Note that the term *metallicity* is typically used to encompass all chemical elements heavier than He, and that the iron abundance [Fe/H] is frequently used as reference for the metallic content of exoplanet host stars.

from model atmospheres and atomic and molecular line data (e.g. Valenti & Fischer 2005, Buchhave et al. 2012, Buchhave et al. 2014). In either case, typical uncertainties are of the order of $40 - 70$ K for T_{eff}, and of $0.02 - 0.5$ dex for metallicity. If high-quality spectra are available, both techniques can be used to derive the abundances of other chemical elements (i.e. Li, C, N, O, Na, Al, Mg, Ti) using individual spectral lines (e.g. Santos et al. 2000, Bodaghee et al. 2003, Valenti & Fischer 2005, Adibekyan et al. 2012, Santos et al. 2013).

Stellar mass, radius, and age cannot be directly inferred from observations, and their derivation is usually based on the comparison with stellar evolutionary models. The comparison with theoretical models is not straightforward, and requires accurate knowledge of (I) stellar temperature (usually derived through spectroscopy), (II) distance (now mainly provided by *Gaia*'s parallaxes), to convert the observed apparent magnitude into absolute magnitude, and (III) bolometric correction (derived from photometric observations in different bands), to convert absolute magnitude into bolometric magnitude, which is the quantity used in the theoretical evolutionary models. Moreover, a variety of theoretical models are available, presenting different implementations and treatments of physical stellar processes (stellar opacity, convective overshooting, rotation). Stellar radius, mass, and age are commonly estimated using the isochrone fitting method, which matches relevant observables to a grid of stellar evolutionary models. Stellar radius can also be derived using various photometric and spectroscopic methods, mainly based on the infrared flux method (IRFM, Blackwell & Shallis 1977), spectral energy distribution fitting, and surface brightness relations. Stellar age can also be derived through gyrochronology using period-age calibrated relationships (e.g. Barnes 2003, Angus et al. 2015), if accurate measurements of the stellar rotation period can be obtained. Moreover, when applicable, asteroseismology can provide accurate age estimations using pulsation frequency analysis (e.g. Christensen-Dalsgaard 2004, Chaplin & Miglio 2013). Finally, lower limits on stellar ages can be obtained from the abundance of Li as a function of T_{eff} based on calibrated relationships (e.g. Jeffries et al. 2002; Sestito & Randich 2005), or from the Ca II activity-age relation (e.g. Pace & Pasquini 2004; Wright et al. 2004).

1.4.2   Stellar activity

In the characterization and understanding of exoplanet hosts stars, stellar activity plays an important role. With current and future spectrographs approaching the m s^{-1} and cm s^{-1} level precision (Section 1.3.1), the contribution of stellar activity to the astrophysical noise, or *jitter*, of the RVs measurements becomes a prominent issue for the accurate determination of the underlying Keplerian motions caused by orbiting planets. Time-varying intrinsic stellar variability can lead to spectral line profile variation causing spurious RV measurements that can mask or mimic planetary signals. For G and K dwarfs, stellar signals affecting RV measurements are mainly due to (Dumusque et al., 2017):

- Solar-type oscillations: pressure waves (p-modes) propagating at the surface of solar-type stars induce a dilatation and contraction of the external envelopes, causing variations of the order of tens of minutes with amplitudes from 10 to 400 cm s^{-1}.
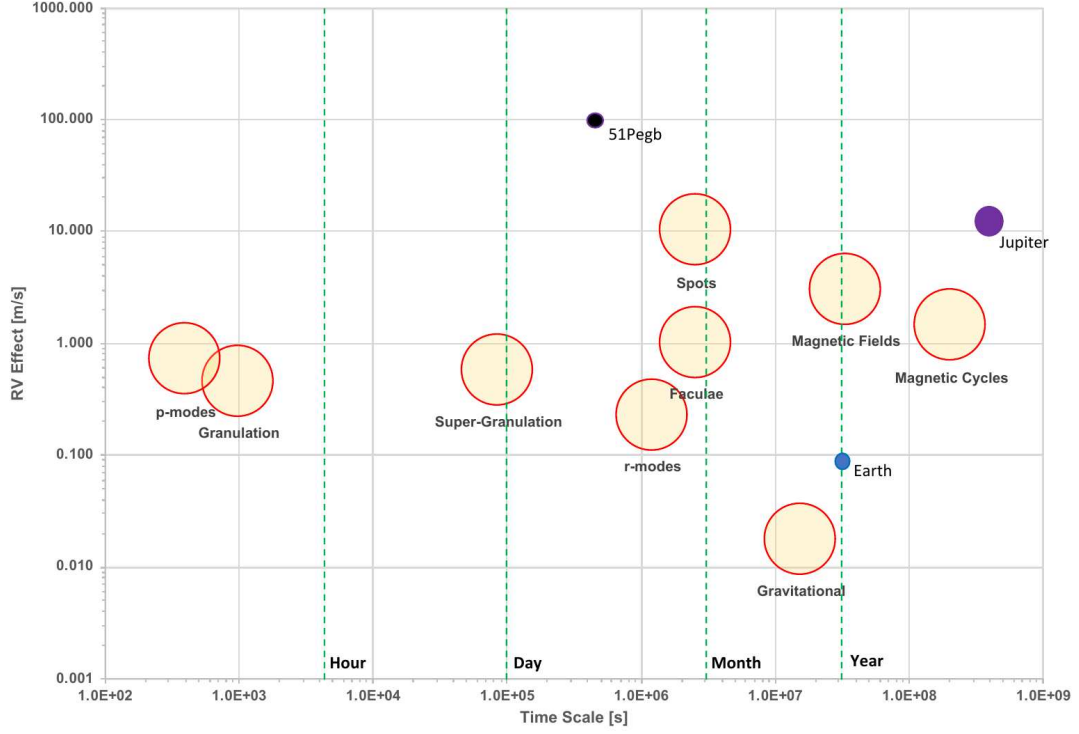
Figure 1.9 Stellar activity effects at changing periods and semi-amplitudes. Credits: S. Gaudi, *The EPRV Initiative*, 2020 Sagan Exoplanet Summer Virtual Workshop.

- Granulation and super-granulation phenomena: the magneto-convective motions on the stellar surface induce variations at the m s^{-1} level on timescale from few minutes to 48 hours.

- Short-term activity on stellar rotation period time scale: in presence of evolving surface magnetic inhomogeneities, mainly spots and plages, stellar rotation induces variations with amplitudes from 1 to 100 m s^{-1}.

- Long-term magnetic activity: magnetic fields induce variations at m s^{-1} level on the magnetic cycle period time scale (several years).

Figure 1.9 summarizes the main activity effects on different timescales. The overall effects of stellar jitter can be accounted for in the RV standard deviation as (Wright, 2005):

$$\sigma_{RV}^2 = \sigma_{meas}^2 + \sigma_j^2, \tag{1.7}$$

where σ_{RV} is the RV standard error, σ_{meas} is the contribution due to the measurement error, and σ_j is the jitter term including all the contributions from stellar activity.

On short timescales, the most difficult signals to treat are the non-periodic, stochastic signals arising from the evolution and decay of active regions. Since the induced RV variations correlate with stellar chromospheric activity, various chromospheric activity indicators can be used as proxies to identify and

mitigate the stellar noise. Among them, the most used ones are the Ca II H and K lines, as well as Hα, He I D3, and Na I D1 and D2, whose emission in the core is enhanced by the strong magnetic fields inducing spots and plagues. A frequently used indicator is the Mt. Wilson S-value, defined as the ratio of the sum of the flux in the cores of the Ca II H and K lines to the sum of two continuum bands (redward and blueward) of the H and K lines (Wilson, 1978). By converting the S-index into a standard scale and correcting for the residual photospheric emission, the non-dimensional chromospheric $\log R'_{HK}$ index can be derived (Noyes et al., 1984). The use of the $\log R'_{HK}$ index allows for accurate comparisons of the chromospheric emission across different spectral types, removing any dependencies on the bolometric flux. Other quantities that can be used to identify stellar activity are the bisector velocity span (BIS, Queloz et al. 2001), i.e. the difference between the average velocity values in regions at the top and the bottom of a typical line profile, and the full width at half-maximum (FWHM) of the cross-correlation function (CCF, Baranne et al. 1996; Pepe et al. 2002). In presence of a correlation between the RV signal and the BIS and/or the FWHM, the signal is likely due to stellar activity. To mitigate and correct the effects of short-term stellar activity, various techniques have been applied, and new methodologies are currently being investigated, with promising results. Among them, the use of linear correlations between different observable, i.e. RVs, BIS, FWHM, photometry, magnetic field strenght (e.g. Queloz et al. 2001, Pepe et al. 2002, Boisse et al. 2009, Hébrard et al. 2014), fitting sine wave and harmonics at the stellar rotation period (Boisse et al., 2011), use of red-noise models (Tuomi et al. 2013; Feroz & Hobson 2014), avoiding the impact of activity using wavelength-depend criteria (Anglada-Escudé & Butler, 2012; Tuomi et al., 2013), modelling activity-induced signals with Gaussian process regression, whose covariant properties are shared either with the stellar photometric variations (Haywood et al. 2014; Grunblatt et al. 2015), or a combination of several spectroscopic indicators (Rajpaul et al., 2015), or determined from the RVs themselfs (Faria et al., 2016), PCA decomposition of the autocorrelation function of the CCF (Collier Cameron et al., 2021), machine-learning algorithms to model the changing shape of the CCF (de Beurs et al., 2020, 2021).

1.5 Planetary characterization

Given the high and constantly increasing number of discovered exoplanets, we can now start focusing not only on planets discovery, but also on planets characterization. The field of exoplanetary characterization hugely benefited from the advent of the transit technique, in particular regarding the investigation of internal structures and atmospheres. Densities derived from radii and masses are now used to investigate the interior structure and composition of exoplanets, and first insights on atmospheric composition and dynamic are coming from optical and infrared transit and eclipse spectroscopy, with huge improvements expected in the near future thanks to *JWST*'s observations. The investigation of terrestrial planets composition and atmospheres is currently of great interest in the wider context of the search for life in the universe. Planets orbiting in the habitable zone with a rocky surface that may support the presence of water would be good targets for detailed atmospheric studies, aiming at identifying bio-signatures that may attributed to life forms.
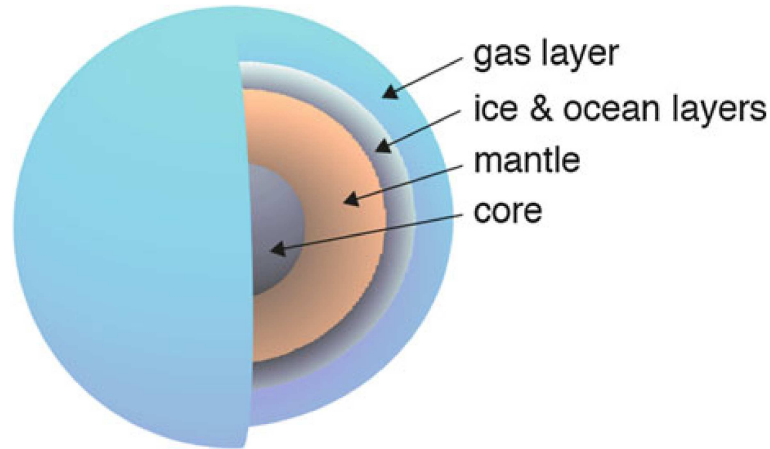
Figure 1.10 Schematic view of a terrestrial exoplanet interior. From Dorn et al. (2018a).

1.5.1 Internal structure

Physical models of exoplanet interiors span two main regimes, namely the high-mass, low-density regime of giant planets dominated by H/He gaseous envelopes, and the small-mass, high-density regime of solid planets, dominated by metallic cores and silicate-rich and/or ice-rich mantles.

In gas-rich planets, interior modelling is closely connected with atmospheric modelling. Recent atmospheric models couple the emergent flux with the assembly by core accretion to predict the pressure–temperature relation, radii as a function of mass, and colours and spectral features arising from specific atomic and molecular species, when combined with estimates on the probable bulk chemical composition (e.g. Cooper & Showman 2006; Fortney et al. 2007; Burrows et al. 2008; Lodders 2010).

In low-mass solid planets, interior modelling aims to determine the most likely internal composition given a specific planet's measured mass and radius, and, in turn, to derive the mass–radius relation for a given internal composition. A generic exoplanet interior model usually consists of concentric shells representing core, mantle, ice, ocean, and gas layers (Figure 1.10). The primary objective of interior characterization is to constrain the mass and composition of each layer to obtain first-order estimate of the hydrostatic (equilibrium) state of a planet (Dorn et al., 2018a). Actually, from the measurement of mass, radius, and density alone it is not possible to derive a unique internal physical and chemical composition. However, by combining the knowledge of solar system planets properties with thermal equilibrium calculations to predict the occurrence of particular species, and computing their equations of state (EoS) under assumed internal and external physical conditions, plausible models of exoplanetary interiors are being developed (e.g. Fortney et al. 2007; Rogers & Seager 2010; Lopez & Fortney 2014; Dorn et al. 2015; Dorn et al. 2017; Zeng et al. 2019; Dorn & Lichtenberg 2021). The three main compounds believed to form from the cooling and accretion of a protoplanetary disk and constituting the building blocks of planets are usually referred to as gas, rock (non-volatile condensates), and ice (volatile condensates). The amounts of gas, rock, and ice accreated by the planet determine its mass

and bulk composition, while the EoS determine which phases will be present, along with the planetary size. The gas component is mainly constituted by H and He, and it is expected to contribute to the $\sim 98.5\%$ of the disk mass, leaving the remaining $\sim 1.5\%$ to the rock and ice components. The term ''rock'' usually refers to elements in mineral phase, including Si, Mg, Ca, Al, and Ti that form oxides and silicates, as well as Fe–Ni metal alloys and FeS. In planetary science, the term ''ice'' encompasses volatiles with a melting point between ~ 100–200 K, even when in a hot and/or liquid form. In this context, ''ice'' embraces various substances containing C, N, and O. Among them, water ice is the most important, both because O is an abundant element, and because it condenses at the highest temperature, but other possibly abundant ices are CH_4, CO, CO_2, N_2, and NH_3. From the initial formation of a planet by accretion of different amounts of ice, rock, and gas, subsequent evolution in temperature and pressure conditions can modify the elements phases and redistribute their radial profile through chemical and gravitational differentiation. In the temperature-pressure conditions of planetary interiors, interactions between molecules, atoms, ions and electrons are dominant and electron degeneracy effects play a crucial role, making the derivation of an accurate EoS a challenging task. The correct description of the structure and cooling of a planet thus requires the knowledge of the EoS and the transport properties of various materials (see Baraffe et al. 2014 and Dorn et al. 2018a for comprehensive reviews of commonly used EoS and internal structure modelling).

As an outcome of the (unexpected) observed properties of various exoplanets, from early models of terrestrial planets supposing a classic Earth-like composition, i.e. dominated by silicates and iron-peak elements, more varied and even exotic planetary compositions have been proposed and investigated. In particular, two classes of Earths/super-Earth received a specific attention, the so-called ''lava planets'' and the ''ocean'' (or ''water'') worlds.

Lava planets are an hypothetical category of planets with the surface mostly or entirely covered by molten lava. This could be due to high stellar irradiation impacting a close-in ($P < 1$ d), tidally locked exoplanet having a density consistent with a rocky composition. The expected high surface temperature ($2500 - 3000$ K) on the day side, continuously facing the star due to spin-orbit synchronisation, will cause fusion and vapour fractionation of rocks, producing a 'lava ocean' of refractory components. Suggested examples of observed exoplanets are CoRoT–7 b (Léger et al., 2009), Kepler-10 b (Batalha et al., 2011), Kepler-78 b (Sanchis-Ojeda et al., 2013), 55 Cnc e (McArthur et al., 2004), and K2-141 b (Malavolta et al., 2018).

Ocean planets, or water worlds, are an hypothetical category of planets dominated by volatiles such as water ice (Kuchner 2003; Léger et al. 2004), which could be formed beyond the the snow line[5], and then possibly migrated inward. One of the first proposed candidates was GJ 1214 b (Charbonneau et al., 2009). With a density of 1.9 g cm^{-3}, the planet could be modelled by a dense Fe-S core surrounded by a H–He envelope. However, its small mass argues against the accretion of an extended gaseous envelope, and suggests instead an internal composition with a Fe–Ni core, a silicate mantle, and $\sim 50\%$ of its mass in water, with a possible thin H–He envelope (Marcy, 2009). Due to the degeneracy in the interior

---

[5]Defined as the distance in the solar nebula from the central protostar where it is cold enough for volatile compounds such as water, ammonia, methane, carbon dioxide, and carbon monoxide to condense into solid ice grains.

models, which results in a wide compositional range that can match a given bulk density, the secure identification of ocean planets may still be questionable (unless a significant gas layer can be excluded by other means), but more and more promising candidates are being identified.

1.5.2 Atmospheres and atmospheric evolution

For low-mass solid planets, a research field correlated to the study of internal structures is the investigation of the nature and evolution of their atmospheres. Indeed, terrestrial planets could have acquired a (modest) gaseous envelope during their formation, by capture of nebular gases (e.g. Pollack & Black 1982; Ikoma & Genda 2006; Stökl et al. 2016) or by outgassing (e.g. Elkins-Tanton & Seager 2008; Kite et al. 2009; Schaefer & Fegley 2010). It is of great interest to investigate the evolution of such atmospheres, that is, whether and how the original envelopes have been retained or eroded during time. In fact, atmospheric evolution processes play an important role in shaping the distribution of the observed planet population. Among the currently observed features in the planet population, the two most evident ones are the hot sub-Jovian desert (Davis & Wheatley 2009; Szabó & Kiss 2011; Mazeh et al. 2016), and the sub-Neptune radius gap (Fulton et al., 2017). Both features are believed to be the result of atmospheric evolution processes, and in particular atmospheric escape, even though for the radius gap the main escape-driving mechanism is still unclear (Owen & Wu 2017; Jin & Mordasini 2018; Ginzburg et al. 2018; Gupta & Schlichting 2019; Loyd et al. 2020). In general, atmospheric escape drives the long-term evolution of planetary atmospheres. Therefore, through atmospheric evolution studies we can obtain further insights on the observed planet population, as well as gather critical information about planet formation (e.g. Jin et al. 2014; Kubyshkina et al. 2019a).

Atmospheric escape is driven by the high-energy X-ray and extreme EU (EUV; together XUV) emission of the host star (blow-off; e.g. Watson et al. 1981; Lammer et al. 2003) and/or by internal atmospheric thermal energy and low planetary gravity (boil-off; e.g. Stökl et al. 2015; Ginzburg et al. 2016; Owen & Wu 2017; Fossati et al. 2017). To compute atmospheric evolution calculations, analytical formulas have been employed (e.g. in the energy-limited approximation; Watson et al. 1981; Erkaev et al. 2007), as well as more detailed models of XUV heating, mass-loss rates, lifetimes and particle trajectories (e.g. Lammer et al. 2008; Tian 2009; Lammer et al. 2013; Jin et al. 2014; ; Kurosaki et al. 2014; Owen & Wu 2016; Dong et al. 2017), including sophisticated computations of mass-loss rates based on hydrodynamic upper atmosphere models accounting simultaneously for boil-off and blow-off process (Kubyshkina et al. 2018; Kubyshkina et al. 2019a; Bonfanti et al. 2021a). Such models have been recently applied to constrain the past atmospheric evolution of various observed systems, e.g. HD3167, K2-32, Kepler-11, and v^2 Lup (Kubyshkina et al. 2019a,b; Delrez et al. 2021).

1.6 Multiplanetary systems

In the context of exoplanetary characterization, multiplanetary systems offer a unique opportunity for investigations of composition, formation and evolution processes, allowing for comparative planetol-

ogy. The first discovery of a star hosting more than one planet occurred with the RV observations of
ν And, found to host a triple planetary system (Butler et al., 1999). Various other RV discoveries came
afterwards, e.g. GJ 876 (Marcy et al., 2001), 47 UMa (Fischer et al., 2002), HIP 14810 (Wright et al.,
2009). After the launch of the *Kepler* spacecraft, Holman et al. (2010) presented the discovery of the
first transiting multiplanetary system around Kepler-9. Analyses of *Kepler* data led to an unprecedented
number of multiplanetary systems discoveries, and now *TESS* is increasing this sample, which counts
more than 820 systems[6]. The highest multiplicity has been reached with the 8-planet system Kepler-90
(Cabrera et al. 2014, Shallue & Vanderburg 2018), whose planets have a similar configuration to our So-
lar System, with the small planets found orbiting close to their star, and the larger planets found farther
away. The second highest-multiplicity system is TRAPPIST-1 (Gillon et al., 2017), which hosts seven
Earth-sized planets, three of them (e, f, and g) located in the habitable zone of the star. Some dozens
of six-, five-, and four-planet systems have been observed, while the great majority of the discovered
systems shows two or three planets (also due to detection biases).

The population of multiplanetary systems show a rich diversity in planetary architectures (Lissauer
et al. 2011a, Fabrycky et al. 2014, Winn & Fabrycky 2015). The observed and statistically inferred prop-
erties of multiplanetary systems can provide important information on planet formation and evolution
theories (e.g. Fang & Margot 2012, Hansen & Murray 2013, Pu & Wu 2015, Steffen & Hwang 2015,
Becker et al. 2020). In fact, the current orbital configuration of any planetary system is a consequence
of all the physical processes that marked its evolution and led the system to its present state. Several
processes can sculpt the architecture of a planetary system, including the specific formation pathways
of individual planets, secular and/or chaotic dynamical interactions, influence of the host star, imprints
due to the initial conditions of the protoplanetary disk, environmental effects due to the properties of
the star forming region, etc. Interpreting the observed diversity of the system architectures is still an
open problem (Winn & Fabrycky, 2015), and it currently triggers active investigations in this research
area (e.g. Mordasini 2018, Mulders et al. 2019, He et al. 2019, Dietrich & Apai 2020, Venturini et al.
2020, Chevance et al. 2021, Mishra et al. 2021).

While exploring the diversity of system architectures, some trends emerged. An anti-correlation
between system multiplicity and orbital eccentricities was first identified in RV-detected systems (Lim-
bach & Turner, 2015), and further confirmed both using the *Kepler* sample of transiting planets (Xie
et al. 2016, Van Eylen et al. 2019) and through the study of combined RV and transit discoveries (Zinzi
& Turrini, 2017).

A trend in the planetary radius distribution, with smaller planets orbiting closer to the host star with
respect to larger planets, was first noted in the *Kepler* exoplanet sample by Lissauer et al. (2011a).
However, the authors attributed the trend to a selection effect, given the preferential detectability of
small planets in close-in orbits with respect to longer period ones. Later on, Ciardi et al. (2013) cor-
rected the sample for detection and geometric biases, and found that in adjacent pairs of planets with
radii similar or larger than Neptune the outer planet is larger than the inner one. This is no longer valid if

---

[6]From the NASA Exoplanet Archive (https://exoplanetarchive.ipac.caltech.edu/) as of 21 December 2021.

both planets are smaller than Neptune, with no apparent size hierarchy among terrestrial planets. Using updated and uniform stellar parameters, Weiss et al. (2018a) further investigated the size distribution of the *Kepler* sample, confirming this size progression. In addition, Weiss et al. (2018a) pointed out several additional correlations in the properties of adjacent planets:

- Planets within a given multiplanetary system have correlated sizes. Adjacent planets tend to have similar radii, i.e. each planet is more likely to have a radius similar to its neighbour rather than having a size drawn at random from the global distribution of observed planetary radii. This pattern is the so-called ''peas-in-a-pod'' structure.

- Systems with at least three planets tend to have regular spacing, with a correlation between the orbital periods of adjacent planets.

- Orbital period ratios are smaller in system with smaller planets, but no planets have period ratio < 1.2, regardless of the size.

- The most common orbital spacing is 20 mutual Hill radii, and 93% of planet pairs are orbiting at least 10 Hill radii apart.

Millholland et al. (2017) confirmed that planets in the same system show similarity both in radii and masses, more than if they were assembled randomly from the global radius and mass distributions. A similarity in mass was also found by Wang (2017) from the analysis of a sample of RV-detected planets.

These and other empirical trends (also on mutual inclinations, see e.g. Fang & Margot 2012, Fabrycky et al. 2014, Dai et al. 2018, Millholland et al. 2021) provide hints about the underlying physical processes, thus posing constraints on theory and helping to discriminate among competing models, which have to be able to reproduce the observed trends. However, to understand if these trends are actually reflecting the underlying 'ground-truth' distribution of exoplanets, or if they are caused (or affected) by observational limitations and detection biases, it is essential to enlarge the sample of well-characterized multiplanetary system, which is one of the motivations this thesis is based on.

Chapter 2

Methods

This chapter reports the main methods and techniques used in the thesis to infer the parameters for star-planet systems characterization.

2.1 Transit modelling

For the modelling of exoplanetary transit light curves we employed the open source package `batman`[1] (BAsic Transit Model cAlculatioN; Kreidberg 2015). Written in Python, `batman` uses C extension modules to speed up model calculation and is parallelized with OpenMP. The code supports calculation of transit light curves for any radially symmetric stellar limb darkening law, using an integration algorithm for models that cannot be quickly calculated analytically. Limb darkening (LD) is an optical effect related to the dependence of the intensity of the stellar radiation in the stellar atmosphere on the optical depth. Since the optical depth increases towards the stellar limb, the limb will appear dimmer than the centre (see also Section 1.2.2). Accurate calculation of transiting light curve is challenging because the model must account for the stellar LD, as well as for the planet size and position on the sky. `batman` supports a variety of LD laws, which assume the following form for the stellar intensity profile:

- $I(\mu) = I_0$ (uniform)

- $I(\mu) = I_0[1 - c_1(1 - \mu)]$ (linear; Schwarzschild & Villiger 1906)

- $I(\mu) = I_0[1 - c_1(1 - \mu) - c_2(1 - \mu)^2]$ (quadratic; Kopal 1950)

- $I(\mu) = I_0[1 - c_1(1 - \mu) - c_2(1 - \sqrt{\mu})]$ (square-root; Diaz-Cordoves & Gimenez 1992)

- $I(\mu) = I_0[1 - c_1(1 - \mu) - c_2\mu \ln \mu]$ (logarithmic; Klinglesmith & Sobieski 1970)

- $I(\mu) = I_0[1 - c_1(1 - \mu) - c_2/(1 - \exp \mu]$ (exponential; Claret & Hauschildt 2003)

- $I(\mu) = I_0[1 - c_1(1 - \mu_2^c)]$ (power2; Morello et al. 2017)

---

[1]https://github.com/lkreidberg/batman
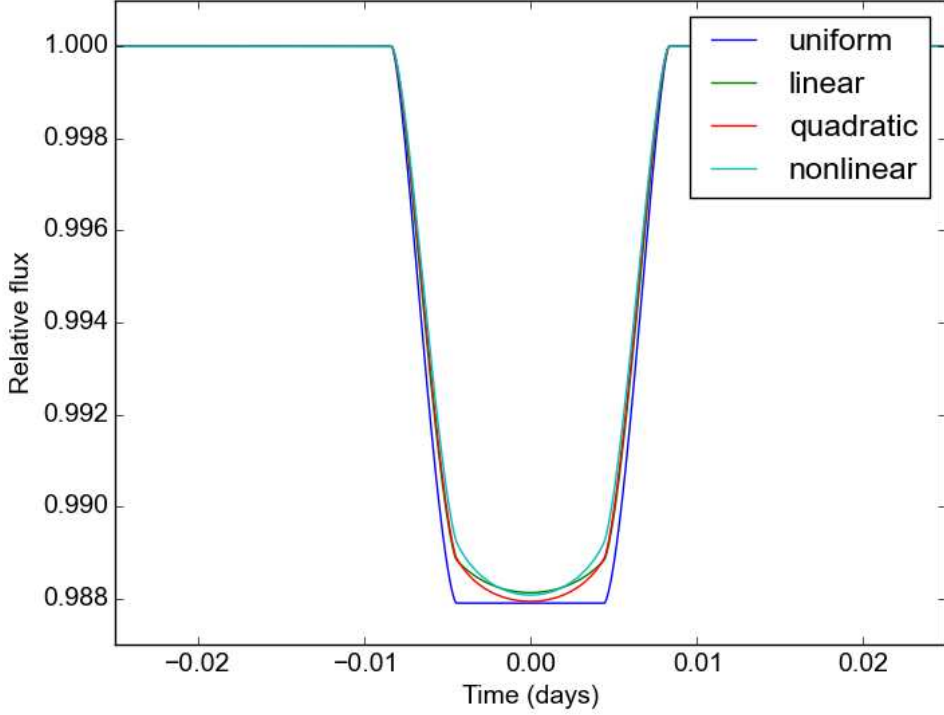
Figure 2.1 Transit model assuming four different LD profiles implemented in `batman`.

- $I(\mu) = I_0[1 - c_1(1 - \mu^{1/2}) - c_2(1 - \mu) - c_3(1 - \mu^{3/2} - c_4(1 - \mu^2)]$ (non-linear; Claret 2000)

where $\mu = \sqrt{1 - x^2}$, $0 \leq x \leq 1$ is the normalized radial coordinate, and I_0 is a normalization constant to ensure that the integrated stellar intensity is equal to one. Figure 2.1 shows the effect of different LD laws on the transit shape for the most common profiles[2]. For the first three listed profiles, `batman` calculates analytically the transit model following the formalism of Mandel & Agol (2002). The other profiles do not have an analytical solution, and are calculated by numerical integration of the the stellar intensity over the disk of the planet as described in Section 2 of Kreidberg (2015). Basically, the fraction δ of stellar flux blocked by a transiting planet can be calculated by integrating the sky-projected intensity of the star (I) over the area obscured by the disk of the planet (S):

$$\delta = \int \int_S I \mathrm{d}S,$$ (2.1)

where I is normalized such that the integrated intensity over the stellar disk is equal to one. To reach high accuracy, differential area elements must be small ($\lesssim 10^{-6}$), thus slowing down the numerical evaluation. However, if the stellar intensity profile is radially symmetric, computation can speed up by

---

[2]The code also allows for the definition of additional custom profiles

reducing Eq. 2.1 from two- to one-dimension as follows:

$$\delta = \sum_{i=1}^{n} I\left(\frac{x_i + x_{i-1}}{2}\right) [A(x_i, r_p, d) - A(x_{i-1}, r_p, d)],$$ (2.2)

where x is the normalized radial coordinate, $I(x)$ is the one-dimension stellar intensity profile, r_p is the planetary radius (in stellar radii), d is the separation between the center of the planet and the center of the star (in stellar radii), and $A(x, r_p, d)$ is the area of intersection between two circles of radii x and r_p at distance d. The sum is computed from $x_0 = \text{MAX}(d - r_p, 0)$ to $x_n = \text{MIN}(d + r_p, 1)$, and the area of intersection is:

$$A(x, r_p, d) = \begin{cases} x^2 \cos^{-1} u + r_p^2 \cos^{-1} v - 0.5\sqrt{w}, & r_p - d < x < r_p + d \\ \pi x^2, & x \leq r_p - d \\ \pi r_p^2 & x \geq r_p + d \end{cases}$$ (2.3)

where

$$\begin{aligned} u &= (d^2 + x^2 - r_p^2)/(2dx) \\ v &= (d^2 + r_p^2 - x^2)/(2dr_p) \\ w &= (-d + x + r_p)(d + x - r_p)(d - x + r_p)(d + x + r_p). \end{aligned}$$ (2.4)

Figure 2.2 shows a schematic illustration of the geometry of the integration. The adopted step-size is:

$$x_i - x_{i-1} = f \cos^{-1}(x_{i-1}),$$ (2.5)

where f is a constant scale factor. This integration scheme is faster than a scheme with a simpler area element (e.g $\Delta A = \Delta x \Delta y$), and the code can reach a photometric accuracy better than 0.001 ppm, in foreseen of ultra-precise transit light curves coming from future facilities.

Finally, `batman` allows for the specification of a ''super-sample factor'', which accounts for long exposure times by calculating the average value of the light curve over the entire exposure.

2.2 Bayesian inference and Markov chain Monte Carlo sampling

Statistical inference plays a crucial role in interpreting exoplanetary, and more generally astrophysical, observations. Understanding the statistical properties of the observations, and taking them carefully into account when carrying out inference is determinant for the reliability of the information we can derive from observations. In the last decades, an increasing interest for Bayesian inference arise among the astrophysical community, and this approach has been successfully applied to a variety of astrophysical problems, including exoplanetology. Even though computationally demanding, Bayesian inference offers a unified, consistent approach to estimate parameters and compare models, allowing us to con-
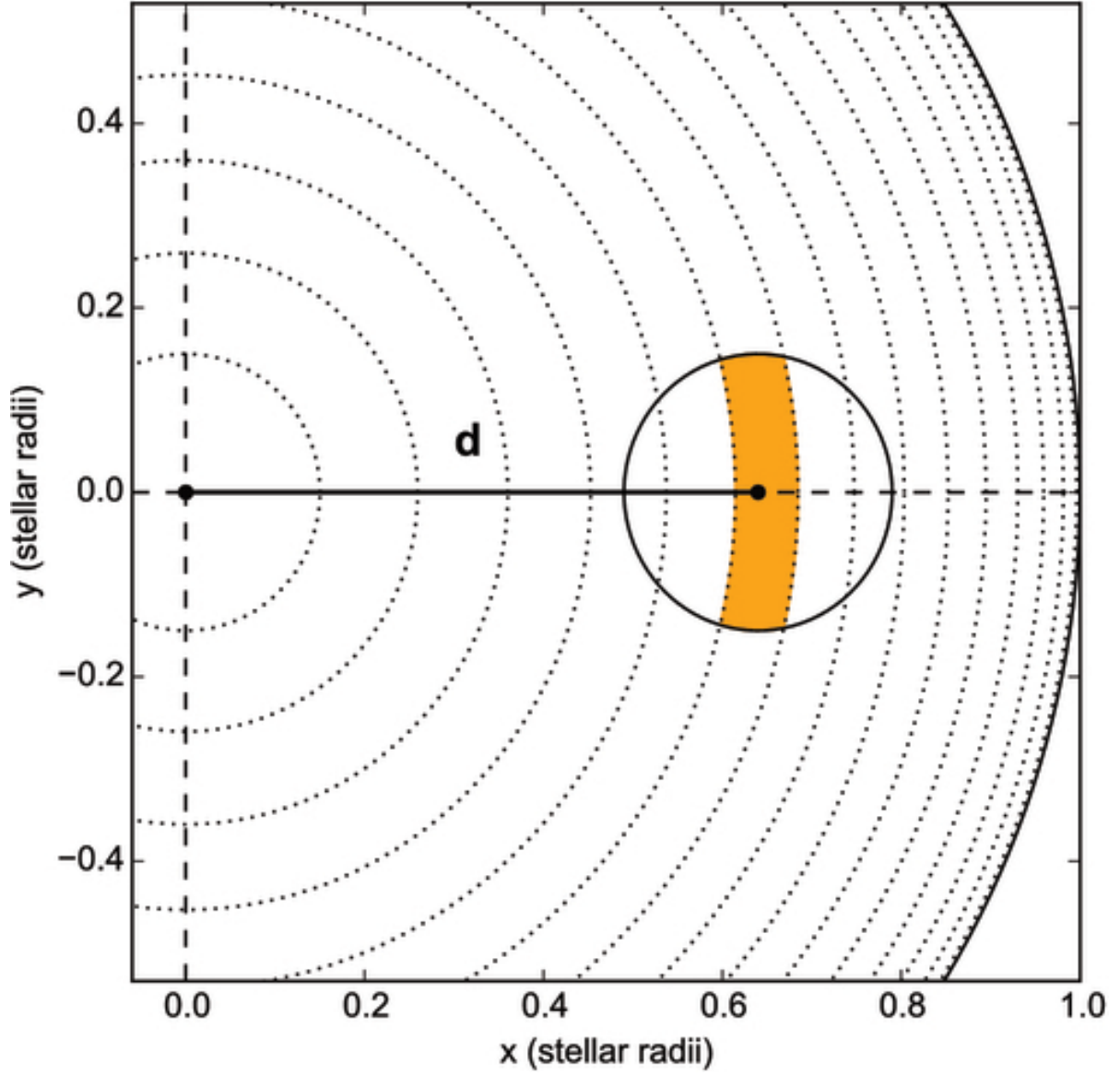
Figure 2.2 Schematic illustration of the `batman` integration scheme. The star is centered in $(x, y) = (0, 0)$ and has a radius of 1. The planet (solid black circle) is separated from the stellar center by a distance d. The star is partitioned into concentric circles (dotted lines) to calculate the integral over the planet disk. The integration step size is enlarged for visual purposes. The orange shaded area represents the single integration element ΔA. From Kreidberg (2015).

sistently combine information coming from different data sets (e.g. RVs, ground- and space-based photometry) with prior information, and to model observational uncertainties in a versatile and robust way (Parviainen, 2018). The Bayesian approach can be used to address the two main problems of statistical inference: parameter estimation (model fitting) and model comparison.

2.2.1 Parameters estimation

When performing Bayesian parameters estimation, we aim at inferring the joint probability distribution for model parameters given an opportune model, prior information, and a set of observations. This probability distribution is called *posterior distribution*, and it is obtained by updating a *prior distribution* with a *sampling distribution* (or *likelihood*). The joint posterior distribution can be obtained starting from the Bayes' theorem:

$$\Pr(H|D) = \frac{\Pr(H)\Pr(D|H)}{\Pr(D)}, \tag{2.6}$$

where $\Pr(H|D)$ is the posterior probability for the hypothesis H given the data D, $\Pr(H)$ is the prior probability for the hypothesis, $\Pr(D|H)$ is the probability for the data D given the hypothesis H, and $\Pr(D)$ is the probability for the data D. When performing parameters estimation, the hypothesis H is a continuous model parameter vector θ, the observed data are contained in the vector $\mathbf{y}$, the probabilities are continuous probability distributions, and therefore we can write the posterior distribution as:

$$P(\theta|\mathbf{y}) = \frac{P(\theta)\,P(\mathbf{y}|\theta)}{P(\mathbf{y})} = \frac{P(\theta)\,P(\mathbf{y}|\theta)}{\int P(\theta)\,P(\mathbf{y})\,d\theta}. \tag{2.7}$$

The integral in the denominator, called marginal probability or model evidence, is a normalizing constant which ensures that the posterior integrates to unity.

The prior probability distribution embeds the information and/or assumptions currently available about a model parameter. In the process of parameter estimation, the prior is updated by the likelihood based on new information (the observations) to produce a posterior distribution, which in turn could be used as a prior in subsequent analyses. Depending on how strong they constrain the parameter space, priors can be either considered informative, if based on previous research or theoretical considerations (i.e. a normal distribution with mean and standard deviation based on previous parameter estimate), or weakly informative (uninformative), if no or little information is available about a parameter. The choice of uninformative distributions aims at minimizing the effect of the prior on the posterior distribution, letting the data to shape the posterior. It is important to stress that the choice of priors is not objective. For a given parameter, different previous estimates can be available, or different assumptions can be adopted, and the choice of a particular prior can influence the final results.

The likelihood represents the probability to obtain the observed data given a model evaluated at a given point in the parameter space. Generally, the model consists of a deterministic part, which can be described using a parametric model, and a stochastic part, which explains the noise. If the observations

can be described with a parametric model and the addition of uncorrelated noise[3], the joint likelihood can be expressed as a product of independent likelihoods:

$$P(\mathbf{d}|\theta) = \prod_i P(d_i|\theta), \tag{2.8}$$

where $\mathbf{d}$ is the dataset, d_i are the individual observations, and θ is the model parameters vector. Due to numerical under- or overflow problems, likelihood is usually computed in logarithmic space:

$$\ln P(\mathbf{d}, \theta) = \sum_i \ln P(d_i|\theta). \tag{2.9}$$

In case of normally distributed noise, a single measurement y_i can be expressed as:

$$y_i \sim \mathcal{N}(m(\theta|\mathbf{x}_i), \sigma_i), \tag{2.10}$$

with $\mathcal{N}$ the normal distribution, m the parametric model, θ the model parameters vector, $\mathbf{x}_i$ the vector of independent variables for observation i, and σ_i the standard deviation (uncertainty) for observation i. For a single observation, the likelihood is:

$$P(y_i|\theta, \mathbf{x}_i, \sigma_i) = \frac{1}{\sqrt{2\pi}\,\sigma_i} \exp{-\frac{(y_i - m(\theta, \mathbf{x}_i))^2}{2\sigma_i^2}}, \tag{2.11}$$

and for a data set of n observations, the log-likelihood is:

$$\ln P(\mathbf{y}|\theta, \mathbf{x}, \sigma) = -\frac{1}{2}\left(n \ln 2\pi + \sum_i^n \ln \sigma_i^2 + \sum_i^n \frac{r_i^2}{2\sigma_i^2}\right), \tag{2.12}$$

where $r_i = y_i - m(\theta, \mathbf{x}_i)$ is the residual.

One of the most powerful tools for Bayesian posterior estimation is Markov chain Mont Carlo (MCMC) sampling. MCMC sampling is a procedure that allows us to empirically explore the posterior probability distribution. This method constructs an iterative Markov chain with the posterior distribution as its equilibrium distribution, and produces a set of samples drawn from the posterior distribution. Starting from a given point in the parameter space, the sampler begins a chain, and it proposes a move to another point. The sampler accepts or rejects the move based on the posterior density ratio between the initial and new locations. In either cases, the location after the proposal is added to the chain, and the sampling continues by proposing a new step. Each move is proposed based on a set of conditions that ensure an asymptotic convergence of the samples to the posterior distribution. However, the speed of convergence is different for different MCMC implementations, and it depends on the complexity of the posteriors (Gregory 2005; Robert 2007; Gelman et al. 2013). MCMC includes a variety of different sampling algorithms, but we focus here in more detail on the affine-invariant ensemble sampler

---

[3]Conversely, in presence of time-correlated noise (i.e. stellar granulation, star spots), more complex models like Gaussian Processes (see Section 2.3) have to be employed.

(Goodman & Weare, 2010) and its implementation within the `emcee` package (Foreman-Mackey et al., 2013a), extensively used in this thesis. `emcee` creates a specified number of chains (or ''walkers'') for each model parameter. Starting from an initial set of model parameters, the chains explore the parameter space by computing the likelihood for a new set of model parameters, and by comparing it to the one of the previous model. If it is more likely, the new set of model parameters is adopted, while if the likelihood is lower than the last model, the difference between the previous and the newly generated likelihood is used to determine the probability of the new model parameters being taken. Therefore, each point in the chain depends only on the position of the previous step. The parameters proposed at each step are usually generated using a specific set of step parameters (i.e. normal distribution with a given variance). This needs to be fine-tuned to ensure that a sufficiently large parameter space region is explored, but without stepping too far into into low-probability regions within which the model parameters are never accepted. `emcee` employs the affine invariance of Goodman & Weare (2010) to parametrize the step computation with only two hyper-parameters.

The starting point of a chain can affect the chain convergence. If the chain starts in a low-probability region, it may take time before it starts sampling the high-probability posterior space. To reduce the influence of the starting point, an initial burn-in (or warm-up) phase is usually cut from the sample. Since consecutive samples in each MCMC chain are correlated, a set of independent samples can be obtained by *thinning* the chain, i.e., by selecting every n-th sample, with n close to the chain autocorrelation length. Even though the MCMC chain approximates the posterior asymptotically, the number of steps required to obtain a representative sample depends on how efficiently the sampler can cover the posterior. Before proceeding with parameters estimation, the chains need to be tested for convergence. Converged chains should be statistically similar to each other. A practical way to test convergence is the Gelman-Rubin diagnostic (Gelman & Rubin 1992; Gelman et al. 2013), which compares the estimate for the marginal posterior variance for a given parameter to the mean within-chain variance. For a set of well-converged chains, the two quantities should be approximately equal. Another good heuristic for assessing the convergence of samplings is the integrated autocorrelation time. If the autocorrelation time cannot be reliably estimated, the chain is likely too short and most likely convergence has not been reached (Goodman & Weare, 2010).

After the exploration of the full parameter space (by running the walkers for a sufficient number of steps), the posterior distribution functions of the model parameters are typically visualised through a corner plot, which flattens the multi-parameter probability space onto a 2-parameter plane for every possible two-parameter combination (see Figure 2.3 for an example). Corner plots are useful tools to visualize and inspect correlations among the model parameters. One-dimensional posterior distributions can be obtained for each parameter by flattening the chains. Value and uncertainties of each parameter can be then estimated from the posterior distribution, e.g. median and 1-σ bounds can be extracted from the 16-th, 50-th, and 84-th percentiles of the distribution.
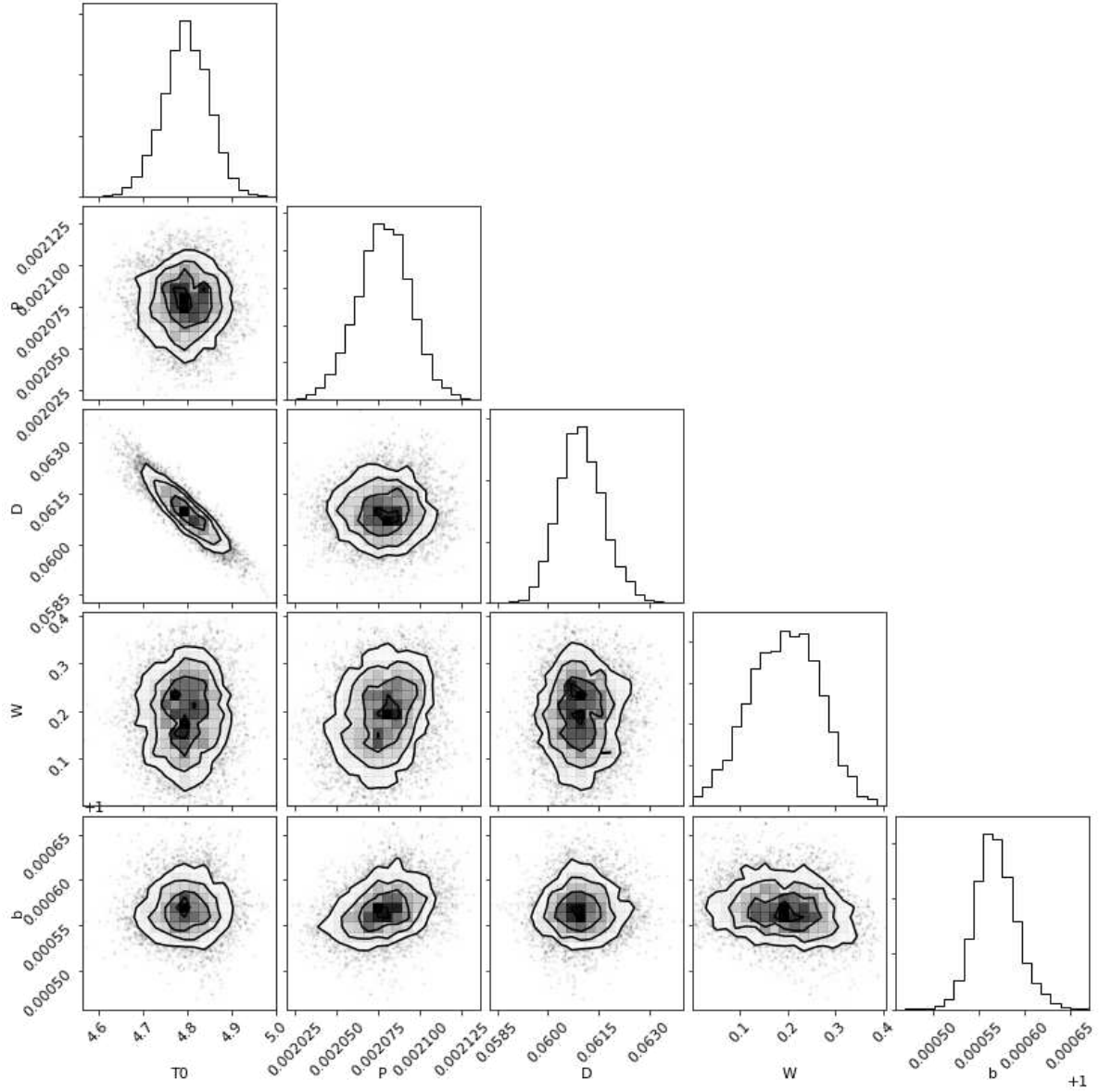
Figure 2.3 Example of a corner plot of the MCMC fit of a planetary transit showing the posterior distributions and correlations between central transit time (T_0), orbital period (P), transit depth (D), transit duration (W) and impact parameter (b). The plots at the top of each column show the one-dimensional posterior distribution of each parameter. From *The* PYCHEOPS *Cookbook*[4].

2.2.2 Model comparison

In addition to parameters estimation, Bayesian inference can also be employed to perform model comparison. In this case, we aim at finding which of the possible models is best suited to explain the observations. In exoplanetary science this approach is mainly used to ascertain what is the most likely physical cause for a signal (e.g. for statistical validation of planetary candidates detected in photometric surveys), or to identify the number of physical signals contained in a given data set (e.g. search for planets in RVs). In the latter case, which is the one applied in Chapter 3 and Chapter 4 for the analysis of the TOI-561 system, the aim is to find out when stopping to introduce complexity to the model (i.e. adding hypothetical planets) to identify the best-fitting model without over-fitting the data. In Bayesian model comparison, the model evidence (or marginal likelihood), which can be ignored in parameters estimation, is a crucial quantity. The model evidence Z is the integral of the posterior over the whole parameter space:

$$Z = \int P(\boldsymbol{\theta}) P(\mathbf{y}) \, d\boldsymbol{\theta}. \tag{2.13}$$

Being rarely analytically solvable, Z is usually computed using specially designed numerical methods for multidimensional integration. Model evidence is used to penalize model complexity not justified by the data. When including in a model a new parameter with its prior distribution, the addition of the parameter must increase the likelihood more than the prior penalizes the posterior, since the posterior is the product of the likelihood and the prior (MacKay 2002; Gregory 2005). Given two competing models M_0 and M_1, the posterior odds favouring M_1 over M_0 are:

$$O_{10} = \frac{\Pr(M_1|\mathbf{y})}{\Pr(M_0|\mathbf{y})} = \frac{Z_1}{Z_0} \frac{P(M_1)}{P(M_0)} = B_{10} \frac{P(M_1)}{P(M_0)}, \tag{2.14}$$

where $P(M_1)$ and $P(M_0)$ are the prior probabilities of the two models, and B_{10} is the Bayes factor, i.e. the ratio of the model evidences. If the models have equal prior probabilities ($P(M_1)/P(M_0) = 1$), model comparison can be performed using the Bayes factor only. Table 2.1 reports general guidelines for interpreting the Bayes factors according to Kass & Raftery (1995).

Table 2.1 Guidelines for the interpretation of the Bayes factors according to Kass & Raftery (1995).

$2 \ln B_{10}$	B_{10}	Evidence against M_0
0 to 2	1 to 3	Not worth more than a bare mentioning
2 to 6	3 to 20	Positive
6 to 10	20 to 150	Strong
>10	>150	Very strong

A variety of methods can be used for evidence estimation, from direct Monte Carlo integration to more sophisticated approaches employing different importance sampling, to even more complicated approaches using advanced nested sampling, bridge and path sampling, and Bayesian quadrature (see Clyde et al. 2007; Ford & Gregory 2007; Robert 2007 for extensive reviews). Among them, nested

sampling (Skilling 2004; Skilling 2006; Chopin & Robert 2010) has recently gained popularity among the exoplanet community, especially with the implementation proposed in the `MultiNest` (Feroz & Hobson, 2008; Feroz et al., 2009, 2019) and `dynesty` (Skilling, 2004; Skilling, 2006; Speagle, 2020) packages. Nested sampling allows for both model selection and parameters estimation.

2.3 Gaussian Processes

In presence of time-correlated (red) noise in the observations, sophisticated statistical methods have to be employed to avoid biases in parameters estimation, underestimation of parameters uncertainties and/or false detection in planet search. For example, stellar granulation could induce variability in stellar light curves with amplitude and time scale comparable to planetary transits, and spots/plagues related to stellar activity could produce signals in RVs time series mimicking a planet (see Section 1.4.2). If the noise process follows a normal distribution, it can be efficiently modelled as a Gaussian process (GP, Williams & Rasmussen 1996; Rasmussen & Williams 2006; Gibson et al. 2012; Roberts et al. 2013). GPs have been recently applied in exoplanetary science to various time-series analysis problems, including modelling of transmission spectroscopy systematics (Gibson et al., 2012), removal of photometric trends in stellar light curves (e.g. Aigrain et al. 2015; Osborn et al. 2017; Barros et al. 2020), modelling of stellar spectra to improve RV measurements (Czekala et al., 2017), and disentangling stellar activity from planetary signals in RVs (e.g. Haywood et al. 2014; Rajpaul et al. 2015; Malavolta et al. 2018).

Gaussian processes are based on covariance. The basic idea is that data points in a time series are not randomly sampled, but they have covariance. Therefore, the position of a subsequent point can be constrained from precise measurements of the previous ones. Generic GPs require the inversion of a $n \times n$ covariance matrix, with n the number of data points, thus implying a high computational cost for long time series. Following the Bayesian formalism introduced in the previous section, the scalar log-likelihood (Eq. 2.12) can be more generically expressed in vector form as:

$$\ln P(\mathbf{y}|\boldsymbol{\theta}) = -\frac{1}{2}\left(n \ln 2\pi + \ln |\boldsymbol{\Sigma}| + \mathbf{r}^{\mathrm{T}}\boldsymbol{\Sigma}^{-1}\mathbf{r} \right), \tag{2.15}$$

where n is the number of data points, $\mathbf{r}$ is the residual vector, and $\boldsymbol{\Sigma}$ is the covariance matrix, which is diagonal for white noise, thus yielding Eq. 2.12. The covariance matrix elements can be expressed as:

$$\boldsymbol{\Sigma}_{i,j} = k(\mathbf{x}_i, \mathbf{x}_j) + \sigma^2 \delta_{ij}, \tag{2.16}$$

where k is the covariance function (or ''kernel''), $\mathbf{x}$ are the input parameter vectors, δ is the Kronecker delta function, and σ^2 represents the white noise for the i-th data point. The kernel defines the behaviour of the GP, determining how the covariance of two points decays with distance, and it is often defined by one or more ''hyper-parameters'', which can be constrained by prior distributions. The kernel is usually chosen at the onset of the modelling, and its choice depends on the problem we want to address. Among some commonly used kernels:

- Exponential squared kernel:

$$k(x_i, x_j) = h^2 \exp{-\left(\frac{x_i - x_j}{\lambda}\right)^2},\qquad(2.17)$$

where h and λ are the hyper-parameters regulating the amplitude and timescale of variations, respectively.

- The ''Matérn-ν'' kernels, which increase in complexity from $\nu = \frac{1}{2}$ (corresponding to an exponential kernel), to $\nu = \frac{3}{2}, \frac{5}{2}$, etc, tending to the squared exponential kernel at increasing ν.

- Period and quasi-period kernels, formed by multiplying the standard kernels (e.g. the exponential kernel) by a periodic component.

In this thesis, we employed a Matérn-3/2 kernel for light curve smoothing (Section 4.5), and a quasi-periodic kernel for investigations of stellar activity in RVs time series (Section 3.6.3 and 4.4.2). We used the `celerite` package (Foreman-Mackey et al., 2017) for light curve smoothing, while for the RVs GP modelling we employed the `george` package (Ambikasaran et al., 2015).

Chapter 3

An unusually low density ultra-short period super-Earth and three mini-Neptunes around the old star TOI-561

Based on HARPS-N radial velocities (RVs) and TESS photometry, we present a full characterisation of the planetary system orbiting the late G dwarf TOI-561. After the identification of three transiting candidates by TESS, we discovered two additional external planets from RV analysis. RVs cannot confirm the outer TESS transiting candidate, which would also make the system dynamically unstable. We demonstrate that the two transits initially associated with this candidate are instead due to single transits of the two planets discovered using RVs. The four planets orbiting TOI-561 include an ultra-short period (USP) super-Earth (TOI-561 b) with period $P_b = 0.45$ d, mass $M_b = 1.59 \pm 0.36$ $M_\oplus$ and radius $R_b = 1.42 \pm 0.07$ $R_\oplus$, and three mini-Neptunes: TOI-561 c, with $P_c = 10.78$ d, $M_c = 5.40 \pm 0.98$ $M_\oplus$, $R_c = 2.88 \pm 0.09$ $R_\oplus$; TOI-561 d, with $P_d = 25.6$ d, $M_d = 11.9 \pm 1.3$ $M_\oplus$, $R_d = 2.53 \pm 0.13$ $R_\oplus$; and TOI-561 e, with $P_e = 77.2$ d, $M_e = 16.0 \pm 2.3$ $M_\oplus$, $R_e = 2.67 \pm 0.11$ $R_\oplus$. Having a density of 3.0 ± 0.8 g cm^{-3}, TOI-561 b is the lowest density USP planet known to date. Our N-body simulations confirm the stability of the system and predict a strong, anti-correlated, long-term transit time variation signal between planets d and e. The unusual density of the inner super-Earth and the dynamical interactions between the outer planets make TOI-561 an interesting follow-up target.

3.1 Introduction

The *Transiting Exoplanet Survey Satellite* (*TESS*, Ricker et al., 2014) is a NASA all-sky survey designed to search for transiting planets around bright and nearby stars, and particularly targeting stars that could reveal planets with radii smaller than Neptune (see Section 1.3.2). Since the beginning of its observations in 2018, *TESS* has already discovered a significant number of new exoplanets, including about a dozen multi-planet systems (e.g. Dragomir et al., 2019; Dumusque et al., 2019; Günther et al., 2019). Multi-planet systems, orbiting the same star and having formed from the same protoplanetary disc, offer a unique opportunity for comparative planetology. They allow for investigations of the formation and evolution processes, i.e. through studies of relative planet sizes and orbital separations, orbital inclinations relative to the star's rotation axis, mutual inclination of the orbits, etc. (see Section 1.6). In order to obtain a complete characterisation of a system, knowledge of the orbital architecture and the bulk composition of the planets are essential. To obtain such information, transit photometry needs to be combined with additional techniques that allow for the determination of the planetary masses, i.e. radial velocity (RV) follow-up or transit time variation (TTV) analysis. Up to now, the large majority of known planetary systems have been discovered by the *Kepler* space telescope (Borucki et al., 2010), which has led to an unprecedented knowledge of the ensemble properties of multiple systems (e.g. Latham et al., 2011; Millholland et al., 2017; Weiss et al., 2018b), their occurrence rate (e.g. Fressin et al., 2013), and their dynamical configurations (e.g. Fabrycky et al., 2014; Lissauer et al., 2011a). However, many of the *Kepler* targets are too faint for RV follow-up, so most of the planets do not have a mass measurement, preventing a comprehensive understanding of their properties, and of the planetary system. Thanks to the *TESS* satellite, which targets brighter stars, an increasing number of candidates suitable for spectroscopic follow-up campaigns are being discovered. These new objects will increase the number of well characterised systems, and will provide a valuable observational counterpart to the theoretical studies on the formation and evolution processes of planetary systems (e.g. Baruteau et al., 2014, 2016; Davies et al., 2014; Helled et al., 2014; Morbidelli et al., 2012; Raymond et al., 2014).

In this work, we combine *TESS* photometry (Section 3.2.1) and high precision RVs gathered with the HARPS-N spectrograph (Section 3.2.2) to characterise the multi-planet system orbiting the star TOI-561. The *TESS* pipeline identified three candidate planetary signals, namely an ultra-short period (USP) candidate ($P \sim 0.45$ days), and two additional candidates with periods of ~ 10.8 and ~ 16.4 days. We determined the stellar properties (Section 3.3) using three independent methods. Based on our activity analysis, we concluded that TOI-561 is an old, quiet star, and therefore quite appropriate for the study of a complex planetary system. After assessing the planetary nature of the transit-like features (Section 3.4), we performed a series of analysis – with the tools described in Section 3.5 – to determine the actual system configuration (Section 3.6). We further address the robustness of our final solution based on a comparison with other possible models (Section 3.7). We finally compare the resulting planetary densities with the distribution of known planets in the mass-radius diagram and we predict the expected TTV signal for the planets in the system (Section 3.8).

3.2 Observations

3.2.1 *TESS* photometry

TOI-561 was observed by *TESS* in two-minute cadence mode during observations of sector 8, between 2 February and 27 February 2019. The astrometric and photometric parameters of the star are listed in Table 3.1. Considering the download time, and the loss of 3.26 days of data due to an interruption in communications between the instrument and the spacecraft that occurred during sector 8[1], a total of 20.22 days of science data were collected. The photometric observations for TOI-561 were reduced by the Science Processing Operations Center (SPOC) pipeline (Jenkins, 2020; Jenkins et al., 2016), which detected three candidate planetary signals, with periods of 10.8 days (TOI-561.01), 0.4 days (TOI-561.02), and 16.4 days (TOI-561.03), respectively. The pipeline identified 55 transits of TOI-561.02, two transits of TOI-561.01, and two transits of TOI-561.03, with depths of 290, 1207, and 923 ppm and signal-to-noise-ratios (S/N) of 10.0, 9.8 and 9.2, respectively. For our photometric analysis, we used the light curve based on the Pre-search Data Conditioning Simple Aperture Photometry (PDCSAP, Smith et al., 2012; Stumpe et al., 2012, 2014). We downloaded the two-minute cadence PDCSAP light curve from the Mikulski Archive for Space Telescopes (MAST)[2], and removed all the observations encoded as *NaN* or flagged as bad-quality (DQUALITY>0) points by the SPOC pipeline[3]. We performed outliers rejection by doing a cut at 3σ for positive outliers and 5σ (i. e. larger than the deepest transit) for negative outliers. We removed the low frequency trends in the light curve using the biweight time-windowed slider implemented in the wotan package (Hippke et al., 2019), with a window of 1.5 days, and masking the in-transit points to avoid modifications of the transit shape. In order to obtain an independent confirmation of the signals detected in the *TESS* light curve, we performed an iterative transit search on the detrended light curve using the Transit Least Squares (TLS) algorithm (Hippke & Heller, 2019). The first three significant identified signals nicely matched the *TESS* suggested periods ($P_{\mathrm{TLS}} = 10.78$ d, 0.44 d, 16.28 d).

In addition, we also extracted the 30-minutes cadence light curve from the *TESS* Full-Frame Images (FFIs) using the PATHOS pipeline (Nardiello et al., 2019), in order to obtain an independent confirmation of the detected signals (Section 3.4).

3.2.2 HARPS-N spectroscopy

We collected 82[4] spectra using HARPS-N at the Telescopio Nazionale Galileo (TNG), in La Palma (Cosentino et al., 2012, 2014), with the goal of precisely determining the masses of the three candidate planets and to search for additional planets. The observations started on November 17, 2019 and ended on June 13, 2020, with an interruption between the end of March and the end of April due to

---

[1] See *TESS* Data Release Notes: Sector 8, DR10 (https://archive.stsci.edu/tess/tess_drn.html).
[2] https://mast.stsci.edu/portal/Mashup/Clients/Mast/Portal.html
[3] https://archive.stsci.edu/missions/tess/doc/EXP-TESS-ARC-ICD-TM-0014.pdf
[4] 62 spectra were collected within the Guaranteed Time Observations (GTO) time (Pepe et al., 2013), while the remaining 20 spectra were collected within the A40_TAC23 program.

Table 3.1 Astrometric and photometric parameters of TOI-561

Property	Value	Source
Other target identifiers		
TIC	377064495	A
Gaia DR2	3850421005290172416	B
2MASS	J09524454+0612589	C
Astrometric parameters		
RA (J2015.5; h:m:s)	09:52:44.44	B
Dec (J2015.5; d:m:s)	06:12:57.97	B
μ_α (mas yr^{-1})	-108.432 ± 0.088	B
μ_δ (mas yr^{-1})	-61.511 ± 0.094	B
Systemic velocity (km s^{-1})	79.54 ± 0.56	B
Parallax[a] (mas)	11.6768 ± 0.0672	B
Distance (pc)	$85.80^{+0.50}_{-0.49}$	D
Photometric parameters		
TESS (mag)	9.527 ± 0.006	A
Gaia (mag)	10.0128 ± 0.0003	B
V (mag)	10.252 ± 0.006	A
B (mag)	10.965 ± 0.082	A
J (mag)	8.879 ± 0.020	C
H (mag)	8.504 ± 0.055	C
K (mag)	8.394 ± 0.019	C
W1 (mag)	8.337 ± 0.023	E
W2 (mag)	8.396 ± 0.020	E
W3 (mag)	8.375 ± 0.023	E
W4 (mag)	7.971 ± 0.260	E

A) *TESS* Input Catalogue Version 8 (TICv8, Stassun et al. 2018).
B) *Gaia* DR2 (Gaia Collaboration et al., 2018). C) Two Micron
All Sky Survey (2MASS, Cutri et al. 2003). D) Bailer-Jones
et al. (2018). E) *Wide-field Infrared Survey Explorer* (*WISE*;
Wright et al., 2010).
[a] *Gaia* DR2 parallax is corrected by $+50 \pm 7$ μas (with the error
added in quadrature) as suggested by Khan et al. (2019).

Table 3.2 HARPS-N Radial Velocity Measurements.

MJD$_{TDB}$	RV	σ_{RV}	BIS	FWHM	V_{asy}	ΔV	$\log R'_{HK}$	Hα
(d)	(m s^{-1})	(m s^{-1})	(m s^{-1})	(km s^{-1})		(km s^{-1})		(dex)
58804.7078	79700.63	1.27	-39.98	6.379	0.048	-0.039	-5.005	0.203
58805.7755	79703.74	0.97	-36.25	6.380	0.049	-0.036	-4.984	0.200
58806.7677	79701.71	1.05	-31.81	6.378	0.045	-0.033	-5.000	0.200
...	...	...	...	...	...	...	...	...

This table is available in its entirety in machine-readable form.

the shut down of the TNG because of Covid-19. In order to precisely characterise the signal of the USP candidate, we collected 6 points per night on February 4 and February 6, 2020, thus covering the whole phase curve of the planet, and two points per night (when weather allowed) during the period of maximum visibility of the target (February-March 2020). The exposure time was set to 1800 seconds, which resulted in a S/N at 550 nm of 77 ± 20 (median $\pm$ standard deviation) and a measurement uncertainty of 1.2 ± 0.6 m s^{-1}. We reduced the data using the standard HARPS-N Data Reduction Software (DRS) using a G2 flux template (the closest match to the spectral type of our target) to correct for variations in the flux distribution as a function of the wavelength, and a G2 binary mask to compute the cross-correlation function (CCF, Baranne et al., 1996; Pepe et al., 2002). All the observations were gathered with the second fibre of HARPS-N illuminated by the Fabry-Perot calibration lamp to correct for the instrumental RV drift, except for the night of May 31, 2020. This observation setting prevented us from using the second fibre to correct for Moon contamination. However, we note that the difference between the systemic velocity of the star and the Moon is always greater than 15 km s^{-1}, therefore preventing any contamination of the stellar CCF (as empirically found by Malavolta et al. 2017a and subsequently demonstrated through simulations by Roy et al. 2020), as the average full width at half maximum (FWHM) of the CCF for TOI-561 is 6.380 ± 0.004 km s^{-1}.

The RV data with their 1σ uncertainties and the associated activity indices (see Section 3.3.3 for more details) are listed in Table 3.2. Before proceeding with the analysis, we removed from the total dataset 5 RV measurements, with associated errors greater than 2.5 m s^{-1} from spectra with S/N < 35, that may affect the accuracy of our results. The detailed procedure performed to identify these points is described in Appendix B1.

3.3 Stellar parameters

3.3.1 Photospheric parameters

We derived the photospheric stellar parameters using three different techniques: the curve-of-growth approach, spectral synthesis match, and empirical calibration.

The first method minimizes the trend of iron abundances (obtained from the equivalent width, EW, of each line) with respect to excitation potential and reduced EW respectively, to obtain the effective

temperature and the microturbulent velocity, ξ_t. The gravity $\log g$ is obtained by imposing the same average abundance from neutral and ionised iron lines. We obtained the EW measurements using ARESv2[5] (Sousa et al., 2015). We used the local thermodynamic equilibrium (LTE) code MOOG[6] (Sneden, 1973) for the line analysis, together with the ATLAS9 grid of stellar model atmosphere from Castelli & Kurucz (2003). The whole procedure is described in more detail in Sousa (2014b). We performed the analysis on a co-added spectrum (S/N> 600), and after applying the gravity correction from Mortier et al. (2014) and adding systematic errors in quadrature (Sousa et al., 2011), we obtained $T_{eff} = 5346 \pm 69$ K, $\log g = 4.60 \pm 0.12$, [Fe/H] $= -0.40 \pm 0.05$ and $\xi_t = 0.78 \pm 0.08$ km s^{-1}.

The spectral synthesis match was performed using the Stellar Parameters Classification tool (SPC, Buchhave et al. 2012, 2014). It determines effective temperature, surface gravity, metallicity and line broadening by performing a cross-correlation of the observed spectra with a library of synthetic spectra, and interpolating the correlation peaks to determine the best-matching parameters. For technical reasons, we ran the SPC on the 62 GTO spectra only[7]: the S/N is so high that the spectra are anyway dominated by systematic errors, and including the A40TAC_23 spectra would not change the results. We averaged the values measured for each exposure, and we obtained $T_{eff} = 5389 \pm 50$ K, $\log g = 4.49 \pm 0.10$, [M/H] $= -0.36 \pm 0.08$ and $v \sin i < 2$ km s^{-1}.

We finally used CCFpams[8], a method based on the empirical calibration of temperature, metallicity and gravity on several CCFs obtained with subsets of stellar lines with different sensitivity to temperature (Malavolta et al., 2017b). We obtained $T_{eff} = 5293 \pm 70$ K, $\log g = 4.50 \pm 0.15$ and [Fe/H] $= -0.40 \pm 0.05$, after applying the same gravity and systematic corrections as for the EW analysis.

We list the final spectroscopic adopted values, i.e., the weighted averages of the three methods, in Table 3.3.

From the co-added HARPS-N spectrum, we also derived the chemical abundances for several refractory elements (Na, Mg, Si, Ca, Ti, Cr, Ni). We used the ARES+MOOG method assuming LTE, as described earlier. The reference for solar values was taken from Asplund et al. (2009), and all values in Table 3.3 are given relative to the Sun. Details on the method and line lists are described in Adibekyan et al. (2012) and Mortier et al. (2013). This analysis shows that this iron-poor star is alpha-enhanced. Using the average abundances of magnesium, silicon, and titanium to represent the alpha-elements and the iron abundance from the ARES+MOOG method (for consistency), we find that [α/Fe] $= 0.23$.

3.3.2 Mass, radius, and density of the star

For each set of photospheric parameters, we determined the stellar mass and radius using isochrones (Morton, 2015), with posterior sampling performed by MultiNest (Feroz & Hobson, 2008; Feroz et al., 2009, 2019). We provided as input the parallax of the target from the *Gaia* DR2 catalogue,

---

[5]Available at http://www.astro.up.pt/~sousasag/ares/

[6]Available at http://www.as.utexas.edu/~chris/moog.html

[7]SPC runs on a server with access to GTO data only, and the required technical effort to enable the use of A40_TAC23 data, complicated by the global Covid-19 sanitary emergency, was not justified by the negligible scientific gain.

[8]Available at https://github.com/LucaMalavolta/CCFpams

Table 3.3 Derived astrophysical stellar parameters.

Parameter	Value	Unit
$T_{\mathrm{eff\,spec}}^{a}$	5372 ± 70	K
$\log g_{\mathrm{spec}}^{a}$	4.50 ± 0.12	-
$[\mathrm{Fe/H}]_{\mathrm{spec}}^{a}$	-0.40 ± 0.05	-
T_{eff}^{b}	5455_{-47}^{+65}	K
$\log g^{b}$	4.47 ± 0.01	-
$[\mathrm{Fe/H}]^{b}$	$-0.33_{-0.05}^{+0.10}$	-
$R_{\star}$	0.849 ± 0.007	$R_{\odot}$
$M_{\star}$	0.785 ± 0.018	$M_{\odot}$
$\rho_{\star}$	1.285 ± 0.040	$\rho_{\odot}$
$\rho_{\star}$	1.809 ± 0.056	g cm^{-3}
A_V	$0.12_{-0.06}^{+0.08}$	mag
age^{c}	> 5	Gyr
$\log R'_{\mathrm{HK}}$	-5.003 ± 0.012	-
$[\mathrm{Na/H}]$	-0.28 ± 0.06	-
$[\mathrm{Mg/H}]$	-0.17 ± 0.05	-
$[\mathrm{Si/H}]$	-0.22 ± 0.05	-
$[\mathrm{Ca/H}]$	-0.27 ± 0.06	-
$[\mathrm{Ti/H}]$	-0.12 ± 0.03	-
$[\mathrm{Cr/H}]$	-0.33 ± 0.08	-
$[\mathrm{Ni/H}]$	-0.37 ± 0.04	-

[a] Weighted average of the three spectroscopic methods. [b] Value inferred from the isochrone fit. [c] Conservative lower limit.

after adding an offset of $+50 \pm 7$ μas (with the error added in quadrature to the parallax error) as suggested by Khan et al. (2019), plus the photometry from the TICv8, 2MASS and *WISE* (Table 3.1). We used two evolutionary models, the MESA Isochrones & Stellar Tracks (MIST, Choi et al. 2016; Dotter 2016; Paxton et al. 2011) and the Dartmouth Stellar Evolution Database (Dotter et al., 2008). For all methods, we assumed $\sigma_{T_{\mathrm{eff}}} = 70$ K, $\sigma_{\log g} = 0.12$, $\sigma_{[\mathrm{Fe/H}]} = 0.05$ (except for SPC, where we kept the original error of 0.08) as a good estimate of the systematic errors regardless of the internal error estimates, to avoid favouring one technique over the others when deriving the stellar mass and radius. We also imposed an upper limit on the age of 13.8 Gyr, i. e. the age of the Universe (Planck Collaboration et al., 2018). From the mean and standard deviation of all the posterior samplings we obtained $M_\star = 0.785 \pm 0.018$ $M_\odot$ and $R_\star = 0.849 \pm 0.007$ $R_\odot$. We derived the stellar density $\rho_\star = 1.285 \pm 0.040$ $\rho_\odot$ ($\rho_\star = 1.809 \pm 0.056$ g cm^{-3}) directly from the posterior distributions of $M_\star$ and $R_\star$.

We summarise the derived astrophysical parameters of the star in Table 3.3, which also reports temperature, gravity and metallicity obtained from the posteriors distributions resulting from the isochrone fit. A lower limit on the age of ~ 10 Gyr is obtained considering the 15.86-th percentile of the distribution of the combined posteriors, as for the other parameters. We note however that an isochrone fit performed through EXOFASTv2 (Eastman et al., 2019), assuming the photometric parameters in Table 3.1 and the spectroscopic parameters in Table 3.3, using only the MIST evolutionary set, returned a lower limit on the age of 5 Gyr, while all the other parameters were consistent with the results quoted in Table 3.3. Thus, we decided to assume 5 Gyr as a conservative lower limit for the age of the system. The old stellar age and the sub-solar metallicity suggest that TOI-561 may belong to an old Galactic population, an hypothesis that is also supported by our kinematic analysis. In fact, we derived the Galactic space velocities using the astrometric properties reported in Table 3.1. For the calculations we used the astropy package, and we assumed the *Gaia* DR2 radial velocity value of 79.54 km s^{-1}, obtaining the heliocentric velocity components $(U, V, W) = (-60.0, -70.8, 16.7)$ km s^{-1}, in the directions of the Galactic center, Galactic rotation, and north Galactic pole, respectively. The derived UVW velocities point toward a thick-disk star, as confirmed by the probability membership derived following Bensby et al. (2014), that implies a $\sim 70\%$ probability that the star belongs to the thick disc, a $\sim 29\%$ probability of being a thin-disc star and a $\sim 0.0004\%$ probability of belonging to the halo.

3.3.3 Stellar activity

The low value of the $\log R'_{\mathrm{HK}}$ index (-5.003 ± 0.012), derived using the calibration by Lovis et al. (2011) and assuming $B - V = 0.71$, indicates that TOI-561 is a relatively quiet star. Given its distance of $\simeq 86$ pc, the lack of interstellar absorption near the Na D doublet in the HARPS-N co-added spectrum, and the total extinction in the V band from the isochrone fit (0.1 mag), we do not expect any significant effect of the interstellar medium on the $\log R'_{\mathrm{HK}}$ index (Fossati et al., 2017). Nevertheless, it is important to check whether the star is showing any sign of activity in all the activity diagnostics at our disposal. In addition to the $\log R'_{\mathrm{HK}}$ index, FWHM, and bisector span (BIS) computed by the HARPS-N DRS,

we included in our analysis the V_{asy} (Figueira et al., 2013) and ΔV (Nardetto et al., 2006) asymmetry indicators, as implemented by Lanza et al. (2018), and the chromospheric activity indicator Hα (Gomes da Silva et al., 2011).

The Generalized Lomb-Scargle (GLS, Zechmeister & Kürster 2009) periodograms of the above-mentioned indexes, computed within the frequency range 0.0005–0.5 d^{-1}, i. e., 2–2000 days, are shown in Figure 3.1, together with the periodograms of the RVs and *TESS* photometry. For each periodogram, we also report the power threshold corresponding to a False Alarm Probability (FAP) of 1% and 0.1%, computed with a bootstrap approach. The periodogram of the RVs reveals the presence of significant peaks at $\simeq 25$ days, $\simeq 180$ days, $\simeq 10$ days (corresponding to one of the transiting planet candidates), and $\simeq 78$ days, ordered decreasingly according to their power. None of these peaks has a counterpart in the activity diagnostics here considered, as no signals with a FAP lower than 2.4% can be identified, strongly supporting that the signals in the RVs are not related to stellar activity. We note that the GLS periodogram of the *TESS* light curve identified a periodicity around 3.5 days with an amplitude of 0.13 ppt and a power of 0.014, that is, above the 0.1% FAP threshold. However, it is unlikely that such variability is associated with stellar activity, since a rotational period of just a few days would be extremely atypical for a star older than 1 Gyr (e.g. Douglas et al. 2019), and in contrast with the lack of any signal in all the other above-mentioned activity indicators. Indeed, the rotational period estimated from the $\log \mathrm{R}'_{\mathrm{HK}}$ using the calibrations of Noyes et al. (1984) and Mamajek & Hillenbrand (2008) supports this assertion, indicating a value around 33 d. We note that this value of the rotational period should be considered as a rough estimate, also because these calibrations are not well tested for old and alpha-enhanced stars like TOI-561. Further evidence against a ~ 3.5 d rotational period is provided by the low value of the $v \sin i$ (< 2 km s^{-1}), that suggests a rotational period > 21.5 d, assuming the stellar radius listed in Table 3.3 and an inclination of 90°. In any case, we verified with a periodogram analysis that our light curve flattening procedure correctly removed the here identified signal at 3.5 days.

In addition, we performed an auto correlation analysis, following the prescription by McQuillan et al. (2013), on the *TESS* light curve (with the transits filtered out), and the ASAS-SN *V* and *g* photometry (Kochanek et al., 2017; Shappee et al., 2014), after applying a 5-σ filtering, but no significant periodicity could be identified. A periodogram analysis of the ASAS-SN light curves in each band, either by taking the full dataset or by analysing each observing season individually, confirmed these results.

In conclusion, if any activity is present, its signature must be below 0.8 ppt in the short period (rotationally-induced activity, < 30 days), and 20 ppt in the long term period (magnetic cycles, > 100 days), from the RMS of *TESS* and ASAS-SN photometry respectively. Incidentally, the former is close to the photometric variations of the Sun during the minimum at the end of Solar Cycle 25, when the Sun also reached a $\log \mathrm{R}'_{\mathrm{HK}}$ very close to the one measured for TOI-561 (Collier Cameron et al., 2019; Milbourne et al., 2019). By comparing our target to the Sun, and in general by taking into account the results of Isaacson & Fischer (2010), it is expected that the contribution to the RVs due to the magnetic activity of our star is likely below 1-2 m s^{-1}. Since this value is quite close to the median internal error of our RVs, no hint of the rotational period is provided by either the photometry or the spectroscopic activity diagnostics, and the low activity level is consistent with our derived stellar age (> 5 Gyr), we
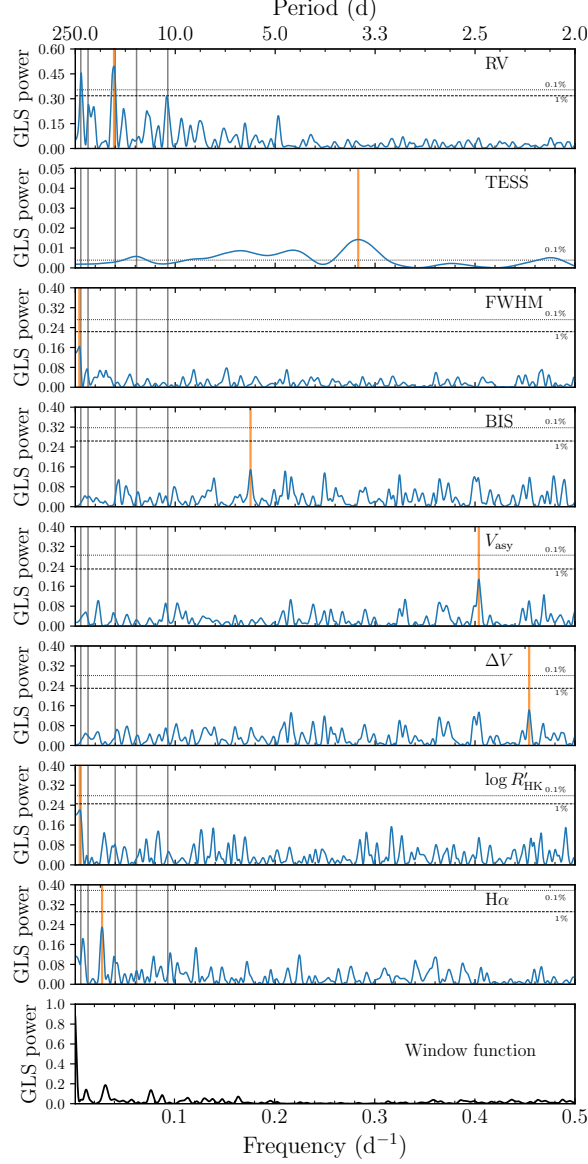
Figure 3.1 GLS periodogram of the RVs, the *TESS* photometry (PDCSAP) and the spectroscopic activity indexes under analysis. The main peak of each periodogram is highlighted with an orange vertical line. The grey vertical lines represent the signals corresponding to the transit-like signals with periods 10.8 and 16.3 days, and the additional signals identified in the RVs (Section 3.6) at $\simeq 25$, $\simeq 78$ and $\simeq 180$ days. The dashed and dotted horizontal lines show the 1% and 0.1% FAP levels, respectively. The *TESS* periodogram shows a series of peaks below 10 days, unlikely to be associated with stellar activity given the old age of the star. The FWHM and the $\log R'_{HK}$ periodograms have the main peak at 244 and 220 days, respectively, so there is no correspondence with the 180 days signal. Moreover, both of them are below the 1% FAP. The bottom panel shows the window function of the data.

do not include any activity contributions in the remaining of our analysis, except for an uncorrelated jitter term (σ_{jitter}).

3.4   Ruling out false positive scenarios

Previous experience with *Kepler* shows that candidates in multiple systems have a much lower probability of being false positives (Latham et al., 2011; Lissauer et al., 2012). Nevertheless, it is always appropriate to perform a series of checks in order to exclude the possibility of a false positive.

We notice that the star has a good astrometric *Gaia* DR2 solution (Gaia Collaboration et al., 2018), with zero excess noise and a re-normalised unit weight error (RUWE) of 1.1, indicating that the single-star model provides a good fit to the astrometric observations. This likely excludes the presence of a massive companion that could contribute to the star's orbital motion in the *Gaia* DR2 astrometry, a fact that agrees with the absence of long-term trends in our RVs (see Section 3.6.1).

Moreover, the overall RV variation below 25 m s^{-1} and the shape of the CCFs of our HARPS-N spectra exclude the eclipsing binary scenario, which would be the most likely alternative explanation for the USP planet.

A further confirmation comes from the speckle imaging on the Southern Astrophysical Research (SOAR) telescope that Ziegler et al. (2020) performed on some of the *TESS* planet candidate hosts. According to their analysis (see Tables 3 and 6 therein), no companion is detected around TOI-561 (being the resolution limit for the star 0.041 arcsec, and the maximum detectable Δmag at separation of 1 arcsec 4.76 mag). Still, the 21 arcsec *TESS* pixels and the few-pixels wide point spread function (PSF) can cause the light from neighbours over an arc-minute away to contaminate the target light curve. In the case of neighbouring eclipsing binaries (EBs), eclipses can be diluted and mimic shallow planetary transits. For example, events at $\sim$ 1 mmag level as in TOI-561.01 and TOI-561.03 can be mimicked by a nearby eclipsing binary within the *TESS* aperture with a 0.5% eclipse, but no more than 7 magnitudes fainter. This condition is not satisfied in our case, as the only three sources within 100 arcsec from TOI-561 are all fainter than T = 19.25 mag and at a distance greater than 59 arcsec, according to the *Gaia* DR2 catalogue.

An independent confirmation was provided by the analysis of the in-/out-of-transit difference centroids on the *TESS* FFIs (Figure 3.2), adopting the procedure described in Nardiello et al. (2020). The analysis of the in-/out-of transit stacked difference images confirms that, within a box of 10×10 pixels^2 ($\sim 200 \times 200$ arcsec^2) centred on TOI-561, the transit events associated with candidates .01 and .03 occur on our target star, while candidate .02 has too few in-transit points in the 30-minute cadence images for this kind of analysis — in any case, its planetary nature will be confirmed by the RV signal of TOI-561 in Section 3.6.

Finally, in order to exclude the possibility that the transit-like features were caused by instrumental artefacts, we performed some additional checks on the light curve. We visually inspected the FFIs to spot possible causes (including instrumental effects) inducing transit-like features, and we could not find
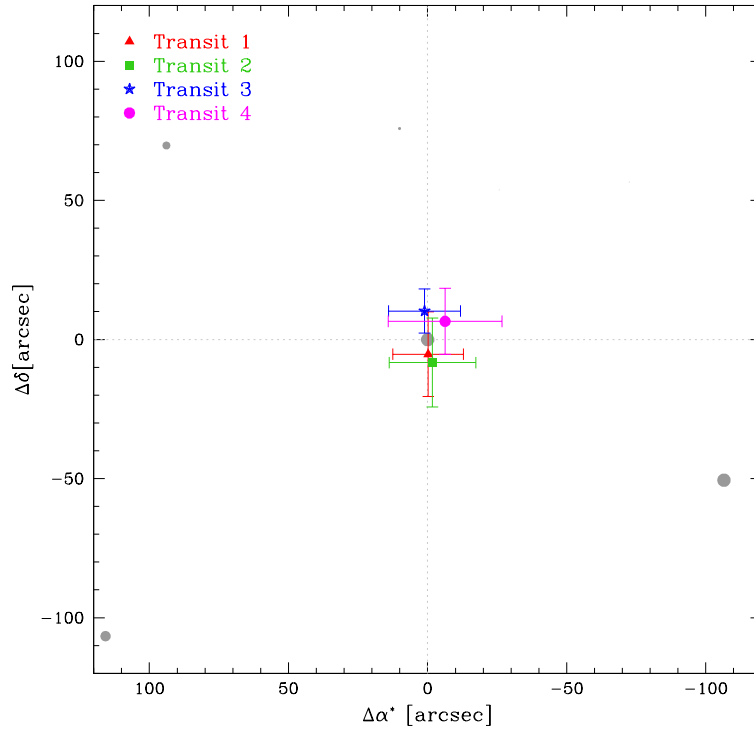
Figure 3.2 In-/out-of-transit difference centroid analysis of the transit events associated with the candidates TOI-561.01 (transit 2 and 3) and TOI-561.03 (transit 1 and 4). The star is centred at (0,0), and the grey circles are all the other stars in the *Gaia* DR2 catalogue, with dimension proportional to their apparent magnitude.

any. We re-extracted the short cadence light curve using the python package `lightkurve`[9] (Lightkurve Collaboration et al., 2018) with different photometric masks and apertures, and we corrected them by using the *TESS* Cotrending Basis Vectors (CBVs); the final results were in agreement with the *TESS*-released PDCSAP light curve. We checked for systematics in every light curve pixel, and we found none. Ultimately, we checked for correlations between the flux, the local background, the (X,Y)-position from the PSF-fitting, and the FWHM, with no results. Therefore, we conclude that all the transit-like features in the light curve are real and likely due to planetary transits.

3.5 Data analysis tools

We performed the analysis presented in the next sections using `PyORBIT`[10] (Malavolta et al., 2016, 2018), a convenient wrapper for the analysis of transit light curves and radial velocities.

In the analysis of the light curve, for each planet we fitted the central time of transit (T_0), period (P), planetary to stellar radius ratio ($R_p/R_\star$), and impact parameter b. In order to reduce computational time, we set a narrow, but still uninformative, uniform prior for period and time of transit, as defined by a visual inspection. We fitted a common value for the stellar density $\rho_\star$, imposing a Gaussian prior based on the value from Table 3.3. We included a quadratic limb-darkening law with Gaussian priors on the coefficients u_1, u_2, obtained through a bilinear interpolation of limb darkening profiles by Claret (2018) [11]. We initially calculated the standard errors on u_1, u_2 using a Monte Carlo approach that takes into account the errors on T_{eff} and $\log g$ as reported in Table 3.3, obtaining $u_1 = 0.393 \pm 0.007$ and $u_2 = 0.204 \pm 0.001$. We however decided to conservatively increase the error on both coefficients to 0.05. In the fit we employed the parametrization (q_1, q_2) introduced by Kipping (2013). Finally, we included a jitter term to take into account possible *TESS* systematics and short-term stellar activity noise. We assumed uniform, uninformative priors for all the other parameters, although the prior on the stellar density will inevitably affect the other orbital parameters. All the transit models were computed with the `batman` package (Kreidberg, 2015), with an exposure time of 120 seconds and an oversampling factor of 10 (Kipping, 2010).

In the analysis of the radial velocities, we allowed the periods to span between 2 and 200 days (i. e., the time span of our dataset) for the non-transiting planets, while we allowed the semi-amplitude K to vary between 0.01 and 100 m s^{-1} for all the candidate planets. These two parameters were explored in the logarithmic space. For the transiting candidates, we used the results from the photometric fit (see Appendix A) to impose Gaussian priors on period and time of transit on RV analysis alone, while using the same uninformative priors as for the photometric fit when including the photometric data as well.

For all the signals except the USP candidate, we assumed eccentric orbits with a half-Gaussian zero-mean prior on the eccentricity (with variance 0.098) according to Van Eylen et al. (2019), unless stated otherwise.

---

[9]https://github.com/KeplerGO/lightkurve
[10]https://github.com/LucaMalavolta/PyORBIT, version 8.1
[11]https://vizier.u-strasbg.fr/viz-bin/VizieR?-source=J/A+A/618/A20

We computed the Bayesian evidence using the `MultiNest` nested-sampling algorithm (Feroz & Hobson, 2008; Feroz et al., 2009, 2019) with the Python wrapper `pyMultiNest` (Buchner, J. et al., 2014). In the specific case of the joint light curve and RV analysis (Section 3.7), we employed the `dynesty` nested-sampling algorithm (Skilling, 2004; Skilling, 2006; Speagle, 2020), which allowed for the computation of the Bayesian evidence in a reasonable amount of time thanks to its easier implementation of the multi-processing mode. We performed a series of test on a reduced dataset, and we verified that the two algorithms provided consistent results with respect to each other. For all the analyses, we assumed 1000 live points and a sampling efficiency of 0.3, including a jitter term for each dataset considered in the model.

Global optimisation of the parameters was performed using the differential evolution code PyDE[12]. The output parameters were used as a starting point for the Bayesian analysis performed with the `emcee` package (Foreman-Mackey et al., 2013a), a Markov chain Monte Carlo (MCMC) algorithm with an affine invariant ensemble sampler (Goodman & Weare, 2010). We ran the chains with $2n_{\text{dim}}$ walkers, where n_{dim} is the dimensionality of the model, for a number of steps adapted to each fit, checking the convergence with the Gelman-Rubin statistics (Gelman & Rubin, 1992), with a threshold value of $\hat{R} = 1.01$. We also performed an auto-correlation analysis of the chains: if the chains were longer than 100 times the estimated auto-correlation time and this estimate changed by less that 1%, we considered the chains as converged. In each fit, we conservatively set the burn-in value as a number larger than the convergence point as just defined, and we applied a thinning factor of 100.

3.6 Unveiling the system architecture

3.6.1 Planetary signals in the RV data

Before proceeding with a global analysis, we checked whether we could independently recover the signals identified by the *TESS* pipeline (Section 3.2.1) in our RV data only. The periodogram analysis of the RVs in Section 3.3.3 highlighted the presence of several peaks not related to the stellar activity. In particular, an iterative frequency search, performed subtracting at each step the frequency values previously identified, supplied the frequencies $f_1 = 0.039 \text{ d}^{-1}$ ($P_1 \simeq 25.6$ d), $f_2 = 0.006 \text{ d}^{-1}$ or 0.013 d^{-1} ($P_2 \simeq 170$ d or $\simeq 78$ d) with the two frequencies being related to each other (i. e., removing one of them implies the vanishing of the other one), $f_3 = 0.093 \text{ d}^{-1}$ ($P_3 \simeq 10.8$ d, corresponding to the TOI-561.01 candidate), and $f_4 = 2.239 \text{ d}^{-1}$ ($P_4 \simeq 0.45$ d, corresponding to the TOI-561.02 candidate). After removing these four signals, no other clear dominant frequency emerged in the residuals. Since any attempt to perform a fit of the RVs to characterise the transiting candidates without accounting for additional dominant signals would lead to unreliable results, we decided to test the presence of additional planets in a Bayesian framework. We considered four models, the first one (Model 0) assuming the three transiting candidates only,i. e., TOI-561.01, .02, .03, and then including an additional planet in each of the successive models,i. e., TOI-561.01, .02, .03 plus one (Model 1), two (Model 2) and three

---

[12]https://github.com/hpparvi/PyDE

(Model 3) additional signals, respectively. We computed the Bayesian evidence for each model using the `MultiNest` nested-sampling algorithm, following the prescriptions as specified in Section 3.5. We report the obtained values in Table 3.4. According to this analysis, we concluded that the model with two additional signals, i. e., Model 2 (with no trend), is strongly favoured over the others, with a difference in the logarithmic Bayes factor $2\,\Delta\ln\mathscr{Z} > 10$ (Kass & Raftery, 1995), both compared to the case with one or no additional signals. In the case of a third additional signal (Model 3), the difference with respect to the two-signal model was less than 2, indicating that there was no strong evidence to favour this more complex model over the simpler model with two additional signals only (Kass & Raftery, 1995). We repeated the analysis first including a linear and then a quadratic trend in each of the four models. In all cases, the Bayesian evidence systematically disfavoured the presence of any trend[13].

The first additional signal was associated with a candidate with $f \simeq 0.04 \, \mathrm{d}^{-1}$ ($P \simeq 25.6 \, \mathrm{d}$), which corresponds to the strongest peak in the RVs periodogram. Concerning the second additional signal, the `MultiNest` run highlighted the presence of two clusters of solutions, peaked at about $f = 0.013 \, \mathrm{d}^{-1}$ or $0.013 \, \mathrm{d}^{-1}$, i. e., $P = 78$ and 180 days respectively. The frequency analysis confirmed that the signals are aliases of each other, since when we subtract one of them, the other one also disappears. The alias peak is visible in the low-frequency regime of the spectral window (Figure 3.1, bottom panel). We should also consider that the longer period is close to the time baseline of our data. In order to disentangle the real frequency from its alias, we computed the Bayesian evidence of the two possible solutions, first allowing the period to vary between 50 and 100 days, and then between 100 and 200 days. The Bayesian evidence slightly favoured the solution with $P \sim 78 \, \mathrm{d}$, even if not with strong significance ($\Delta\ln\mathscr{Z} \simeq 2$). Since we could not definitely favour one solution over the other, we decided to perform all the subsequent analyses using both sets of parameters.

Another important outcome of our frequency search is the absence of a signal with a periodicity of ~ 16 days, that is, the transiting candidate TOI-561.03. Therefore, in order to test our ability to recover the planetary signals, we performed a series of injection/retrieval simulations, thoroughly explained in Appendix B2. The results of this injection/retrieval test are summarised in Figure 3.3. We found that the injected RV amplitude of .01 is not significantly affecting the retrieved value for .03, i. e. the cross-talk between the two signals is negligible. We verified that the same conclusion applies to the other signals as well. More importantly, any attempt to retrieve a null signal at the periodicity of the candidate planet .03 would result in an upper limit of $\approx 0.5 \, \mathrm{m \, s}^{-1}$ as we actually observe with the real dataset, when exploring the K parameter in logarithmic space. Any signal equal or higher than $1 \, \mathrm{m \, s}^{-1}$ would have been detected ($> 2\sigma$), even if marginally. A signal with amplitude of $0.5 \, \mathrm{m \, s}^{-1}$ would not lead to the detection of the planet (intended as a 3-σ detection), but the retrieved posterior is expected to differ substantially from the observed one, especially on the lower tail of the distribution. We conclude that the planetary candidate TOI-561.03 is undetected in our RV dataset, with an upper limit on the semi-amplitude of $0.5 \, \mathrm{m \, s}^{-1}$ ($M_{\mathrm{p}} < 2.0 \, M_{\oplus}$).

---

[13]For the model with three additional signals and a quadratic trend, the calculation of the Bayesian evidence did not converge.
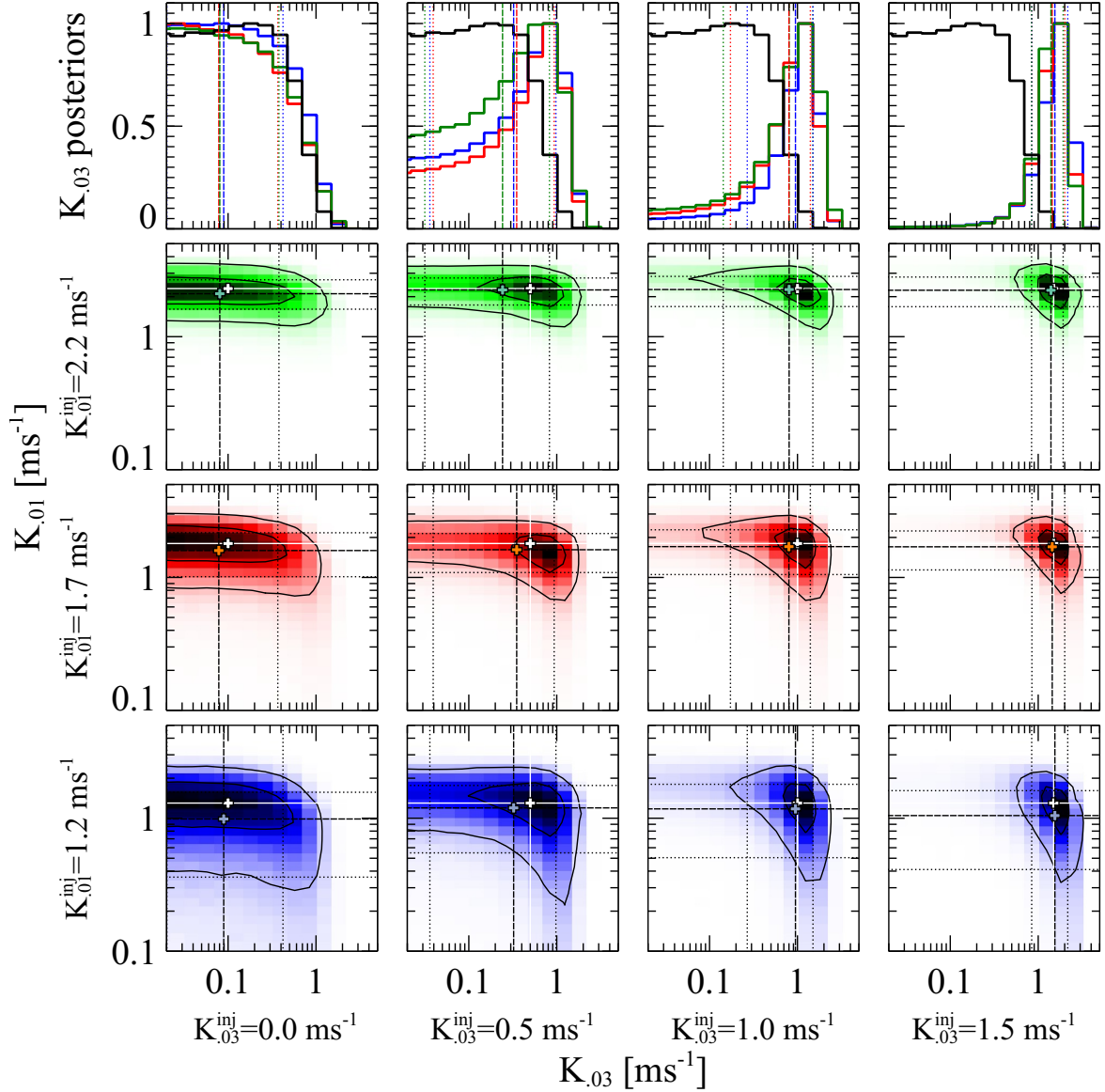
Figure 3.3 Posterior distributions (in the top panels, the blue, red and green lines respectively) of the retrieved RV signal of TOI-561.03 according to different injected values for the RV semi-amplitudes of candidates .01 and .03. The black line in the top panels corresponds to the observed posterior of the RV semi-amplitude of candidate .03. Median and 1-σ values are marked with vertical dashed and dotted lines respectively.

Table 3.4 Logarithmic Bayesian evidences for the different models under exam. Model 0 corresponds to the model with no additional RVs signal other than the signals from the three transiting candidates i. e., TOI-561.01, .02, .03. Model 1, 2 and 3 correspond to the models with the three transiting candidates plus one, two and three additional planets, respectively. All the values are expressed with respect to Model 0. We note that the reported errors, as obtained from the nested sampling algorithm, are likely underestimated (Nelson et al., 2020).

|	Model 0	Model 1	Model 2	Model 3
$\ln \mathcal{Z}$	0.0 ± 0.1	13.4 ± 0.2	26.1 ± 0.2	28 ± 0.2

56

3.6.2 Transit attribution

Given the non-detection of the planetary candidate TOI-561.03 in the RV data, we investigated more closely the transit-like features associated with this candidate in the *TESS* light curve, at T_0[14] $\simeq 1521.9$ d and $T_0 \simeq 1538.2$ d, referred from now on as transit 1 and 4 respectively, given their sequence in the TESS light curve (when excluding the transits of the USP candidate). From our preliminary three-planet photometric fit (Figure A.1), we noted that, with respect to the other candidates, TOI-561.03 appears to have a longer transit duration compared to the model, and the residuals show some deviations in the ingress/egress phases. To better understand the cause of these deviations, we checked how the model fits each transit. As Figure 3.4 shows, the global model appears to better reproduce the first transit associated with TOI-561.03 (transit 1) than the second transit (transit 4), that has a duration that looks underestimated by the model. Moreover, a two-sample Kolmogorov–Smirnov statistical test[15] (Hodges, 1958) on the residuals of transit 1 and 4 suggests that the two residual samples are not drawn from the same distribution (threshold level $\alpha = 0.05$, statistics KS = 0.178, $p-$value $\ll 0.01$).

Therefore, we hypothesised that the two transit-like features may be unrelated, i. e., they correspond to the transits of two distinct planets. Since two additional planets are actually detected in the RV data, and their periods are longer than the *TESS* light curve interval (i.e., that *TESS* can detect, at most, only one transit for each of them), we tested the possibility that the two transits previously associated with TOI-561.03 could indeed be due to the two additional planets inferred from the RV analysis. To check our hypothesis, we first analysed the RV dataset with a model encompassing four planets, of which only .01 and .02 have period and time of transit constrained by *TESS*. In other words, we performed the same RV analysis as described in Appendix B2, but without including TOI-561.03 in the model. We repeated the analysis twice in order to disentangle the periodicity at 78 d from its alias at 180 d, and *vice versa*. We used the posteriors of the fit to compute the expected time of transit of the outer planets. We then performed two independent fits of transit 1 and 4 with PyORBIT, following the prescriptions as specified in Section 3.5. We imposed a lower boundary on the period of 22 days, in order to exclude the periods that would imply a second transit of the same planet in the *TESS* light curve, and an upper limit of 200 days. As a counter-measure against the degeneracy between eccentricity and impact parameter in a single-transit fit, we kept the Van Eylen et al. (2019) eccentricity prior knowing that high eccentricities for such a compact, old system are quite unlikely (Van Eylen et al., 2019). Finally we compared the posteriors of period and time of transit from the photometric fit with those from radial velocities, knowing that the former will provide extremely precise transit times, but a broad distribution in period, while RVs give us precise periods, but little information on the transit times. The results are summarised in Figure 3.5: the 25.7 ± 0.3 d signal detected in the RVs is located in the vicinity of the main peak of transit 1 period distribution, while the $78.6^{+1.8}_{-2.5}$ d signal is close to the main peak in transit 4 period distribution. Moreover, Figure 3.5 definitely confirms that both the conjunction times inferred from the RV fit corresponding to the ~ 25 and ~ 78 days signals, respectively $T_0 = 1520^{+3}_{-6}$ d

---

[14] All the T_0s in this section are expressed in BJD-2457000.

[15] We used the Python version implemented in `scipy.stats.ks_2samp`.
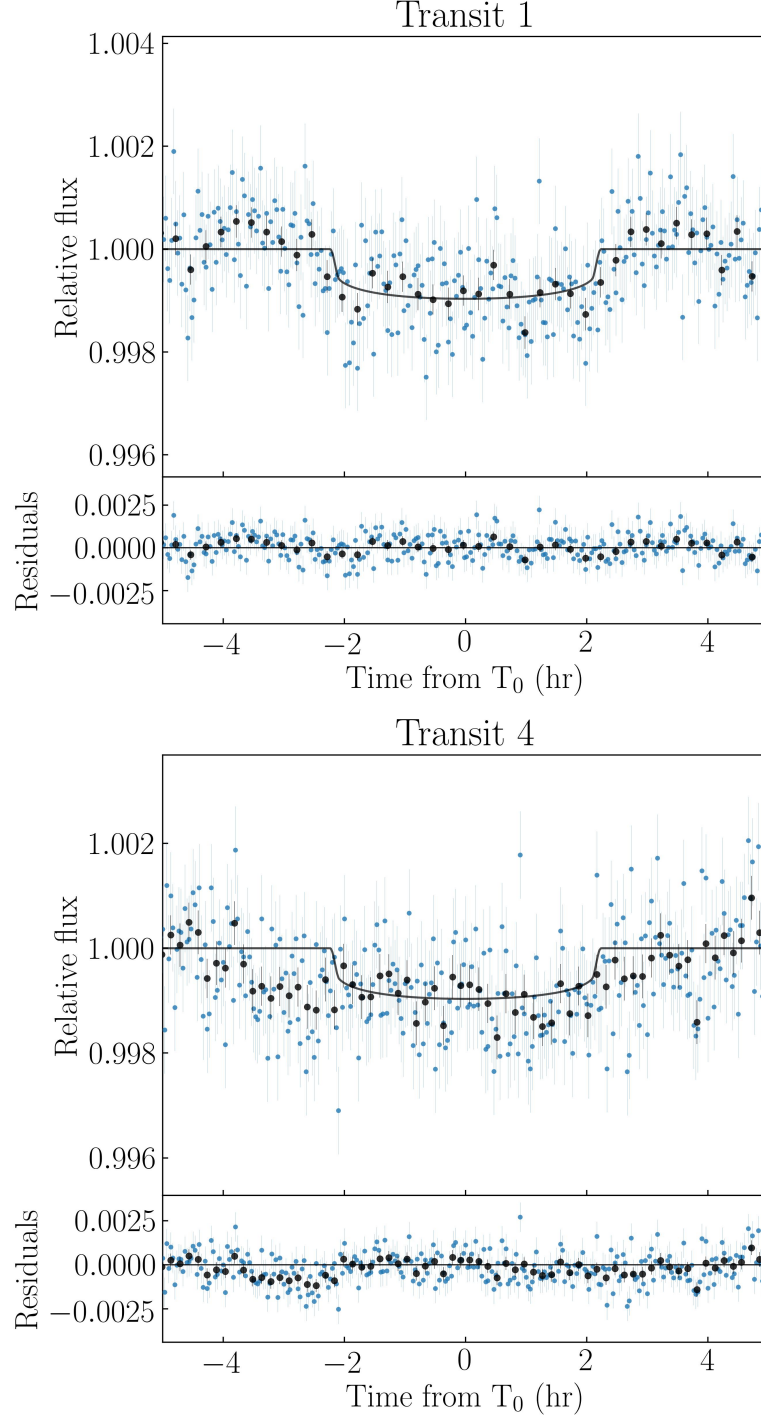
Figure 3.4 Transit 1 ($T_0 \simeq 1521.9$ d) and 4 ($T_0 \simeq 1538.2$ d) in the *TESS* detrended light curve associated with the candidate TOI-561.03. The best-fitting transit model from the three-planet model photometric fit is over-plotted (black solid line). The black dots are the data points binned over 15 minutes. With respect to transit 1, the duration of transit 4 looks underestimated by the global model, with a systematic offset in the residuals, especially in the pre-transit phase.

and $T_0 = 1532^{+12}_{-9}$ d, are consistent with the (much more precise) T_0s inferred from the individual fit of transit 1 ($T_0 = 1521.885 \pm 0.004$ d) and 4 ($T_0 = 1538.178 \pm 0.006$ d) respectively. Regarding the alias at 182 ± 7 days, while the RV period is consistent with the corresponding posterior from the transit fit, the conjunction time $T_0 = 1628 \pm 13$ d that is derived from our analysis is not compatible with any of the transits in the *TESS* light curve. We also note that the proportion of the orbital period covered by the *TESS* photometry is ~ 2.3 times larger for the candidate with 78 d period, thus increasing the chance of getting a transit of it. In conclusion, taking into account both photometric and RV observations, the most plausible solution for the TOI-561 system is a four-planet configuration in which transits 1 and 4 are associated with the planets that have periods of ~ 25 d and ~ 78 d detected in the RV data, and the 180 d signal is considered an alias of the 78 d signal.

Given this final configuration, hereafter we will refer to the planets with period ~ 0.45, ~ 10.8, ~ 25 and ~ 78 days as planets b, c, d and e, respectively.

3.6.3 The system architecture

Given the presence of two single-transit planets in our data, a joint photometric and RV modelling is necessary in order to characterise the orbital parameters of all members of the TOI-561 system in the best possible way. We considered a four-planet model, with a circular orbit for the USP planet and allowing nonzero-eccentricity orbits for the others. We performed the `PyORBIT` fit as specified in Section 3.5, running the chains for 150 000 steps, and discarding the first 50 000 as burn-in. We summarise the results of our best-fitting model in Table 3.5, and show the transit models, the phase folded RVs, and the global RV model in Figures 3.6, 3.7, and 3.8 respectively.

We obtained a robust detection of the USP planet (planet b) RV semi-amplitude ($K_b = 1.39 \pm 0.32$ m s^{-1}), that corresponds to a mass of $M_b = 1.42 \pm 0.33$ $M_\oplus$, while for the 10.8 d period planet (planet c) we obtained $K_c = 1.84 \pm 0.33$ m s^{-1}, corresponding to $M_c = 5.40 \pm 0.98$ $M_\oplus$. We point out that the here reported value of K_b and M_b is obtained from the joint photometric and RV fit. However, the final value of K_b and M_b that we decided to adopt (see Section 3.6.4 for more details) is the weighed mean between the values obtained from the joint fit reported in this section and from the floating chunk offset method described in the next section. In addition, we inferred the presence of two additional planets, with periods of 25.62 ± 0.04 days (planet d) and 77.23 ± 0.39 days (planet e), and robustly determined semi-amplitudes of $K_d = 3.06 \pm 0.33$ m s^{-1}($M_d = 11.95 \pm 1.28$ $M_\oplus$) and $K_e = 2.84 \pm 0.41$ m s^{-1}($M_e = 16.0 \pm 2.3$ $M_\oplus$). Both planets show a single transit in the *TESS* light curve, previously attributed to a transiting planet with period ~ 16 d, whose presence has however been ruled out by our analysis. This allowed us to infer a planetary radius of $R_d = 2.53 \pm 0.13$ $R_\oplus$ and $R_e = 2.67 \pm 0.11$ $R_\oplus$ for planet d and e respectively.

We performed the stability analysis of our determined solution, computing the orbits for 100 Kyr with the `whfast` integrator (with fixed time-step of 0.1 d) implemented within the `rebound` package (Rein & Liu, 2012; Rein & Tamayo, 2015). During the integration we checked the dynamical stability of the solution with the Mean Exponential Growth factor of Nearby Orbits (MEGNO or $\langle Y \rangle$) indicator
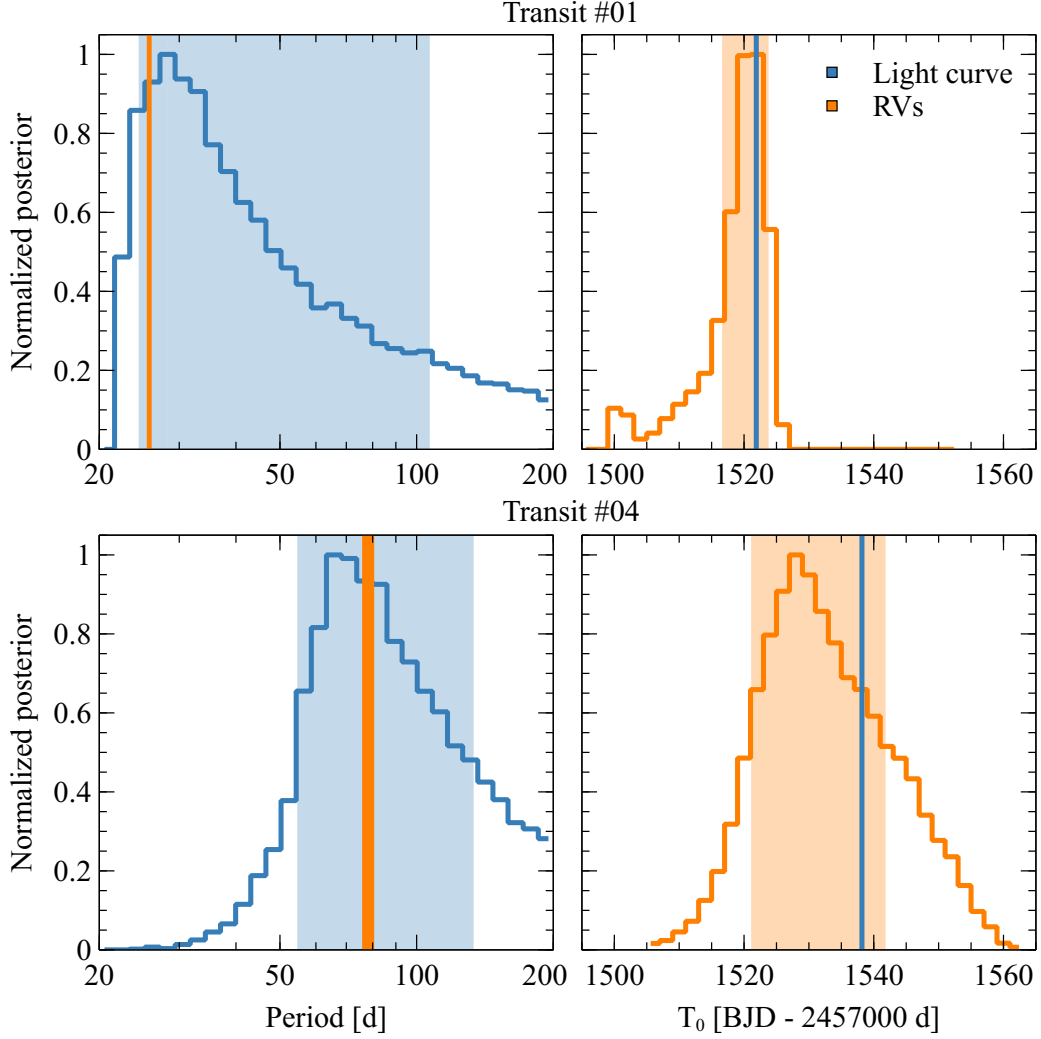
Figure 3.5 Comparison between period (left panels) and T_0 (right panels) obtained from the RV fit and from the fit of each single transit. Top and bottom panels refer to transit 1 and 4, respectively. Each panel shows the posterior distribution of the analysed parameter, and the shaded area indicates the region within the 68.27-th percentile from the mode of the distribution. The vertical solid lines indicate the inferred best-fitting value of the parameter, with thickness proportional to the associated error.

Table 3.5 Final parameters of the TOI-561 system.

Parameter	TOI-561b	TOI-561c	TOI-561d	TOI-561e
P (d)	0.446578 ± 0.000017	10.779 ± 0.004	25.62 ± 0.04	77.23 ± 0.39
T_0^{a} (d)	1517.498 ± 0.001	1527.060 ± 0.004	1521.882 ± 0.004	1538.181 ± 0.004
$a/R_\star$	2.646 ± 0.031	22.10 ± 0.26	39.35 ± 0.46	82.13 ± 0.99
a (AU)	0.01055 ± 0.00008	0.08809 ± 0.0007	0.1569 ± 0.0012	$0.3274^{+0.0028}_{-0.0027}$
$R_{\text{p}}/R_\star$	0.0152 ± 0.0007	0.0308 ± 0.0009	0.0271 ± 0.0014	0.0286 ± 0.0011
R_{p} ($R_\oplus$)	1.423 ± 0.066	2.878 ± 0.096	2.53 ± 0.13	2.67 ± 0.11
b	$0.14^{+0.13}_{-0.10}$	$0.18^{+0.16}_{-0.12}$	$0.32^{+0.17}_{-0.19}$	$0.34^{+0.13}_{-0.20}$
i (deg)	$87.0^{+2.1}_{-2.8}$	$89.53^{+0.32}_{-0.39}$	$89.54^{+0.28}_{-0.21}$	$89.75^{+0.14}_{-0.08}$
T_{14} (hr)	$1.327^{+0.021}_{-0.030}$	$3.77^{+0.07}_{-0.15}$	$4.85^{+0.20}_{-0.35}$	$6.96^{+0.34}_{-0.38}$
e	0 (fixed)	$0.060^{+0.067}_{-0.042}$	$0.051^{+0.064}_{-0.036}$	$0.061^{+0.051}_{-0.042}$
ω (deg)	90 (fixed)	200^{+55}_{-49}	246^{+67}_{-124}	155 ± 83
K^{b} (m s^{-1})	1.56 ± 0.35	1.84 ± 0.33	3.06 ± 0.33	2.84 ± 0.41
M_{p}^{b} ($M_\oplus$)	1.59 ± 0.36	5.40 ± 0.98	11.95 ± 1.28	16.0 ± 2.3
ρ_{p} ($\rho_\oplus$)	0.55 ± 0.14	0.23 ± 0.05	0.74 ± 0.14	0.84 ± 0.16
ρ_{p} (g cm^{-3})	3.0 ± 0.8	1.3 ± 0.3	4.1 ± 0.8	4.6 ± 0.9
Common parameter				
$\rho_\star$ ($\rho_\odot$)	1.248 ± 0.043			
u_1	0.401 ± 0.048			
u_2	0.208 ± 0.049			
$\sigma_{\text{jitter,ph}}^{\text{c}}$	$0.000024^{+0.000018}_{-0.000011}$			
$\sigma_{\text{jitter}}^{\text{d}}$ (m s^{-1})	1.29 ± 0.23			
γ^{e} (m s^{-1})	79702.58 ± 0.29			

[a] BJD_{TDB}-2457000. [b] The reported values of planet b correspond to the weighted mean between the values inferred from the nightly offset method ($K_{\text{b}} = 1.80 \pm 0.38$ m s^{-1}, $M_{\text{b}} = 1.83 \pm 0.39$ $M_\oplus$) and from the joint photometric and RV fit ($K_{\text{b}} = 1.39 \pm 0.32$ m s^{-1}, $M_{\text{b}} = 1.42 \pm 0.33$ $M_\oplus$). [c] Photometric jitter term. [d] Uncorrelated RV jitter term. [e] RV offset.
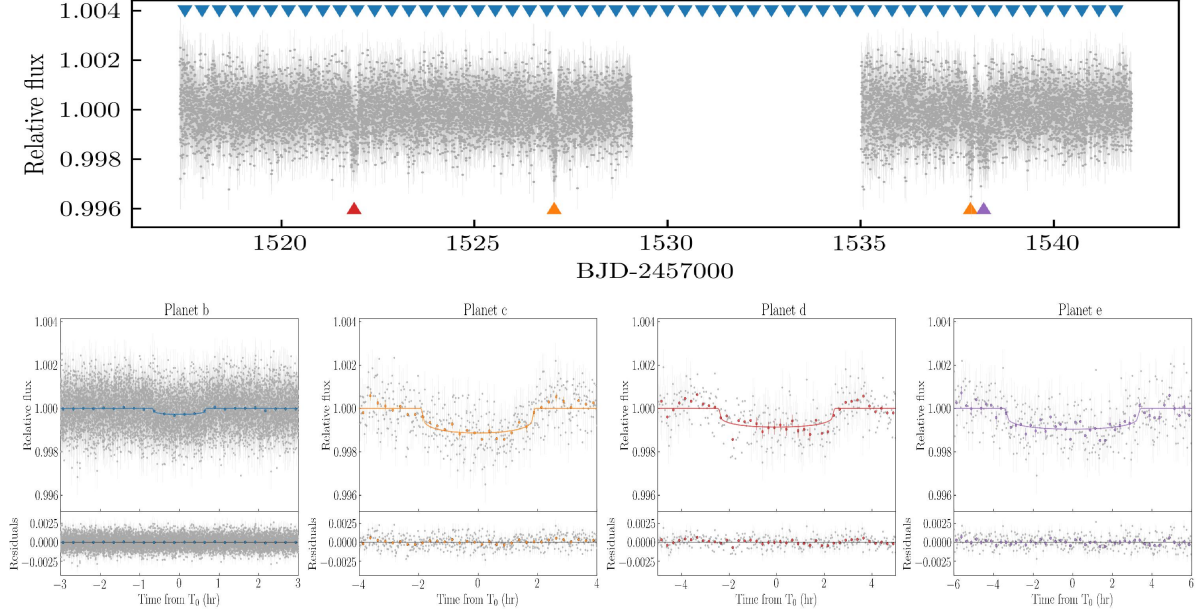
Figure 3.6 *Top*: 2-minute cadence flattened light curve of TOI-561. The transits of planet b ($P \sim 0.45$ d), c ($P \sim 10.8$ d), d ($P \sim 25.6$ d), e ($P \sim 77.2$ d) are highlighted with blue, orange, red and purple triangles, respectively. *Bottom*: TOI-561 phase-folded 2-minute light curves over the best-fitting models (solid lines) for the four planets. The light curve residuals are shown in the bottom panel.

developed by Cincotta & Simó (2000) and implemented within `rebound` by Rein & Tamayo (2016). We ran 10 simulations with initial parameters drawn from a Gaussian distribution centred on the best-fitting parameters and standard deviation derived in this section. All the 10 runs resulted in a MEGNO value of 2, indicating that the family of solutions is stable.

Finally, we checked the presence of any additional signal in the RVs residuals after removing the four-planet model contribution. The GLS periodogram showed a non-significant peak at ~ 2.5 days, with a normalised power of 0.20, that is, below the 1% FAP threshold (0.26). As a supplemental confirmation, we ran a `PyORBIT` fit of the RVs, assuming first a four-planet model plus an additional signal, and then a four-planet model adding a Gaussian Process (GP) regression. For the latter approach, we employed the quasi-periodic kernel as formulated by Grunblatt et al. (2015), with no priors on the GP hyper-parameters, since we could not identify any activity-related signal in the ancillary datasets (see Section 3.3.3)[16]. In both cases, the (hyper-)parameters of the additional signal did not reach convergence, while the results for the four transiting planets were consistent with those reported above. Considering these results, we adopt the parameters and configuration determined in this section as the representative ones for the TOI-561 system, with the only exception of the mass and semi-amplitude of TOI-561 b, that we discuss in the next section.

---

[16]We are well aware that this is a sub-optimal use of GP regression, and that this approach may be justified in this specific case only as an attempt to identify additional signals.
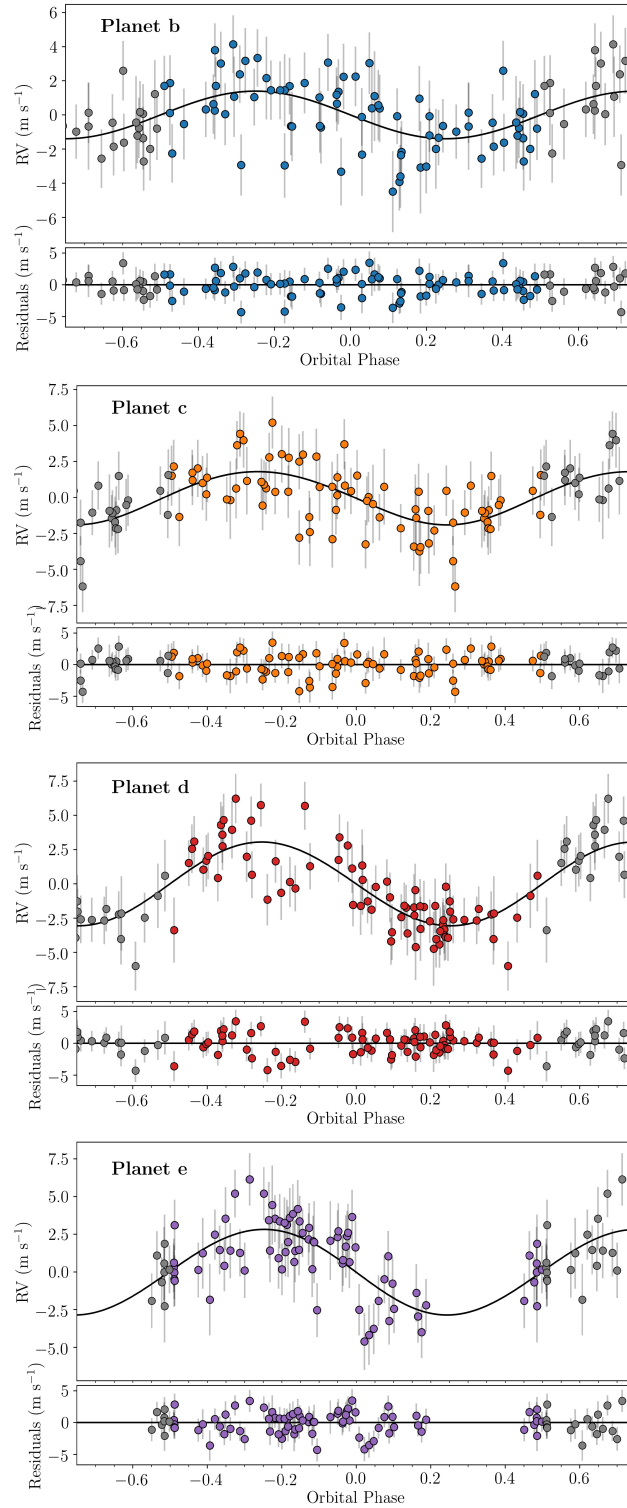
Figure 3.7 Phase-folded RV fit with residuals from the joint four-planet photometric and RV analysis. Planets b, c, d, and e are shown in blue, orange, red and purple, respectively. The reported errorbars include the jitter term, added in quadrature.
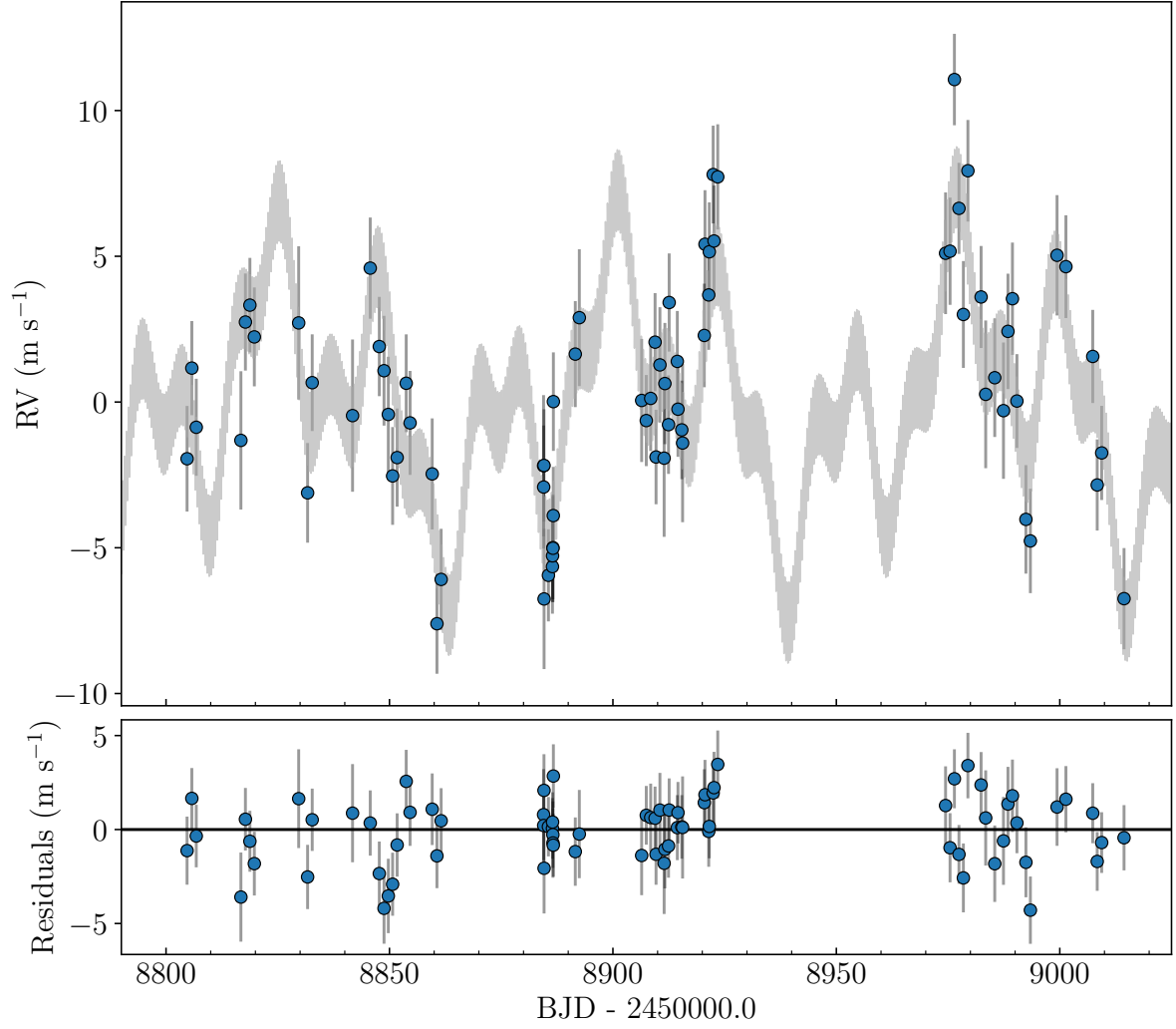
Figure 3.8 Four-planet model from the joint photometric and RV analysis. The grey curve is the the best-fitting model, and the blue points are the HARPS-N data. The residuals are shown in the bottom panel. The reported errorbars include the jitter term, added in quadrature.

3.6.4 Alternative characterisation of the USP planet

If the separation between the period of the planet and all the other periodic signals is large enough, and the RV signal has a similar or larger semi-amplitude, it is possible to determine the RV semi-amplitude for an USP planet without any assumptions about the number of planets in the system or the activity of the host star. Under such conditions, during a single night, the influence of any other signal is much smaller than the measurement error and thus it can be neglected. If two or more observations are gathered during the same night and they span a large fraction of the orbital phase, the RV semi-amplitude of the USP planet can be precisely measured by just applying nightly offsets to remove all the other signals (e.g. Frustagli et al. 2020; Hatzes et al. 2010; Howard et al. 2013; Pepe et al. 2013 for a recent example). Such an approach, also known as floating chunk offset method (FCO; Hatzes 2014), has proven extremely reliable even in the presence of complex activity signals, as shown by Malavolta et al. (2018). In our case, the shortest, next periodic signal (i. e., TOI-561 c at 10.78 days) is $\simeq 24$ times the period of TOI-561 b (i. e., the USP planet at 0.45 days), with similar predicted RV semi-amplitude, making this target suitable for the FCO approach. Thanks to our observational strategy (see Section 3.2.2) we could use ten different nights for this analysis. Most notably, during two nights we managed to gather six observations spanning nearly 5 hours, i. e., more than 40% of the orbital period of TOI-561 b, at opposite orbital phases, thus providing a good coverage in phase of the RV curve. We did not include RV measurements with an associated error greater than 2.5 m s^{-1} (see Appendix B1). We performed the analysis with `PyORBIT` as specified in Section 3.5, assuming a circular orbit for the USP planet and including a RV jitter as a free parameter to take into account possible short-term stellar variability and any underestimation of the errorbars. From our analysis, we obtained a RV semi-amplitude of $K_p = 1.80 \pm 0.38$ m s^{-1}, corresponding to a mass of $M_p = 1.83 \pm 0.39$ $M_\oplus$. The resulting RV jitter is $j < 0.9$ m s^{-1}(84.13-th percentile of the posterior). We show the phase folded RVs of the USP planet in Figure 3.9.

Since the greater reliability of this method over a full fit of the RV dataset is counter-balanced by the smaller number of RVs, we decided not privilege one over the other. Therefore, we assumed as final semi-amplitude and mass of TOI-561 b the weighted mean of the values obtained from the two methods (FCO approach and joint photometric and RV fit), i. e. $K_b = 1.56 \pm 0.35$ m s^{-1}, corresponding to a mass of $M_b = 1.59 \pm 0.36$ $M_\oplus$. Table 3.5 lists the above-mentioned values for TOI-561 b.

3.7 Comparison with other models

Our final configuration is quite different from the initial one suggested by the *TESS* automatic pipeline. However, the analyses performed on the currently available data clearly disfavour the scenario with a ~ 16 d period candidate. In fact, in addition to the previous analyses, we also performed a joint photometric and RV fit assuming a five-planet model including the 16 d period candidate, and assuming that the two additional signals seen in the RVs were caused by two non-transiting planets, the inner one with period of ~ 25 d and the outer one both in the case of ~ 78 d and ~ 180 d period. Such a model,
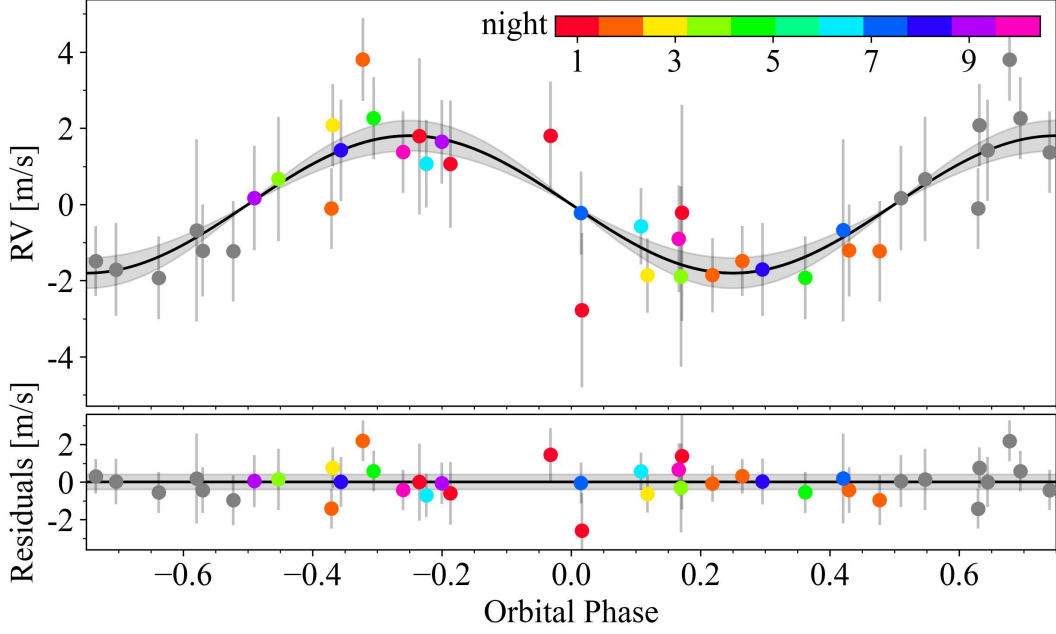
Figure 3.9 Phase folded RVs of the ten nights used to model the RV semi-amplitude of the USP planet using the FCO approach.

including the TOI-561.01, .02, .03 candidates plus two additional signals, corresponds to the favoured model (Model 2) identified in Section 3.6.1, and is therefore representative of the best-fitting solution when assuming the *TESS* candidate attribution. In fact, Table 3.4 suggests that in this case two additional signals need to be added to the three transiting candidates to best reproduce the RV dataset, and therefore the five-planet model should be considered also in the joint photometric and RV modelling.

According to the Bayesian evidence (Table 3.6), computed with the `dynesty` algorithm as specified in Section 3.5, the four-planet model is strongly favoured with respect to the five-planet model in both cases, with a difference in the logarithmic Bayes factor $2\Delta\ln\mathscr{Z} \gg 10$ (Kass & Raftery, 1995).

Moreover, we checked the stability of the five-planet model solutions as described in Section 3.6.3, with the external planet both on an orbit of 78 d and 180 d. For all the planetary parameters, including the mass of the 16 d period planet[17], we used the values and standard deviations derived from the joint photometric and RV fit, except for the inclination of the two external planets, that we fixed to 90°.

All of 10 runs yielded unstable solutions, with a close encounter or an ejection occurring within the integration time. In order to assess the origin of the instability of the system, we tested a four-planet configuration following the same procedure as above, removing one planet each time. We found that the orbital configuration of the system could be stable only if we remove the candidate with period of ~ 16 d. Therefore, the stability analysis additionally confirms our determined four-planet configuration, ruling out the presence of a ~ 16 d period planet.

---

[17]The mass of the 16 d period planet obtained from the fit was $0.62 \pm 1.03\ M_{\oplus}$ and $1.19 \pm 1.27\ M_{\oplus}$ for the ~ 78 d and ~ 180 d external planet period, respectively. Obviously, when selecting the 10 samples, the mass was constrained to positive values.

Table 3.6 Logarithmic Bayesian evidences for the models considered in Section 3.7. Model 0 corresponds to the four-planet model, that includes TOI-561.01, .02 and the two additional planets identified in the RVs, showing a single transit each. Model 1 and 2 correspond the five-planet model, i. e., including TOI-561.01, .02, .03 and the two additional RV planets (assumed in this case not to transit), in the case of an outer planet at ~ 78 d and ~ 180 d period respectively (see Section 3.6.1). All the values are expressed with respect to Model 0. We note that the reported errors, as obtained from the nested sampling algorithm, are likely underestimated (Nelson et al., 2020).

	Model 0	Model 1	Model 2
$\ln \mathscr{Z}$	0.0 ± 0.9	-77.8 ± 1.0	-76.9 ± 1.0

3.8 Discussion and Conclusions

According to our analysis, TOI-561 hosts four transiting planets, including an USP planet, a ~ 10.8 d period planet and two external planets with periods of ~ 25.6 and ~ 77.2 days. The latter were initially detected in the RVs data only, but based on our subsequent analyses we were able to identify a single transit of each planet in the *TESS* light curve; those transits were initially associated with a candidate planet with period of ~ 16 d, whose presence we ruled out. As a 'lesson learned', we would suggest that caution should be taken when candidate planets, detected by photometric pipelines, are based on just two transits. In such cases, one should not hesitate to consider alternative scenarios.

TOI-561 joins the sample of 88 confirmed systems with 4 or more planets[18], and it is one of the few multi-planet systems with both a mass and radius estimate for all the planets. Our global photometric and RV model allowed us to determine the masses and densities of all the planets with high precision, with a significance of $\sim 4.4\sigma$ for planet b and $> 5\sigma$ for planets c, d and e. In Figure 3.10 we show the position of TOI-561 b, c, d and e in the mass-radius diagram of exoplanets with masses and radiii measured with a precision better than 30%. The comparison with the theoretical mass-radius curves excludes an Earth-like composition ($\sim 33\%$ iron and 67% silicates) for all planets in the system, whose internal structure we further analyse in the following sections.

3.8.1 TOI-561 b

The density ($\rho_b = 3.0 \pm 0.8$ g cm^{-3}) of the USP planet is consistent with a 50% (or even more) water composition. Such a composition may be compatible with a water-world scenario, where 'water worlds' are planets with massive water envelopes, in the form of high pressure H_2O ice, comprising $> 5\%$ of the total mass. Even assuming the higher mass value inferred with the FCO method ($M_b = 1.83 \pm 0.39$ $M_{\oplus}$, implying a density of $\rho_b = 3.5 \pm 0.9$ g cm^{-3}), TOI-561 b would be located close to the 25% water composition theoretical curve in the mass-radius diagram, and it would be consistent with a rocky composition only at a confidence level greater than 2σ in both radius and mass. Given its proximity to the host star (incident flux $F_p \simeq 5100$ $F_{\oplus}$), the presence of any thick H-He envelope has to be excluded due the photo-evaporation processes that such old close-in planets are expected to suffer (e.g. Lopez,

---

[18]According to the https://exoplanetarchive.ipac.caltech.edu/.
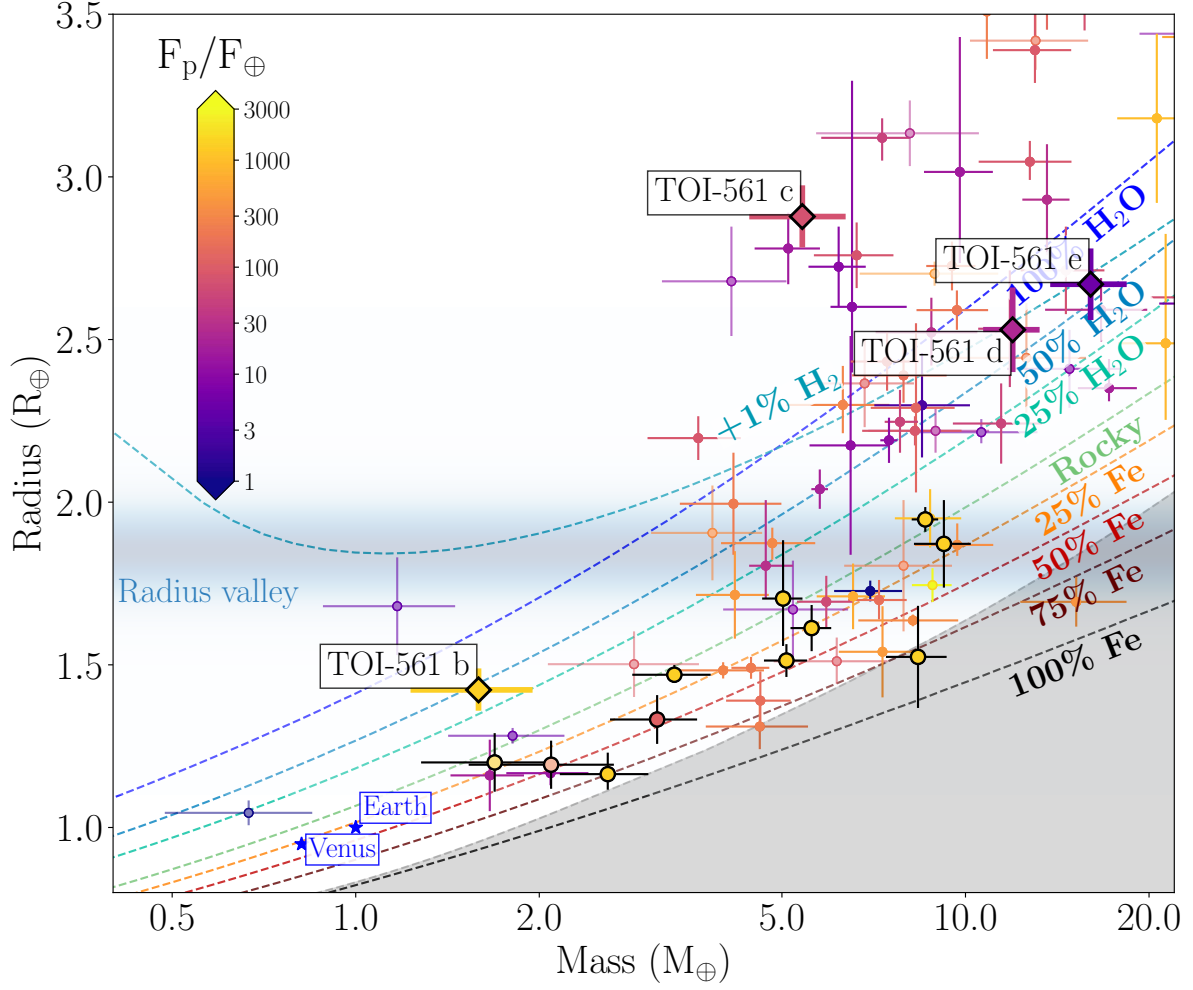
Figure 3.10 Mass-radius diagram for known exoplanets with mass and radius measurements more precise than 30%, colour-coded according to their incidental flux in Earth units. The TOI-561 planets are labelled and represented with coloured diamonds. The USP planets are highlighted with black thick contours. The solid coloured lines represent the theoretical mass-radius curves for various chemical compositions according to Zeng et al. (2019). The shaded grey region marks the maximum value of iron content predicted by collisional stripping (Marcus et al., 2010). The planetary data are taken from the The Extrasolar Planets Encyclopaedia catalogue (http://exoplanet.eu/catalog/) updated to August 17, 2020.

2017). Nevertheless, the possibility of a water-world scenario is an intriguing one. An H_2O-dominated composition would imply that the planet formed beyond the snow line, accreted a considerable amount of condensed water, and finally migrated inwards (Zeng et al., 2019). While the determination of the precise interior composition of TOI-561 b is beyond the scope of this work, if such an interpretation is proven trustworthy by future observational campaigns, TOI-561 b would support the hypothesis that the formation of super-Earths with a significant amount of water is indeed possible. However, an important caveat should be considered while investigating this scenario. If TOI-561 b was a water world, being more irradiated than the runaway greenhouse irradiation limit, the planet would present a massive and very extended steam atmosphere. Such an atmosphere would substantially increase the measured radius compared to a condensed water world (Turbet et al., 2020). Therefore, a comparison with the condensed water-world theoretical curves should be used with caution, since in this case it could lead to an overestimation of the bulk water content (Turbet et al., 2020).

Finally, we note that the USP planet is located on the opposite side of the radius valley, i. e. the gap in the distribution of planetary radii at $\sim$ 1.7-2 $R_\oplus$ (Fulton et al., 2017), with respect to all the other planets in the system. The origin of the so-called radius valley is likely due to a transition between rocky and non-rocky planets with extended H-He envelopes, with several physical mechanisms proposed as explanation, i.e. photoevaporation (Chen & Rogers, 2016; Jin & Mordasini, 2018; Lopez & Rice, 2018; Owen & Wu, 2017), core-powered mass loss (Ginzburg et al., 2018; Gupta & Schlichting, 2019), or superposition of rocky and non-rocky planet populations (Lee & Chiang, 2016; Lopez & Rice, 2018). In the TOI-561 system, planet c is located above the radius valley and it indeed appears to require a thick H-He envelope (see next section). In the same way, the compositions of planet d and e are consistent with the presence of a gaseous envelope. However, the density of TOI-561 b is lower than expected for a planet located below the radius valley, where we mainly expect rocky compositions. Moreover, TOI-561 b is the first USP planet with such a low measured density (see Figure 3.10). We note that also the USP planets WASP-47 e and 55 Cnc e are less dense than an Earth-like rocky planet, even if both of them have higher densities than TOI-561 b, i. e., $\rho_{W47_e} = 6.4 \pm 0.6$ g cm^{-3} (Vanderburg et al., 2017) and $\rho_{55Cnc_e} = 6.3 \pm 0.8$ g cm^{-3} (Demory et al., 2016) respectively. Vanderburg et al. (2017) proposed the presence of water envelopes as a possible explanation for the low densities of these two planets, even though the inferred amount of water was smaller than the one required to explain TOI-561 b location in the mass-radius diagram. It should also be considered that both planets are more massive than TOI-561 b, i. e., $M_{W47_e} = 6.83 \pm 0.66$ $M_\oplus$ (Vanderburg et al., 2017) and $M_{55Cn_e} = 8.08 \pm 0.31$ $M_\oplus$ (Demory et al., 2016), thus increasing their chances of retaining a small envelope of high-metallicity volatile materials (or water steam) that could explain their low densities Vanderburg et al. (2017). Given its smaller mass, this scenario is less probable for TOI-561 than for WASP-47 e and 55 Cnc e, making the object even more peculiar. With its particular properties, this planet could be an intriguing case to test also other extreme planetary composition models. For example, given the metal-poor alpha-enriched host star, the planet is likely to have a lighter core composition.

3.8.2 TOI-561 c, d and e

TOI-561 c, with a density of $\rho_c \sim 1.3$ g cm^{-3}, is located above the threshold of a 100% water composition, and given its position in the mass-radius diagram we suppose the presence of a significant gaseous envelope surrounding an Earth-like iron core and a silicate mantle, and possibly a significant water layer (high-pressure ice). If the inner USP planet is water-rich, there is no simple planet formation scenario in which the outer three planets are water-poor. It is simpler to assume that all four planets were formed with similar volatile abundances, and that the inner USP planet lost all of its H-He layer, plus much of its water content, while the outer planets could keep them. Following Lopez & Fortney (2014), assuming a rocky Earth-like core and a solar composition H-He envelope, we estimate that an H-He envelope comprising $\sim 4.9\%$ of the planet mass could explain the density of TOI-561 c, using our derived stellar and planetary parameters.

Planets TOI-561 d and e are consistent with a > 50% water composition, a feature that may place them among the water worlds. However, such densities are also consistent with the presence of a rocky core plus water mantle surrounded by a gaseous envelope. We estimate that a H-He envelope of $\sim 1.8\%$ and $\sim 2.3\%$ of the planet mass could explain the observed planetary properties.

3.8.3 Dynamical insights

Our analysis shows that the orbital inclinations of planets c, d and e are all consistent within 1σ (see Table 3.5), and that the difference with the inclination of the USP planet is of the order of $\Delta i \sim 2.5°$. According to the analysis of Dai et al. (2018), when the innermost planet has $a/R_\star < 5$, the minimum mutual inclination with other planets in the system often reaches values up to 5°-10°, with larger period ratios ($P_c/P_b > 5$-6) implying an higher mutual inclination. Considering the large period ratio of TOI-561 ($P_c/P_b \sim 24$) and the value of $a_b/R_\star = 2.6$, the measured $\Delta i \sim 2.5°$ in this case is much lower that the expected inclination dispersion of $6.7 \pm 0.7°$ that Dai et al. (2018) inferred for systems with similar orbital configurations, indicating that the TOI-561 system probably evolved through a mechanism that did not excite the inclination of the innermost planet.

We also performed a dynamical N-body simulation to check if significant TTVs are expected in the TOI-561 system with our determined configuration. In fact, the period ratio of TOI-561 d and e indicates that the planets are close to a 3:1 commensurability, hint of a second order mean motion resonance (MMR), that may suggest the presence of a strong dynamical interaction between these planets. Starting from the initial configuration (as reported in Table 3.5), we numerically integrated the orbits using the N-body integrator `ias15` within the `rebound` package (Rein & Liu, 2012). We assumed as reference time the T_0 of the USP planet (see Table 3.5), that roughly corresponds to the beginning of the *TESS* observations of TOI-561. During the integration, we computed the transit times of each planet following the procedure described in Borsato et al. (2019), and we compared the inferred transit times with the linear ephemeris in order to obtain the TTV signal, reported as an observed-calculated diagram ($O-C$, Agol & Fabrycky 2018) in Figure 3.11. According to our simulation, TOI-561 d and e display an anti-correlated TTV signal, with a very long TTV period of ~ 4850 days (~ 13 yr), and TTV amplitudes

of ~ 62 minutes (planet d) and ~ 84 minutes (planet e), calculated computing the GLS periodogram of the simulated TTVs. The anti-correlated signal demonstrates that the two planets are expected to dynamically interact (Agol & Fabrycky, 2018). In contrast, the predicted TTV amplitude of planet c is extremely low (~ 0.9 min), being the planet far from any period commensurability, as well as the USP planet, which has a negligible TTV signal (< 1 sec). With the solution for the planetary system we propose in this work, TOI-561 is a good target for a TTV follow-up, that will however require a very long time baseline in order to tackle the long-period TTV pattern. To better sample such a long-period TTV signal, it could be worth specifically re-observing the target when the deviations from the linear ephemeris are higher, i. e., during the periods corresponding to the $O-C$ peaks (or dips) in Figure 3.11. According to our simulation, the first peak (dip) corresponds to the period between March–December 2020, while the second one will be between January–October 2026, i. e., corresponding to the time-spans between ~ 400–700 and ~ 2500–3000 days of integration in Figure 3.11 respectively. We remark that this calculation is performed assuming the T_0s inferred from single transit observations, thus implying a significant uncertainty in the TTV phase determination. Therefore, additional photometric observations are necessary to refine the linear ephemeris of the planets, and consequently also the prediction of the TTV phase.

3.8.4 Prospects for atmospheric characterization

Given the interesting composition of the planets in the system, we checked if the TOI-561 planets would be accessible targets for atmospheric characterisation through transmission spectroscopy, e.g. with the *James Webb Space Telescope* (*JWST*). For all the planets in the system, we calculated the Transmission Spectroscopy Metric (TSM, Kempton et al. 2018), which predicts the expected transmission spectroscopy SNR of a 10-hour observing campaign with *JWST*/Near Infrared Imager and Slitless Spectrograph (NIRISS) under the assumptions of cloud-free atmospheres, the same atmospheric composition for all planets of a given type, and a fixed mass–radius relation. We obtained TSM values of 19, 107, 24, and 14 for planets b, c, d, and e, respectively. According to Kempton et al. (2018)[19], this classifies TOI-561 b and c as high-quality atmospheric characterisation targets among the *TESS* planetary candidates. However, it should be noted that the TSM metric assumes rocky composition for planets with radius $< 1.5\ R_\oplus$ and according to our analysis TOI-561 b is not compatible with such a composition. The same caveat holds for planet c, for which the assumptions under which the TSM is calculated may not be totally valid (e.g. the mass obtained from our analysis is not the same as if calculated with the Chen & Kipping (2017) mass-radius relation, that is the relation assumed in Kempton et al. (2018), and that would imply a mass of $M_c \simeq 8.7\ M_\oplus$). Therefore, this estimate of the atmospheric characterisation feasibility should be used with caution, especially as the TSM metric has been conceived to prioritise targets for follow-up, and not to precisely determine the atmospheric transmission properties.

---

[19]The authors suggest to select planets with TSM > 12 for $R_p < 1.5\ M_\oplus$, TSM > 92 for $1.5\ R_\oplus < R_p < 2.75\ R_\oplus$, and TSM > 84 for $2.75\ R_\oplus < R_p < 4\ R_\oplus$.
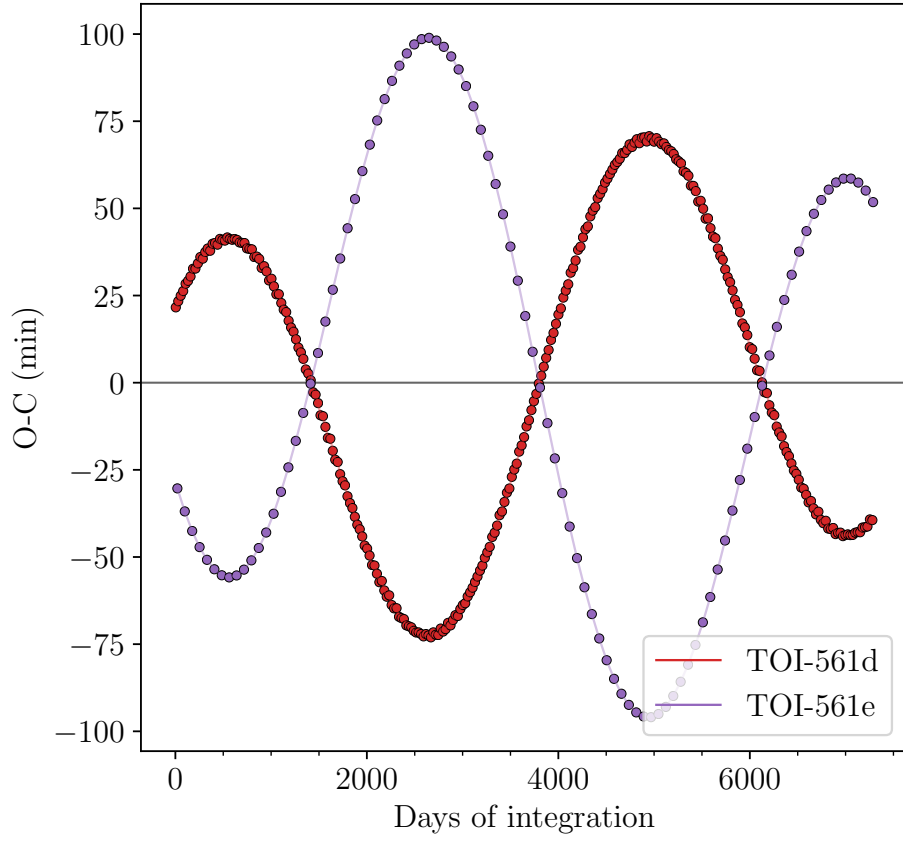
Figure 3.11 Predicted TTV signal of TOI-561 d and e assuming our best-fitting model (see Table 3.5). The planets show a strong, anti-correlated signal. The signals of the USP planet (< 1 sec) and of planet c (< 1 min) are not reported.

3.8.5 Summary and conclusions

According to our analysis, TOI-561 hosts a nearly co-planar four-planet system, with an unusually low density USP super-Earth (planet b), a mini-Neptune (planet c) with a significant amount of volatiles surrounding a rocky core, and two mini-Neptunes, which are both consistent with a water-world scenario or with a rocky core surrounded by a gaseous envelope, and that are expected to show a strong, long-term TTV signal. The multi-planetary nature of TOI-561 offers a unique opportunity for comparative exoplanetology. TOI-561 planets may be compared with the known population of multi-planet systems to understand their underlying distribution and occurrences, and to give insights on the formation and evolution processes of close-in planets, especially considering the intriguing architecture of the system, with the presence of a uncommonly low-density USP super-Earth and three mini-Neptunes on the opposite side of the radius valley.

Considering the few available data (i. e., 2 transits for planet c, 1 transit for planets d, e), additional observations are needed to unequivocally confirm our solution. Further high-precision photometric (i.e. with *TESS*, that will re-observe TOI-561 in sector 35 – February/March 2021, or with the *CHEOPS* satellite) and RVs observations will help improving the precision on the planets parameters, both allowing for the detection of eventual TTVs and increasing the time-span of the RV dataset, that could also unveil possible additional long-period companions.

Note

Chapter 4

Investigating the architecture and internal structure of the TOI-561 system planets with CHEOPS, HARPS-N and TESS

We present a precise characterization of the TOI-561 planetary system obtained by combining previously published data with new TESS and CHEOPS photometry, and a new set of 62 HARPS-N radial velocities (RVs). Our joint analysis confirms the presence of four transiting planets, namely TOI-561 b (P = 0.45 d, R = 1.42 $R_\oplus$, M = 2.0 $M_\oplus$), c (P = 10.78 d, R = 2.91 $R_\oplus$, M = 5.4 $M_\oplus$), d (P = 25.7 d, R = 2.82 $R_\oplus$, M = 13.2 $M_\oplus$) and e (P = 77 d, R = 2.55 $R_\oplus$, M = 12.6 $R_\oplus$). Moreover, we identify an additional, long-period signal (> 450 d) in the RVs, which could be due to either an external planetary companion or to stellar magnetic activity. The precise masses and radii obtained for the four planets allowed us to conduct interior structure and atmospheric escape modelling. TOI-561 b is confirmed to be the lowest density (ρ_b = 3.8 ± 0.5 g cm^{-3}) ultra-short period (USP) planet known to date, and the low metallicity of the host star makes it consistent with the general bulk density-stellar metallicity trend. According to our interior structure modelling, planet b has basically no gas envelope, and it could host a certain amount of water. In contrast, TOI-561 c, d, and e likely retained an H/He envelope, in addition to a possibly large water layer. The inferred planetary compositions suggest different atmospheric evolutionary paths, with planets b and c having experienced significant gas loss, and planets d and e showing an atmospheric content consistent with the original one. The uniqueness of the USP planet, the presence of the long-period planet TOI-561 e, and the complex architecture make this system an appealing target for follow-up studies.

4.1 Introduction

Since the announcement of the first exoplanet orbiting a Sun-like star (Mayor & Queloz, 1995), the growing number of discoveries in exoplanetary science have yielded a surprising variety of exoplanets and exoplanetary systems. The field has benefited hugely from dedicated space-based missions, such as *CoRoT, Kepler, K2* (Baglin et al., 2006; Borucki et al., 2010; Howell et al., 2014), and recently *TESS* (Ricker et al., 2014). With more than 170 confirmed planets, and $\sim$ 4000 planet candidates, the majority of which will likely turn out to be planets, *TESS* has increased the census of confirmed exoplanets to more than 4500[1]. Alongside the aforementioned missions, which are designed to discover a large number of exoplanets by searching for transit-like signatures around hundreds of thousands of stars, new characterization missions, with a specific focus on the detailed study of known exoplanets, are now starting to operate. Among them, the *CHaracterising ExOPlanet Satellite* (*CHEOPS*, Benz et al. 2021), launched on 18 December 2019, is a 30-cm telescope which is collecting ultra-high precision photometry of known exoplanets, aiming at their precise characterization (see Section 1.3.2). The importance of *CHEOPS*'s high photometric precision is reflected in its first scientific results, which span a variety of different fields (Lendl et al. 2020, Bonfanti et al. 2021b, Leleu et al. 2021a, Delrez et al. 2021, Morris et al. 2021a, Borsato et al. 2021, Van Grootel et al. 2021, Szabó et al. 2021, Hooton et al. 2021, Swayne et al. 2021, Maxted et al. 2021, Barros et al. 2022, Deline et al. 2022 *accepted*, Wilson et al. *submitted*). As part of its main scientific goals, *CHEOPS* is refining the radii of known exoplanets to achieve the precision on the bulk density needed for internal structure and atmospheric evolution modelling. To fulfil this aim, radial velocity (RV) follow-ups using high-precision spectrographs are essential to provide the precise planetary masses that can be combined with radii measurements to determine accurate densities. Among the exoplanets having both radius and mass measurements, the ones in well-characterised multiplanetary systems are of particular interest, since they allow for investigation of their formation and evolution processes through comparative planetology (see Section 1.6).

Within this context, TOI-561, announced simultaneously by Lacedelli et al. (2021) (reported in Chapter 3) and Weiss et al. (2021) (L21 and W21 hereafter, respectively), is a particularly interesting system, both from the stellar (Section 4.2.1) and planetary (Section 4.2.2) perspective. The low stellar metallicity, the presence of an ultra-short period (USP) planet, where USP planets are meant here as planets with periods shorter than one day and radii smaller than $2\,R_{\oplus}$, and the complexity of its planetary configuration make TOI-561 an appealing target for in-depth investigations. In this study, we combine literature data with new *TESS* observations (Section 4.3.1), *CHEOPS* photometry (Section 4.3.2), and HARPS-N RVs (Section 4.3.3) to shed light on the planetary architecture and infer the internal structure of the transiting planets. After assessing the planetary configuration using *CHEOPS* observations (Section 4.4.1) and performing a thorough analysis of the global RV data set (Section 4.4.2), we jointly modelled the photometric and spectroscopic data to obtain the planetary parameters (Section 4.5). We used our derived stellar and planetary properties to model the internal structures of the transiting planets

---

[1]From NASA Exoplanet Archive, https://exoplanetarchive.ipac.caltech.edu/.

(Section 4.6) and their atmospheric evolution (Section 4.7), before discussing our results and presenting our conclusions (Section 4.8).

4.2 The TOI-561 system

4.2.1 The host star

TOI-561 is an old, metal-poor, thick disk star (L21, W21), slightly smaller and cooler than the Sun, located ~ 84 pc away from the Solar System. We report the main astrophysical properties of the star in Table 4.1.

We adopted the spectroscopic parameters and stellar abundances from L21 (Table 3.3), which were derived exploiting the high SNR, high-resolution HARPS-N co-added spectrum through an accurate analysis using three independent methods (Section 3.3.1), namely the ARES+MOOG equivalent width method (Mortier et al., 2014; Sousa, 2014a), the Stellar Parameter Classification (Buchhave et al., 2012, 2014) and the CCFpams method (Malavolta et al., 2017b).

Taking advantage of the updated parameters coming from the *Gaia* EDR3 release (Gaia Collaboration et al., 2021), we then used the L21 spectral parameters as priors on spectral energy distribution selection to infer the stellar radius ($R_\star$) of TOI-561 using the infrared flux method (IRFM, Blackwell & Shallis 1977). The IRFM compares optical and infrared broadband fluxes and synthetic photometry of stellar atmospheric models, and uses known relationships between stellar angular diameter, $T_{\rm eff}$ and parallax to derive $R_\star$, in a MCMC fashion as detailed in Schanche et al. (2020). For this study, we retrieved from the most recent data releases the *Gaia G*, $G_{\rm BP}$, $G_{\rm RP}$ (Gaia Collaboration et al., 2021), 2MASS *J*, *H*, *K* (Skrutskie et al., 2006), and *WISE W*1, *W*2 (Wright et al., 2010) broadband photometric magnitudes, and we used the stellar atmospheric models from the ATLAS Catalogues (Castelli & Kurucz, 2003) and the *Gaia* EDR3 parallax with the offset of Lindegren et al. (2021) applied, to obtain $R_\star = 0.843 \pm 0.005\ R_\odot$.

We combined two different sets of stellar evolutionary tracks and isochrones, PARSEC[2] (*PA*dova & T*R*ieste *S*tellar *E*volutionary *C*ode, v1.2S; Marigo et al., 2017) and CLES (Code Liègeois d'Évolution Stellaire, Scuflaire et al., 2008), to derive the stellar mass ($M_\star$) and age ($t_\star$) of TOI-561. As the star is significantly alpha-enhanced, we avoided using [Fe/H] as a proxy for the stellar metallicity; instead, we inserted both [Fe/H] and [α/Fe] in relation (3) provided by Yi et al. (2001), obtaining an overall scaling of metal abundances [M/H] $= -0.23 \pm 0.06$. Besides [M/H], the main input parameters for computing $M_\star$ and $t_\star$ were $T_{\rm eff}$ and $R_\star$. In addition, we used as inputs $\log{\rm R}'_{\rm HK}$ and the upper limit on $v \sin i$ from L21, and the yttrium over magnesium abundance [Y/Mg] $= -0.22 \pm 0.07$, as computed from [Mg/H] and [Y/H] reported by W21. These indices improve the model convergence by discarding unlikely young isochrones, as broadly discussed in Section 2.2.3 of Bonfanti & Gillon (2020), and references therein. The PARSEC results were obtained using the isochrone placement algorithm of Bonfanti et al. (2015, 2016), which retrieves the best-fit parameters by interpolating within a pre-computed grid

---

[2]http://stev.oapd.inaf.it/cgi-bin/cmd

of models, while the CLES algorithm models directly the star through a Levenberg-Marquardt minimisation (Salmon et al., 2021). The final adopted values ($M_\star = 0.806 \pm 0.036\ M_\odot$, $t_\star = 11.0^{+2.8}_{-3.5}$ Gyr) are a combination of the outputs from both sets of models, as described in detail in Bonfanti et al. (2021b). The derived mass and radius, listed in Table 4.1, are consistent within 1σ with the values reported in L21 ($R_\star = 0.849 \pm 0.007\ R_\odot$, $M_\star = 0.785 \pm 0.018\ M_\odot$).

4.2.2 The planetary system

The discovery of a multiplanetary system orbiting TOI-561 was announced simultaneously by L21 and W21 in two independent papers. The main planetary parameters from both studies are reported in Table 4.2.

The two papers presented different RV data sets, collected with HARPS-N and HIRES respectively, to confirm the planetary nature of three candidates identified by *TESS* in sector 8, the only available sector at the time of the publications. The *TESS*-identified signals had periods of ~ 0.45, ~ 10.8, and ~ 16 days. The two inner candidates were confirmed by both L21 and W21, with the names of TOI-561 b (an USP super-Earth, with period $P_b \sim 0.4465$ d, and radius $R_b \sim 1.4\ R_\oplus$), and TOI-561 c (a warm mini-Neptune, with $P_c \sim 10.779$ d, and $R_c \sim 2.9\ R_\oplus$). However, two different interpretations for the third *TESS* signal were proposed by the authors. In the scenario presented in L21, the two transits related to the third *TESS* signal were interpreted as single transits of two distinct planets, TOI-561 d ($P_d \sim 25.6$ d, $R_d \sim 2.5\ R_\oplus$), and TOI-561 e ($P_e \sim 77$ d, $R_e \sim 2.7\ R_\oplus$). The periods of these two planets were inferred from the RV analysis, which played an essential role in determining the final planetary architecture. In fact, the ephemeris match between the RV and photometric fits (See Fig. 5 of L21) and the non-detection of the 16 d signal in the HARPS-N data set, combined with the different durations of the two *TESS* transits and results from the long-term stability analysis led the authors to converge on a 4-planet configuration, presenting robust mass and radius detection for all the four planets in the system (L21, Table 5). In contrast, W21 proposed the presence of a single planet at the period suggested by *TESS* (TOI-561 f, $P_f \sim 16.29$ d, $R_f \sim 2.3\ R_\oplus$), based on the analysis of the two available transits. W21 pointed out that the 8.1 d alias of planet f's orbital period is also consistent with the *TESS* data, with the even transit falling into the *TESS* download gap, even though in this case the transit duration would be too long compared to what is expected for a 8 d period planet (§4.9, W21). However, the authors could not obtain an accurate mass determination for this planet, with the 60 HIRES RVs being consistent with a non-detection (§ 7.2, W21). An additional discrepancy between the two studies is the mass of the USP planet, differing by almost a factor two. According to the W21 analysis, TOI-561 b has a mass of $3.2 \pm 0.8\ M_\oplus$, making it consistent with a rocky composition and placing it among the population of typical small ($< 2\ R_\oplus$), extremely irradiated USP planets (Sanchis-Ojeda et al. 2015, Dai et al. 2021). Instead, assuming the low mass ($M_b = 1.59 \pm 0.36\ M_\oplus$) inferred from L21 analysis, TOI-561 b is not consistent with a pure rocky composition, and it is the lowest density USP super-Earth known to date, calling for a more complex interpretation (e.g. lighter core composition, deep water reservoirs, presence of a high-metallicity, volatile materials or water steam envelope, etc.).

Table 4.1 Stellar properties of TOI-561.

| TIC | 377064495 | |
| *Gaia* EDR3 | 3850421005290172416 | |

Parameter	Value	Source
RA (J2016; hh:mm:ss.ss)	09:52:44.43	A
Dec (J2016; dd:mm:ss.ss)	+06:12:57.94	A
μ_α (mas yr^{-1})	-108.504 ± 0.022	A
μ_δ (mas yr^{-1})	-61.279 ± 0.019	A
γ (km s^{-1})	79.54 ± 0.56	A
Parallax (mas)	11.8342 ± 0.0208	A
Distance (pc)	84.25 ± 0.12	B
TESS (mag)	9.527 ± 0.006	C
G (mag)	10.0181 ± 0.0028	A
G_{BP} (mag)	10.3945 ± 0.0028	A
G_{RP} (mag)	9.4692 ± 0.0038	A
V (mag)	10.252 ± 0.006	C
B (mag)	10.965 ± 0.082	C
J (mag)	8.879 ± 0.020	D
H (mag)	8.504 ± 0.055	D
K (mag)	8.394 ± 0.019	D
W1 (mag)	8.337 ± 0.023	E
W2 (mag)	8.396 ± 0.020	E
T_{eff} (K)	5372 ± 70	F
$\log g$ (cgs)	4.50 ± 0.12	F
[Fe/H] (dex)	-0.40 ± 0.05	F
[Mg/H] (dex)	-0.17 ± 0.05	F
[Si/H] (dex)	-0.22 ± 0.05	F
[Ti/H] (dex)	-0.12 ± 0.03	F
[α/Fe] (dex)	0.23 ± 0.04	F
[M/H] (dex)	-0.23 ± 0.06	G
[Y/Mg] (dex)	-0.22 ± 0.07	G[a]
$\log R'_{HK}$	-5.003 ± 0.012	F
$v \sin i$ (km s^{-1})	< 2	F
$R_\star$ ($R_\odot$)	0.843 ± 0.005	G, IRFM
$M_\star$ ($M_\odot$)	0.806 ± 0.036	G, isochrones
$t_\star$ (Gyr)	$11.0^{+2.8}_{-3.5}$	G, isochrones
$\rho_\star$ ($\rho_\odot$)	1.34 ± 0.06	G, from $R_\star$ and $M_\star$
$\rho_\star$ (g cm^{-3})	1.89 ± 0.09	G, from $R_\star$ and $M_\star$
$L_\star$ ($L_\odot$)	0.533 ± 0.029	G, from $R_\star$ and T_{eff}
Spectral type	G9V	F

A) *Gaia* EDR3 (Gaia Collaboration et al., 2021). B) Bailer-Jones et al. (2021). C) *TESS* Input Catalogue Version 8 (TICv8, Stassun et al. 2018). D) Two Micron All Sky Survey (2MASS, Cutri et al. 2003). E) *Wide-field Infrared Survey Explorer* (*WISE*; Wright et al., 2010). F) L21. G) This work. [a] Based on W21 abundances.

The complexity of this system and the differences between the two studies demanded further investigations. We therefore decided to collect additional, precise photometric and RV data (Section 4.3) to shed light on the planetary configuration and on the internal composition of the TOI-561 planets.

4.3 Observations

4.3.1 *TESS* photometry

During its two-year primary mission (Ricker et al., 2014), *TESS* observed TOI-561 in two-minute cadence mode between 2 February and 27 February 2019 (sector 8). After entering its extended mission, *TESS* re-observed the star in two-minute cadence mode during sector 35, between 9 February and 6 March 2021. At the beginning of the second orbit, the spacecraft dropped out of Fine Pointing mode for 3.44 days, entering Coarse Pointing mode[3]. Data collected during Coarse Pointing mode were flagged and removed from the Pre-search Data Conditioning Simple Aperture Photometry (PDCSAP, Smith et al., 2012; Stumpe et al., 2012, 2014) light curves, leading to a total of 19.86 days of science data. The photometric observations of TOI-561 were reduced by the Science Processing Operations Center (SPOC) pipeline and searched for evidence of transiting planets (Jenkins et al. 2016, Jenkins 2020). For our photometric analysis, we used the light curves based on the PDCSAP, downloading the two-minute cadence data from the Mikulski Archive for Space Telescopes (MAST)[4], and removing all the observations encoded as *NaN* or flagged as bad-quality (DQUALITY>0) points by the SPOC pipeline[5]. We performed outlier rejection by doing a cut at 3σ for positive outliers and 5σ (i. e. larger than the deepest transit) for negative outliers. The resulting *TESS* light curves of sectors 8 and 35 are shown in Figure 4.1, and Table 4.3 summarizes the total number of transits observed by *TESS* for each planet.

To refine the ephemeris of planet d in time for the scheduling of the *CHEOPS* observations (Section 4.4.1), we also extracted the 10-minute cadence light curve of sector 35 using the quick-look *TESS* Full Frame Images (FFIs) calibrated using the *TESS* Image CAlibrator[6] package (tica, Fausnaugh et al. 2020).

4.3.2 CHEOPS photometry

To confirm the planetary architecture and improve the planetary parameters, we obtained three visits of TOI-561 with *CHEOPS*, the ESA small class mission dedicated to the characterization of known exoplanets (Benz et al., 2021). The observations, collected within the Guaranteed Time Observing (GTO) programme, were carried out between 23 January and 15 April 2021, for a total of 73.85 hours on target. During the three visits, we observed a total of eight transits of TOI-561 b, two transits of TOI-561 c, and one transit of TOI-561 d. The three *CHEOPS* light curves have an observing efficiency,

---

[3]See *TESS* Data Release Notes: Sector 35, DR51 (https://archive.stsci.edu/tess/tess_drn.html).
[4]https://mast.stsci.edu/portal/Mashup/Clients/Mast/Portal.html
[5]https://archive.stsci.edu/missions/tess/doc/EXP-TESS-ARC-ICD-TM-0014-Rev-F.pdf
[6]https://archive.stsci.edu/hlsp/tica

Table 4.2 Literature parameters of the proposed planets orbiting TOI-561.

TOI-561 b	Lacedelli et al. (2021)	Weiss et al. (2021)
P (d)	0.446578 ± 0.000017	$0.446573^{+0.000032}_{-0.000021}$
T_0 (TBJD)	1517.498 ± 0.001	1517.4973 ± 0.0018
R_p ($R_\oplus$)	1.423 ± 0.066	1.45 ± 0.11
K (m s^{-1})	1.56 ± 0.35	3.1 ± 0.8
M_p ($M_\oplus$)	1.59 ± 0.36	3.2 ± 0.8
TOI-561 c		
P (d)	10.779 ± 0.004	10.77892 ± 0.00015
T_0 (TBJD)	1527.060 ± 0.004	1527.05825 ± 0.00053
R_p ($R_\oplus$)	2.878 ± 0.096	2.90 ± 0.13
K (m s^{-1})	1.84 ± 0.33	2.4 ± 0.8
M_p ($M_\oplus$)	5.40 ± 0.98	7.0 ± 2.3
TOI-561 d		
P (d)	25.62 ± 0.04	-
T_0 (TBJD)	1521.882 ± 0.004	-
R_p ($R_\oplus$)	2.53 ± 0.13	-
K (m s^{-1})	3.06 ± 0.33	-
M_p ($M_\oplus$)	11.95 ± 1.28	-
TOI-561 e		
P (d)	77.23 ± 0.39	-
T_0 (TBJD)	8538.181 ± 0.004	-
R_p ($R_\oplus$)	2.67 ± 0.11	-
K (m s^{-1})	2.84 ± 0.41	-
M_p ($M_\oplus$)	16.0 ± 2.3	-
TOI-561 f [a]		
P (d)	-	16.287 ± 0.005
T_0 (TBJD)	-	1521.8828 ± 0.0035
R_p ($R_\oplus$)	-	2.32 ± 0.16
K (m s^{-1})	-	0.9 ± 0.6
M_p ($M_\oplus$)	-	$3.0^{+2.4}_{-1.9}$
$M_\star$ ($M_\odot$)	0.785 ± 0.018	0.805 ± 0.030

[a] Referred as TOI-561 d in W21.

Table 4.3 Number of TOI-561 transits observed by *TESS*.

|	TOI-561 b	TOI-561 c	TOI-561 d	TOI-561 e
Sector 8	41	2	1	1
Sector 35	43	1	-	-

i.e. the actual time spent observing the target with respect to the total visit duration, of 64%, 75%, and 61%, respectively. The observing efficiency is linked to data gaps, which are intrinsically present in all *CHEOPS* light curves (see e.g. Delrez et al. 2021, Bonfanti et al. 2021b, Leleu et al. 2021a), and are related to *CHEOPS*'s low-Earth orbit. In fact, during (1) South Atlantic Anomaly (SAA) crossing, (2) target occultation by the Earth, and (3) too high stray light contamination, no data are downlinked. This results in data gaps, whose number and extension depend on the target sky position (Benz et al., 2021). For all the visits, we adopted an exposure time of 60 s. The summary log of the *CHEOPS* observations is reported in Table 4.4.

Data were reduced using the latest version of the *CHEOPS* automatic Data Reduction Pipeline (DRP v13; Hoyer et al. 2020), which performs aperture photometry of the target after calibrating the raw images (event flagging, bias, gain, non-linearity, dark current, and flat field) and correcting them for instrumental and environmental effects (smearing trails, cosmic rays, de-pointing, stray light, and background). The target flux is obtained for a set of three fixed-radius apertures, namely $R = 22.5$ arcsec (RINF), 25.0 arcsec (DEFAULT), 30.0 arcsec (RSUP), plus an additional one specifically computed to optimize the radius based on the instrumental noise and contamination level of each target (OPTIMAL). Moreover, the DRP estimates the contamination in the photometric aperture due to nearby targets using the sources listed in the *Gaia* DR2 catalog (Gaia Collaboration et al., 2018) to simulate the *CHEOPS* Field-of-View (FoV) of the target, as described in detail in Hoyer et al. (2020). No strong contaminants are present in the TOI-561 FoV, and the main contribution to the contamination is due to the smearing trails of a $G = 10.20$ mag star at a projected sky distance of ~ 117.9 arcsec, which rotates around the target inside the CCD window because of the *CHEOPS* field rotation (Benz et al., 2021). During the third visit three telegraphic pixels (pixels with a non-stable and abnormal behaviour during the visit) appeared within the *CHEOPS* aperture, one of them inside the *CHEOPS* PSF (Figure 4.2). A careful treatment, described in detail in Appendix C, was applied to correct for their effect. In the subsequent analysis we adopted for all the visits the RINF photometry (see Figure C.1 in Appendix C), which minimized the light curve root mean square (RMS) dispersion, and we removed the outliers by applying a 4σ clipping.

Finally, a variety of non-astrophysical sources, such as varying background, nearby contaminants or others, can produce short-term photometric trends in the *CHEOPS* light curves on the timescale of one orbit, due to the rotation of the *CHEOPS* FoV around the target and due to the nature of the spacecraft orbit. To correct for these effects, we detrended the light curves using the basis vectors provided by the DRP, as detailed in Section 4.5. The resulting detrended light curves are shown in Figure 4.3.

Table 4.4 Log of TOI-561 *CHEOPS* observations.

Visit	File key	Starting date	Duration	Data points	Efficiency	Exposure time	Planets
(#)		(UTC)	(h)	(#)	(%)	(s)	
1	CH_PR100031_TG037001_V0200	2021-01-23T15:29:07	15.67	604	64	60	b,c
2	CH_PR100008_TG000811_V0200	2021-03-29T10:19:08	4.42	207	75	60	b,c
3	CH_PR100031_TG039301_V0200	2021-04-12T23:52:28	53.76	1978	61	60	b,d
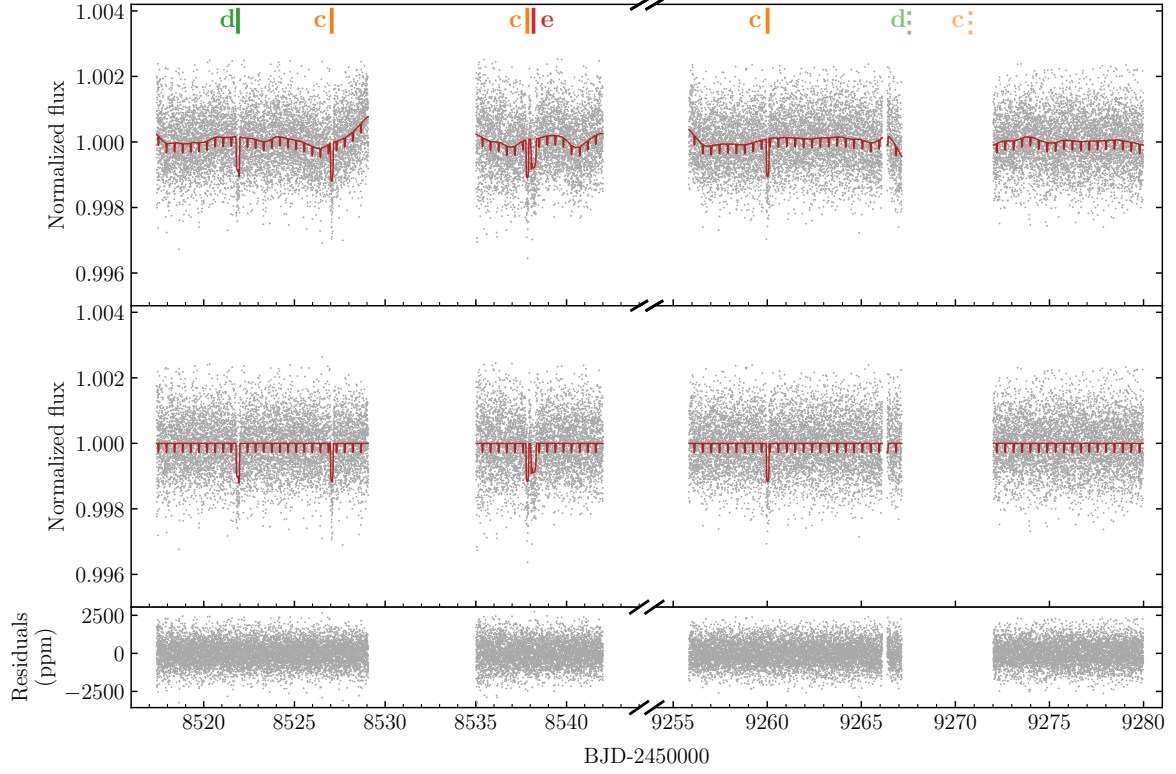
Figure 4.1 *TESS* sector 8 (*left*) and 35 (*right*) PDCSAP light curves of TOI-561. In the top panel, the dark red solid line shows the best-fitting transit and Matérn-3/2 kernel Gaussian Process (GP) model, as detailed in Section 4.5. The central panel shows the flattened light curve after the removal of the GP component, with the best-fitting transit model superimposed (dark red solid line). The transits of planets c, d and e are labelled and highlighted with orange, green and red vertical lines, respectively. The expected locations of the transits of planets c and d occurring during the data gaps of sector 35 are marked with pale, dashed orange and green lines, respectively. Planet e is not expected to transit in sector 35. The transits of the USP planet are too shallow to be individually visible, and are not indicated. Light curve residuals are shown in the bottom panel.

4.3.3 HARPS-N spectroscopy

In addition to the 82 RVs published in L21, we collected 62 high-resolution spectra using HARPS-N at the Telescopio Nazionale Galileo (TNG), in La Palma (Cosentino et al., 2012, 2014). These were used to refine the planetary masses and confirm the system configuration. The new observations were collected between 15 November 2020 and 1 June 2021. Following the same strategy of the previous season (L21), in addition to 30 single observations, we collected six points per night on 8 and 10 February 2021, and two points per night on ten additional nights, specifically targeting the USP planet. The exposure time for all the observations was set to 1800 s, resulting in a signal-to-noise ratio (SNR) at 550 nm of 83 ± 20 (median $\pm$ standard deviation) and a radial velocity measurement uncertainty of $1.0 \pm 0.4 \, \mathrm{m \, s^{-1}}$. All the observations were gathered with the second HARPS-N fibre illuminated by the Fabry–Perot calibration lamp to correct for the instrumental RV drift.
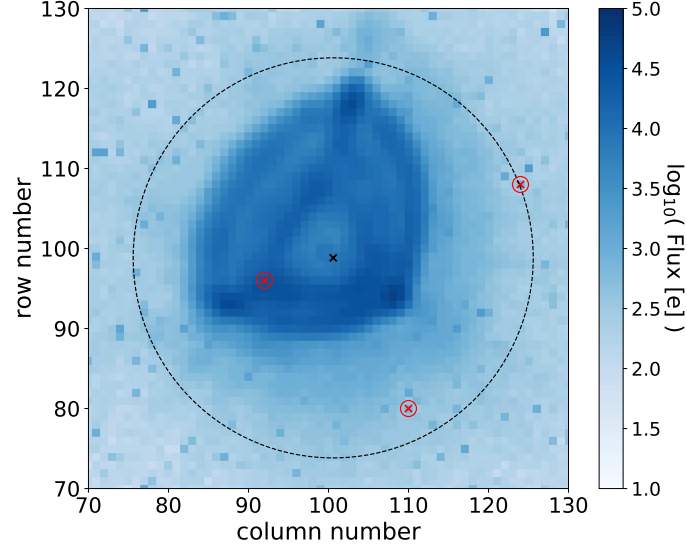
Figure 4.2 Extraction of 60×60 arcsec of the *CHEOPS* FoV during the third visit centered on TOI-561. The dashed black circle represents the RINF photometric aperture surrounding the *CHEOPS* PSF, whose centroid is marked by the black cross. The positions of the three identified telegraphic pixels, including the one located within the *CHEOPS* PSF (see Appendix C), are highlighted by the red, circled crosses.
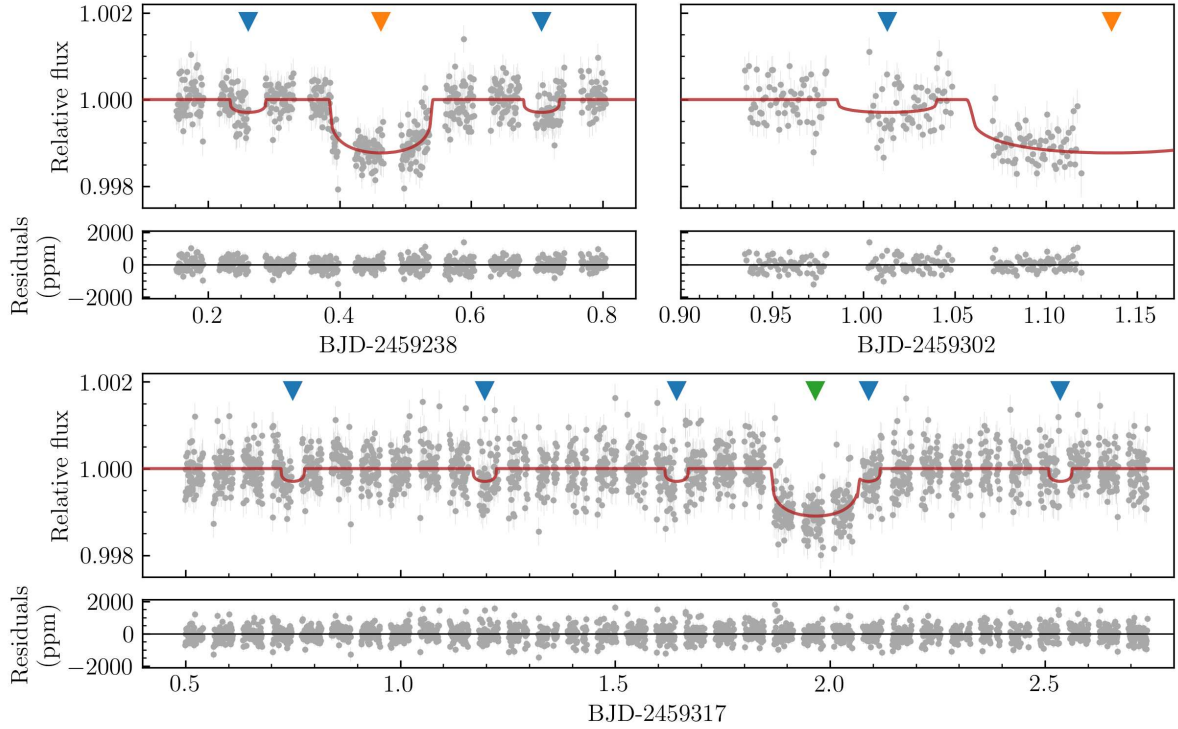
Figure 4.3 *CHEOPS* detrended light curves of TOI-561. Visits 1, 2 and 3 are shown in the top left, top right, and bottom panel, respectively. The best-fitting model is over-plotted as a red solid line, and residuals are shown for each visit. The transits of planets b, c, and d are highlighted with blue, orange, and green triangles, respectively.

We reduced the global HARPS-N data set (144 RVs in total) using the new version of the HARPS-N Data Reduction Software based on the ESPRESSO pipeline (DRS, version 2.3.1; see Dumusque et al. 2021 for more details). We used a G2 flux template to correct for variations in the flux distribution as a function of wavelength, and a G2 binary mask to compute the cross-correlation function (CCF, Baranne et al. 1996; Pepe et al. 2002). We report the RVs and the associated activity indices (see Section 4.4.2) with their 1σ uncertainties in Table 4.5. As in L21, we removed from the first season data set five RVs with associated errors > 2.5 m s^{-1} from spectra with SNR < 35 (see Appendix B.1). All the RV uncertainties of the second season data set were below 2.5 m s^{-1}, so no points were removed.

4.3.4 HIRES spectroscopy

We included in our analysis 60 high-resolution spectra collected with the W.M. Keck Observatory HIRES instrument on Mauna Kea, Hawaii between May 2019 and October 2020. The data set was published in W21, and we refer to that paper for details regarding the observing and data reduction procedures. The HIRES data set has an RMS of 5 m s^{-1}, and a median individual RV uncertainty of 1.4 m s^{-1} (W21).

4.4 Probing the system architecture

4.4.1 CHEOPS confirmation of TOI-561 d

To solve the discrepancy among the planetary architectures proposed by L21 and W21 (Section 4.2.2), we initially looked for the transits of TOI-561 d (~ 25 d) and TOI-561 f (~ 16 d) in the *TESS* sector 35 light curve, whereas TOI-561 e (~ 77 d) was not expected to transit during those *TESS* observations. However, as shown in the top panel of Figure 4.4, the transits of planet d and f occurred during the light curve gap (Section 4.3.1), and so we could not use the new *TESS* data to conclusively discriminate between the two planetary configurations. Nonetheless, these observations ruled out the planet f alias at ~ 8.1 d mentioned in W21, since no transit events were detected at its predicted transit times.

We therefore decided to probe the L21 scenario collecting a transit of TOI-561 d using *CHEOPS*. We opted for the scheduling of the last seasonal observing window, in April, in order to take advantage of the most updated ephemeris to optimize the scheduling. For this reason, we performed a global fit adding to the literature data a partial set of the new HARPS-N RVs, as of 16 March 2021, and including the *TESS* sector 35 light curve extracted from the second data release of the `tica` FFIs in March 2021. Even if no transit was detected, the new *TESS* sector helped to reduce the time window in which to search. In fact, the *TESS* data partially covered the 3σ-uncertainty transit window, enabling us to exclude some time-spans in the computation of the *CHEOPS* visit. Thanks to the ephemeris update, the *CHEOPS* 3σ observing window shrank from ~ 7.4 d to ~ 2.2 d, demonstrating the importance of the early *TESS* data releases in the scheduling of follow-up observations. The bottom panel of Figure 4.4 shows the *CHEOPS* visit scheduled to observe TOI-561 d, whose transit occurred almost exactly at the

Table 4.5 HARPS-N radial velocity and activity indices measurements.

$\mathrm{MJD_{TDB}}$ (d)	RV (m s^{-1})	σ_RV (m s^{-1})	FWHM (km s^{-1})	σ_FWHM (km s^{-1})	BIS (m s^{-1})	σ_BIS (m s^{-1})	Contrast	σ_contr	S-index	σ_S	Hα (dex)	$\sigma_\mathrm{H\alpha}$ (dex)
58804.70780	79695.97	1.13	6.415	0.002	-86.82	2.26	59.879	0.021	0.1643	0.0005	0.2101	0.0002
58805.77552	79699.66	0.85	6.419	0.002	-85.13	1.71	59.810	0.016	0.1702	0.0003	0.2124	0.0001
58806.76769	79697.50	0.91	6.415	0.002	-83.66	1.82	59.861	0.017	0.1689	0.0003	0.2082	0.0001
...	...	...	...	...	...	...	...	...	...	...	...	...

This table is available in its entirety in machine-readable form.
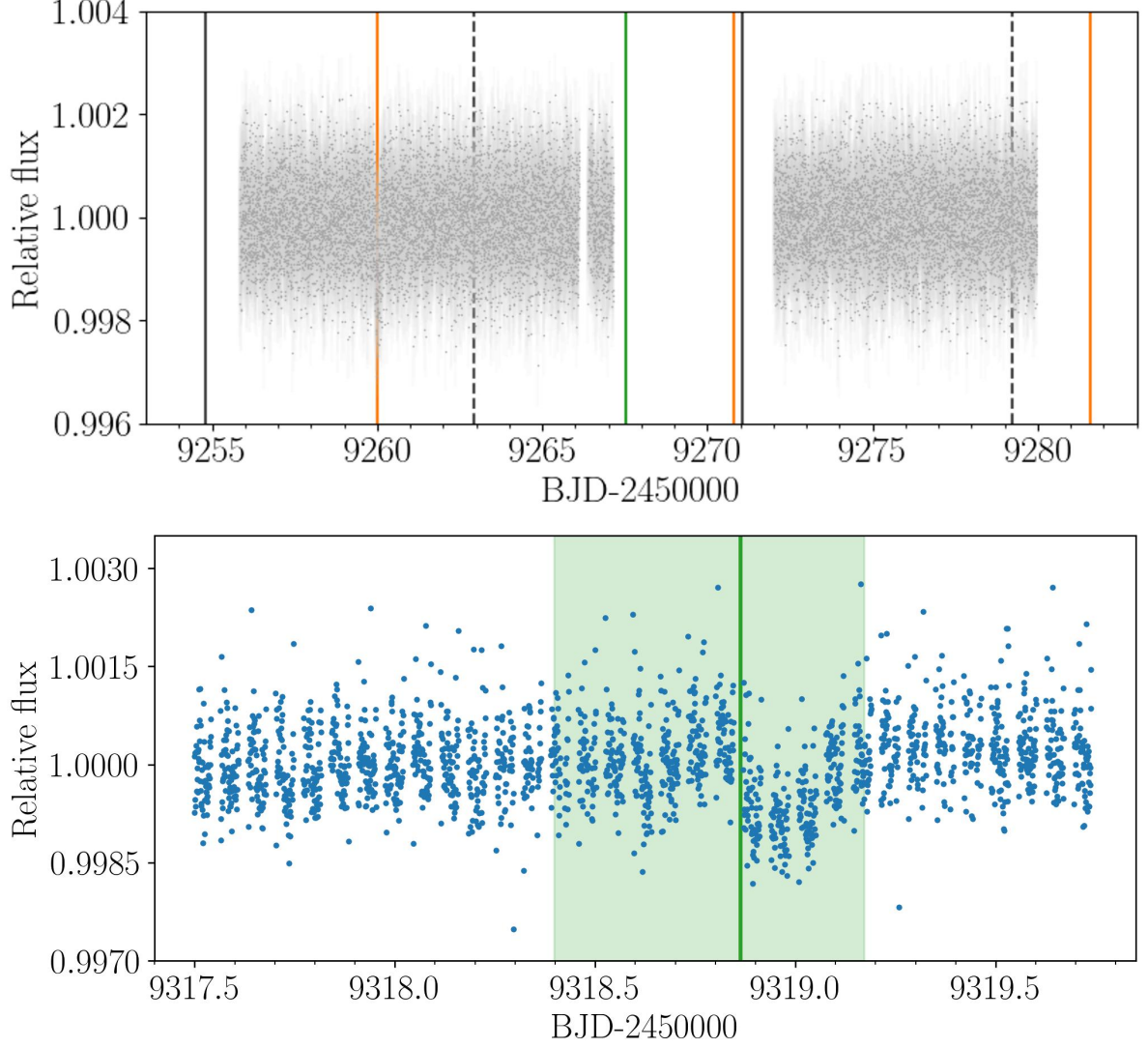
Figure 4.4 *Top*: 2-min cadence detrended *TESS* light curve of sector 35. The predicted transit times of TOI-561 c and d (according to L21 ephemeris), and TOI-561 f (according to W21 ephemeris), are highlighted with orange, green and black vertical solid lines, respectively. The black dashed lines indicate the predicted position of planet f alias at ∼ 8.1 d. The only transit present in the light curve is the one of TOI-561 c at ∼ 9260 BJD−2450000, while no transit events occurred at the predicted times of planet f alias. The transits of planet d and f fall into the time series gap. *Bottom*: *CHEOPS* visit scheduled to observe TOI-561 d. The green vertical solid line indicates the predicted transit time used to compute the *CHEOPS* observing window after the ephemeris update (Section 4.4.1). The transit occurred within the 68 per cent highest probability density interval, highlighted by the pale green region. We note that this transit is not consistent with the ephemeris propagation of planet f, which would have transited at 9319.94 BJD−2450000, so almost one day after the observed *CHEOPS* transit.

predicted time, so confirming the planetary period and giving further credence to the 4-planet scenario proposed by L21.

Even updating the ephemeris using the partial new HARPS-N data set, the last possible *CHEOPS* observing window of TOI-561 e in the 2021 season was still longer than seven days because of ephemeris uncertainties. Even including the full set of RVs would have not helped as the target was no longer observable with *CHEOPS* when the HARPS-N campaign finished. Given the high pressure on the *CHEOPS* schedule, we therefore plan the TOI-561 e observations for the 2022 observing season. The ephemeris for the 2022 *CHEOPS* observations will be updated using the *TESS* Sectors 45 and 46 observations in Nov-Dec 2021, and the results will be presented in a future publication.

### 4.4.2 Additional signals in the RV data

Before proceeding with the global modelling, we analyzed the RV data sets in order to confirm the robustness of the L21 scenario and search for potential new signals. The ℓ_1-periodogram[7] (Hara et al., 2017) of the combined HARPS-N and HIRES RVs (Figure 4.5) shows four significant peaks corresponding to the planetary periods reported in L21, plus hints of a possible longer period signal with a broad peak around $400 - 600$ days. We investigated the presence of this additional signal in a Bayesian framework using PyORBIT[8] (Malavolta et al., 2016, 2018), a package for light curve and RVs analysis. We employed the dynesty nested-sampling algorithm (Skilling, 2004; Skilling, 2006; Speagle, 2020), assuming 1000 live points, and including offset and jitter terms for each data set. We first performed a 4-planet fit of the combined data sets, using the L21 values to impose Gaussian priors on periods and transit times,[9] and assuming eccentric orbits with a half-Gaussian zero-mean prior on the eccentricity (with variance 0.098; Van Eylen et al. 2019), except for the circular orbit of the USP planet. We let the semi-amplitude K vary between 0.01 and 100 m s^{-1}. As can be seen in Figure 4.6, the RV residuals show an anomalous positive variation at ~ 9000 BJD-2450000, and the Generalized Lomb-Scargle (GLS, Zechmeister & Kürster 2009) periodogram of the RV residuals revealed the presence of a significant, broad peak at low frequencies. Moreover, the HARPS-N jitter was 1.84 m s^{-1}, which is unusually high when compared to the value reported in L21 ($\sigma_{\mathrm{HARPS-N}} = 1.29 \pm 0.23$ m s^{-1}). We therefore performed a second fit including a fifth Keplerian signal, allowing the period to span between 2 and 900 d. According to the Bayesian Evidence, this model is strongly favoured with respect to the 4-planet model, with a difference in the logarithmic evidences $\Delta \ln \mathcal{Z} = 19.0$ (Kass & Raftery, 1995).[10] Moreover, the HARPS-N jitter decreased to ~ 1.37 m s^{-1}. After this fit, the periodogram of the residuals did not show evidence of additional significant peaks (Figure 4.6). This is confirmed also by the comparison with a 6-Keplerian model that we tested, with the period of the sixth Keplerian free to span between 2 and

---

[7]https://github.com/nathanchara/l1periodogram.
[8]https://github.com/LucaMalavolta/PyORBIT, V8.1.
[9]We note that we obtained the same results when using uniform, uninformative priors, also for the 5- and 6-Keplerian fits.
[10]According to Kass & Raftery (1995), a difference $\Delta \ln \mathcal{Z} > 5$ sets a strong evidence against the null hypothesis, which in our case corresponds to the 4-planet model.
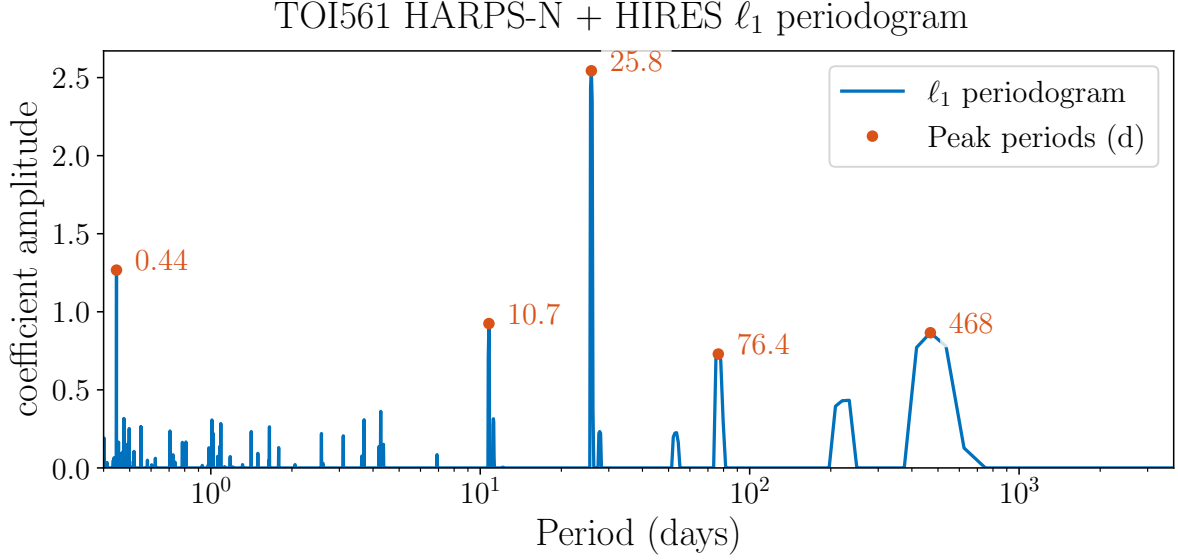
Figure 4.5 ℓ_1-periodogram of the combined HARPS-N and HIRES data sets, computed on a grid of frequencies from 0 to 2.5 cycles per day. The total time-span of the observations is 768 days. The code automatically accounts for the offset between HARPS-N and HIRES data by using the mean value of each data set.

900 d, whose Bayesian Evidence differed by less than 2 from the 5-Keplerian model one, indicating that there was no strong evidence to favour a more complex model (Kass & Raftery, 1995).

The fitted period of the fifth Keplerian was ~ 480 d. Such a long-term signal could be induced either by stellar activity, considering that stellar magnetic fields related to magnetic cycles can show variability on timescales of the order of $1 - 3$ years (e.g. Collier Cameron 2018, Hatzes 2019, Crass et al. 2021), or by an additional long-period planet. We refer here to an eventual long-period planet because, given the inferred semi-amplitude of ~ 2 m s^{-1} (Table 4.6), an external companion with mass equal to 13 M_j (assuming this value to be the threshold between planetary and sub-stellar objects) would have an inclination of ~ 0.03 deg. Such an inclination would imply an almost perpendicular orbit with respect to the orbital plane of the four inner planets, hinting at a very unlikely configuration. Therefore, in the hypothesis of the presence of an external companion, it would most likely be a planetary-mass object.

On one hand, all the five signals, including the long-term one, are recovered in an independent analysis that we performed with the CCF-based scalpels algorithm (Collier Cameron et al., 2021). Concisely, scalpels projects the RV time series onto the highest variance principal components of the time series of autocorrelation functions of the CCF, with the aim of distinguishing RV variations caused by orbiting planets from activity-induced distortions on each CCF. The absence of the signal in the scalpels shape-driven velocities indicates that the long-term periodicity is not due to shape changes in the line profiles, supporting the idea of a planetary origin. Moreover, TOI-561 is not expected to be a particularly active star given its old age and low log R$'_{HK}$, as assessed in the L21 and W21 activity analyses. As can be seen in Figure 4.7, the GLS periodogram of the majority of the activity indicators extracted with the
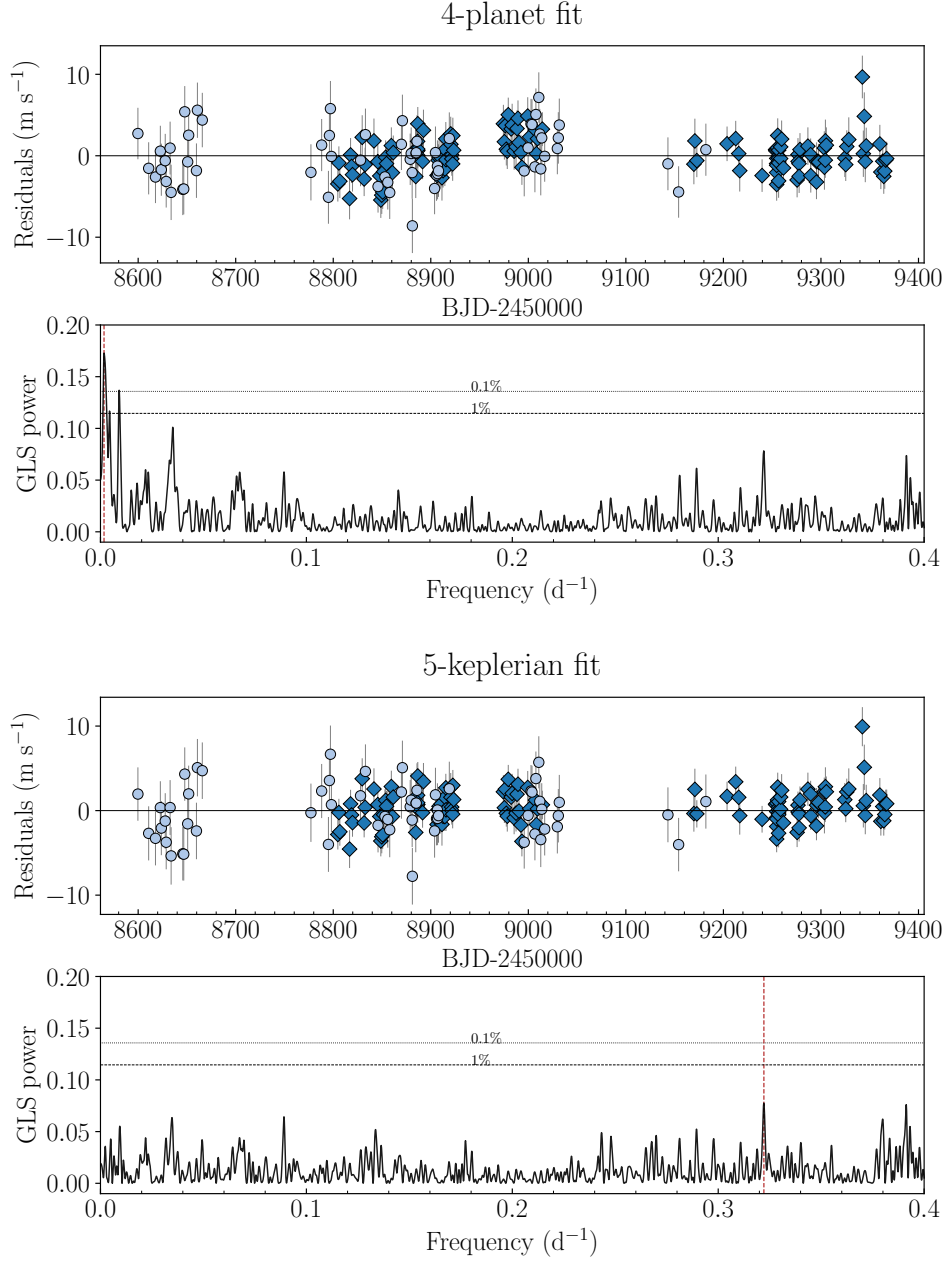
Figure 4.6 Time series and GLS periodogram of the RV residuals after the 4-planet and 5-Keplerian fits as described in Section 4.4.2. In the residuals plot, the HARPS-N and HIRES RVs are plotted with dark blue diamonds and light blue circles, respectively. In the periodogram plots, the dashed and dotted horizontal lines show the 1 and 0.1 per cent False Alarm Probability (FAP) level, respectively. The red vertical line indicates the main peak of each periodogram. The long-period peak around frequencies $0.0017 - 0.0025$ d^{-1} ($P = 400 - 600$ d) in the 4-planet residuals periodogram is modelled by the fifth Keplerian, and no more significant peaks are identified in the 5-Keplerian residuals periodogram. Moreover, the positive variation at ~ 9000 BJD-2450000 in the 4-planet fit residuals disappears in the 5-Keplerian fit residuals.

HARPS-N DRS, i.e. full width at half maximum (FWHM), bisector span (BIS), contrast and H$_\alpha$, do not show significant peaks, with none of them exceeding the 0.1 False Alarm Probability (FAP) threshold, which we computed using a bootstrap approach, at the frequency of interest. On the other hand, the periodogram of the S-index, which is particularly sensitive to magnetically-induced activity, shows a significant, broad peak at low frequencies, potentially suggesting that the previously identified long-term variability is related to stellar activity. Considering this, we performed an additional dynesty fit assuming a 4-planet model and including a Gaussian Process (GP) regression with a quasi-periodic kernel, as formulated in Grunblatt et al. (2015), to account for the long-term signal. We modelled simultaneously the RVs and the S-index time series in order to better inform the GP (Langellier et al. 2021, Osborn et al. 2021), using two independent covariance matrices for each dataset with common GP hyper-parameters except for the amplitude of the covariance matrix, assuming uniform, non-informative priors on all of them. The fit suggests a periodicity longer than ~ 570 d, but the GP model is too flexible to derive a precise period value, considering also that the global RV baseline (~ 768 d) is comparable with the periodicity of the long-term signal. The inferred semi-amplitudes of the four known planets differed by less than 0.07σ from the 5-Keplerian model ones, indicating that the different modelling of the long-term signal is not influencing the results for the known, transiting planets. Finally, as in the case of the 5-Keplerian fit, the HARPS-N jitter is significantly improved ($\sigma_{\mathrm{HARPS-N}} \sim 1.30$ m s^{-1}) when including the GP model. Therefore, since our Bayesian analyses showed that the modelling of the long-term signal is necessary to obtain the best picture of the system, we decided to perform the global fit assuming a 5-Keplerian model, but without drawing conclusions on the origin of the fifth signal. We stress that the 5-Keplerian fit does not provide absolute evidence of the presence of a fifth planet, since also poorly sampled stellar activity could be well modelled using a Keplerian (Pepe et al. 2013, Affer et al. 2016, Mortier & Collier Cameron 2017), especially in our case where the RV baseline is of the order of the signal periodicity. Since it is not possible to distinguish a true planetary signal from an activity signal that has not been observed long enough to exhibit a loss of coherence in its phase or amplitude, only a follow-up campaign over several years can allow one to better understand the nature of this long-term signal.

4.5   Joint photometric and RV analysis

To infer the properties of the TOI-561 planets, we jointly modelled all photometric and spectroscopic data with PyORBIT, using PyDE[11] + emcee (Foreman-Mackey et al., 2013a) as described in Section 3.5, and adopting the same convergence criteria. We ran 96 chains (twice the number of the model parameters) for 250000 steps, discarding the first 50000 as burn-in.

Based on the analysis presented in the previous section, we assumed a 5-Keplerian model, including four planets plus a fifth Keplerian with period free to span between 2 to 900 d. We fitted a common value for the stellar density, using the value reported in Table 4.1 as Gaussian prior. We adopted the

---

[11]https://github.com/hpparvi/PyDE.
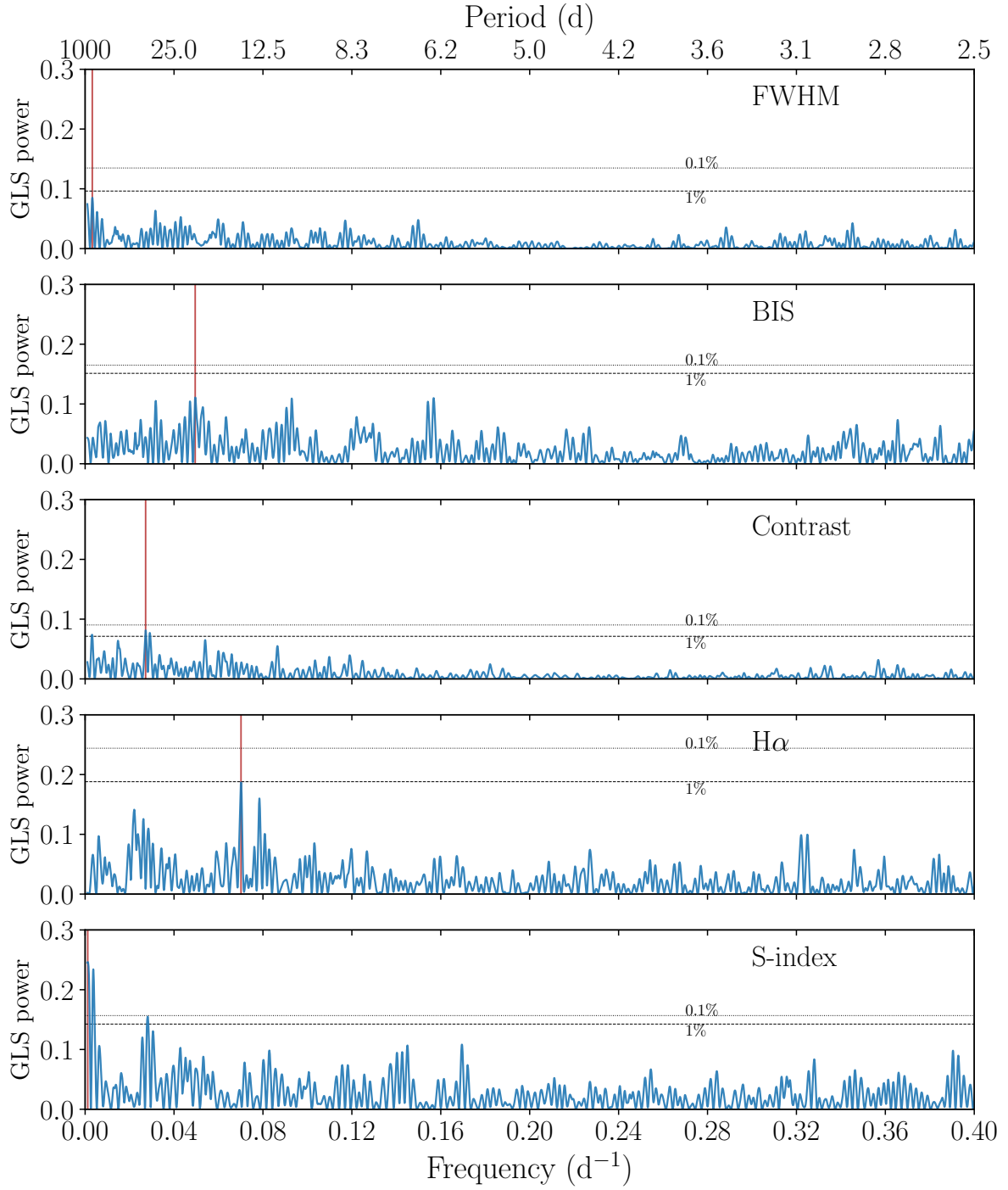
Figure 4.7 GLS periodogram of the HARPS-N activity indices. The main peak of each periodogram is highlighted with a red vertical line. The dashed and dotted horizontal lines indicate the 1 and 0.1 per cent FAP levels, respectively. The only peak above the 0.1 FAP level is the low-frequency peak in the S-index periodogram, as discussed in Section 4.4.2.

quadratic limb-darkening law as parametrized by Kipping (2013), putting Gaussian priors on the u_1, u_2 coefficients, obtained for the *TESS* and *CHEOPS* passband through a bilinear interpolation of limb darkening profiles by Claret (2017) and Claret (2021) respectively, and assuming a 1σ uncertainty of 0.1 for each coefficient. We imposed a half-Gaussian zero-mean prior (Van Eylen et al., 2019) on the planet eccentricities, except for the USP planet, whose eccentricity was fixed to zero. We assumed uniform priors for all the other parameters.

To model the long-term correlated noise in the *TESS* light curve, we included in the fit a GP regression with a Matérn-3/2 kernel against time, as shown in Figure 4.1, and we added a jitter term to account for possible extra white noise. We pre-decorrelated the *CHEOPS* light curves with the `pycheops`[12] package (Maxted et al., 2021), selecting the detrending parameters according to the Bayes factor to obtain the best correlated noise model for each visit. For all the three *CHEOPS* visits, a decorrelation for the first three harmonics of the roll angle was necessary, plus first-order polynomials in time, x-y centroid position, and smearing. We then used the detrended light curves (Figure 4.3) for the global `PyORBIT` fit. In order to check if the detrending was affecting our results for the planetary parameters, we also performed an independent global analysis with the `juliet` package (Espinoza et al., 2019), including in the global modelling the basis vectors selected with `pycheops` to detrend the data simultaneously. All the results were consistent within 1σ, indicating that the pre-detrending did not significantly alter our inferred results. Finally, for both the HARPS-N and HIRES data sets we included jitter and offset terms as free parameters.

We summarize our best-fitting model results in Table 4.6, and we show the transit model, phase-folded RVs and global RV model in Figures 4.8, 4.9, and 4.10, respectively. We inferred precise masses and radii for all the four planets in the system, whose positions in the mass-radius diagram are shown in Figure 4.11. With a radius of $R_b = 1.425 \pm 0.037\ R_\oplus$ and a mass of $M_b = 2.00 \pm 0.23\ M_\oplus$ (from $K_b = 1.93 \pm 0.21$ m s^{-1}), TOI-561 b is located in a region of the mass-radius diagram which is not consistent with a pure rocky composition, as will be also shown in Section 4.6 by our internal structure modelling. Our analysis confirms TOI-561 b to be the lowest density ($\rho_b = 3.8 \pm 0.5$ g cm^{-3}) USP planet known to date (Figure 4.12).

In order to further confirm the planetary density, we also performed a specific RV analysis of TOI-561 b using the Floating Chunk Offset method (FCO; Hatzes 2014). The FCO analysis, detailed in Appendix D, confirms the low mass inferred for TOI-561 b, and consequently its low density. Thanks to the *CHEOPS* observations, we also improved significantly the radius of TOI-561 c, for which we obtained a value of $R_c = 2.91 \pm 0.04\ R_\oplus$. From the semi-amplitude $K_c = 1.81^{+0.23}_{-0.22}$ m s^{-1} we inferred a mass of $M_c = 5.39^{+0.69}_{-0.68}\ M_\oplus$, implying a density of $\rho_c = 1.2 \pm 0.2$ g cm^{-3}. From the combined fit of one *TESS* and one *CHEOPS* transit, we inferred a radius of $2.82 \pm 0.07\ R_\oplus$ for planet d, which has a mass of $M_c = 13.2^{+1.0}_{-0.9}\ M_\oplus$ (from $K_d = 3.34^{+0.23}_{-0.22}$ m s^{-1}) and a resulting density of $\rho_d = 3.2 \pm 0.3$ g cm^{-3}. Finally, for TOI-561 e, which shows a single transit in *TESS* sector 8, we derived a radius of $R_e = 2.55^{+0.12}_{-0.13}\ R_\oplus$, a mass of $M_e = 12.6 \pm 1.4\ M_\oplus$, and an average density of $\rho_d = 4.2 \pm 0.8$ g cm^{-3}.

[12]https://github.com/pmaxted/pycheops.

Table 4.6 Parameters of the TOI-561 system, including the fifth Keplerian signal, as determined from the joint photometric and spectroscopic fit described in Section 4.5.

	TOI-561 b	TOI-561 c	TOI-561 d	TOI-561 e	5$^{\text{th}}$ Keplerian
\multicolumn{6}{c}{Planetary parameters}					
P (d)	$0.4465688^{+0.0000007}_{-0.0000008}$	$10.778831^{+0.000034}_{-0.000036}$	$25.7124^{+0.0001}_{-0.0002}$	$77.03^{+0.25}_{-0.24}$	473^{+36}_{-25}
T_0 (TBJD)[a]	2317.7498 ± 0.0005	$2238.4629^{+0.0008}_{-0.0009}$	$2318.966^{+0.003}_{-0.004}$	$1538.180^{+0.004}_{-0.005}$	1664^{+28}_{-33}
$a/R_\star$	$2.685^{+0.024}_{-0.025}$	$22.43^{+0.20}_{-0.21}$	$40.04^{+0.36}_{-0.37}$	$83.22^{+0.77}_{-0.79}$	279^{+14}_{-10}
a (AU)	0.0106 ± 0.0001	0.0884 ± 0.0009	0.158 ± 0.002	0.328 ± 0.003	$1.1^{+0.6}_{-0.4}$
$R_{\text{p}}/R_\star$	0.0155 ± 0.0004	0.0316 ± 0.0004	0.0306 ± 0.0008	$0.0278^{+0.0016}_{-0.0014}$	-
R_{p} ($R_\oplus$)	1.425 ± 0.037	2.91 ± 0.04	2.82 ± 0.07	$2.55^{+0.12}_{-0.13}$	-
b	$0.13^{+0.10}_{-0.09}$	$0.12^{+0.13}_{-0.08}$	$0.45^{+0.11}_{-0.17}$	$0.28^{+0.15}_{-0.18}$	-
i (deg)	$87.2^{+1.9}_{-2.1}$	$89.69^{+0.21}_{-0.31}$	$89.40^{+0.21}_{-0.11}$	$89.80^{+0.13}_{-0.10}$	-
T_{14} (h)	1.31 ± 0.02	$3.75^{+0.05}_{-0.08}$	$4.54^{+0.32}_{-0.29}$	$6.98^{+0.24}_{-0.40}$	-
e	0 (fixed)	$0.030^{+0.035}_{-0.021}$	$0.122^{+0.054}_{-0.048}$	$0.079^{+0.058}_{-0.050}$	$0.085^{+0.083}_{-0.059}$
ω (deg)	90 (fixed)	291^{+55}_{-84}	235^{+14}_{-26}	143^{+42}_{-44}	348^{+198}_{-53}
K (m s^{-1})	1.93 ± 0.21	$1.81^{+0.23}_{-0.22}$	$3.34^{+0.23}_{-0.22}$	2.19 ± 0.23	1.94 ± 0.27
M_{p} ($M_\oplus$)	2.00 ± 0.23	$5.39^{+0.69}_{-0.68}$	$13.2^{+1.0}_{-0.9}$	12.6 ± 1.4	20 ± 3 [b]
ρ_{p} ($\rho_\oplus$)	0.69 ± 0.10	0.22 ± 0.03	0.59 ± 0.06	0.76 ± 0.14	-
ρ_{p} (g cm^{-3})	3.8 ± 0.5	1.2 ± 0.2	3.2 ± 0.3	4.2 ± 0.8	-
S_{p} ($S_\oplus$)	4745 ± 269	68.2 ± 3.9	21.4 ± 1.3	4.96 ± 0.28	-
T_{eq}^c (K)	2310 ± 33	800 ± 11	598 ± 9	415 ± 6	-
g_{p}^d (m s^{-2})	9.7 ± 1.2	6.2 ± 0.8	16.3 ± 1.5	19.0 ± 2.9	-

Common parameters					
$R_\star^{\text{e}}$ ($R_\odot$)	0.843 ± 0.005				
$M_\star^{\text{e}}$ ($M_\odot$)	0.806 ± 0.036				
$\rho_\star$ ($\rho_\odot$)	1.31 ± 0.05				
$u_{1,\text{TESS}}$	0.33 ± 0.08				
$u_{2,\text{TESS}}$	0.23 ± 0.09				
$u_{1,\text{CHEOPS}}$	0.46 ± 0.07				
$u_{2,\text{CHEOPS}}$	0.22 ± 0.09				
$\sigma_{\text{HARPS-N}}^{\text{f}}$ (m s^{-1})	$1.40^{+0.15}_{-0.14}$				
$\sigma_{\text{HIRES}}^{\text{f}}$ (m s^{-1})	$2.77^{+0.36}_{-0.31}$				
$\gamma_{\text{HARPS-N}}^{\text{g}}$ (m s^{-1})	79700.41 ± 0.26				
$\gamma_{\text{HIRES}}^{\text{g}}$ (m s^{-1})	-1.20 ± 0.42				

[a] TESS Barycentric Julian Date (BJD-2457000). [b] Minimum mass in the hypothesis of a planetary origin. [c] Computed as $T_{\text{eq}} = T_\star \left(\dfrac{R_\star}{2a} \right)^{1/2} [f(1 - A_{\text{B}})]^{1/4}$, assuming $f = 1$ and a null Bond albedo ($A_{\text{B}} = 0$). [d] Planetary surface gravity. [e] As determined from the stellar analysis in Section 4.2.1. [f] RV jitter term. [g] RV offset.
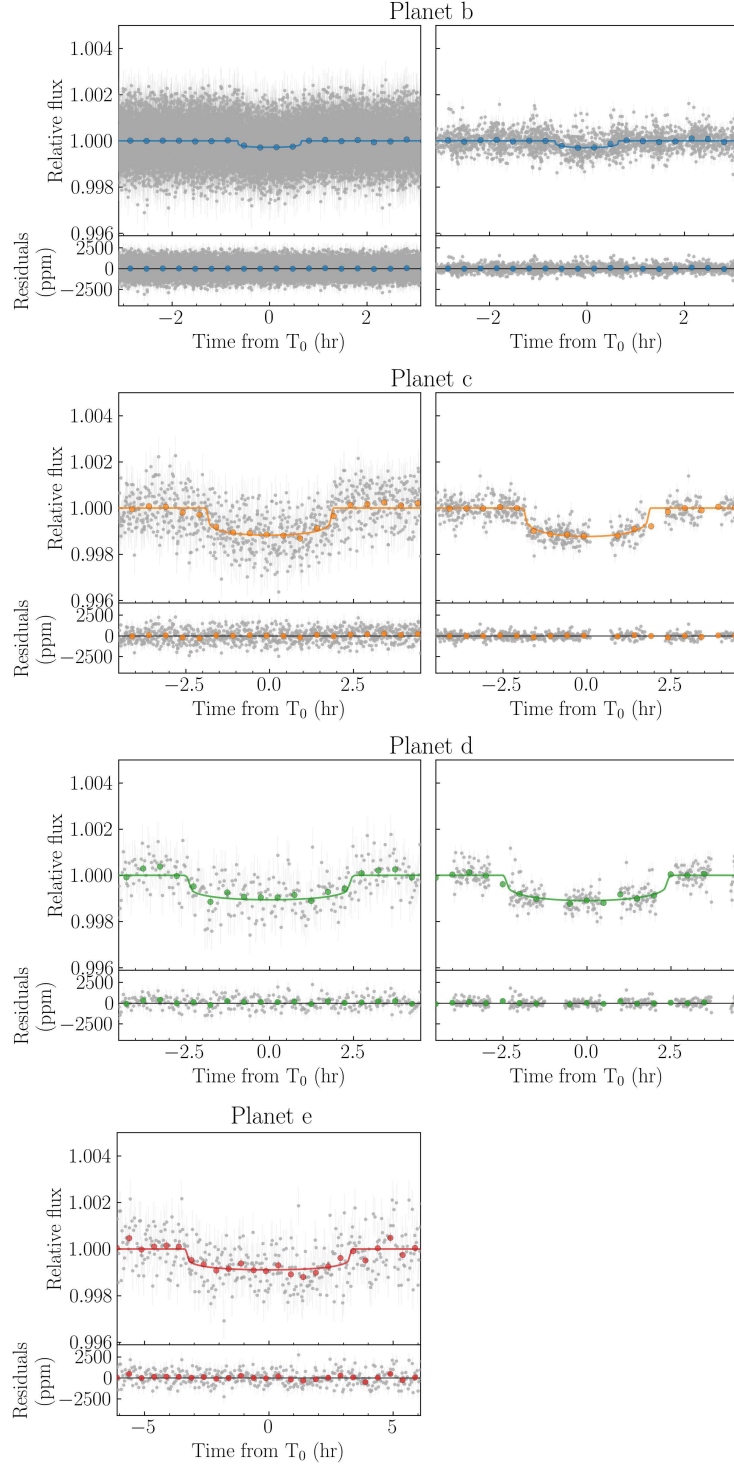
Figure 4.8 Phase-folded *TESS* (*left*) and *CHEOPS* (*right*) light curves of TOI-561 b, c, and d. Planet e shows a single transit in the *TESS* light curve, and it has no *CHEOPS* observations. For each planet, the coloured line indicates the best-fitting model, and residuals are shown in the bottom panels. Data points binned over 20 min (planet b) and 30 min (planets c, d and e) are shown with coloured dots.
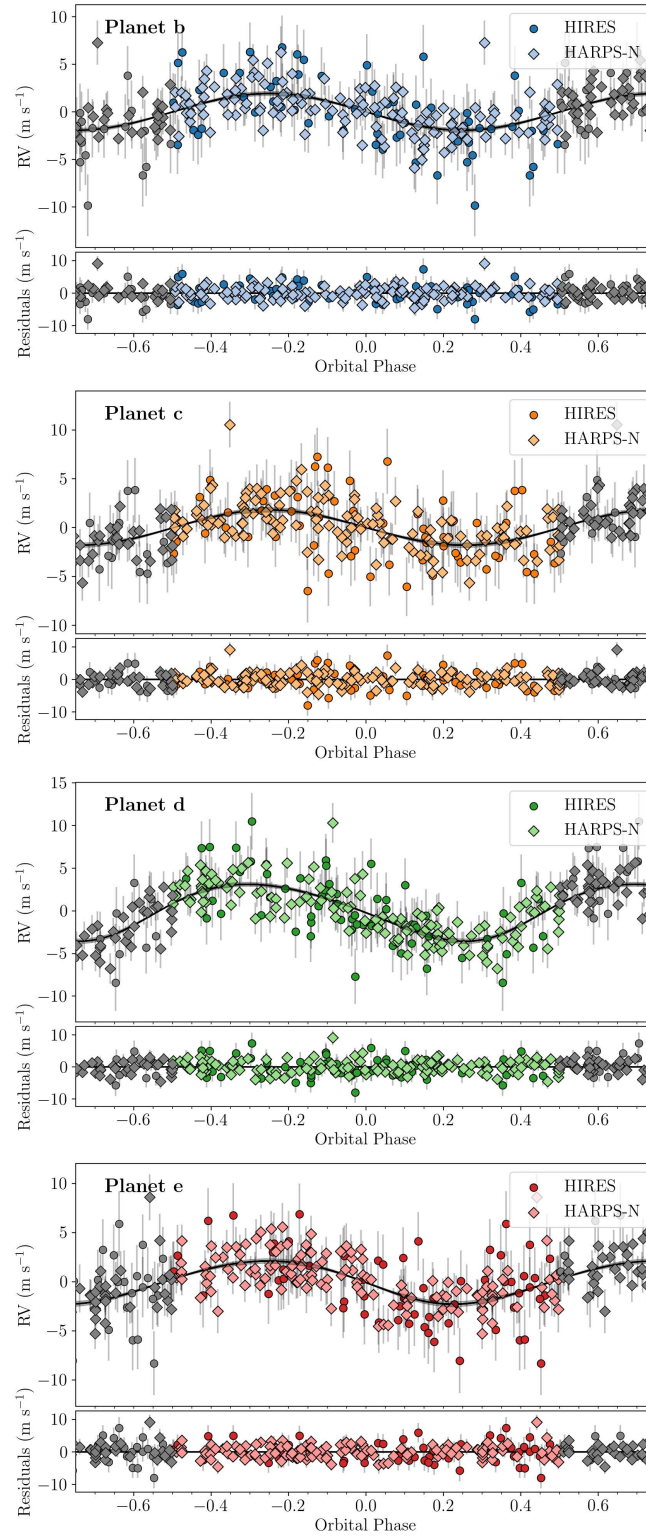
Figure 4.9 Phase-folded HARPS-N and HIRES RVs with residuals of TOI-561 b, c, d and e, as resulting from the joint photometric and spectroscopic fit. The error bars include the jitter term added in quadrature.
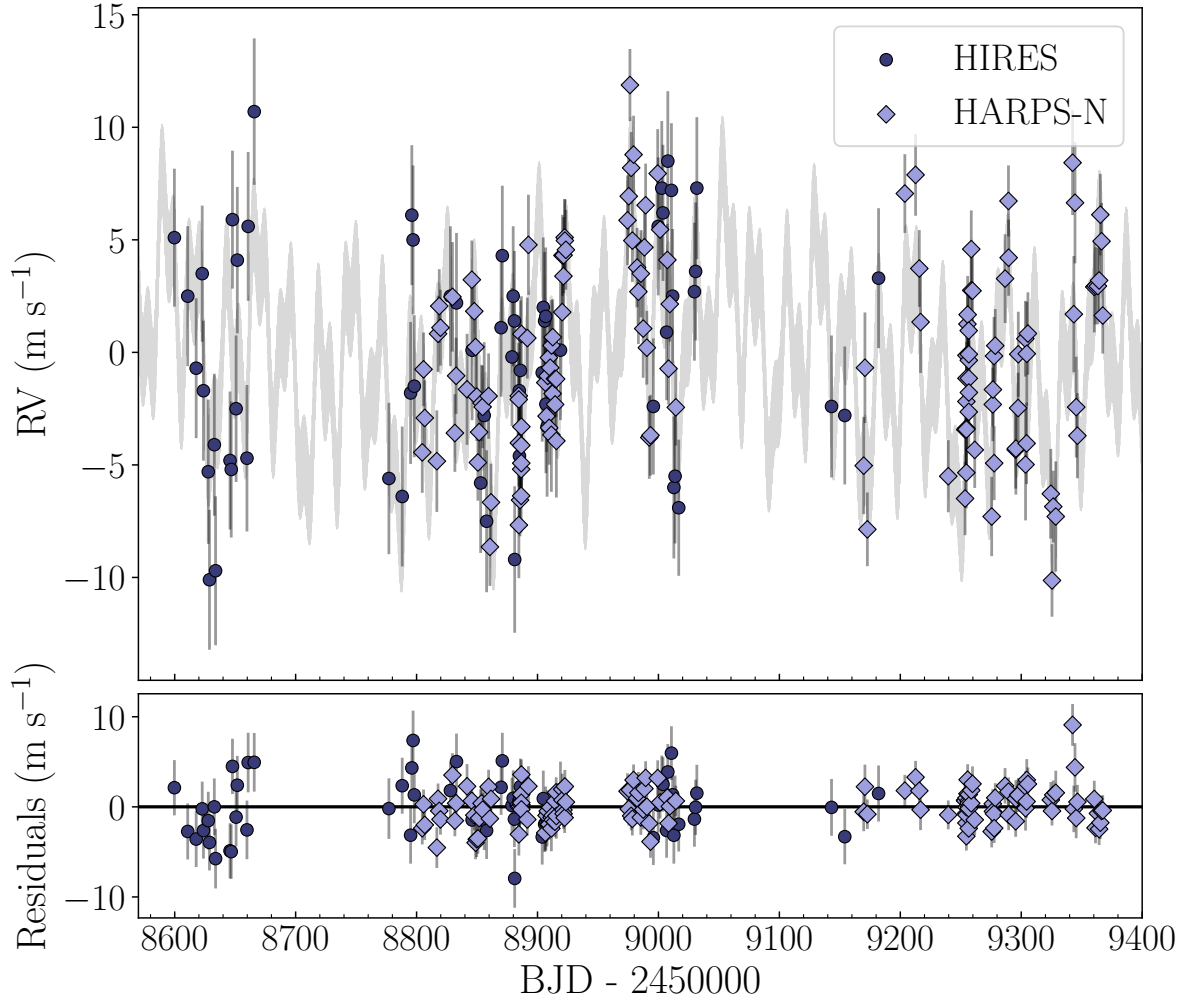
Figure 4.10 Global model (grey line) with residuals of HARPS-N and HIRES RVs according to the 5-Keplerian photometric and spectroscopic fit. The error bars include the jitter term added in quadrature.
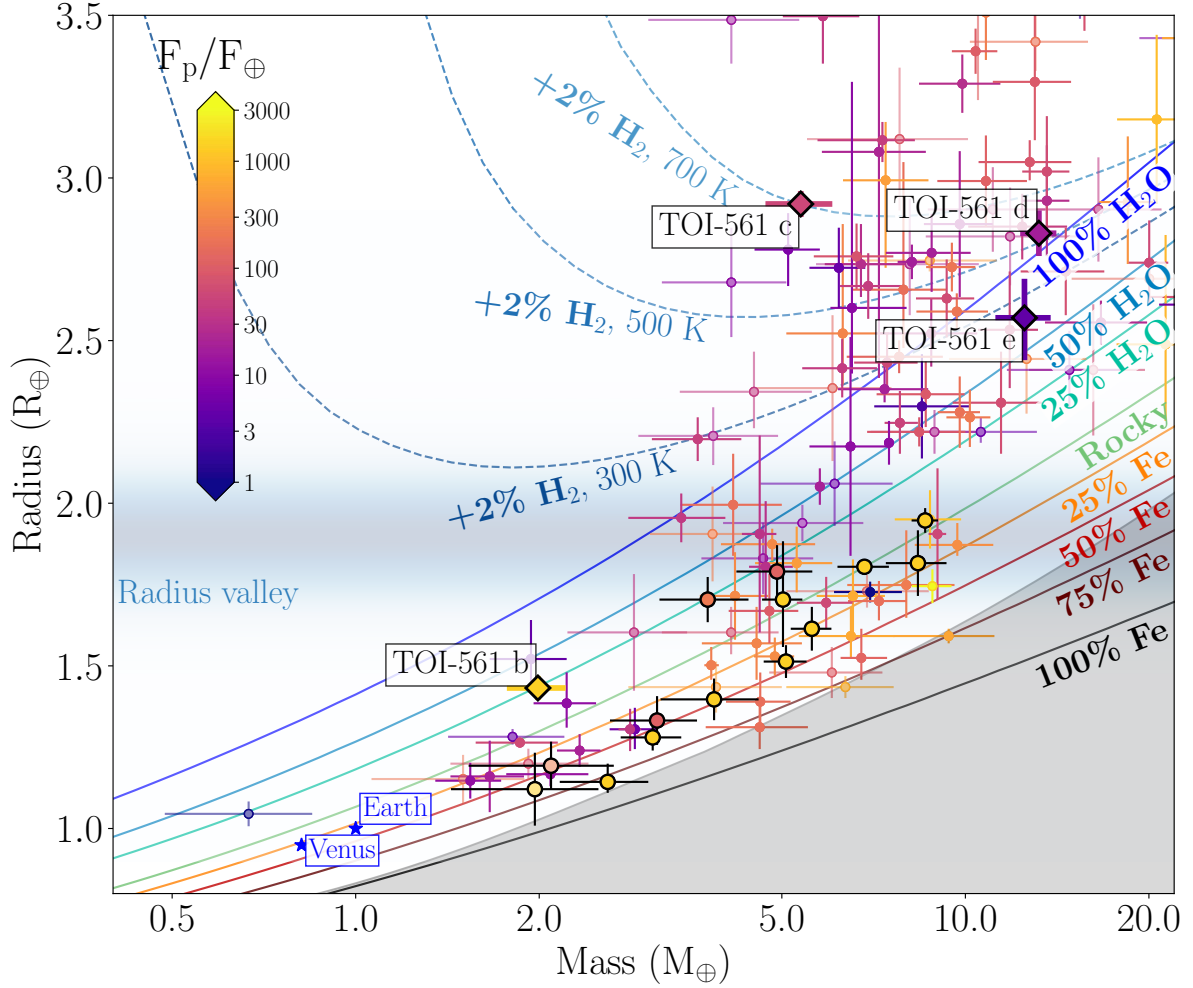
Figure 4.11 Mass-radius diagram for exoplanets with radii and masses measured with a precision better than 30%, colour coded according to their incidental flux. Data are taken from the Extrasolar Planets Encyclopaedia catalogue (http://exoplanet.eu/catalog/) as of 18 October 2021. The TOI-561 planets are labelled, and highlighted with coloured diamonds. The USP planets are emphasized with thick, black-contoured circles. The theoretical mass-radius curves for various chemical compositions (Zeng et al., 2019) are represented by solid coloured lines, while the dashed lines indicate the curves for an Earth-like core surrounded by a H_2 envelope (2% mass fraction) at varying equilibrium temperatures. The forbidden region predicted by collisional stripping (Marcus et al., 2010) is marked by the shaded grey region.

Lastly, the period inferred for the fifth Keplerian in the model was 473^{+36}_{-25} d, with a 7.2σ detected semi-amplitude of 1.94 ± 0.27 m s^{-1}. As discussed in Section 4.4.2, additional data spanning a longer baseline are needed to definitively confirm the planetary nature of this long-term signal.
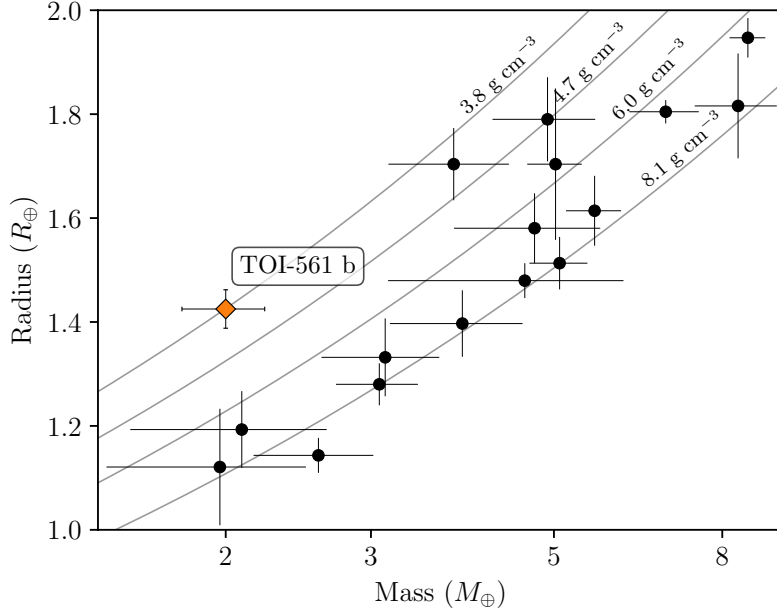
Figure 4.12 Mass-radius diagram of confirmed USP planets ($P < 1$ d, $R_{\mathrm{p}} < 2\ R_{\oplus}$) as taken from the Extrasolar Planets Encyclopaedia catalogue in date 18 October 2021. Iso-density lines are plotted in grey. TOI-561 b stands out as the lowest density USP planet known to date ($\rho_{\mathrm{b}} = 3.8 \pm 0.5$ g cm^{-3}).

4.6 Internal structure modelling

We modelled the internal planetary structure in a Bayesian framework, following the procedure detailed in Leleu et al. (2021a). Our model assumes fully-differentiated planets composed of four layers, comprising an iron and sulfur central core, a silicate mantle which includes Si, Mg and Fe, a water layer, and a pure H/He gas layer. The inner core is modelled assuming the Hakim et al. (2018) equation of state (EOS), the silicate mantle uses the Sotin et al. (2007) EOS, and the water layer uses the Haldemann et al. (2020) EOS. The core, mantle and water layer compose the 'solid' part of the planet. The thickness of the gas envelope is computed as a function of stellar age and irradiation, and mass and radius of the solid part, according to the model presented in Lopez & Fortney (2014). We assumed no compression effects of the gas envelope on the solid part, a hypothesis which is justified *a posteriori* given the low mass fraction of gas obtained for each planet (see below).

Our Bayesian model fits the planetary system as a whole, rather than performing an independent fit for each planet, in order to account for the correlations between the absolute planetary masses and radii, which depend on the stellar properties. The model fits the stellar (mass, radius, effective temperature,

age, chemical abundances of Fe, Mg, Si), and planetary properties (RV semi-amplitudes, transit depths, orbital periods) to derive the posterior distributions of the internal structure parameters. The internal structure parameters modelled for each planet are the mass fractions of the core, mantle and water layer, the mass of the gas envelope, the iron molar fraction in the core, the silicon and magnesium molar fraction in the mantle, the equilibrium temperature and the age of the planet (equal to the age of the star). For a more extensive discussion on the relation among input data and derived parameters we refer to Leleu et al. (2021a). We assumed the mass fraction of the inner core, mantle, and water layer to be uniform on the simplex (the surface on which they add up to one), with the water mass fraction having an upper boundary of 0.5 (Marboeuf et al., 2014; Thiabaud et al., 2014). For the mass of the gas envelope, we assumed a uniform prior in logarithmic space. Finally, we assumed the Si/Mg/Fe molar ratios of each planet to be equal to the stellar atmospheric values (even though Adibekyan et al. (2021a) recently showed that the stellar and planetary abundances may not be always correlated in a one-to-one relation). We emphasize the fact that, as in many Bayesian analyses, the results presented below in terms of planet internal structure depend to some extent on the selection of the priors, which we chose following i.e. Dorn et al. (2017), Dorn et al. (2018c), and Leleu et al. (2021a). Analysing the same data with very different priors (e.g. non uniform core/mantle/water mass fraction or gas fraction uniform in linear scale) would lead to different conclusions.

We show the results of the internal structure modelling for the four planets in Figure 4.13. As expected from its closeness to the host star, planet b has basically no H/He envelope, while the other three planets show a variable amount of gas mass. Planet c hosts a relatively massive gaseous envelope, with a gas mass of (5 and 95 per cent quantiles) $M_{\mathrm{gas,c}} = 0.07^{+0.04}_{-0.02} \, M_{\oplus}$ ($1.3^{+0.8}_{-0.4}$ weight percent wt%). Planet d hosts the most massive envelope ($M_{\mathrm{gas,d}} = 0.10^{+0.13}_{-0.07} \, M_{\oplus}$), which, considering the total mass of the planet, correspond to a smaller relative mass fraction of $0.8^{+1.0}_{-0.5}$ wt%, while TOI-561 e's envelope spans a range between $-10.7 < \log M_{\mathrm{gas,e}} < -1.0$, implying an upper limit on the gas mass of 0.11 $M_{\oplus}$ (< 0.9 wt%). As expected from its low density, TOI-561 b could host a significant amount of water, having a water mass of $M_{\mathrm{H_2O,b}} = 0.62^{+0.32}_{-0.44} \, M_{\oplus}$ (31^{+16}_{-22} wt%). We stress that this result is highly dependent on the caveat of including only a solid water layer in the model. In fact, a massive water layer, if present on a planet with such a high equilibrium temperature, would imply the presence of a massive steam atmosphere (Turbet et al., 2020). This would in turn considerably change the inferred water mass fraction with respect to a model that includes only a solid water layer. Due to the presence of the gas envelope, the amount of water in both planet c and d is almost unconstrained ($M_{\mathrm{H_2O,c}} = 1.29^{+1.24}_{-1.14} \, M_{\oplus}$, i.e. 24^{+23}_{-21} wt%; $M_{\mathrm{H_2O,d}} = 3.56^{+2.78}_{-3.18} \, M_{\oplus}$, i.e. 27^{+21}_{-24} wt%), while TOI-561 e modelling points toward a massive water layer, with $M_{\mathrm{H_2O,e}} = 4.50^{+1.69}_{-3.65} \, M_{\oplus}$ (36^{+13}_{-29} wt%).

4.7 Atmospheric evolution

We employed the system parameters derived in this work to constrain the evolution of the stellar rotation period, which we use as a proxy for the evolution of the stellar high-energy emission affecting atmospheric escape, and the predicted initial atmospheric mass fraction of the detected transiting plan-
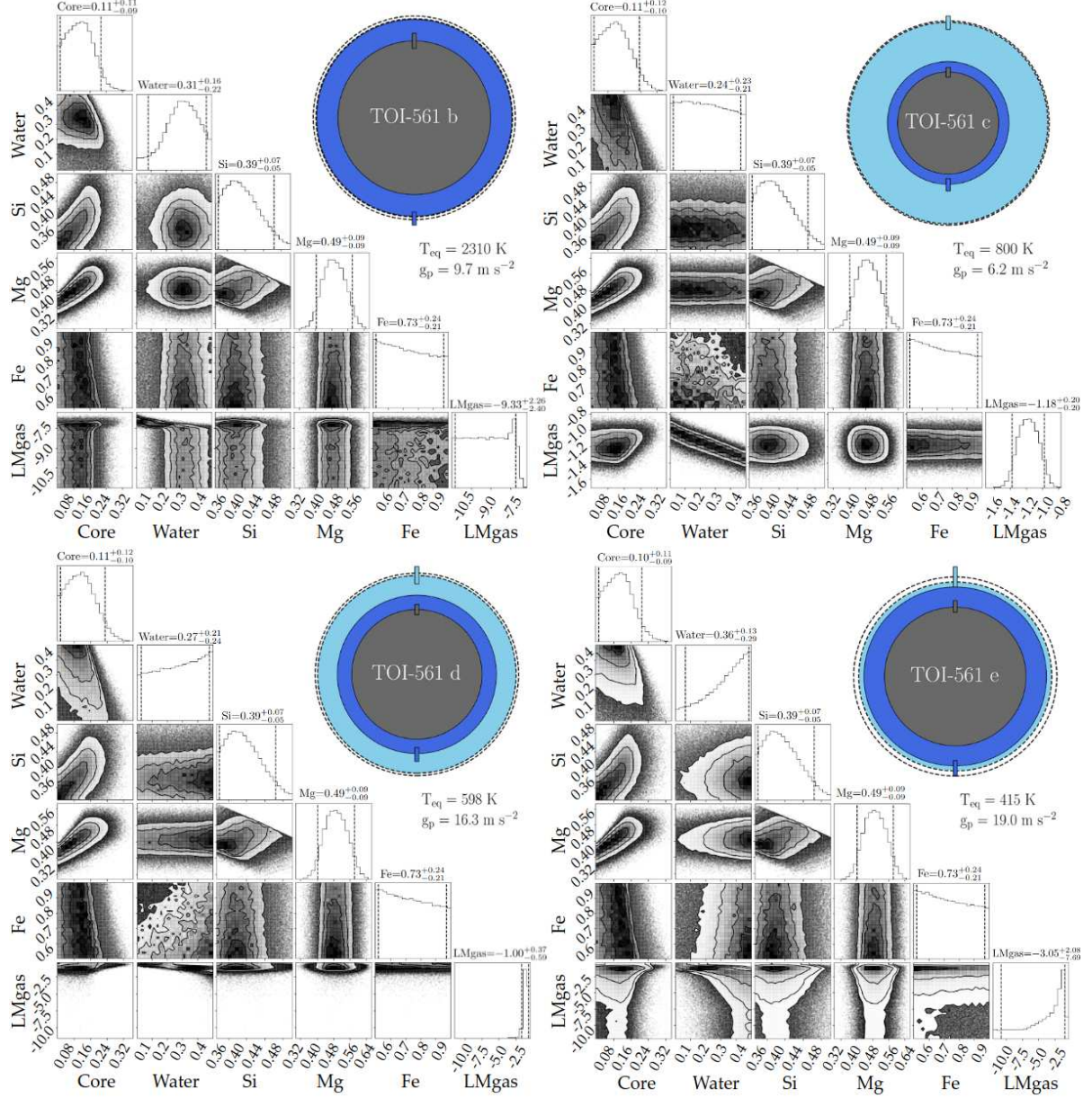
Figure 4.13 Posterior distributions of the main parameters describing the internal structure of TOI-561 b (*top left*), c (*top right*), d (*bottom left*), and e (*bottom right*). Each corner plot shows the mass fraction of the inner core and of the water layer, the molar fractions of silicon and magnesium in the mantle, the iron molar fraction in the inner core, and the mass of gas in logarithmic scale. On top of each column are printed the mean and the 5 per cent and 95 per cent quantiles values. For each planet, and we show an illustration of the radius fractions of the inner core+mantle (dark gray), water layer (dark blue), and gas envelope (light blue), corresponding to the medians of the posterior distributions. The coloured rectangles indicate the uncertainty on the corresponding layer thickness, while the black dashed outer rings represent the uncertainty on the total radius. Equilibrium temperature and planetary surface gravity are reported for each planet.

ets $f_{\mathrm{atm}}^{\mathrm{start}}$, that is the mass of the planetary atmosphere at the time of the dispersal of the protoplanetary disk. To this end, we used the planetary atmospheric evolution code PASTA described by Bonfanti et al. (2021a), which is an updated version of the original code presented by Kubyshkina et al. (2019a,b). The code models the evolution of the planetary atmospheres combining a model predicting planetary atmospheric escape rates based on hydrodynamic simulations (this has the advantage over other commonly used analytical estimates to account for both XUV-driven and core-powered mass loss; Kubyshkina et al., 2018), a model of the stellar high-energy (X-ray plus extreme ultraviolet; XUV) flux evolution (Bonfanti et al., 2021a), a model relating planetary parameters and atmospheric mass (Johnstone et al., 2015b), and stellar evolutionary tracks (Choi et al., 2016). The main assumptions of the framework are that planet migration did not occur after the dispersal of the protoplanetary disk, and that the planets hosted at some point in the past or still host a hydrogen-dominated atmosphere.

For each planet, the evolution calculations begin at an age of 5 Myr, which is the age assumed in the code for the dispersal of the protoplanetary disk. At each time step, the framework derives the mass-loss rate from the atmospheric escape model employing the stellar flux and the system parameters, and uses it to update the atmospheric mass fraction. This procedure is then repeated until the age of the system is reached or the planetary atmosphere has completely escaped. The free parameters of the algorithm are the initial atmospheric mass fraction at the time of the dispersal of the protoplanetary disk, and the indexes of the power law controlling the stellar rotation period (see Bonfanti et al., 2021a, for a detailed description of the mathematical formulation of the power law), that we use as proxy for the stellar XUV emission.

The free parameters are constrained by implementing the atmospheric evolution algorithm in a Bayesian framework employing the MCMC tool presented by Cubillos et al. (2017). The framework uses the system parameters with their uncertainties as input priors. It then computes millions of forward planetary evolutionary tracks, varying the input parameters according to the shape of the prior distributions, and varying the free parameters within pre-defined ranges, fitting the current planetary atmospheric mass fractions obtained as described in Section 4.6. The fit is done at the same time for all planets, thus simultaneously constraining the rotational period, and the results are posterior distributions of the free parameters. In particular, we opted for fitting for the planetary atmospheric mass fractions instead of the planetary radii. This enables the code to be more accurate by avoiding the continuous conversion of the atmospheric mass fraction into planetary radius, given the other system parameters (see also Delrez et al., 2021).

Figure 4.14 shows the results of the planetary atmospheric evolution simulations. As a proxy for the evolution of the stellar rotation period, in Figure 4.14, we show the posterior distribution of the stellar rotation period at an age of 150 Myr, further comparing it to the distribution of stellar rotation periods observed in stars member of young clusters of comparable age and with masses that deviate from $M_\star$ less than 0.1 $M_\odot$ (from Johnstone et al., 2015a). The inferred posterior distribution for the rotation period is consistent with membership of the slowly-rotating period-colours sequence in clusters of this age. However, this comparison should be taken with some caution, since there are no comprehensive studies on the rotation-colour distributions of 150 Myr-old clusters with the same metallicity as TOI-
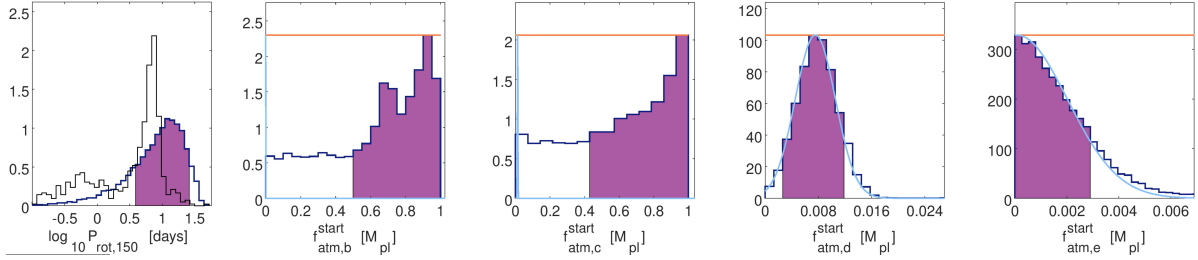
Figure 4.14 *From left to right:* Posterior distributions (dark blue lines) of the stellar rotation period at an age of 150 Myr and of the initial atmospheric mass fractions of TOI-561 b, c, d and e. In each panel, the purple region represents the 68 per cent highest probability density intervals. In the left panel, the black thin line shows the rotation period distribution of stars member of open clusters with ages around 150 Myr. Data are taken from Johnstone et al. (2015a), who report the rotation period of $\sim$ 2000 stars belonging to the Pleiades, M50, M35, and NGC 2516, whose ages are between 125 and 150 Myr. To generate the black histogram we selected a sub-sample of 578 stars, which have masses that deviate from $M_\star$ less than 0.1 $M_\odot$. In the other panels, the horizontal orange lines mark the uniform prior used in the fit, scaled to the highest peak of each posterior distribution for better visualization. The light blue lines indicate the current atmospheric mass fraction of each planet determined as described in Section 4.6.

561. The initial atmospheric mass fractions of planets b and c are rather broad and peak at about one planetary mass. This is because both planets are close enough to the host star and have a small enough mass to have been subject to significant atmospheric escape. Therefore, to enable the presence of a thin hydrogen atmosphere, as predicted by the internal structure model, both planets had to host a significant hydrogen envelope after the formation and atmospheric accretion processes. Instead, planets d and e are far from the host star and massive enough not to have been subject to significant atmospheric escape, which is why we obtain an initial atmospheric mass fraction that resembles the current one. We also find that the posterior distributions of all input parameters match well the inserted priors (not shown here). As a whole, the results indicate that the currently observed system parameters are compatible with a scenario in which migration happened (if at all) exclusively inside the protoplanetary disk. Otherwise the code would have led to mismatches between the prior and posterior of the input parameters (particularly for what concerns the planetary masses and/or the stellar mass and age), in addition to showing incoherent results in the posterior distribution of the output parameters. This is for example the case of the TOI-1064 system, which is composed by two transiting planets with comparable masses and irradiation levels, but significantly different radii (Wilson et al. *submitted*). In our framework in which planets do not migrate after the dispersal of the protoplanetary nebula, reproducing the physical parameters of the planets composing the TOI-1064 system requires different evolutions of the stellar rotation rate, which is not possible, thus calling for a post-nebula migration.

4.8   Discussion and conclusions

In this study, we confirm the presence of four transiting planets around TOI-561, with orbital periods of approximately 0.44, 10.8, 25.7, and 77 days (Table 4.6). Our analysis disproves the presence of the previously suggested planet TOI-561 f ($P \sim 16.3$ day; W21). TOI-561 is one of the few 4-planet systems
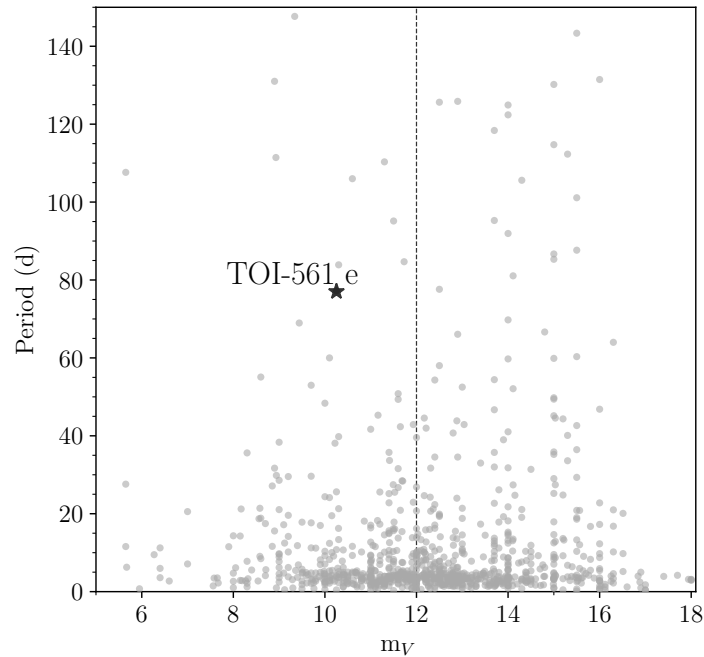
Figure 4.15 *V* magnitude versus planetary periods for confirmed transiting exoplanets as reported in the Extrasolar Planets Encyclopaedia catalogue (http://exoplanet.eu/catalog/) in date 18 October 2021. The dashed vertical line marks $V = 12$ mag. TOI-561 e is one of the few long-period planets orbiting a star bright enough for precise RV characterization.

having precise radius and mass measurements for all the planets. Thanks to our global photometric and RV analysis, we refined all masses and radii with respect to the L21 values, and we precisely determined the planetary bulk densities, with uncertainties of 14.4%, 13.6%, 10.2%, and 18.4% for planets b, c, d, and e, respectively. The higher uncertainty on planet e reflects the lower precision in the radius determination (5% uncertainty), which is based on the analysis of a single *TESS* transit, and highlights the importance of the high-precision *CHEOPS* photometry. In fact, with a single *CHEOPS* transit we managed to decrease the uncertainty on the radius of planet d from 5.1% (L21, based on one *TESS* transit) to 2.5%. Including also the improvement on the mass, this implied a decrease on the density uncertainty from 18.9% to 10.2%. We expect a similar improvement for planet e with future *CHEOPS* observations scheduled for 2022. The improvement in the radius of TOI-561 e is particularly important, since the planet is an interesting target for the study of the internal structure of cold sub-Neptunes. Its long period ($P_d = 77.03^{+0.25}_{-0.24}$ d) implies an insolation flux of $S_e = 4.96 \pm 0.28\ S_\oplus$ and a relatively cool zero Bond albedo equilibrium temperature of $T_{eq,e} = 415 \pm 6$ K. As shown in Figure 4.15, TOI-561 e is one of the few cool, long-period planets orbiting a star bright enough for precise RV characterization, and it is therefore an optimal test-case to refine tools and models that will be useful to characterize targets of future long-staring missions like *PLATO*.

TOI-561 hosts one of the most intriguing USP planets discovered to date. As initially suggested by L21, our analysis confirms that TOI-561 b is the lowest density ($\rho_b = 3.8 \pm 0.5$ g cm^{-3}) USP super-

Earth that we know of (see Figure 4.12), and it paves the way for in-depth studies of interior composition, and formation and evolution processes of USP planets. Even though now the mass values are consistent within 1σ, contrary to what proposed by W21 (see Section 4.2.2) TOI-561 b is not consistent with a pure rocky composition, and to explain the planetary density our internal structure modelling (Section 4.6) predicts basically no H/He envelope, and a massive water layer. In this regard, an important point to consider is that, with an insolation flux of $S_{\rm b} \simeq 4745\, S_{\oplus}$, the planet receives more irradiation from the star than the theoretical runaway greenhouse limit (Kasting et al. 1993, Goldblatt & Watson 2012, Kopparapu et al. 2013). In this case, a large water content would imply the presence of an extended steam atmosphere, which in turn would increase the measured radius with respect to a purely condensed water world, leading in our model to an overestimation of the bulk water content (Turbet et al., 2020). The presence of a water steam envelope could eventually be tested with the *James Webb Space Telescope* (*JWST*). In fact, with an Emission Spectroscopy Metric (ESM, Kempton et al. 2018) value of 8.2, TOI-561 b is a promising target for secondary eclipse and phase curve observations. More complex models, including a lighter core compositions (i.e. a Ca/Al enriched core), the modelling of water steam envelopes, or wet-melt solid interiors related to deep water reservoirs (Dorn & Lichtenberg, 2021), could be an interesting step forward in the understanding of the planet structure and composition. The low density of TOI-561 b could also be related to the fact that the host star is a metal-poor, thick-disk star. Adibekyan et al. (2021a) showed that the composition of the rocky planets reflects the chemical abundances of the host star (even though not in a one-to-one relation), so implying a lighter composition for TOI-561 b with respect to other USP planets that orbit more metal-rich stars[13]. According to Adibekyan et al. (2021a), the low density of TOI-561 b is consistent with the general $\rho/\rho_{\rm Earth-like} - f_{\rm iron}^{\rm star}$ trend and dispersion inferred from the sample of rocky planets analysed by the authors (see Figs. 2, 3 therein), where $\rho/\rho_{\rm Earth-like}$ is the planetary density normalised to that expected for an Earth-like composition, and $f_{\rm iron}^{\rm star}$ is the iron-to-silicate mass fraction of the protoplanetary disk as inferred from the stellar properties. An additional interesting remark concerns the Galactic kinematics of the host star. According to our analysis, performed as described in Mustill et al. (2021), TOI-561 is located in a low-density region of the 6-dimensional Galactic phase space (see Winter et al. 2020, Mustill et al. 2021, and Kruijssen et al. 2021 for definition and discussion), which is not surprising given that TOI-561 is a thick disk star (Mustill et al., 2021). Kruijssen et al. (2020) showed that stars in low-density regions seem to host no super-Earths, but only sub-Neptunes, i.e. planets having a significant H/He envelope and therefore located above the radius gap. In this context, TOI-561 b is an interesting object that runs counter to this finding. We point out that this result should be taken with some caution, since the Kruijssen et al. (2020) sample does not include planets with periods shorter than one day, and it excludes stars with ages > 4.5 Gyr[14].

---

[13] All the USP planets shown in Figure 4.11 have [Fe/H] > −0.14.

[14] We note however that the stellar ages used in Kruijssen et al. (2020) are quite inhomogeneous, coming directly from the NASA Exoplanet Archive, and can therefore show a large scatter with respect to a homogeneous determination (Adibekyan et al., 2021b).

All the four planets seem to host a large water layer (Section 4.6), although with high uncertainties, especially for planet c and d, due to the degeneracy related to the possible presence of a gas envelope. Also in this case, the presence of a considerable amount of water could be linked with the stellar properties. In fact, Santos et al. (2017) showed that metal-poor, thick disk stars are expected to form planetary building blocks with a higher water mass fraction ($\sim 76\%$) compared to metal-rich, thin disk stars ($\sim 58\%$). Therefore, we would expect these stars to produce water-rich planets, a result that is in agreement with our findings on the TOI-561 system.

Except for TOI-561 b, all the other planets are suggested to host a non-negligible H/He envelope. In particular, the gas content of planet c (~ 1.3 wt%, the highest mass fraction among the four planets) implies a much lower density with respect to the density of planet d, even though the two planets have a similar size. This is reflected in the different positions of the planets in the mass-radius diagram (Figure 4.11). The two planets show hints of a different evolution for what concerns their gas content. In fact, our atmospheric evolution model (Section 4.7) suggests that planet c underwent a strong envelope loss after the atmospheric accretion and the dispersal of the protoplanetary nebula, while planet d (as well as planet e) did not experience strong atmospheric escape, with a current gas content that is comparable to the original one. The surprising difference in gas mass fraction between planets c, d and e, not only at present time but also at the end of their formation phase, takes probably its origin in the conditions that prevailed during the protoplanetary disk phase. Planet c is indeed likely sub-critical because of its low mass, where sub-critical planets are those with masses below the critical value required to initiate runaway gas accretion (see Helled et al. 2014 for a recent review on the core accretion model), whereas planets d and e never accreted large amounts of gas as demonstrated in Section 4.7, and so they also remained always below the critical mass. The interpretation of the different gas mass fractions could therefore result from the structure of sub-critical planets. In this case, the gas mass fraction depends on the core mass, the thermodynamical properties in the disk, and more importantly the accretion rate of solids (lower accretion rate translating in larger gas mass fraction). Interpreting the internal structure of the four planets of the system in a global planetary system formation model could therefore constrain these parameters.

With its derived properties, TOI-561 c has a Transmission Spectroscopy Metric (TSM, Kempton et al. 2018) of 110.4, and is therefore a suitable target for atmospheric characterization with *JWST*.[15] Instead, planets d and e have lower TSM values of 30.7 and 16.2, respectively. As the TSM is proportional to the equilibrium temperature, it is not surprising to obtain lower values for the two planets, given their longer periods.

In addition to the characterization of the four planets, we also identified a significant long-term signal ($P \sim 473$ d) in the RVs. On the basis of our current dataset, we are not able to distinguish between a stellar (magnetically-induced) or planetary origin. Long-term monitoring using both spectroscopic ground-based facilities and future long-staring missions like the *PLATO* spacecraft will allow us to shed light on the nature of this additional signal, and to potentially find new outer companions. It is

---

[15]Kempton et al. (2018) suggest to select planets with TSM > 92 for 1.5 $R_\oplus < R_p < 2.75$ $R_\oplus$, and TSM > 84 for 2.75 $R_\oplus < R_p < 4$ $R_\oplus$.

worth noting that, if the above-mentioned signal proves in future to be of planetary origin, there is a non-zero chance that, under the assumption of co-planarity, such a planet would transit. In fact, assuming the same inclination of planet e and using the semi-major axis $a/R_{\star} = 279^{+14}_{-10}$ derived from our global fit, we infer an impact parameter of $0.97^{+0.49}_{-0.63}$. Moreover, the planet would orbit in TOI-561's empirical habitable zone ($175 \lesssim P \lesssim 652$ d), as originally defined by Kasting et al. (1993) using a 1D climate model, and later updated in Kopparapu et al. (2013); Ramirez & Kaltenegger (2016) for main-sequence stars with $2600 < T_{\text{eff}} < 10000$ K (Kaltenegger et al., 2019).

This work bears witness to the fruitful results that can be obtained by the timely combination of data coming from different instruments. It adds to the works (Bonfanti et al., 2021b; Delrez et al., 2021; Leleu et al., 2021a) that prove the potential of *CHEOPS* in precisely characterizing *TESS*-discovered exoplanets, as well as demonstrating the key role of high-precision spectrographs such as HARPS-N when working in synergy with space-based facilities.

Note

This chapter reports the work published in Lacedelli et al. (2022). This project was carried out in collaboration between the *CHEOPS* GTO Consortium, which I am a collaborator of, and the HARPS-N GTO Consortium, with contributions from the *TESS* Collaboration. I personally coordinated the HARPS-N and *CHEOPS* observing campaigns and the planning of the observations, with the support of L. Malavolta, T. G. Wilson, R. Haywood, M. Hooton, and Y. Alibert. I led the data analysis, with the support of T. G. Wilson, L. Malavolta, L. Borsato and A. Mortier. I coordinated the interpretation of the results and the writing of the manuscript. G. Piotto supervised the whole project. T. G. Wilson, A. Bonfanti, S. Salmon, V. Van Grootel, and V. Adibekyan performed the stellar characterization. A. Vanderburg, C. X. Huang, and H. Osborn extracted the light curve from the *TESS* FFIs. A. Collier Cameron performed the SCALPELS analysis of the HARPS-N data. I performed the global photometric and RV analysis, including the alternative determination of the mass of the ultra-short period planet using the floating chunk offset method, and the Bayesian evidence calculation to select the model describing the system architecture. I analyzed and interpreted the activity indexes in order to correctly interpret the new long-period RV signal reported in this chapter. Y. Alibert led the analysis of the internal structures. A. Bonfanti and L. Fossati performed the atmospheric evolution simulations. S. Hoyer performed the telegraphic pixels analysis. D. W. Latham, J. M. Jenkins, S. Seager, and J. N. Winn are architects of the *TESS* mission, whose data were used to identify and analyse the target. M. Fausnaugh and C. Burke are responsible for the development of the *TESS* `tica` algorithm. The other co-authors provided key contributions to the development and maintenance of the HARPS-N project and of the *CHEOPS* mission. All co-authors read and commented the manuscript, and helped with its revision.

Chapter 5

A photodynamical approach to multiplanetary systems

5.1 Introduction

In the two-body problem, the gravitational potential gives rise to closed orbits. In absence of perturbations the trajectory is strictly periodic, with period $P = 2\pi a^{3/2} (GM)^{-1/2}$, where a is the semi-major axis, G is the universal gravitational constant and M is the total mass of the system. Consequently, a single planet on a *Keplerian* orbit should be seen to transit at regular time intervals. However, if there is a second planet (not necessarily transiting) in the same system, it gravitationally perturbs the orbit of the transiting one. As a consequence, a variation in the transit time relative to the unperturbed one is expected (Holman & Murray, 2005). The interactions among three or more bodies due to the mutual gravitational force are the base of the Transit Time Variations (TTVs) technique (Agol et al., 2005; Miralda-Escudè, 2002). The present state-of-the-art demonstrates that the TTVs technique is an excellent method for the discovery and characterisation of multiple planetary systems (Lissauer et al. 2011b, Becker et al. 2015, Gillon et al. 2017, Freudenthal et al. 2019, Leleu et al. 2021b), with now more than 250 known systems showing significant TTVs (Holczer et al., 2016; Kane et al., 2019).

If detectable, TTVs and transit shape variations (e.g. transit duration variations) carry unique and valuable information for the understanding of multiplanetary systems. They can help investigating the system architectures by inferring and constraining the existence of non-transiting planets (i.e. Xie et al. 2014; Zhu et al. 2018), and so allowing for a better comparison with synthetic population synthesis models (see e.g. Alibert et al. 2013, Mordasini 2018, Coleman et al. 2019, Emsenhuber et al. 2021). Moreover, TTVs can be used to constrain the system parameters (Ragozzine & Holman, 2010), and especially the planetary masses (e.g. Nesvorný et al. 2013), which are not available for single-planet systems in absence of a dedicated spectroscopic follow-up. In this case, the derived average densities can put constraints on the planetary internal structures, as for example in the Trappist-1 system (Grimm et al. 2018; Agol et al. 2021). In addition, dynamically active systems can provide constraints on planetary

formation theories, since the current orbital configuration could reflect the orbital evolution processes occurred in the system history (see e.g. Batygin & Morbidelli 2013, Delisle 2017).

When dynamical interactions are present, to exploit simultaneously and consistently all the available information coming from photometric data (and from spectroscopy, if available), a so-called photodynamical modelling is needed (Nesvorný et al. 2014; Almenara et al. 2015; Ragozzine et al. 2021). A photodynamical model describes the light curve (LC) and radial velocity (RV) values at any moment in time, combining photometric and dynamical analysis to simultaneously determine the mass and radius of both the star and planets, accounting for possible TTVs due the gravitational dynamic interactions via an N-body simulation (Almenara et al., 2015). By coupling N-body integration with a model of every transit, the photodynamical approach leads to a much better precision in the inferred transit times and, consequently, also in the transit parameters. Even if computationally expensive, a photodynamical model permits to fully exploit the observations of interacting multiplanetary systems, and it is the only approach that allows for the simultaneous determination of planetary mass and radius, in addition to the system orbital parameters.

In this chapter, we present the initial implementation of our photodynamical code (Section 5.2) and its preliminary vetting tests on the planetary system WASP-47 (Section 5.3). Future optimization and developments planned to be added to the code are presented in Section 5.4. We conclude the chapter by reporting the dynamical analyses of some multiplanetary systems performed using selected modules of the photodynamical code (Section 5.5).

5.2   The photodynamical code

We started developing a photodynamical code for determining stellar and planetary parameters of interacting multiplanetary systems using photometric and spectroscopic observations. The code, totally implemented in Python, is designed to deal with LCs collected with different telescopes, and RV data coming from different spectrographs, accounting for the different precision of each dataset. It selects and analyzes only the portions of LCs spanning the time region $\Delta T = T_0 \pm 1.5\,t_\mathrm{T}$, where T_0 is the central time of transit and t_T is the full transit duration, for every T_0s of each planet. In this way, only the portions of LCs including the transits and the relative out-of-transit region are modelled, so reducing the computational time. Concerning the RV data, the code sorts all the observations by time, flagging each point with a label corresponding to the relative spectrograph, to allow for the subtraction of the instrumental offset and the addition of the stellar jitter for each dataset. Using an initial set of parameters $(M_\star, R_\star, u_1, u_2, M_\mathrm{p}, R_\mathrm{p}, P, e, i, \omega, \mathcal{M}, \Omega)$ defined at a specific reference time (t_epoch), where $M_\star$, $R_\star$ ($M_\mathrm{p}, R_\mathrm{p}$) are the stellar (and planetary) mass and radius, (u_1, u_2) are the quadratic limb-darkening coefficients, P is the period, e the eccentricity, i the inclination, ω the argument of the pericenter, $\mathcal{M}$ the mean anomaly, and Ω the longitude of the node, the code integrates numerically the orbits using the N-body integrator rebound (Rein & Liu, 2012; Rein & Spiegel, 2015), spanning the whole observational baseline. In particular, we adopted the ias15 (**I**ntegrator with **A**daptive **S**tep-size control, **15**th order) integrator of rebound. ias15 is a very high order, non-symplectic integrator which can handle

arbitrary forces (including those who are velocity dependent), and it allows for variable time-steps. To reduce the computational time, if the t_{epoch} is not located at the beginning of the observational baseline (considering both photometric and RV data), the code first integrates the orbits backward, from t_{epoch} until the first observation, then it resets the orbital configuration at t_{epoch} and it integrates forward, until the last observation.

In each LC portion, the code searches for the transits of every planet using the procedure described in Sections 2.1 and 2.2 of Borsato et al. (2014), then it extracts the orbital parameters at T_0 and it creates a transit model using the software `batman` (Kreidberg, 2015), assuming a quadratic limb-darkening law. For each observed RV, the code integrates the orbits of the planets up to the instant of the RV observation, and it computes the RV value as the opposite of the z-component of the barycentric velocity of the star $(-v_{z,\star})$. Then, it adds the instrumental offset γ of the corresponding spectrograph to be fitted as a free parameter.

To find the best-model solution, the code performs a Bayesian analysis using the `emcee` package (Foreman-Mackey et al., 2013b), an affine invariant Markov chain Monte Carlo (MCMC) ensemble sampler. Following Feigelson & Babu (2012), we implemented a Gaussian log-likelihood:

$$\ln \mathscr{L} = -\ln 2\pi \frac{dof}{2} - \frac{\sum \ln \sigma^2}{2} - \frac{\chi^2}{2} \tag{5.1}$$

where dof is the degree of the freedom of the problem , and χ^2 is calculated comparing the simulated transit models and RV values with the observed ones. For each parameter, we implemented broad, physically meaningful default boundaries (see Tab. 5.1), allowing however for the specification of custom boundaries in the input file. Moreover, we allowed for the inclusion of a Gaussian prior distribution for each parameter, which, if specified, contributes to the log-likelihood with the penalty term

$$\ln \mathscr{L}_{\text{p}} = -\frac{1}{2} \frac{(x - \mu)^2}{\sigma^2}, \tag{5.2}$$

where x is the parameter value, and μ, σ^2 are the mean and variance of the Gaussian prior distribution, respectively. Whenever one of the parameters is out of the specified boundaries after the integration, the corresponding log-likelihood is set to $-\infty$, so that the combination of those parameters is rejected. We implemented an additional constraint on the orbital semi-major axis, setting a maximum value of 100 times the semi-major axis of the outer planet. Above this threshold, the body is considered ejected from the system and the combination of parameters is discarded.

To minimize the correlations between the model parameters, we adopted the following parametrizations for the fit:

- We fitted $\rho_\star$ (stellar density) and $M_\star$, instead of fitting directly $R_\star$ and $M_\star$.

- Regarding the stellar limb-darkening coefficients, we employed the parametrization (q_1, q_2) introduced by (Kipping, 2013).

Table 5.1 Default boundaries of the photodynamical code parameters.

Parameter	Boundaries
$M_\star$ ($M_\odot$)	$[0.08, 100.]$
$R_\star$ ($R_\odot$)	$[5 \times 10^{-4}, 1000.]$
u_1	$[0, 1]$
u_2	$[0, 1]$
M_p ($M_\odot$)	$[1 \times 10^{-8}, 0.01]$
R_p ($R_\odot$)	$[1 \times 10^{-5}, 0.6]$
P (d)	$[0.01, 365 \times 10^2]$
e	$[0, 1]$
ω (deg)	$[0, 360]$
$\mathcal{M}$ (deg)	$[0, 360]$
i (deg)	$[0, 180]$
Ω (deg)	$[0, 360]$
σ_{ph}	$[10^{-10}, 0.5]$
σ_{RV} (m s^{-1})	$[10^{-5}, 10^4]$
γ_{RV} (m s^{-1})	$[-10^{-8}, 10^8]$

- For the planetary mass, we fitted $\dfrac{M_i}{M_{i-1}}$, with $i = 1, ..., N$, where N is the number of planets in the system, and M_0 corresponds to the stellar mass. For each planetary radii, we fitted $R_p/R_\star$.

- We explored the planetary periods in logarithmic space, fitting $\log_2(P)$.

- We adopted the $\sqrt{e}\sin\omega$, $\sqrt{e}\cos\omega$ parametrization introduced by Eastman et al. (2013).

- We fitted the combination of parameters $i\sin\Omega$, $i\cos\Omega$. We always kept fixed the longitude of the ascending node of the innermost planet to $180°$. This is equivalent to fitting the difference of longitudes of the ascending nodes. For a spherical star, the model does not depend on the values of the individual Ω of each planet (Almenara et al., 2015).

- Concerning the orbital angles, we decided to fit the mean longitude ℓ, defined as $\ell = \mathcal{M} + \omega + \Omega$.

We also included in the fit a jitter term for each photometric and RV dataset (σ_{ph} and σ_{RV}, respectively) to take into account possible systematics and short-term stellar activity noise.

Finally, we parallelized the code using mpi4py (Dalcín et al. 2005; Dalcín et al. 2008; Dalcin et al. 2011; Dalcin & Fang 2021), a Python package that provides bindings for the *Message Passing Interface* (MPI) standard using any back-end MPI implementation.

5.3 Test case: the WASP-47 system

5.3.1 System overview

WASP-47 is a G9V star located $\sim 260\,\mathrm{pc}$ away from the Solar System. Using WASP-South observations, Hellier et al. (2012) discovered the presence of a transiting hot Jupiter with a period of $\sim 4.16\,\mathrm{d}$ (WASP-47 b), further confirmed with a set of 19 RVs collected with the CORALIE spectrograph (Hellier et al., 2012). Seven years later, between November 2014 and February 2015, the star was observed in Field 3 of the *K2* mission, revealing the presence of two additional transiting planets, an ultra-short period (USP) super-Earth in a 0.78 d orbit (WASP-47 e), and a Neptune-sized planet with an orbital period of $\sim 9\,\mathrm{d}$ (WASP-47 d), whose mass was inferred thanks to a TTV analysis. In fact, planets b and d, being close to a 2:1 mean-motion resonance (MMR), show an anti-correlated TTV signal of the order of some minutes (Becker et al., 2015). Additional long-term monitoring with CORALIE revealed the presence of a fourth companion in a wide orbit ($\sim 600\,\mathrm{d}$), with a minimum mass of $\sim 390\,M_{\oplus}$ (WASP-47 c), using a total of 46 RVs collected over a time-span of 4.5 years (Neveu-VanMalle et al., 2016). Given the peculiarity of the system architecture, including an hot Jupiter with nearby companions (see Figure 5.1), new observations followed. Dai et al. (2015) measured the mass of WASP-47 e using 26 RVs collected with PFS. WASP-47 e's mass was further improved thanks to 46 additional HIRES RVs (Sinukoff et al., 2017), which allowed also for the detection of WASP-47 d's mass. Finally, Vanderburg et al. (2017) presented a dataset of 69 HARPS-N RVs, used to further improve the precision on the radii and masses of all WASP-47 planets with a global re-analysis of the system.

The large number of different photometric and spectroscopic datasets, the presence of two interacting planets, and the in-depth knowledge of the system, analyzed under various perspectives by many different authors (Sanchis-Ojeda et al. 2015, Almenara et al. 2016, Batygin et al. 2016, Huang et al. 2016, Weiss et al. 2017, Becker & Adams 2017, Dai et al. 2019) make the WASP-47 system an optimal benchmark target to test our photodynamical code.

5.3.2 Testing the photodynamical code

We performed a preliminar photodynamical fit of the WASP-47 system including the *K2* photometry and six sets of RVs, including CORALIE, PFS, HIRES and HARPS-N data. We treated the CORALIE observations as three independent datasets, with different zero-point offsets. We refer to the CORALIE measurements presented by Hellier et al. (2012) as the CORALIE12 dataset, to those presented by Neveu-VanMalle et al. (2016) and performed before the spectrograph upgrade in 2014 as CORALIE16, and to those presented in the same study but performed after the spectrograph upgrade as CORALIE16a.

We assumed as initial guess for the planetary parameters the most updated values reported in Vanderburg et al. 2017, and we imposed the gaussian priors on the stellar mass and radius coming from Vanderburg et al. 2017 spectroscopic analysis. We chose as reference time for the orbital elements $t_{\mathrm{epoch}} = 2456979.5\,\mathrm{BJD_{TDB}}$ (immediately before the first *K2* transit), initializing the N-body integrator with the positions and velocities of the system bodies at t_{epoch}. We report here the results of an initial

113
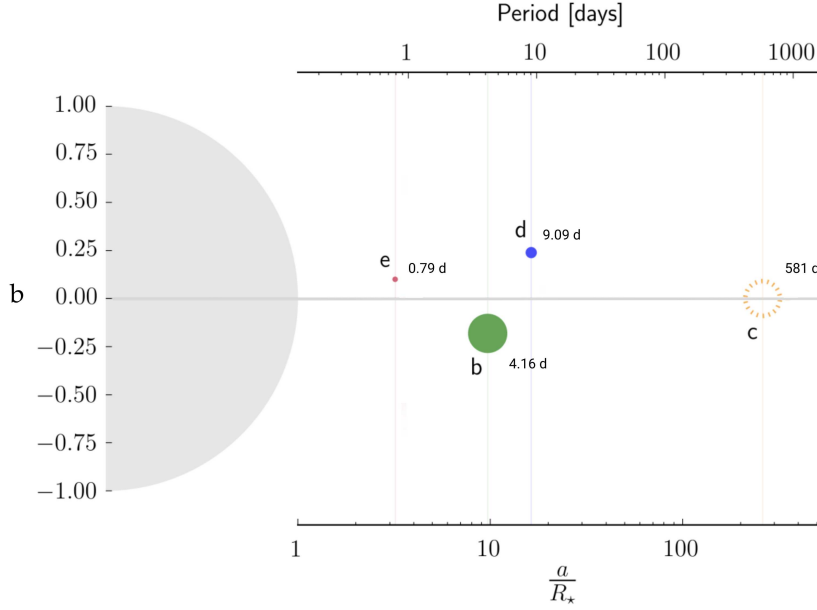
Figure 5.1 Schematic view of the WASP-47 system. Planet sizes are on scale, and the vertical position reflects the impact parameter, *b*, of each planet, except for WASP-47 c, which is not known to transit and whose radius is unknown. Adapted from Almenara et al. (2016).
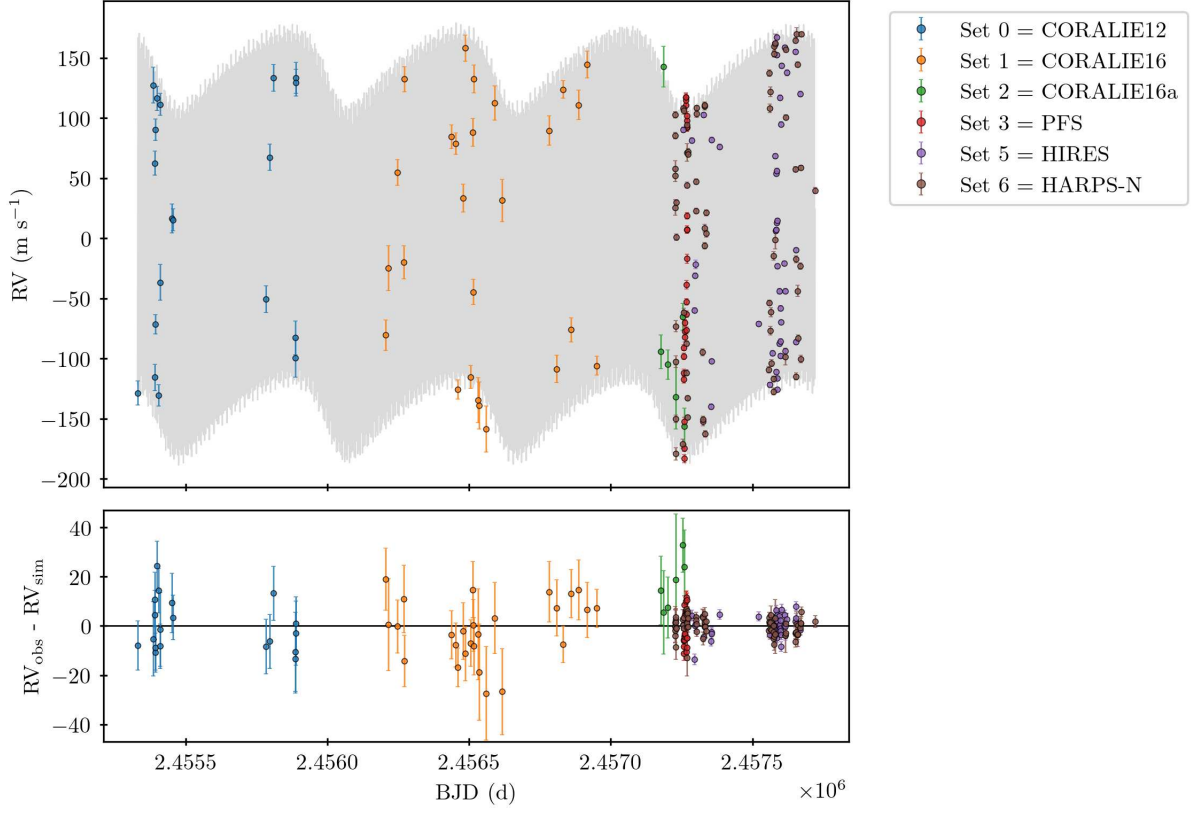
test performed running 100 walkers for 25000 steps, discarding the first 10000 steps as burn-in[1]. We list in Table 5.2 the best-fitting planetary parameters, assumed as the ones that maximize the likelihood (MLE), and we show in Figure 5.2 the global RV modelling. All parameters are consistent with literature values within errorbars, even though a fit with longer chains is needed to obtain more reliable uncertainties. To better show the effects of the photodynamical modelling, we report in Figures 5.3 and 5.4 the initial-guess and the best-fitting light curve models, respectively. As can be seen by comparing the two figures, the use of a model with linear ephemeris is insufficient to account for the system TTVs, while when dynamical interactions are taken into account by the photodynamical code, each transit is well-modelled even in presence of TTVs.

5.4 Future developments and optimization of the code

Given the assessment of the basic code functionality thanks to the preliminary test on the WASP-47 system, we plan now to proceed with further developments and optimization of the code. In particular, we will work on reducing the computational time by optimising the code structure. Moreover, we will implement an easy-to-use input interface, i.e. using YAML (YAML Ain't Markup Language) for input files configuration, and provide automatic, but easy to personalize, scripts for visualizing and plotting the results. We plan on implementing different prior distributions (i.e. truncated Gaussians, Jeffreys) to allow the user to choose the most appropriate ones. We also plan on implementing an algorithm for the

---

[1]We note that longer chains are needed to ensure the convergence of all the parameters. However, given the very long computational time, we decided to initially test the code behaviour on a short run.

Figure 5.2 RV best-fitting model (grey line) of the six datasets included in the photodynamical analysis. Residuals are shown in the bottom panel.

Table 5.2 Preliminary planetary parameters of the WASP-47 system at $t_{\text{epoch}} = 2456979.5\,\text{BJD}_{\text{TDB}}$ from the initial photodynamical fit.

	WASP-47 e	WASP-47 b	WASP-47 d	WASP-47 c
M_{p} $(M_{\oplus})$	10.0 ± 1.0	357^{+9}_{-11}	13.6 ± 1.1	412 ± 20
R_{p} $(R_{\oplus})$	$1.78^{+0.03}_{-0.04}$	12.5 ± 0.2	$3.55^{+0.07}_{-0.05}$	-
P (d)	$0.789616^{+0.000018}_{-0.000013}$	$4.15849^{+0.00001}_{-0.00003}$	$9.096192^{+0.001}_{-0.0015}$	588 ± 3
e	$0.022^{+0.012}_{-0.019}$	$0.003^{+0.0012}_{-0.0008}$	$0.004^{+0.005}_{-0.001}$	0.31 ± 0.02
ω (deg)	96^{+53}_{-54}	30^{+18}_{-14}	25^{+16}_{-25}	124 ± 6
$\mathcal{M}$ (deg)	233^{+54}_{-44}	119^{+14}_{-18}	73^{+25}_{-16}	220 ± 5
i (deg)	92 ± 2	89.0 ± 0.3	$90.81^{+0.16}_{-0.12}$	83^{+12}_{-10}
Ω (deg)	180 (fixed)	179^{+6}_{-1}	179 ± 4	173^{+23}_{-17}
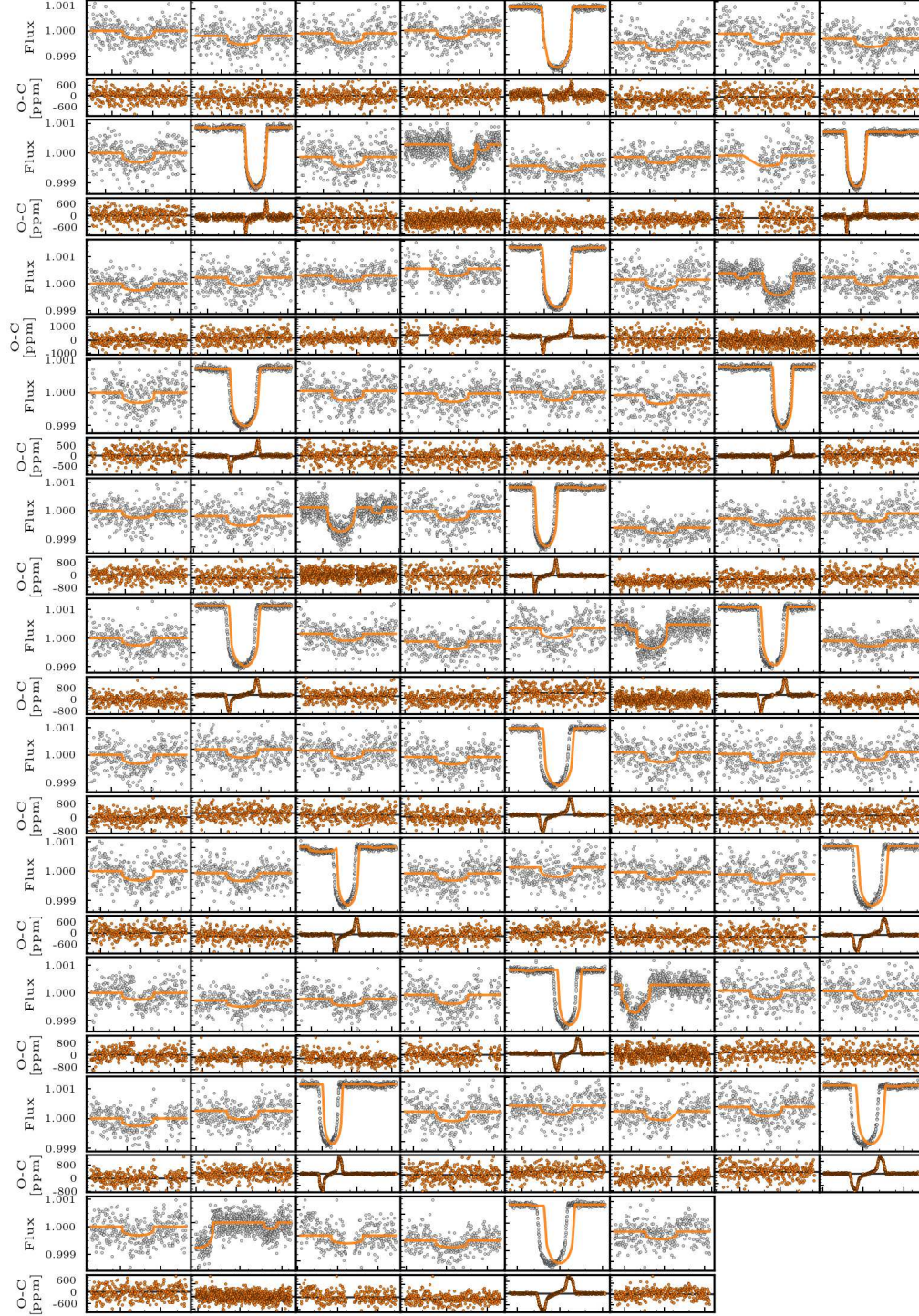
Figure 5.3 Light curve portions of *K2* photometry considered in this analysis for the WASP-47 system, with over-imposed the initial-guess model. Residuals for each light curve portion are shown in the bottom plots. The use of a model based on linear ephemeris is insufficient to account for the system TTVs, as can be clearly seen from the residuals of the hot Jupyter's transits.
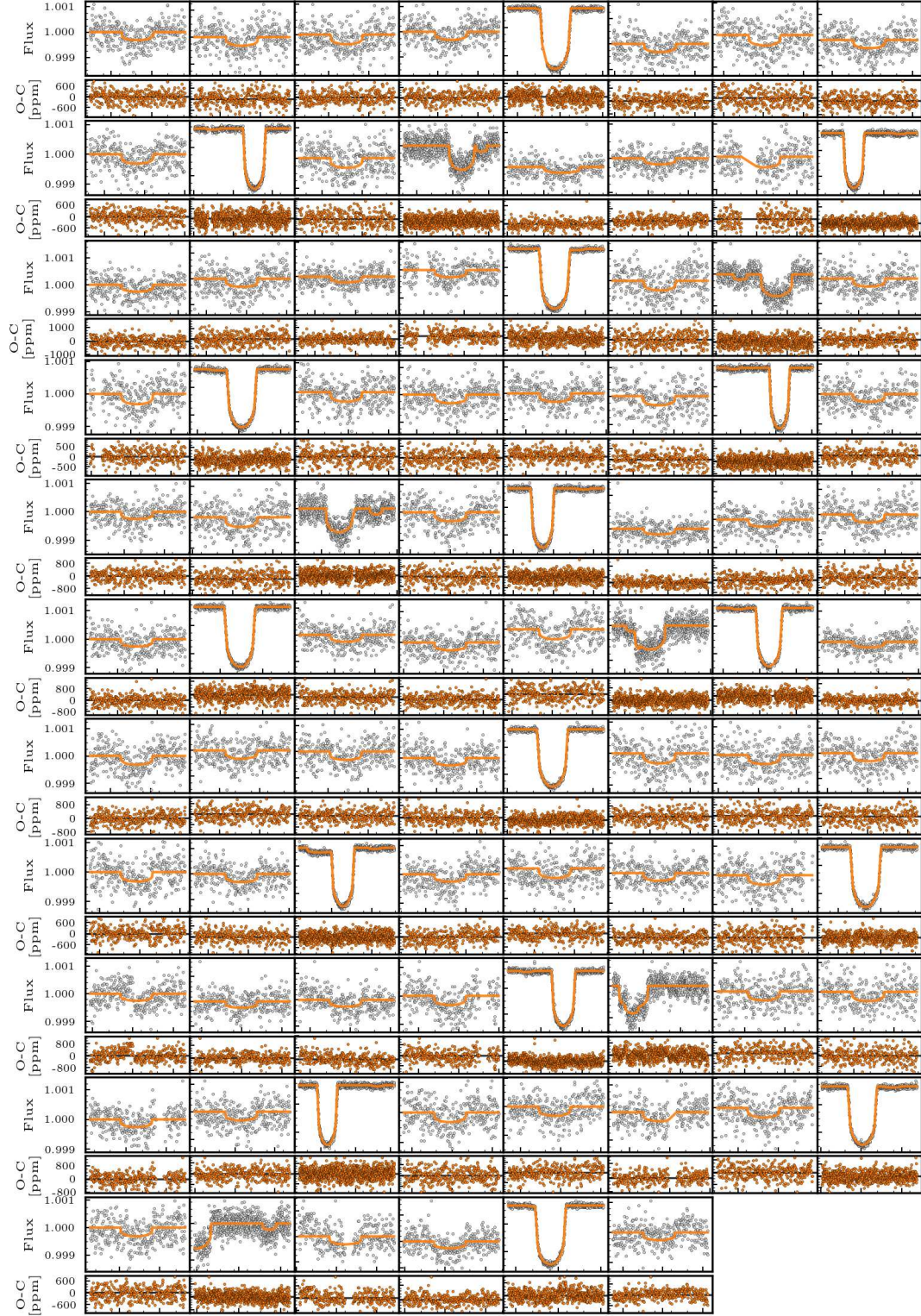
Figure 5.4 Same as Figure 5.3, but with over-imposed the best-fitting photodynamical model. When dynamical interactions are taken into account, transits are well-modelled even in presence of TTVs.

global optimization of the parameters before the start of the Bayesian analysis, i.e. using the differential evolution code PyDE[2]. Regarding the Bayesian analysis, we will test different inference algorithms in addition to the affine invariant MCMC ensamble sampling, such as nested sampling, i.e. with the dynesty (Skilling, 2004; Skilling, 2006; Speagle, 2020) and UltraNest (Buchner, 2014, 2017, 2021) packages.

Once completed, optimized, and more extensively tested, we will publicly release our photodynamical code, which will be an important tool for the understanding and characterisation of known (Holczer et al., 2016) and newly-detected multiplanetary systems showing TTVs, especially in the current context of *TESS* and *CHEOPS* discoveries, and in prospects of future exoplanetary facilities, in particular long-staring missions like *PLATO*.

5.5   Byproduct analyses: dynamical investigations

We used part of the functionalities of the photodynamical code to perform dynamical investigations on some multiplanetary system, as described in the following sections.

5.5.1   TOI-836

TOI-836 (HIP 73427) is a K5V star of $V = 9.92$ mag observed by *TESS* in sectors 11 and 38. The *TESS* Quick Look Pipeline (QLP, Huang et al. 2020) identified the presence of two planetary candidate at periods of 3.817 d (TOI-836.02) and 8.595 d (TOI-836.01), with radii of 1.69 $R_{\oplus}$ and 2.64 $R_{\oplus}$, respectively[3].

In the context of the *CHEOPS* 2020 follow-up campaign of TOI-836, an initial fit of the available *TESS*, NGTS, MEarth, and *CHEOPS* transits suggested the presence of a significant TTV signal on the external planet of the order of ~ 7 min. To investigate the presence of possible dynamical interactions among the detected planets, we performed a dynamical N-body simulation using the integration module of the photodynamical code. We first computed the planetary masses assuming the probabilistic mass-radius relation of Wolfgang et al. (2016)[4]. We then integrated the orbits over a time-span of 10 yr assuming as reference time $t_{\text{epoch}} = 2458797.4461$ BJD$_{\text{TDB}}$, we extracted the simulated transit times (see Section 5.2 for more details), and we performed a comparison with a linear ephemeris to obtain a synthetic O−C diagram and identify possible TTV signals. We performed multiple simulations varying the initial planetary configuration, in particular testing different values of eccentricities and arguments of pericenter, while keeping fixed (1) the longitudes of the ascending nodes, at 180°, and (2) the planetary inclinations, as derived from the transit fit. Figure 5.5 shows the results of some representatives simulations. We found that a non-zero eccentricity for one of the two planets is required to explain a 7-min TTV signal, with a TTV super-period that could be consistent with the variation observed in the photometric data.

---

[2]https://github.com/hpparvi/PyDE
[3]https://exofop.ipac.caltech.edu/tess/target.php?id=440887364.
[4]https://github.com/dawolfgang/MRrelation.

All the configurations presented in Figure 5.5 are dynamically stable, according to the stability analysis that we performed using the Mean Exponential Growth factor of Nearby Orbits (MEGNO) indicator (Cincotta & Simó, 2000), as implemented in `rebound` (Rein & Tamayo, 2016). However, our analysis showed that if both planets have eccentric orbits, the system is unstable already on a time-scale of 500 yr. We also found that for a given stable configuration, the argument of pericenter can play an important role in shaping the behaviour of the TTV profile. For example, if the difference $\Delta\omega$ among the two arguments of pericenters is larger than 30°, the TTV signal can be boosted up to 20 min or even more, and the TTV super-period can increase up to more than 2020 days. We concluded that there are some plausible, stable planetary configurations that could reproduce the suggested TTV signal, but more observations are necessary to constraint the TTV period and amplitude, and so to derive the actual planetary parameters.

Finally, we investigated the possibility of the TTV signal of TOI-836.01 to be induced by an external planetary companion, still not detected using the available dataset. Following the procedure described in Borsato et al. (2021), we simulated a grid of 30 values of masses, ranging from 1 to 30 $M_{\oplus}$, and 30 values of periods for an external perturber. The period grid ranges from 8.5 days, period of TOI-836.01, to 30 days, since planets with longer periods are likely too far to interact significantly. We integrated the orbits of the 3-planet system for 10 yr, and we computed the distribution of possible TTV amplitudes for planet .01 over the mass-period grid. As Figure 5.6 shows, there are two possible configurations that could reproduce a TTV signal of the order of 7 min or more:

1. The external perturber has a period around $11 - 12$ days. This would imply the closeness to a 3:2 mean-motion resonance (MMR) with TOI-836.01. Given the 27-d coverage of the *TESS* sectors (with the 1-d download gap occurring between the two orbits of ~ 13 days each that together form a sector), this would imply a non-transiting planet.

2. The external perturber has a period around 17 days, implying the closeness to a 2:1 MMR with TOI-836.01. In this case, in addition to the non-transiting planet option, another possibility is that the transit of this eventual companion was not observed as it occurred during the *TESS* download gap (see the case of TOI-561 d, Chapter 4.4.1), being the period longer than a single *TESS* orbit.

Also in this case, more observations are needed to confirm/exclude the presence of an eventual external perturber, and to constrain its properties.

5.5.2 Kepler-37

Kepler-37 (KOI-245) is a G8V star of $V = 9.77$ mag, located ~ 64 pc away from the Sun. The star hosts three transiting planets, with periods of 13.4 d (Kepler-37 b), 21.3 d (Kepler-37 c), and 39.8 d (Kepler-37 d), and radii of 0.28, 0.72, and 1.92 $R_{\oplus}$, respectively (Barclay et al., 2013). With such a low radius, being only slightly bigger than the Moon, Kepler-37 b is the smallest exoplanet known to date.

In the context of pushing towards the detection of very small RV signals ($K < 2$ m s^{-1}) by disentangling planetary features and stellar intrintsic variability, Rajpaul et al. (2021) presented a study of the

Kepler-37 system reporting the detection of Kepler-37 d's mass ($M_p = 5.4 \pm 1.4\ M_\oplus$) using 110 high-precision HARPS-N RVs. Kepler-37 d's semi-amplitude of 1.22 ± 0.31 m s^{-1} is among the smallest detected RV signal of any transiting planet, together with the one of TOI-178 b ($K = 1.05^{+0.25}_{-0.30}$ m s^{-1}, Leleu et al. 2021a). Given their extremely small size, both planet b and c's expected semi-amplitudes lie far below the threshold of current detectability (Rajpaul et al., 2021).

While studying the system architecture, Rajpaul et al. (2021) also investigated the presence of an additional planetary candidate with a period of ~ 51.2 d (KOI-245.04, or Kepler-37 e[5]). As Rajpaul et al. (2021) report in Section 2.2.2, the presence of this candidate was first noted in Barclay et al. (2013), but at that time the authors commented that they ''did not trust that KOI-245.04 is a valid planet candidate'', as the SNR of the putative transit signal decreased with the inclusion of additional data released after the initial detection by the *Kepler* team, suggesting that it was likely caused by random noise, or by correlated stellar or instrumental noise. In the same year, Mazeh et al. (2013) published a catalogue of TTVs measurements from observations of the first twelve *Kepler* quarters. The catalogue included both the transit times of Kepler-37 d and those of the KOI-245.04 candidate (Kepler-37 e from that time on), whose planetary nature was however not confirmed at that time. Subsequently, based on the ephemeris reported in Mazeh et al. (2013) catalogue, Hadden & Lithwick (2014) analysed the TTVs of 139 sub-Jovian planets to extract their densities and eccentricities. In the Hadden & Lithwick (2014) study, the apparent TTVs of Kepler-37 e were used to put constraints on the mass of Kepler-37 d, presupposing that Kepler-37 e was a real planet (which was however not established yet). Note that, vice-versa, no constraints on the mass of the putative planet Kepler-37 e could be inferred from the timing analysis of Kepler-37 d. Later studies suggested that no significant TTVs are present in the Kepler-37 system (Holczer et al. 2016, Gajdoš et al. 2019), and further planet-searching pipelines failed to identify the Kepler-37 e signal (Huang & Bakos 2014, Kunimoto & Matthews 2020). Given the lack of literature consensus, and the absence of a universally accepted confirmation, Rajpaul et al. (2021) presented an investigation on the presence of the putative planet Kepler-37 e, both through the modelling of the HARPS-N dataset and with a re-analysis of Kepler-37 d's TTVs, that I performed. I personally carried out the dynamical analysis, using some modules of the photodynamical code, presented in Section 6.4 of Rajpaul et al. (2021), which I report here.

From Section 6.4 of Rajpaul et al. (2021):

The periods of Kepler-37 d and e are close to a 4:3 commensurability, hinting at a first-order mean motion resonance, which may suggest the presence of a detectable TTV signal induced on planet d due to strong dynamical interactions between the two planets. Consequently, by studying the TTV signal of Kepler-37 d, we can infer some information on the hypothetical perturbing planet, i.e. Kepler-37 e. According to Mazeh et al. (2013), whose transit times were used in the analysis by Hadden & Lithwick (2014), Kepler-37 d has a shallow TTV signal with an amplitude of order 1 min, as reported in the

---

[5]At the time of the writing, this candidate was reported as a confirmed planet with the name of Kepler-37 e in the NASA Exoplanet Archive (https://exoplanetarchive.ipac.caltech.edu/), in the Open Exoplanet Catalog (www.openexoplanetcatalogue.com), and in SIMBAD (Wenger et al., 2000).

$O - C$ diagram in Figure 5.7. We numerically integrated the orbits of Kepler-37 b, c, d and e using the N-body integrator `ias15` within the `rebound` package (Rein & Liu, 2012), assuming as reference time the transit mid-point time ($T_{0,d}$) of Kepler-37 d. As initial configuration, we assumed the planetary parameters in Table 2[6], except for the mass and eccentricity of Kepler-37 d, for which we used our inferred values. For planet e, since Hadden & Lithwick (2014) only report the planetary period, we used the mid-transit time as originally reported by Batalha et al. (2013), $T_0 = 2455028.727 \pm 0.0096$ $\mathrm{BJD_{TDB}}$, and we derived the radius from the planet-to-star radius ratio given by Batalha et al. (2013): $R_e/R_\star = 0.0054 \pm 0.0002$, $R_e = 0.43 \pm 0.03 \, R_\oplus$. We estimated the masses of planets b, c, and e using the Wolfgang et al. (2016) probabilistic mass-radius relation: $M_b = 0.01 \, M_\oplus$, $M_c = 0.6 \, M_\oplus$, $M_e = 0.06 \, M_\oplus$. During the integration, we computed the synthetic transit times (O) of each planet following the procedure described in Borsato et al. (2019), and compared the inferred transit times with the linear ephemeris (C) of Mazeh et al. (2013), obtaining the synthetic $O - C$ diagram to identify a possible TTV signal.

Despite the low expected mass of the putative planet e, the predicted TTV signal induced on Kepler-37 d has a high amplitude, due to the suggested resonant configuration of the planets and to the eccentricity of planet d. Figure 5.7 shows that neither the amplitude nor the period of such TTV signal corresponds to the observed TTVs.

It is worth noting that the TTV prediction is highly dependent on the planetary parameters, and in particular, even small changes in the eccentricity of Kepler-37 d imply a variation of TTV amplitude from 0 to more than 160 minutes. However, our simulations predict that in order to obtain a TTV amplitude of order of the observed one, the eccentricity of Kepler-37 d would need to be negligible ($e_d \leq 0.01$), whereas our RV modelling points towards a non-trivial eccentricity.

We also computed the same forward modelling assuming a 3-planet system, i.e. without the presence of Kepler-37 e. In this case, the amplitude of the predicted TTV signal of Kepler-37 d was of order 0.2 minutes, that is, lower than the average error on the transit times of Mazeh et al. (2013), indicating that the two inner planets do not significantly perturb the orbit of planet d.

In summary, our TTV analysis disfavours the presence of the putative planet Kepler-37 e. Considering the dubious way in which Kepler-37 e became a ''confirmed'' planet in the first place, the fact that our RV analysis did not lead to the detection of a signal with ~ 51 d period, the prominence of the ~ 51 d periodicity in two activity indicators, and the additional doubts introduced by our TTV forward modelling, we suggest that Kepler-37 e should be stripped of its status of a ''confirmed'' planet.

We do not exclude the possibility of a non-transiting planet inducing the small observed TTV signal of Kepler-37 d, which cannot be totally accounted for by a 3-planet system, but the properties of such a non-transiting planet would not seem to correspond to those of Kepler-37 e as reported in the literature.

---

[6]Here, we refer to Table 2 in Rajpaul et al. (2021).

(a) $e_{.01} = e_{.02} = 0$

(b) $e_{.01} = 0.1 \; ; \; e_{.02} = 0$

(c) $e_{.01} = 0 \; ; \; e_{.02} = 0.1$
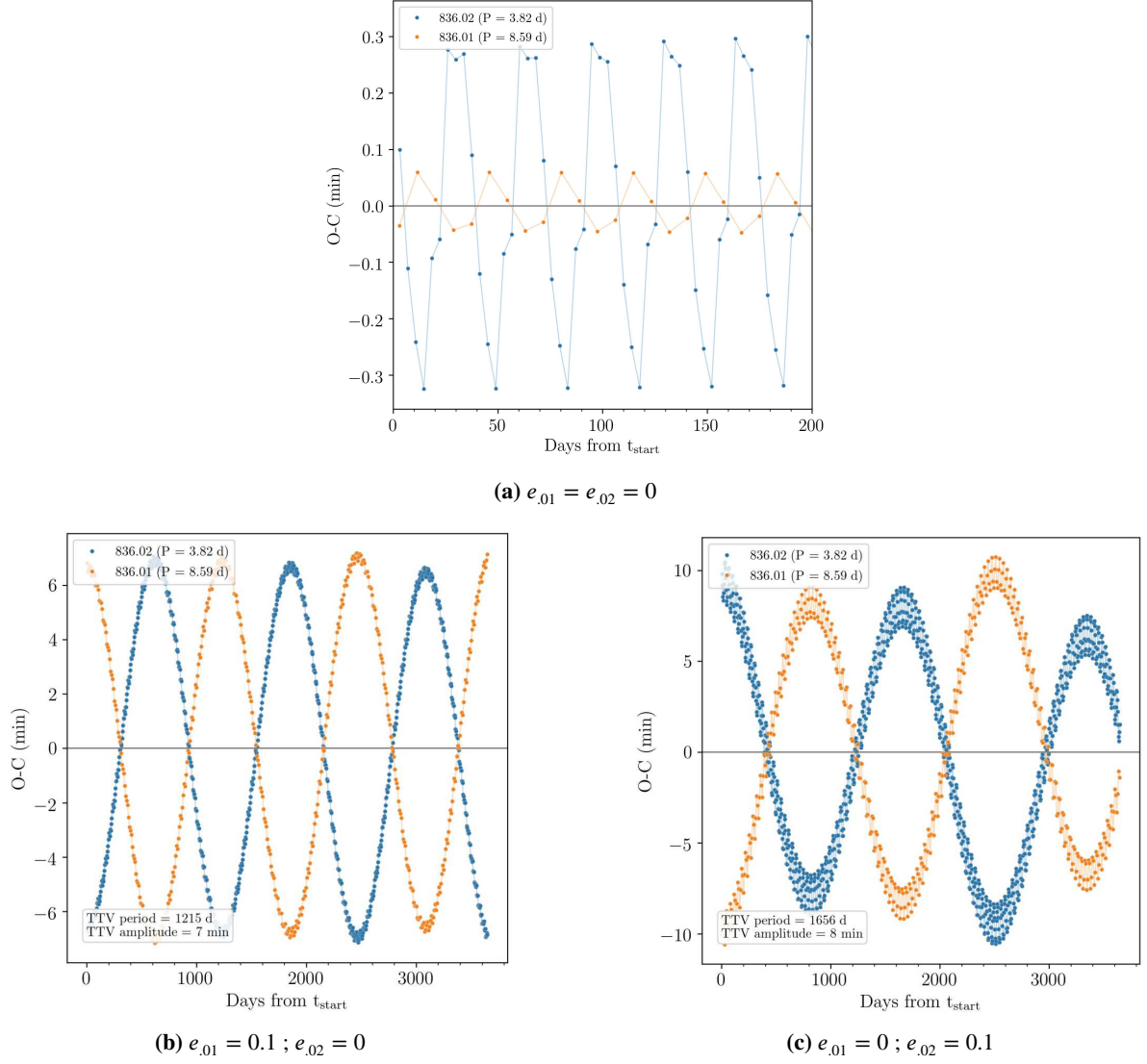
Figure 5.5 $O - C$ diagram of the TOI-836 planets at varying eccentricities. In panel a) the temporal baseline is zoomed in the range $0 - 200$ d for better visualization.
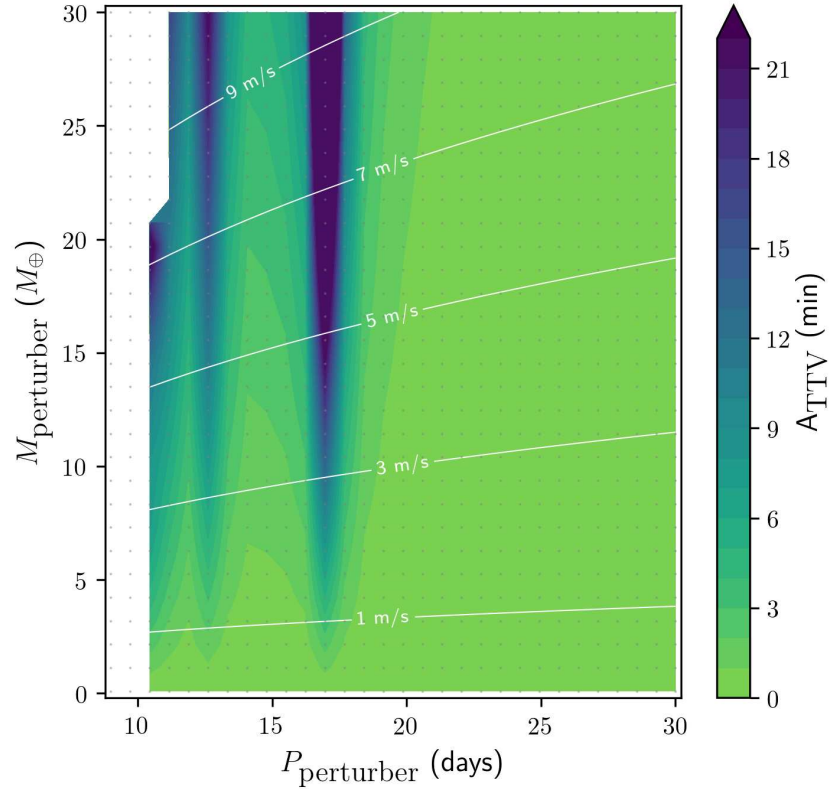
Figure 5.6 TTV amplitude (A_{TTV}) map for TOI-836.01 from the 900 numerical integrations of a possible external perturber with 30 linear values of mass and period. The grey dots indicate the mass-period combinations used for each simulation. The white lines represent the expected RV semi-amplitude (K_{RV}) of the perturber for each configuration.
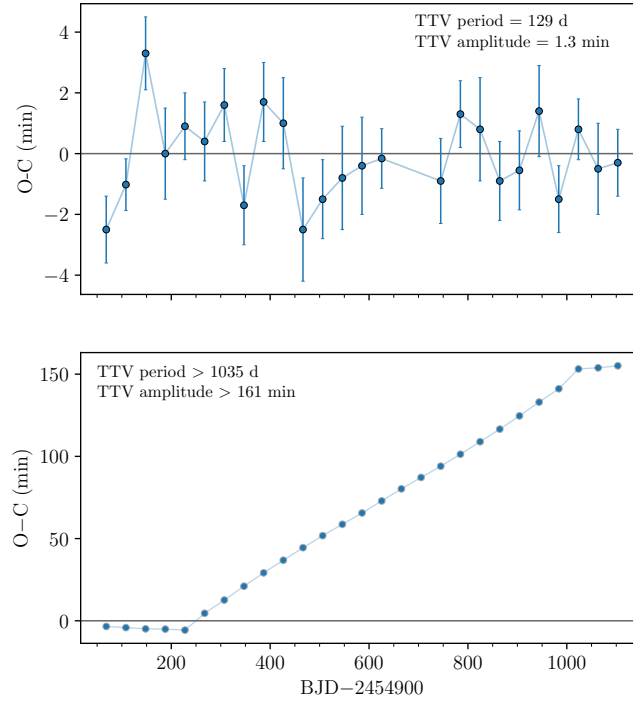
Figure 5.7 *Top*: measured TTV signal of Kepler-37 d according to the transit times reported in Mazeh et al. (2013). The TTV period and amplitude are computed via the GLS periodogram (Zechmeister & Kürster, 2009). *Bottom*: predicted TTV signal of Kepler-37 d according to our numerical simulation, assuming the presence of a planet with ~ 51 d period. The simulation suggests a TTV period longer than the observed baseline, and amplitude ≳ 160 min. From Rajpaul et al. (2021).

Chapter 6

Conclusions and future perspectives

6.1   The TOI-561 system

In this thesis we present the discovery and characterization of the four-planet system orbiting the late G dwarf TOI-561 using state-of-the-art instruments such as the HARPS-N spectrograph and the *TESS* and *CHEOPS* space telescopes.

We characterized TOI-561 as an old ($\sim$ 10 Gyr), metal-poor ([Fe/H] $= -0.40$ dex), alpha-enhanced ([α/Fe] $= 0.23$) star, slightly smaller and cooler than the Sun. TOI-561 is one of the few thick-disk stars hosting a multiplanetary system, and it is therefore a valuable addition for future studies focused on the investigation of the planetary properties across different Galactic populations.

The investigation of TOI-561's system architecture proved to be not trivial. From the initial configurations with three transiting candidates suggested by the *TESS* detection, we ended up discovering a 4-planet system, with a USP super-Earth (TOI-561 b), a $\sim$ 10.8 d period gaseous mini-Neptune (TOI-561 c), and two additional external mini-Neptunes with periods of $\sim$ 25.7 d and $\sim$ 77 d (TOI-561 d, e). We could not confirm the third planet candidate with $\sim$ 16 d period originally proposed by *TESS*. We could not identify the signal in our RV dataset, and we proved that the duration of the two transits associated with this candidate were significantly different. Moreover, the presence of such a candidate would have led the system to dynamical instability.

Our extensive analysis greatly benefited from the inclusion of datasets coming from different instruments. The high-resolution HARPS-N RVs played an essential role not only in providing precise mass measurements, but also in unveiling the system architecture. In fact, our first-season RV analysis immediately pointed out the presence of the two external planets, with periods not matching the ones suggested by *TESS*. Combining the two datasets we were eventually able to identify a single transit of each planet in the *TESS* light curve. Those transits were initially associated with the third *TESS* candidate ($\sim$ 16 d period), whose presence we ruled out. A significant obstacle that affected our investigation was the short photometric baseline. With only one *TESS* sector available at the time (lasting $\sim$ 27 d), the initial *TESS* detection of the planetary candidates (except for the USP planet) was based on just two transits identified by the SPOC automatic pipeline. Our work showed that in such cases caution should

be taken, and that inclusion of different datasets and evaluation of alternative scenarios can be decisive for an accurate validation process. The importance of a long, continuous observational baseline was further stressed by the arrival of a new *TESS* sector two years later than the first observations. Despite the undeniable usefulness of new, high-precision photometric data from space, also in this case the short observational baseline, further hampered by the presence of unavoidable data gaps, did not allow us to definitively solve the ambiguity on the long-period planets. However, we could take full advantage of the *CHEOPS* satellite in complementing *TESS* observations and in characterizing *TESS*-discovered exoplanets prominently emerged. The pointing flexibility and the possibility of scheduling specific observing windows for targets of interest sum up to the ultra-high precision capabilities of the instrument, making *CHEOPS* a fundamental resource in the current context of exoplanetary characterization. It was in fact thanks to the *CHEOPS*'s observation of a second transit of TOI-561 d, previously showing only a single transit in the *TESS* light curve, that we refining the ephemeris and definitely confirmed TOI-561's planetary architecture. Moreover, the precise radii of the three inner planets inferred from *CHEOPS* photometry, combined with precise mass measurements coming from the combined HARPS-N and HIRES datasets, allowed us to investigate the internal structure of the planets, and to model their atmospheric evolution.

From our discovery and characterization work on the TOI-561 system, the emerging key word is *synergy*. As mentioned before, the synergy between *TESS* and HARPS-N was essential to initially build the 4-planet scenario. Later on, the second season of HARPS-N RVs was decisive to confirm the planetary periods and improve the ephemeris of the long-period planets, a crucial step for the scheduling of *CHEOPS* observations, needed in turn to definitely confirm the planetary architecture and to improve the planetary parameters. The synergic work among *TESS*, HARPS-N and *CHEOPS* produced results which could have not been obtained from the exploiting of a single instrument dataset alone, even though all of these facilities are state-of-the-art instruments.

New insights on the TOI-561 system will also come from additional *TESS*, HARPS-N and *CHEOPS* data to be collected in the current and future months/years. Short-cadence *TESS* light curves of two new consecutive sectors will be released in the first months of 2022. Very recently, the analysis of the *TESS* early data release of these sectors allowed us to confirm the transit of the long-period planet TOI-561 e, and consequently to schedule new *CHEOPS* observations in the coming months, both to confirm the planetary period and to improve the radius measurement, as already done with the other three planets in the system. Given the long period of the planet ($\sim$ 77 d), TOI-561 e could also be a possible target of interest for the study of moons and rings, within a dedicated program carried out by the *CHEOPS* GTO Consortium. Moreover, an intensive *CHEOPS* monitoring campaign specifically targeting TOI-561 b has already started, and it will continue during the next observing season, with the aim of studying in-depth the composition and properties of such a unique USP super-Earth. Finally, a HARPS-N long-term monitoring campaign of TOI-561 recently started, and it will possibly continue also in the next years. The reason of the long-term monitoring is the investigation of the long-period signal at $\sim$ 470 d identified in our latest RV analysis. With the current dataset, we cannot disentangle the planetary or stellar nature of the signal, and an extended RV observational baseline will be of great help. The interest

in unveiling the nature of this signal is also enforced by the fact that, if proved to be of planetary origin, such a planet would orbit in the habitable zone of the host star, and it would have a non-zero probability of transiting.

In summary, TOI-561 is a new multiplanetary systems with numerous interesting properties, both from a stellar (a thick-disk, metal-poor star) and planetary point of view (a low density USP super-Earth, a long-period planet in the cold sub-Neptunes regime, a possible external planet in the habitable zone), and it sums up to the sample of well-characterized multiplanetary systems.

6.2 The photodynamical code

The second project presented in this thesis is the development of a new photodynamical code. With regards to interacting multiplanetary systems showing TTVs, the photodynamical approach is the most rigorous and informative one, coupling photometric analysis with N-body integration to derive the planetary and stellar properties in the most consistent way.

We implemented our code fully in `Python`, using the `batman` package for the transit modelling, the numerical integrator `rebound` for the N-body integration, and deriving the posterior distribution of the parameters with a Bayesian analysis using the `emcee` package. It is built to handle photometric and spectroscopic datasets coming from different instruments. Our code is still in its refinement and optimization stage, but we already obtained some promising results on the initial testing on the well-known multiplanetary system WASP-47. We plan on optimizing the code, already parallelized with OpenMPI, and on implementing other functionalities (see Section 5.4), before performing more extensive tests on WASP-47, and eventually running the code on a second well-known system showing significant TTVs, Kepler-89 (KOI-94; Hirano et al. 2012, Albrecht et al. 2013, Masuda et al. 2013, Weiss et al. 2013). We plan on making the code publicly available as soon as it will be completed and optimized, with the purpose of providing a complete tool for the analysis of the increasing number of interacting systems showing TTVs. We foreseen the code to be particularly useful for the characterization of new multiplanetary systems expected to be discovered with *PLATO*. With the predicted long-staring fields (Nascimbeni et al., 2021), *PLATO*'s targets will have a long, continuous observational baseline particularly suited for TTV analysis, like the *Kepler*-discovered systems, with the further advantage of orbiting bright stars and so being suited for spectroscopic follow-up.

In addition, exploiting its modularity, we also used some partial code functionalities to perform new dynamical investigations of other multiplanetary systems, in particular TOI-836 and Kepler-37 (Rajpaul et al., 2021), proving various ancillary potentialities of the code.

In the context of dynamical analyses, we are also currently involved also in the global re-analysis of the Kepler-10 system, carried out within the HARPS-N GTO Consortium following the HARPS-N monitoring accomplished in the last few years. We performed a dynamical investigation of the system including all the available data and exploiting the information from Kepler-10 c's TTVs to investigate the presence of a possible additional planet (Bonomo at al., *in prep*), and more detailed analyses are still ongoing.

127

6.3 Future perspectives

The discovery of the TOI-561 system falls within the picture of the unexpected exoplanet diversity that started to emerge since the discovery of 51 Peg b. Peculiarities with respect to the Solar System are evident. The TOI-561 planets are all orbiting within the orbit of Mercury ($P \sim 88$ d), the innermost planet of the Solar System. None of them resembles a planet of the Solar System, and, on contrary, they can be categorized as members of two categories of planets not present in the Solar System, namely mini-Neptunes and super-Earths. The category of super-Earths is the focus of an increasing interest in the exoplanet community, both from the point of view of formation mechanisms (how do they actually form, and why are they not present in the Solar System? How common are actually they?), and from an atmospheric/habitability perspective. Super-Earths are likely to retain a wide range of atmospheres, from thick envelope dominated by H/He, to atmospheres with a moderate abundance of hydrogen due to escape and/or molecular hydrogen outgassing (Miller-Ricci et al., 2009), to thin atmospheres resembling the one of Earth, with the presence of heavier molecules. In perspective of the detection and character-ization of Earth twins, not feasible with current facilities, the study of super-Earths atmospheres could give us insights on some of the most fascinating questions the human kind has always wondered about: are we alone in the universe, or is life present on other planets? How could we spot ''life fingerprints'' when observing an exoplanet? Encouraging results are coming from the investigation of super-Earths atmospheres, with the first detection of water vapor in the atmosphere of K2-18 b (Benneke et al. 2019, Tsiaras et al. 2019), and the improvements expected from *JWST*'s observations are substantial.

Another peculiarity about the TOI-561 system is the presence of an ultra-short period (USP) planet, that is, a planet with $R < 2 \ R_{\oplus}$ and $P < 1$ d. The study of the USP planets population is currently of great interest to probe the composition of terrestrial planets. While a true Earth analog has an expected RV semi-amplitude of ~ 10 cm s^{-1}, USP planets have typical signals of the order of few m s^{-1}, making their detection and mass measurements feasible with current instrumentation. Their short orbital periods make it also easier to disentangle the planetary signal from stellar activity (i.e. with the floating chunk offset method; Hatzes 2014). Moreover, USP planets are so strongly irradiated that any primordial H/He envelope has probably been eroded, enabling the direct constrain of the composition of the rocky cores without incurring in the high level of degeneracy caused by the presence of thick gaseous envelopes. Finally, given their high temperatures, USP planets are suitable targets for phase curve variation and secondary eclipse studies. The resultant albedo, phase offset and day-night temperature contrast can directly probe the surface composition (Demory et al. 2016; Kreidberg et al. 2019). In this field, *JWST* will provide unprecedented accurate observations, allowing for the investigation of even sub-Earth size planets (e.g. GJ 376 b; Cycle I *JWST* GO proposal n.° 2508, PI: M. Zhang) and shading light on the processes occurring on such extreme worlds (e.g. day-night heat re-circulation efficiency, presence of clouds, presence of a metal-rich primary crust versus presence of an Earth-like granitoid tertiary crust created by plate tectonics). And we just started scratching the surface of the USP planets misteries. For example, among the currently known USP planets population TOI-561 b is a ''peculiar among the peculiars''. Its extremely low density makes it inconsistent with the pure rocky composition expected
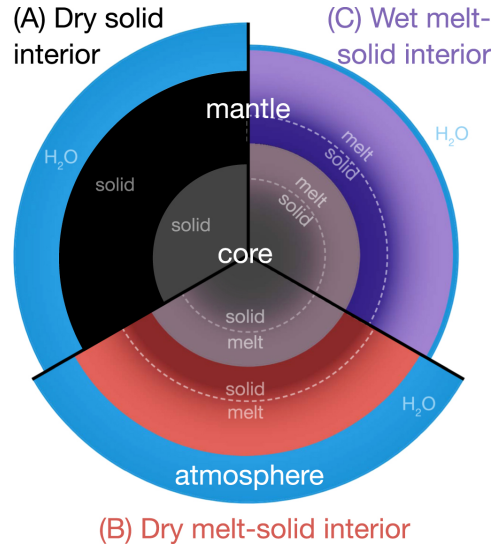
Figure 6.1 Schematic view of the structure of a exoplanet assuming different interior models. In Model A, the liquid rock phase are neglected. When solid and melt phases are present in the core and mantle (Model B), the planetary radius increases, while it decreases if the effect of water partitioning into the magma ocean is taken into account (Model C). This last model most accurately reflects the current knowledge of mineral physics and exoplanet interiors. From Dorn & Lichtenberg (2021).

for such irradiated worlds, and claims for more complex explanations. Its already precise mass and radius measurements are expected to improve in the next future with further photometric (*CHEOPS*) and RV data (HARPS-N, Maroon-X, HIRES), making it an optimal test-case to probe recently developed, extreme theories of planetary interiors and composition. The current internal modelling we propose assumes a fully differentiated four-layers model, but the suggested presence of water on such an extreme world most likely requires more complex modelling. More advanced models could be tested, like for example models that account for the effect of runaway greenhouse irradiation for water-rich planets (Turbet et al., 2020), models of planetary interiors accounting for the possible presence of deep water reservoirs and the subsequent effects of rock melting and redistribution of water between the magma ocean and atmosphere on planetary radius (Figure 6.1; Dorn & Lichtenberg 2021), and models testing different compositions of the inner core and mantle, dominated by lighter elements like Ca and Al instead of the commonly used Fe/S/Ni-dominated cores (Dorn et al., 2018b). Testing and probing this kind of theories on well-characterized planets, as well as possibly develop new ones, will be essential to understand and explain the properties of the population of USP planets in a broader context. For example, two other USP planets with low densities have been recently discovered (TOI-1685; Bluhm et al. 2021, and TOI-1634; Cloutier et al. 2021). Both planets orbit an M-dwarf star, and it will surely be interesting to investigate the USP planets properties as a function of the spectral type, and more in general of the stellar properties (metallicity, age, etc.) Finally, a further topic of future investigations on USP planets concerns their evolution mechanisms. The extreme orbits of USP planets challenge the evolution theories. Most of the USP planets orbit within the dust sublimation radius ($a/R_\star \sim 8$ for Sun-like stars; Isella et al. 2006), or even within what would have been the radius of the once younger

host stars. Therefore, in-situ formation appears extremely unlikely, and migration mechanisms seem to be required to explain the existence of the USP planets population. Among the currently proposed theories:

- The possibility of these planets to be the tidally disrupted cores of hot Jupiters that likely formed further out in the disk before migrating inwards (e.g. Jackson et al. 2013). It could be tested for example through comparison of the stellar properties (metallicity, kinematic, age) of the two populations.

- Formation involving secular interaction that launched the planets into eccentric, inclined orbits that eventually tidally shrunk to the current-day configuration (Petrovich et al. 2019; Pu & Lai 2019). It could be tested through studies on mutual inclinations and orbital separations in multi-planetary systems.

- Theories involving coplanar disk migration and host star oblateness to excite mutual inclinations (Li et al., 2020), for which analyses on the stellar obliquity distribution of the USP planets are required.

- Theories involving obliquity tides (Millholland & Spalding, 2020), to be tested through studies of stellar obliquities and close-in companions, together with theoretical explorations of the potential for chaotic obliquity dynamics.

- Formation mechanisms involving a distant companion, to be investigated by increasing the sample of USP planets in multiplanetary systems, with a special attention on USP planets with wide-orbit companions (Becker et al., 2015).

Testing and applying evolutionary theories on TOI-561 b will be fundamental for a deeper understanding of the planet and of the whole system. More generally, increasing the sample of well-characterized USP planets (currently only 19 objects are known) will be a crucial step to test and probe the composition and evolutionary theories of this fascinating population of exoplanets.

A further interesting trait of the TOI-561 system is the presence of a long-period planet (TOI-561 e, $P \sim 77$ d). Currently, the great majority of known exoplanets have periods below 20 days, mainly due to observational biases. Increasing the number of cool, long-period planets will be crucial not only for demographic studies (Gaudi et al., 2021), but also because, for dynamical considerations (Barnes & O'Brien 2002; Namouni 2010), long-period planets are optimal targets to search for exomoons, which is one of the most exciting next frontiers in exoplanetary science. Active investigations are currently ongoing in this area, and some candidates have been recently proposed (Teachey & Kipping 2018; Kipping et al. 2022), even though no indisputable detection has been yet confirmed. In this context, *CHEOPS* is on the forefront, with a dedicated program searching for moons and rings around exoplanets (Benz et al., 2021), within which we are currently investigating the possible presence of moons around TOI-561 e. Even though the identification of suitable candidates for the search of exomoons is not trivial (bright stars hosting long-period transiting planet with observations covering at least the full Hill

sphere are needed), the number of good targets is expected to increase in the near future, i.e. with the *Gaia* survey, and later on with the *PLATO* mission. In this context, TTVs could play an important role for the detection and characterization of long-period planets, both in new and already known systems (Section 1.2.3). A tool for the complete characterization of these systems, like the photodynamical code we developed, will then provide important constraints in this field.

Finally, TOI-561 is interesting not only from a planetary, but also from a stellar point of view. In fact, it is one of the few thick disk stars hosting a multiplanetary system. The distribution of planets in the Galaxy, their occurrence as a function of the Galactic components (thin disk, thick disk, halo), and their correlation with galactic arms and cluster are currently poorly understood and studied topics. Specific investigations targeting stars belonging to different Galactic populations, like the X-GAL program we are currently carrying out within the *CHEOPS* Consortium, which includes TOI-561, will help us to contextualize exoplanet properties in a broader, Galactic perspective.

Bibliography

Adibekyan V. Z., Sousa S. G., Santos N. C., Delgado Mena E., González Hernández J. I., Israelian G., Mayor M., Khachatryan G., 2012, A&A, 545, A32

Adibekyan V., et al., 2021a, arXiv e-prints, p. arXiv:2102.12444

Adibekyan V., et al., 2021b, A&A, 649, A111

Affer L., et al., 2016, A&A, 593, A117

Agol E., Fabrycky D. C., 2018, Handbook of Exoplanets, pp 797–816

Agol E., et al., 2005, MNRAS, 359, 567

Agol E., et al., 2021, The Planetary Science Journal, 2, 1

Aigrain S., Hodgkin S. T., Irwin M. J., Lewis J. R., Roberts S. J., 2015, MNRAS, 447, 2880

Albrecht S., Winn J. N., Marcy G. W., Howard A. W., Isaacson H., Johnson J. A., 2013, ApJ, 771, 11

Alibert Y., Carron, F. Fortier, A. Pfyffer, S. Benz, W. Mordasini, C. Swoboda, D. 2013, A&A, 558, A109

Almenara J. M., Díaz R. F., Mardling R., Barros S. C. C., Damiani C., Bruno G., Bonfils X., Deleuil M., 2015, MNRAS, 453, 2644

Almenara J. M., Díaz R. F., Bonfils X., Udry S., 2016, A&A, 595, L5

Ambikasaran S., Foreman-Mackey D., Greengard L., Hogg D. W., O'Neil M., 2015, IEEE Transactions on Pattern Analysis and Machine Intelligence, 38

Anglada-Escudé G., Butler R. P., 2012, ApJS, 200, 15

Angus R., Aigrain S., Foreman-Mackey D., McQuillan A., 2015, MNRAS, 450, 1787

Armstrong D. J., et al., 2020, Nature, 583, 39

Asplund M., Grevesse N., Sauval A. J., Scott P., 2009, ARA&A, 47, 481

Baglin A., et al., 2006, in 36th COSPAR Scientific Assembly. p. 3749

Bailer-Jones C. A. L., Rybizki J., Fouesneau M., Mantelet G., Andrae R., 2018, AJ, 156, 58

Bailer-Jones C. A. L., Rybizki J., Fouesneau M., Demleitner M., Andrae R., 2021, VizieR Online Data Catalog, p. I/352

Bakos G. Á., 2018, The HATNet and HATSouth Exoplanet Surveys. p. 111, doi:10.1007/978-3-319-55333-7_111

Bibliography

Bakos G. Á., Lázár J., Papp I., Sári P., Green E. M., 2002, PASP, 114, 974

Bakos G., Noyes R. W., Kovács G., Stanek K. Z., Sasselov D. D., Domsa I., 2004, PASP, 116, 266

Bakos G., et al., 2009, HAT-South: A Global Network of Southern Hemisphere Automated Telescopes to Detect Transiting Exoplanets. pp 354–357, doi:10.1017/S174392130802663X

Bakos G. Á., et al., 2013, PASP, 125, 154

Ballard S., et al., 2011, ApJ, 743, 200

Baraffe I., Chabrier G., Fortney J., Sotin C., 2014, in Beuther H., Klessen R. S., Dullemond C. P., Henning T., eds, Protostars and Planets VI. p. 763 (arXiv:1401.4738), doi:10.2458/azu_uapress_9780816531240-ch033

Baranne A., et al., 1996, A&AS, 119, 373

Barclay T., et al., 2013, Nature, 494, 452

Barnes S. A., 2003, ApJ, 586, 464

Barnes J. W., O'Brien D. P., 2002, ApJ, 575, 1087

Barros S. C. C., Demangeon, O. Díaz, R. F. Cabrera, J. Santos, N. C. Faria, J. P. Pereira, F. 2020, A&A, 634, A75

Barros S. C. C., Akinsanm B., Boué G., Smith A. M. S., Laskar J., Ulmer-Moll S., Lillo-Box J., the CHEOPS Team 2022, arXiv e-prints, p. arXiv:2201.03328

Baruteau C., et al., 2014, in Beuther H., Klessen R. S., Dullemond C. P., Henning T., eds, Protostars and Planets VI. p. 667 (arXiv:1312.4293), doi:10.2458/azu_uapress_9780816531240-ch029

Baruteau C., Bai X., Mordasini C., Mollière P., 2016, Space Sci. Rev., 205, 77

Batalha N. M., et al., 2011, ApJ, 729, 27

Batalha N. M., et al., 2013, ApJS, 204, 24

Batygin K., Morbidelli A., 2013, A&A, 556, A28

Batygin K., Bodenheimer P. H., Laughlin G. P., 2016, ApJ, 829, 114

Becker J. C., Adams F. C., 2017, MNRAS, 468, 549

Becker J. C., et al., 2015, ApJ, 812, L18

Becker J., Batygin K., Fabrycky D., Adams F. C., Li G., Vanderburg A., Rodriguez J. E., 2020, AJ, 160, 254

Benneke B., et al., 2019, ApJ, 887, L14

Bensby T., Feltzing S., Oey M. S., 2014, A&A, 562, A71

Benz W., et al., 2021, Experimental Astronomy, 51, 109

Blackman R. T., et al., 2020, AJ, 159, 238

Blackwell D. E., Shallis M. J., 1977, Monthly Notices of the Royal Astronomical Society, 180, 177

Bluhm P., et al., 2021, A&A, 650, A78

Bodaghee A., Santos N. C., Israelian G., Mayor M., 2003, A&A, 404, 715

Boisse I., et al., 2009, A&A, 495, 959

Boisse I., Bouchy F., Hébrard G., Bonfils X., Santos N., Vauclair S., 2011, in Sozzetti A., Lattanzi M. G., Boss A. P., eds, Vol. 276, The Astrophysics of Planetary Systems: Formation, Structure, and Dynamical Evolution. pp 399–400, doi:10.1017/S1743921311020515

Bonfanti A., Gillon M., 2020, A&A, 635, A6

Bonfanti A., Ortolani S., Piotto G., Nascimbeni V., 2015, A&A, 575, A18

Bonfanti A., Ortolani S., Nascimbeni V., 2016, A&A, 585, A5

Bonfanti A., Fossati L., Kubyshkina D., Cubillos P. E., 2021a, arXiv e-prints, p. arXiv:2110.09106

Bonfanti et al., 2021b, A&A, 646, A157

Bonomo A. S., et al., 2014, A&A, 572, A2

Borsato L., Marzari F., Nascimbeni V., Piotto G., Granata V., Bedin L. R., Malavolta L., 2014, A&A, 571, A38

Borsato L., et al., 2019, MNRAS, 484, 3233

Borsato L., et al., 2021, MNRAS, 506, 3810

Borucki W. J., et al., 2010, Science, 327, 977

Bouchy F., 2021, in The Star-Planet Connection. p. 27, doi:10.5281/zenodo.5635581

Bouchy F., et al., 2017, The Messenger, 169, 21

Brown T. M., et al., 2013, PASP, 125, 1031

Buchhave L. A., et al., 2012, Nature, 486, 375

Buchhave L. A., et al., 2014, Nature, 509, 593

Buchhave L. A., et al., 2016, AJ, 152, 160

Buchner J., 2014, arXiv e-prints, p. arXiv:1407.5459

Buchner J., 2017, arXiv e-prints, p. arXiv:1707.04476

Buchner J., 2021, The Journal of Open Source Software, 6, 3001

Buchner, J. et al., 2014, A&A, 564, A125

Burrows A., Budaj J., Hubeny I., 2008, ApJ, 678, 1436

Burt J. A., et al., 2021, AJ, 162, 87

Butler R. P., Marcy G. W., Fischer D. A., Brown T. M., Contos A. R., Korzennik S. G., Nisenson P., Noyes R. W., 1999, ApJ, 526, 916

Cabrera J., et al., 2014, ApJ, 781, 18

135

Bibliography

Carleo I., et al., 2021, A&A, 645, A71

Castelli F., Kurucz R. L., 2003, in Piskunov N., Weiss W. W., Gray D. F., eds, IAU Symposium Vol. 210, Modelling of Stellar Atmospheres. p. A20 (arXiv:astro-ph/0405087)

Chaplin W. J., Miglio A., 2013, ARA&A, 51, 353

Charbonneau D., Brown T. M., Latham D. W., Mayor M., 2000, ApJ, 529, L45

Charbonneau D., et al., 2009, Nature, 462, 891

Chen J., Kipping D., 2017, ApJ, 834, 17

Chen H., Rogers L. A., 2016, The Astrophysical Journal, 831, 180

Chevance M., Kruijssen J. M. D., Longmore S. N., 2021, ApJ, 910, L19

Choi J., Dotter A., Conroy C., Cantiello M., Paxton B., Johnson B. D., 2016, ApJ, 823, 102

Chopin N., Robert C. P., 2010, Biometrika, 97, 741

Christensen-Dalsgaard J., 2004, in Danesy D., ed., ESA Special Publication Vol. 559, SOHO 14 Helio- and Asteroseismology: Towards a Golden Future. p. 1

Ciardi D. R., Fabrycky D. C., Ford E. B., Gautier T. N. I., Howell S. B., Lissauer J. J., Ragozzine D., Rowe J. F., 2013, ApJ, 763, 41

Cincotta P. M., Simó C., 2000, A&AS, 147, 205

Claret A., 2000, A&A, 363, 1081

Claret A., 2017, A&A, 600, A30

Claret A., 2018, A&A, 618, A20

Claret A., 2021, Research Notes of the American Astronomical Society, 5, 13

Claret A., Hauschildt P. H., 2003, A&A, 412, 241

Claudi R., et al., 2017, European Physical Journal Plus, 132, 364

Cloutier R., et al., 2019, A&A, 621, A49

Cloutier R., et al., 2021, AJ, 162, 79

Clyde M. A., Berger J. O., Bullard F., Ford E. B., Jefferys W. H., Luo R., Paulo R., Loredo T., 2007, in Babu G. J., Feigelson E. D., eds, Astronomical Society of the Pacific Conference Series Vol. 371, Statistical Challenges in Modern Astronomy IV. p. 224

Coleman G. A. L., Leleu A., Alibert Y., Benz W., 2019, A&A, 631, A7

Collier Cameron A., 2018, The Impact of Stellar Activity on the Detection and Characterization of Exoplanets. p. 23, doi:10.1007/978-3-319-55333-7_23

Collier Cameron A., Pollacco D., Hellier C., West R., WASP Consortium SOPHIE & CORALIE Planet-Search Teams 2009, The WASP transit surveys. pp 29–35, doi:10.1017/S1743921308026203

Collier Cameron A., et al., 2019, MNRAS, 487, 1082

Collier Cameron A., et al., 2021, MNRAS, 505, 1699

Cooper C. S., Showman A. P., 2006, ApJ, 649, 1048

Cosentino R., et al., 2012, in Society of Photo-Optical Instrumentation Engineers (SPIE) Conference Series. p. 1, doi:10.1117/12.925738

Cosentino R., et al., 2014, in Society of Photo-Optical Instrumentation Engineers (SPIE) Conference Series. p. 8, doi:10.1117/12.2055813

Crass J., et al., 2021, Extreme Precision Radial Velocity Working Group Final Report (arXiv:2107.14291)

Cretignier M., Dumusque X., Hara N. C., Pepe F., 2021, A&A, 653, A43

Cubillos P., Harrington J., Loredo T. J., Lust N. B., Blecic J., Stemm M., 2017, AJ, 153, 3

Cutri R. M., et al., 2003, VizieR Online Data Catalog, 2246

Czekala I., Mandel K. S., Andrews S. M., Dittmann J. A., Ghosh S. K., Montet B. T., Newton E. R., 2017, ApJ, 840, 49

Dai F., et al., 2015, ApJ, 813, L9

Dai F., Masuda K., Winn J. N., 2018, ApJ, 864, L38

Dai F., Masuda K., Winn J. N., Zeng L., 2019, ApJ, 883, 79

Dai F., et al., 2021, The Astronomical Journal, 162, 62

Dalcin L., Fang Y.-L. L., 2021, Computing in Science Engineering, 23, 47

Dalcin L. D., Paz R. R., Kler P. A., Cosimo A., 2011, Advances in Water Resources, 34, 1124

Dalcín L., Paz R., Storti M., 2005, Journal of Parallel and Distributed Computing, 65, 1108

Dalcín L., Paz R., Storti M., D'Elía J., 2008, Journal of Parallel and Distributed Computing, 68, 655

Damasso M., et al., 2020, A&A, 642, A133

Davies M. B., Adams F. C., Armitage P., Chambers J., Ford E., Morbidelli A., Raymond S. N., Veras D., 2014, in Beuther H., Klessen R. S., Dullemond C. P., Henning T., eds, Protostars and Planets VI. p. 787 (arXiv:1311.6816), doi:10.2458/azu_uapress_9780816531240-ch034

Davis T. A., Wheatley P. J., 2009, MNRAS, 396, 1012

Davis A. B., et al., 2020, The Astronomical Journal, 160, 229

Dawson R. I., et al., 2021, AJ, 161, 161

Delisle J. B., 2017, A&A, 605, A96

Delrez L., et al., 2021, Nature Astronomy, 5, 775

Demory B.-O., Gillon M., Madhusudhan N., Queloz D., 2016, MNRAS, 455, 2018

Diaz-Cordoves J., Gimenez A., 1992, A&A, 259, 227

Dietrich J., Apai D., 2020, AJ, 160, 107

Bibliography

Dong C., Huang Z., Lingam M., Tóth G., Gombosi T., Bhattacharjee A., 2017, ApJ, 847, L4

Dorn C., Lichtenberg T., 2021, arXiv e-prints, p. arXiv:2110.15069

Dorn C., Khan A., Heng K., Connolly J. A. D., Alibert Y., Benz W., Tackley P., 2015, A&A, 577, A83

Dorn C., Venturini, Julia Khan, Amir Heng, Kevin Alibert, Yann Helled, Ravit Rivoldini, Attilio Benz, Willy 2017, A&A, 597, A37

Dorn C., Bower D. J., Rozel A., 2018a, Handbook of Exoplanets, p. 3111–3135

Dorn C., Harrison J. H. D., Bonsor A., Hands T. O., 2018b, Monthly Notices of the Royal Astronomical Society, 484, 712

Dorn C., Mosegaard K., Grimm S. L., Alibert Y., 2018c, ApJ, 865, 20

Dotter A., 2016, ApJS, 222, 8

Dotter A., Chaboyer B., Jevremović D., Kostov V., Baron E., Ferguson J. W., 2008, ApJS, 178, 89

Douglas S. T., Curtis J. L., Agüeros M. A., Cargile P. A., Brewer J. M., Meibom S., Jansen T., 2019, ApJ, 879, 100

Dragomir D., et al., 2019, The Astrophysical Journal, 875, L7

Dumusque X., 2018, A&A, 620, A47

Dumusque X., et al., 2017, A&A, 598, A133

Dumusque X., et al., 2019, A&A, 627, A43

Dumusque X., et al., 2021, A&A, 648, A103

Eastman J., Gaudi B. S., Agol E., 2013, PASP, 125, 83

Eastman J. D., et al., 2019, EXOFASTv2: A public, generalized, publication-quality exoplanet modeling code (arXiv:1907.09480)

Elkins-Tanton L. T., Seager S., 2008, ApJ, 685, 1237

Emsenhuber A., Mordasini, Christoph Burn, Remo Alibert, Yann Benz, Willy Asphaug, Erik 2021, A&A, 656, A69

Erkaev N. V., Kulikov Y. N., Lammer H., Selsis F., Langmayr D., Jaritz G. F., Biernat H. K., 2007, A&A, 472, 329

Espinoza N., Kossakowski D., Brahm R., 2019, MNRAS, 490, 2262

Esposito M., et al., 2017, A&A, 601, A53

Fabrycky D. C., et al., 2012, ApJ, 750, 114

Fabrycky D. C., et al., 2014, The Astrophysical Journal, 790, 146

Fang J., Margot J.-L., 2012, The Astrophysical Journal, 761, 92

Faria J. P., Haywood R. D., Brewer B. J., Figueira P., Oshagh M., Santerne A., Santos N. C., 2016, A&A, 588, A31

Fausnaugh M. M., Burke C. J., Ricker G. R., Vanderspek R., 2020, Research Notes of the American Astronomical Society, 4, 251

Feigelson E. D., Babu G. J., 2012, Modern Statistical Methods for Astronomy

Feroz F., Hobson M. P., 2008, MNRAS, 384, 449

Feroz F., Hobson M. P., 2014, MNRAS, 437, 3540

Feroz F., Hobson M. P., Bridges M., 2009, MNRAS, 398, 1601

Feroz F., Hobson M. P., Cameron E., Pettitt A. N., 2019, The Open Journal of Astrophysics, 2, 10

Figueira P., Santos N. C., Pepe F., Lovis C., Nardetto N., 2013, A&A, 557, A93

Fischer D. A., Marcy G. W., Butler R. P., Laughlin G., Vogt S. S., 2002, ApJ, 564, 1028

Ford E. B., Gaudi B. S., 2006, ApJ, 652, L137

Ford E. B., Gregory P. C., 2007, in Babu G. J., Feigelson E. D., eds, Astronomical Society of the Pacific Conference Series Vol. 371, Statistical Challenges in Modern Astronomy IV. p. 189 (arXiv:astro-ph/0608328)

Foreman-Mackey D., Hogg D. W., Lang D., Goodman J., 2013a, PASP, 125, 306

Foreman-Mackey D., Hogg D. W., Lang D., Goodman J., 2013b, PASP, 125, 306

Foreman-Mackey D., Agol E., Ambikasaran S., Angus R., 2017, AJ, 154, 220

Fortney J. J., Marley M. S., Barnes J. W., 2007, ApJ, 659, 1661

Fossati L., et al., 2017, A&A, 601, A104

Fossati L., et al., 2021, arXiv e-prints, p. arXiv:2112.11179

Fressin F., et al., 2013, The Astrophysical Journal, 766, 81

Freudenthal et al., 2019, A&A, 628, A108

Frustagli G., et al., 2020, A&A, 633, A133

Fulton B. J., et al., 2017, AJ, 154, 109

Gaia Collaboration et al., 2018, A&A, 616, A1

Gaia Collaboration et al., 2021, A&A, 649, A1

Gajdoš P., Vaňko M., Parimucha Š., 2019, Research in Astronomy and Astrophysics, 19, 041

Gardner J. P., et al., 2006, Space Sci. Rev., 123, 485

Gaudi B. S., Meyer M., Christiansen J., 2021, in Madhusudhan N., ed., , ExoFrontiers; Big Questions in Exoplanetary Science. pp 2–1, doi:10.1088/2514-3433/abfa8fch2

Gelman A., Rubin D. B., 1992, Statistical Science, 7, 16

Gelman A., et al., 2013, Bayesian Data Analysis. Chapman and Hall/CRC

Gibson N. P., Aigrain S., Roberts S., Evans T. M., Osborne M., Pont F., 2012, MNRAS, 419, 2683

Bibliography

Gillon M., et al., 2017, Nature, 542, 456

Ginzburg S., Schlichting H. E., Sari R., 2016, ApJ, 825, 29

Ginzburg S., Schlichting H. E., Sari R., 2018, Monthly Notices of the Royal Astronomical Society, 476, 759

Goldblatt C., Watson A. J., 2012, Philosophical Transactions of the Royal Society of London Series A, 370, 4197

Gomes da Silva J., Santos N. C., Bonfils X., Delfosse X., Forveille T., Udry S., 2011, A&A, 534, A30

Goodman J., Weare J., 2010, Commun. Appl. Math. Comput. Sci., 5, 65

Gregory P., 2005, Bayesian Logical Data Analysis for the Physical Sciences: A Comparative Approach with Mathematica Support. Cambridge University Press, doi:10.1017/CBO9780511791277

Grimm S., et al., 2018, A&A, 613, A68

Grunblatt S. K., Howard A. W., Haywood R. D., 2015, ApJ, 808, 127

Günther M. N., Pozuelos F. J., Dittmann J. A., et al., 2019, Nature Astronomy, 3, 1099

Gupta A., Schlichting H. E., 2019, Monthly Notices of the Royal Astronomical Society, 487, 24

Hadden S., Lithwick Y., 2014, The Astrophysical Journal, 787, 80

Hakim K., Rivoldini A., Van Hoolst T., Cottenier S., Jaeken J., Chust T., Steinle-Neumann G., 2018, Icarus, 313, 61

Haldemann Alibert, Yann Mordasini, Christoph Benz, Willy 2020, A&A, 643, A105

Halverson S., et al., 2016, A comprehensive radial velocity error budget for next generation Doppler spectrometers. SPIE, pp 2022 – 2041, doi:10.1117/12.2232761, https://doi.org/10.1117/12.2232761

Hansen B. M. S., Murray N., 2013, The Astrophysical Journal, 775, 53

Hara N. C., Boué G., Laskar J., Correia A. C. M., 2017, Monthly Notices of the Royal Astronomical Society, 464, 1220

Hatzes A. P., 2014, A&A, 568, A84

Hatzes A. P., 2019, The Doppler Method for the Detection of Exoplanets. 2514-3433, IOP Publishing, doi:10.1088/2514-3433/ab46a3, http://dx.doi.org/10.1088/2514-3433/ab46a3

Hatzes A. P., et al., 2010, A&A, 520, A93

Haywood R. D., et al., 2014, MNRAS, 443, 2517

Haywood R. D., et al., 2018, AJ, 155, 203

He M. Y., Ford E. B., Ragozzine D., 2019, MNRAS, 490, 4575

Hébrard É. M., Donati J. F., Delfosse X., Morin J., Boisse I., Moutou C., Hébrard G., 2014, MNRAS, 443, 2599

Helled R., et al., 2014, in Beuther H., Klessen R. S., Dullemond C. P., Henning T., eds, Protostars and Planets VI. p. 643 (arXiv:1311.1142), doi:10.2458/azu_uapress_9780816531240-ch028

Hellier C., et al., 2012, MNRAS, 426, 739

Henry G. W., Marcy G. W., Butler R. P., Vogt S. S., 2000, ApJ, 529, L41

Hippke M., Heller R., 2019, A&A, 623, A39

Hippke M., David T. J., Mulders G. D., Heller R., 2019, AJ, 158, 143

Hirano T., et al., 2012, ApJ, 759, L36

Hobson M. J., et al., 2021, AJ, 161, 235

Hodges J. L., 1958, Arkiv för Matematik, 3, 469

Holczer T., et al., 2016, ApJS, 225, 9

Holman M. J., Murray N. W., 2005, Science, 307, 1288

Holman M. J., et al., 2010, Science, 330, 51

Hooton M. J., et al., 2021, arXiv e-prints, p. arXiv:2109.05031

Howard A. W., et al., 2013, Nature, 503, 381

Howell S. B., et al., 2014, PASP, 126, 398

Hoyer S., Guterman P., Demangeon O., Sousa S. G., Deleuil M., Meunier J. C., Benz W., 2020, A&A, 635, A24

Huang C. X., Bakos G. �., 2014, Monthly Notices of the Royal Astronomical Society, 442, 674

Huang C., Wu Y., Triaud A. H. M. J., 2016, ApJ, 825, 98

Huang C. X., et al., 2020, Research Notes of the American Astronomical Society, 4, 204

Ikoma M., Genda H., 2006, ApJ, 648, 696

Isaacson H., Fischer D., 2010, ApJ, 725, 875

Isella A., Testi L., Natta A., 2006, A&A, 451, 951

Jackson B., Stark C. C., Adams E. R., Chambers J., Deming D., 2013, ApJ, 779, 165

Jeffries R. D., Totten E. J., Harmer S., Deliyannis C. P., 2002, MNRAS, 336, 1109

Jenkins J. M., 2020, Kepler Data Processing Handbook, Kepler Science Document KSCI-19081-003, https://archive.stsci.edu/kepler/documents.html

Jenkins J. M., et al., 2016, in Chiozzi G., Guzman J. C., eds, Society of Photo-Optical Instrumentation Engineers (SPIE) Conference Series Vol. 9913, Software and Cyberinfrastructure for Astronomy IV. SPIE, pp 1232 – 1251, doi:10.1117/12.2233418, https://doi.org/10.1117/12.2233418

Jin S., Mordasini C., 2018, The Astrophysical Journal, 853, 163

Jin S., Mordasini C., Parmentier V., van Boekel R., Henning T., Ji J., 2014, ApJ, 795, 65

Johnstone C. P., Güdel M., Brott I., Lüftinger T., 2015a, A&A, 577, A28

Johnstone C. P., et al., 2015b, ApJ, 815, L12

Bibliography

Jurgenson C., Fischer D., McCracken T., Sawyer D., Szymkowiak A., Davis A., Muller G., Santoro F., 2016, in Evans C. J., Simard L., Takami H., eds, Society of Photo-Optical Instrumentation Engineers (SPIE) Conference Series Vol. 9908, Ground-based and Airborne Instrumentation for Astronomy VI. p. 99086T (arXiv:1606.04413), doi:10.1117/12.2233002

Kaltenegger L., Pepper J., Stassun K., Oelkers R., 2019, ApJ, 874, L8

Kane M., Ragozzine D., Flowers X., Holczer T., Mazeh T., Relles H. M., 2019, AJ, 157, 171

Kass R. E., Raftery A. E., 1995, Journal of the American Statistical Association, 90, 773

Kasting J. F., Whitmire D. P., Reynolds R. T., 1993, Icarus, 101, 108

Kempton E. M. R., et al., 2018, PASP, 130, 114401

Khan S., et al., 2019, A&A, 628, A35

Kipping D. M., 2009a, MNRAS, 392, 181

Kipping D. M., 2009b, MNRAS, 396, 1797

Kipping D. M., 2010, MNRAS, 408, 1758

Kipping D. M., 2013, MNRAS, 435, 2152

Kipping D., et al., 2022, Nature Astronomy,

Kite E. S., Manga M., Gaidos E., 2009, ApJ, 700, 1732

Klinglesmith D. A., Sobieski S., 1970, AJ, 75, 175

Kochanek C. S., et al., 2017, PASP, 129, 104502

Kopal Z., 1950, Harvard College Observatory Circular, 454, 1

Kopparapu R. K., et al., 2013, ApJ, 765, 131

Kreidberg L., 2015, PASP, 127, 1161

Kreidberg L., et al., 2019, Nature, 573, 87

Kruijssen J. M. D., Longmore S. N., Chevance M., 2020, ApJ, 905, L18

Kruijssen J. M. D., Longmore S. N., Chevance M., Laporte C. F. P., Motylinski M., Keller B. W., Henshaw J. D., 2021, arXiv e-prints, p. arXiv:2109.06182

Kubyshkina D., et al., 2018, A&A, 619, A151

Kubyshkina D., et al., 2019a, A&A, 632, A65

Kubyshkina D., et al., 2019b, ApJ, 879, 26

Kuchner M. J., 2003, ApJ, 596, L105

Kunimoto M., Matthews J. M., 2020, The Astronomical Journal, 159, 248

Kurosaki K., Ikoma M., Hori Y., 2014, A&A, 562, A80

Kurucz R. L., 1993, SYNTHE spectrum synthesis programs and line data

Lacedelli G., et al., 2021, MNRAS, 501, 4148

Lacedelli G., et al., 2022, MNRAS,

Lai D., Pu B., 2017, AJ, 153, 42

Lammer H., Selsis F., Ribas I., Guinan E. F., Bauer S. J., Weiss W. W., 2003, ApJ, 598, L121

Lammer H., Kasting J. F., Chassefière E., Johnson R. E., Kulikov Y. N., Tian F., 2008, Space Sci. Rev., 139, 399

Lammer H., Erkaev N. V., Odert P., Kislyakova K. G., Leitzinger M., Khodachenko M. L., 2013, MN-RAS, 430, 1247

Langellier N., et al., 2021, AJ, 161, 287

Lanza A. F., et al., 2018, A&A, 616, A155

Latham D. W., et al., 2011, ApJ, 732, L24

Lee E. J., Chiang E., 2016, The Astrophysical Journal, 817, 90

Léger A., et al., 2004, Icarus, 169, 499

Léger A., et al., 2009, A&A, 506, 287

Leleu et al., 2021a, A&A, 649, A26

Leleu A., Chatel G., Udry S., Alibert Y., Delisle J. B., Mardling R., 2021b, A&A, 655, A66

Lendl M., et al., 2020, A&A, 643, A94

Lewis K. M., 2013, MNRAS, 430, 1473

Li G., Dai F., Becker J., 2020, ApJ, 890, L31

Lightkurve Collaboration et al., 2018, Lightkurve: Kepler and TESS time series analysis in Python, Astrophysics Source Code Library (ascl:1812.013)

Limbach M. A., Turner E. L., 2015, Proceedings of the National Academy of Science, 112, 20

Lindegren L., et al., 2021, A&A, 649, A4

Lissauer J. J., et al., 2011a, The Astrophysical Journal Supplement Series, 197, 8

Lissauer J. J., et al., 2011b, Nature, 470, 53

Lissauer J. J., et al., 2012, ApJ, 750, 112

Lithwick Y., Xie J., Wu Y., 2012, The Astrophysical Journal, 761, 122

Lodders K., 2010, in , Formation and Evolution of Exoplanets. p. 157, doi:10.1002/9783527629763.ch8

Lopez E. D., 2017, MNRAS, 472, 245

Lopez E. D., Fortney J. J., 2014, The Astrophysical Journal, 792, 1

Lopez E. D., Rice K., 2018, Monthly Notices of the Royal Astronomical Society, 479, 5303

Lovis C., Fischer D., 2010, Radial Velocity Techniques for Exoplanets. pp 27–53

Bibliography

Lovis C., et al., 2011, preprint, (arXiv:1107.5325)

Loyd R. O. P., Shkolnik E. L., Schneider A. C., Richey-Yowell T., Barman T. S., Peacock S., Pagano I., 2020, ApJ, 890, 23

Luck R. E., Heiter U., 2005, AJ, 129, 1063

MacKay D. J. C., 2002, Information Theory, Inference & Learning Algorithms. Cambridge University Press, USA

Madhusudhan N., Winn J. N., 2009, A Search for Exotrojans in Transiting Exoplanetary systems. pp 496–498 (arXiv:0807.4570), doi:10.1017/S1743921308027038

Malavolta L., et al., 2016, A&A, 588, A118

Malavolta L., et al., 2017a, AJ, 153, 224

Malavolta L., Lovis C., Pepe F., Sneden C., Udry S., 2017b, MNRAS, 469, 3965

Malavolta L., et al., 2018, AJ, 155, 107

Mamajek E. E., Hillenbrand L. A., 2008, ApJ, 687, 1264

Mancini L., et al., 2018, A&A, 613, A41

Mandel K., Agol E., 2002, ApJ, 580, L171

Marboeuf Thiabaud, Amaury Alibert, Yann Cabral, Nahuel Benz, Willy 2014, A&A, 570, A36

Marcus R. A., Sasselov D., Stewart S. T., Hernquist L., 2010, ApJ, 719, L45

Marcy G., 2009, Nature, 462, 853

Marcy G. W., Butler R. P., Fischer D., Vogt S. S., Lissauer J. J., Rivera E. J., 2001, ApJ, 556, 296

Marigo et al., 2017, The Astrophysical Journal, 835, 77

Masuda K., 2017, AJ, 154, 64

Masuda K., Hirano T., Taruya A., Nagasawa M., Suto Y., 2013, ApJ, 778, 185

Masuda K., Winn J. N., Kawahara H., 2020, AJ, 159, 38

Maxted P. F. L., et al., 2021, arXiv e-prints, p. arXiv:2111.08828

Mayor M., Queloz D., 1995, Nature, 378, 355

Mayor M., et al., 2003, The Messenger, 114, 20

Mazeh T., et al., 2013, The Astrophysical Journal Supplement Series, 208, 16

Mazeh T., Holczer T., Faigler S., 2016, A&A, 589, A75

McArthur B. E., et al., 2004, ApJ, 614, L81

McQuillan A., Aigrain S., Mazeh T., 2013, MNRAS, 432, 1203

Milbourne T. W., et al., 2019, ApJ, 874, 107

Miller-Ricci E., Seager S., Sasselov D., 2009, ApJ, 690, 1056

144

Millholland S. C., Spalding C., 2020, ApJ, 905, 71

Millholland S., Wang S., Laughlin G., 2016, ApJ, 823, L7

Millholland S., Wang S., Laughlin G., 2017, ApJ, 849, L33

Millholland S. C., He M. Y., Ford E. B., Ragozzine D., Fabrycky D., Winn J. N., 2021, AJ, 162, 166

Miralda-Escudè J., 2002, ApJ, 564, 1019

Mishra L., Alibert Y., Leleu A., Emsenhuber A., Mordasini C., Burn R., Udry S., Benz W., 2021, A&A, 656, A74

Morbidelli A., Lunine J., O'Brien D., Raymond S., Walsh K., 2012, Annual Review of Earth and Planetary Sciences, 40, 251

Mordasini C., 2018, Planetary Population Synthesis. p. 143, doi:10.1007/978-3-319-55333-7_143

Morello G., Tsiaras A., Howarth I. D., Homeier D., 2017, AJ, 154, 111

Morris B. M., et al., 2021a, arXiv e-prints, p. arXiv:2106.07443

Morris Heng, Kevin Brandeker, Alexis Swan, Andrew Lendl, Monika 2021b, A&A, 651, L12

Mortier A., Collier Cameron A., 2017, A&A, 601, A110

Mortier A., Santos N. C., Sousa S. G., Fernandes J. M., Adibekyan V. Z., Delgado Mena E., Montalto M., Israelian G., 2013, A&A, 558, A106

Mortier A., Sousa S. G., Adibekyan V. Z., Brandão I. M., Santos N. C., 2014, A&A, 572, A95

Mortier A., et al., 2018, MNRAS, 481, 1839

Morton T. D., 2015, isochrones: Stellar model grid package (ascl:1503.010)

Mulders G. D., Mordasini C., Pascucci I., Ciesla F. J., Emsenhuber A., Apai D., 2019, ApJ, 887, 157

Mustill A. J., Lambrechts M., Davies M. B., 2021, arXiv e-prints, p. arXiv:2103.15823

Namouni F., 2010, ApJ, 719, L145

Nardetto N., Mourard D., Kervella P., Mathias P., Mérand A., Bersier D., 2006, A&A, 453, 309

Nardiello D., et al., 2019, MNRAS, 490, 3806

Nardiello D., et al., 2020, MNRAS, 495, 4924

Nascimbeni V., et al., 2021, arXiv e-prints, p. arXiv:2110.13924

Nelson B. E., et al., 2020, AJ, 159, 73

Nesvorný D., Kipping D., Terrell D., Hartman J., Bakos G. Á., Buchhave L. A., 2013, The Astrophysical Journal, 777, 3

Nesvorný D., Kipping D., Terrell D., Feroz F., 2014, ApJ, 790, 31

Neveu-VanMalle M., et al., 2016, A&A, 586, A93

Noyes R. W., Hartmann L. W., Baliunas S. L., Duncan D. K., Vaughan A. H., 1984, ApJ, 279, 763

Bibliography

Ofir A., Dreizler, Stefan Zechmeister, Mathias Husser, Tim-Oliver 2014, A&A, 561, A103

Oliva E., et al., 2012, in McLean I. S., Ramsay S. K., Takami H., eds, Society of Photo-Optical Instrumentation Engineers (SPIE) Conference Series Vol. 8446, Ground-based and Airborne Instrumentation for Astronomy IV. p. 84463T, doi:10.1117/12.925274

Osborn H. P., et al., 2017, A&A, 604, A19

Osborn H. P., et al., 2021, MNRAS, 502, 4842

Owen J. E., Wu Y., 2013, ApJ, 775, 105

Owen J. E., Wu Y., 2016, ApJ, 817, 107

Owen J. E., Wu Y., 2017, ApJ, 847, 29

Pace G., Pasquini L., 2004, A&A, 426, 1021

Parviainen H., 2018, in Deeg H. J., Belmonte J. A., eds, , Handbook of Exoplanets. p. 149, doi:10.1007/978-3-319-55333-7_149

Pascale E., et al., 2018, in Lystrup M., MacEwen H. A., Fazio G. G., Batalha N., Siegler N., Tong E. C., eds, Society of Photo-Optical Instrumentation Engineers (SPIE) Conference Series Vol. 10698, Space Telescopes and Instrumentation 2018: Optical, Infrared, and Millimeter Wave. p. 106980H, doi:10.1117/12.2311838

Paxton B., Bildsten L., Dotter A., Herwig F., Lesaffre P., Timmes F., 2011, ApJS, 192, 3

Pepe F., Mayor M., Galland F., Naef D., Queloz D., Santos N. C., Udry S., Burnet M., 2002, A&A, 388, 632

Pepe F., et al., 2013, Nature, 503, 377

Pepe F., et al., 2021, A&A, 645, A96

Perryman M., 2014, The Exoplanet Handbook

Perryman M., 2018, The Exoplanet Handbook

Petrovich C., Deibert E., Wu Y., 2019, AJ, 157, 180

Pino L., et al., 2020, ApJ, 894, L27

Planck Collaboration et al., 2018, arXiv e-prints, p. arXiv:1807.06205

Pollacco D. L., et al., 2006, PASP, 118, 1407

Pollack J. B., Black D. C., 1982, Icarus, 51, 169

Pu B., Lai D., 2019, MNRAS, 488, 3568

Pu B., Wu Y., 2015, The Astrophysical Journal, 807, 44

Queloz D., et al., 2001, A&A, 379, 279

Quirrenbach A., et al., 2014, in Ramsay S. K., McLean I. S., Takami H., eds, Society of Photo-Optical Instrumentation Engineers (SPIE) Conference Series Vol. 9147, Ground-based and Airborne Instrumentation for Astronomy V. p. 91471F, doi:10.1117/12.2056453

Ragozzine D., Holman M. J., 2010, The Value of Systems with Multiple Transiting Planets (arXiv:1006.3727)

Ragozzine D., Jones D., Fabrycky D., 2021, in AAS/Division of Dynamical Astronomy Meeting. p. 304.04

Rainer M., et al., 2021, A&A, 649, A29

Rajpaul V., Aigrain S., Osborne M. A., Reece S., Roberts S., 2015, MNRAS, 452, 2269

Rajpaul V. M., et al., 2021, MNRAS, 507, 1847

Ramirez R. M., Kaltenegger L., 2016, ApJ, 823, 6

Rasmussen C. E., Williams C. K. I., 2006, Gaussian Processes for Machine Learning

Rauer H., et al., 2014, Experimental Astronomy, 38, 249

Raymond S. N., Kokubo E., Morbidelli A., Morishima R., Walsh K. J., 2014, in Beuther H., Klessen R. S., Dullemond C. P., Henning T., eds, Protostars and Planets VI. p. 595 (arXiv:1312.1689), doi:10.2458/azu_uapress_9780816531240-ch026

Rein H., Liu S. F., 2012, A&A, 537, A128

Rein H., Spiegel D. S., 2015, MNRAS, 446, 1424

Rein H., Tamayo D., 2015, MNRAS, 452, 376

Rein H., Tamayo D., 2016, MNRAS, 459, 2275

Rice K., et al., 2019, MNRAS, 484, 3731

Ricker G. R., et al., 2014, Journal of Astronomical Telescopes, Instruments, and Systems, 1, 1

Robert C., 2007, The Bayesian Choice: From Decision Theoretic Foundations to Computational Implementation. Springer

Roberts S. J., Osborne M. R., Ebden M., Reece S., Gibson N. P., Aigrain S., 2013, Philosophical Transactions of the Royal Society A: Mathematical, Physical and Engineering Sciences, 371

Rodriguez J. E., et al., 2021, AJ, 161, 194

Rogers L. A., Seager S., 2010, ApJ, 712, 974

Roy A., et al., 2020, AJ, 159, 161

Salmon S. J. A. J., Van Grootel V., Buldgen G., Dupret M. A., Eggenberger P., 2021, A&A, 646, A7

Sanchis-Ojeda R., Rappaport S., Winn J. N., Levine A., Kotson M. C., Latham D. W., Buchhave L. A., 2013, ApJ, 774, 54

Sanchis-Ojeda R., et al., 2015, The Astrophysical Journal, 812, L11

Santos N. C., Israelian G., Mayor M., 2000, A&A, 363, 228

Santos N. C., et al., 2013, A&A, 556, A150

Santos N. C., et al., 2017, A&A, 608, A94

Bibliography

Schaefer L., Fegley B., 2010, Icarus, 208, 438

Schanche N., et al., 2020, MNRAS, 499, 428

Schwab C., et al., 2016, in Evans C. J., Simard L., Takami H., eds, Society of Photo-Optical Instrumentation Engineers (SPIE) Conference Series Vol. 9908, Ground-based and Airborne Instrumentation for Astronomy VI. p. 99087H, doi:10.1117/12.2234411

Schwarzschild K., Villiger W., 1906, ApJ, 23, 284

Scuflaire R., Théado S., Montalbán J., Miglio A., Bourge P. O., Godart M., Thoul A., Noels A., 2008, Ap&SS, 316, 83

Seager S., Mallen-Ornelas G., 2003, The Astrophysical Journal, 585, 1038

Seifahrt A., Stürmer J., Bean J. L., Schwab C., 2018, in Evans C. J., Simard L., Takami H., eds, Society of Photo-Optical Instrumentation Engineers (SPIE) Conference Series Vol. 10702, Ground-based and Airborne Instrumentation for Astronomy VII. p. 107026D (arXiv:1805.09276), doi:10.1117/12.2312936

Sestito P., Randich S., 2005, A&A, 442, 615

Shallue C. J., Vanderburg A., 2018, AJ, 155, 94

Shappee B. J., et al., 2014, ApJ, 788, 48

Shporer A., et al., 2021, in Posters from the TESS Science Conference II (TSC2). p. 136, doi:10.5281/zenodo.5130728

Sinukoff E., et al., 2017, AJ, 153, 70

Skilling J., 2004, in Fischer R., Preuss R., Toussaint U. V., eds, American Institute of Physics Conference Series Vol. 735, Bayesian Inference and Maximum Entropy Methods in Science and Engineering: 24th International Workshop on Bayesian Inference and Maximum Entropy Methods in Science and Engineering. pp 395–405, doi:10.1063/1.1835238

Skilling J., 2006, Bayesian Anal., 1, 833

Skrutskie M. F., et al., 2006, AJ, 131, 1163

Smith J. C., et al., 2012, PASP, 124, 1000

Sneden C., 1973, ApJ, 184, 839

Sotin C., Grasset O., Mocquet A., 2007, Icarus, 191, 337

Sousa S. G., 2014a, [arXiv:1407.5817],

Sousa S. G., 2014b, ARES + MOOG: A Practical Overview of an Equivalent Width (EW) Method to Derive Stellar Parameters. Springer, Cham, pp 297–310, doi:10.1007/978-3-319-06956-2_26

Sousa S. G., Santos N. C., Israelian G., Mayor M., Monteiro M. J. P. F. G., 2007, A&A, 469, 783

Sousa S. G., Santos N. C., Israelian G., Lovis C., Mayor M., Silva P. B., Udry S., 2011, A&A, 526, A99

Sousa S. G., Santos N. C., Adibekyan V., Delgado-Mena E., Israelian G., 2015, A&A, 577, A67

Spalding C., Millholland S. C., 2020, AJ, 160, 105

Speagle J. S., 2020, MNRAS, 493, 3132

Stassun K. G., et al., 2018, The Astronomical Journal, 156, 102

Steffen J. H., Hwang J. A., 2015, Monthly Notices of the Royal Astronomical Society, 448, 1956

Steffen J. H., et al., 2012a, Proceedings of the National Academy of Sciences of the United States of America, 109, 7982

Steffen J. H., et al., 2012b, Monthly Notices of the Royal Astronomical Society, 428, 1077

Sterken C., 2005, The O-C Diagram: Basic Procedures. p. 3

Stökl A., Dorfi E., Lammer H., 2015, A&A, 576, A87

Stökl A., Dorfi E. A., Johnstone C. P., Lammer H., 2016, ApJ, 825, 86

Stumpe M. C., et al., 2012, PASP, 124, 985

Stumpe M. C., Smith J. C., Catanzarite J. H., Van Cleve J. E., Jenkins J. M., Twicken J. D., Girouard F. R., 2014, PASP, 126, 100

Swayne M. I., et al., 2021, MNRAS, 506, 306

Szabó G. M., Kiss L. L., 2011, ApJ, 727, L44

Szabó G. M., et al., 2021, arXiv e-prints, p. arXiv:2108.02149

Teachey A., Kipping D. M., 2018, Science Advances, 4, eaav1784

Thiabaud A., Marboeuf U., Alibert Y., Cabral N., Leya I., Mezger K., 2014, A&A, 562, A27

Thompson S. J., et al., 2016, in Evans C. J., Simard L., Takami H., eds, Society of Photo-Optical Instrumentation Engineers (SPIE) Conference Series Vol. 9908, Ground-based and Airborne Instrumentation for Astronomy VI. p. 99086F (arXiv:1608.04611), doi:10.1117/12.2232111

Tian F., 2009, ApJ, 703, 905

Tinetti G., et al., 2018, Experimental Astronomy, 46, 135

Tsiaras A., Waldmann I. P., Tinetti G., Tennyson J., Yurchenko S. N., 2019, Nature Astronomy, 3, 1086

Tuomi M., Anglada-Escudé G., Gerlach E., Jones H. R. A., Reiners A., Rivera E. J., Vogt S. S., Butler R. P., 2013, A&A, 549, A48

Turbet M., Bolmont E., Ehrenreich D., Gratier P., Leconte J., Selsis F., Hara N., Lovis C., 2020, A&A, 638, A41

Valenti J. A., Fischer D. A., 2005, ApJS, 159, 141

Van Eylen V., et al., 2019, AJ, 157, 61

Van Grootel V., et al., 2021, A&A, 650, A205

Vanderburg A., et al., 2017, AJ, 154, 237

Venturini J., Guilera O. M., Ronco M. P., Mordasini C., 2020, A&A, 644, A174

Bibliography

Vogt S. S., et al., 1994, in Crawford D. L., Craine E. R., eds, Society of Photo-Optical Instrumentation Engineers (SPIE) Conference Series Vol. 2198, Instrumentation in Astronomy VIII. p. 362, doi:10.1117/12.176725

Wang S., 2017, Research Notes of the American Astronomical Society, 1, 26

Wang D., Miguel Y., Lunine J., 2017, ApJ, 850, 199

Watson A. J., Donahue T. M., Walker J. C. G., 1981, Icarus, 48, 150

Weiss L. M., et al., 2013, ApJ, 768, 14

Weiss L. M., et al., 2017, AJ, 153, 265

Weiss L. M., et al., 2018a, AJ, 155, 48

Weiss L. M., et al., 2018b, AJ, 156, 254

Weiss L. M., et al., 2021, AJ, 161, 56

Wenger M., et al., 2000, A&AS, 143, 9

Wheatley P. J., et al., 2017, Monthly Notices of the Royal Astronomical Society, 475, 4476

Williams C., Rasmussen C., 1996, in Advances in neural information processing systems 8. MIT Press, Cambridge, MA, USA, pp 514–520

Wilson O. C., 1978, ApJ, 226, 379

Winn J. N., 2010, arXiv e-prints, p. arXiv:1001.2010

Winn J. N., Fabrycky D. C., 2015, ARA&A, 53, 409

Winter A. J., Kruijssen J. M. D., Longmore S. N., Chevance M., 2020, Nature, 586, 528

Wise A. W., Dodson-Robinson S. E., Bevenour K., Provini A., 2018, AJ, 156, 180

Wolfgang A., Rogers L. A., Ford E. B., 2016, ApJ, 825, 19

Wright J. T., 2005, PASP, 117, 657

Wright J. T., Marcy G. W., Butler R. P., Vogt S. S., 2004, ApJS, 152, 261

Wright J. T., et al., 2009, ApJ, 699, L97

Wright E. L., et al., 2010, AJ, 140, 1868

Wu D.-H., Wang S., Zhou J.-L., Steffen J. H., Laughlin G., 2018, The Astronomical Journal, 156, 96

Xie J.-W., 2013, The Astrophysical Journal Supplement Series, 208, 22

Xie J.-W., Wu Y., Lithwick Y., 2014, ApJ, 789, 165

Xie J.-W., et al., 2016, Proceedings of the National Academy of Science, 113, 11431

Yi S., Demarque P., Kim Y.-C., Lee Y.-W., Ree C. H., Lejeune T., Barnes S., 2001, ApJS, 136, 417

Zechmeister M., Kürster M., 2009, A&A, 496, 577

Zeng L., et al., 2019, Proceedings of the National Academy of Science, 116, 9723

Zhu W., Petrovich C., Wu Y., Dong S., Xie J., 2018, The Astrophysical Journal, 860, 101

Ziegler C., Tokovinin A., Briceño C., Mang J., Law N., Mann A. W., 2020, AJ, 159, 19

Zinzi A., Turrini D., 2017, A&A, 605, L4

de Beurs Z. L., et al., 2020, arXiv e-prints, p. arXiv:2011.00003

de Beurs Z. L., et al., 2021, in Posters from the TESS Science Conference II (TSC2). p. 134, doi:10.5281/zenodo.5130697

Appendix A

TOI-561: photometric analysis of *TESS* sector 8

We performed a preliminary light curve fit of the three candidate planets found in *TESS* sector 8 by the SPOC pipeline and our independent TLS analysis, that is TOI-561.01, .02, and .03 with periods of about 10.8 d, 0.45 d, and 16.3 d, respectively. We fit the transits using PyORBIT, as specified in Section 3.5, but assuming circular orbits for all the candidate planets, given the uncertainty associated with the eccentricity from the analysis of *TESS* data alone (Winn, 2010). We ran the chains for 100 000 steps, discarding the first 20 000 as burn-in. We list the obtained parameters in Table A.1 and we show the best-fitting transit models in Figure A.1. In order to test whether our light curve flattening of the PDCSAP photometry affected the inferred parameters of the planetary candidates, we also ran the PyORBIT fit on the original PDCSAP light curve. For all the candidates, the difference between the parameters of the two runs was lower than the error on the parameters themselves, indicating that the flattening did not significantly alter the results.

We stress that, at last, our global analysis disclaimed the presence of the planetary candidate TOI-561.03, linking the transits here associated with this candidate to single transits of two additional planets discovered in the system (see Section 3.6).
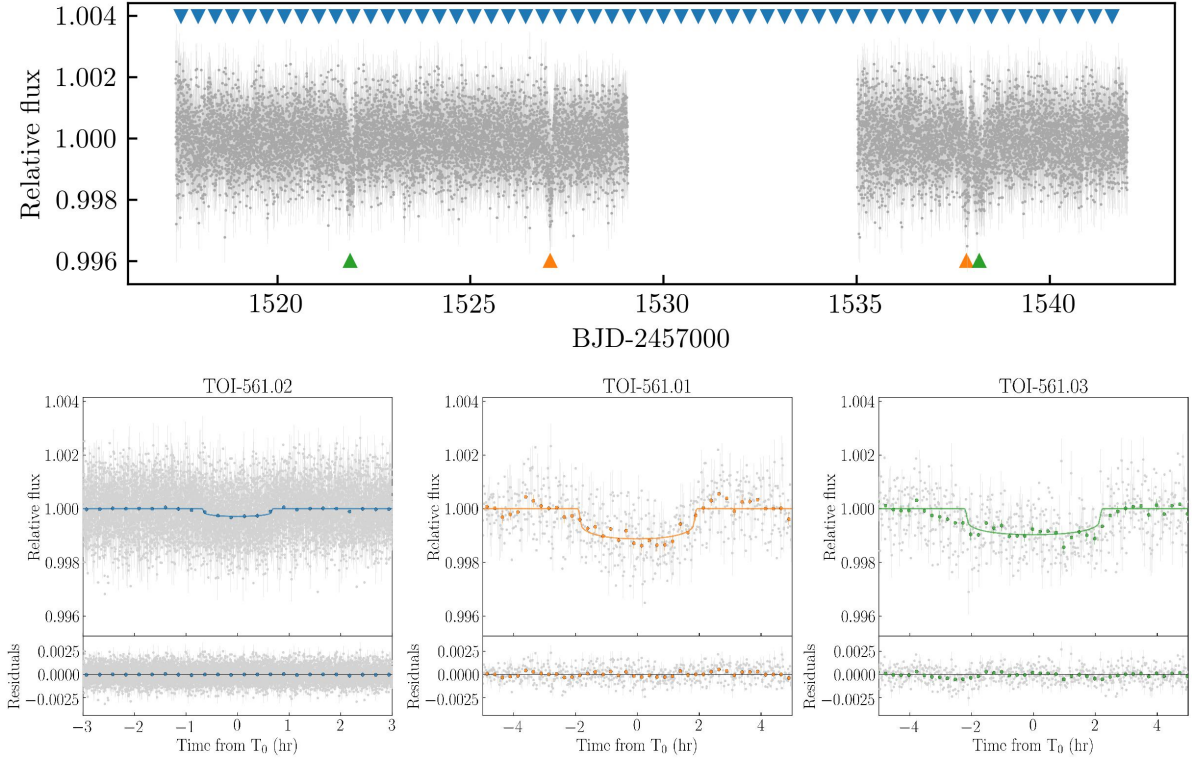
Figure A.1 *Top*: 2-minute cadence flattened light curve of TOI-561. The transits of candidates TOI-561.02 ($P \sim 0.45$ d), .01 ($P \sim 10.8$ d), and .03 ($P \sim 16.3$ d) are highlighted with blue, orange and green triangles, respectively. *Bottom*: TOI-561 phase-folded light curves over the best-fitting models (solid lines) for the three planets. The grey points are the *TESS* 2-minute data, the coloured dots are the data points binned over 15 minutes. The light curve residuals are shown in the bottom panel. Note the deviations from zero of the residuals in the ingress/egress phase for TOI-561.03.

Table A.1 Planetary parameters of the three transiting candidates from the initial light curve fitting.

Parameter	TOI-561.02	TOI-561.01	TOI-561.03
P (d)	0.44656 ± 0.00007	10.780 ± 0.005	$16.309^{+0.010}_{-0.008}$
T_0^{a} (d)	1517.4988 ± 0.0019	1527.060 ± 0.004	$1521.884^{+0.003}_{-0.006}$
$a/R_\star$	2.611 ± 0.030	21.81 ± 0.25	28.75 ± 0.33
a (AU)	0.01055 ± 0.00008	0.0881 ± 0.0007	0.1161 ± 0.0009
$R_{\mathrm{p}}/R_\star$	0.01544 ± 0.0007	0.0308 ± 0.0009	0.0285 ± 0.0008
R_{p} ($R_\oplus$)	1.46 ± 0.06	2.91 ± 0.10	2.70 ± 0.09
b	$0.16^{+0.14}_{-0.11}$	0.17 ± 0.12	$0.07^{+0.07}_{-0.05}$
i (deg)	$86.5^{+2.7}_{-3.0}$	$89.54^{+0.30}_{-0.33}$	$89.86^{+0.10}_{-0.15}$
T_{14}^{b} (hr)	$1.343^{+0.022}_{-0.034}$	$3.82^{+0.06}_{-0.10}$	4.44 ± 0.06
Common parameter			
$\rho_\star$ ($\rho_\odot$)	1.200 ± 0.041		
u_1	0.381 ± 0.047		
u_2	0.192 ± 0.050		

[a] $\mathrm{BJD_{TDB}}$-2457000. [b] Transit duration is derived from the posterior distributions using the formulas in Seager & Mallen-Ornelas (2003).

Appendix B

TOI-561: RV analysis of the first HARPS-N dataset

B.1 Removal of anomalous points

Before proceeding with a detailed analysis of the HARPS-N dataset (Section 3.2.2), we verified if any anomalous RV measurement was affecting our analysis. We followed a similar approach to that of Cloutier et al. (2019), but slightly more sophisticated due to the presence of (possibly up to) five planetary signals. Instead of analysing the power variation of the periodogram's peaks associated with the candidate planets while removing one point at the time, we decided to perform a full RV fit with the methodology described in Section 3.5, and to compare the resulting RV semi-amplitudes with those derived using the full dataset. To reduce computational time, we decided to remove from the dataset 5 consecutive observations at once (i.e., performing 17 iterations rather than 82), and then performed the leave-one-out cross-validation on those subsets showing deviating RV semi-amplitudes in order to identify the anomalous RV measurement. With this approach, we found out that a total of 5 RV measurements, with associated errors greater than 2.5 m s^{-1} and S/N < 35 were systematically producing a decrease in the semi-amplitude of candidates .01 and .02 by $\approx$ 0.1 − 0.2 m s^{-1}, and we therefore removed these points from our dataset in order to improve the accuracy of our results, even if the total variation in RV semi-amplitude was within the error bars. We note that these observations are clearly outliers at more than 2σ in both the S/N of the spectra and the RV error distributions (see Section 3.2.2), which is simply the consequence of having been gathered in sub-optimal weather conditions. A much simpler sigma-clipping selection would have led to the exclusion of the same data points. The complex approach we employed in this work can thus be avoided in future analysis involving HARPS-N data.

B.2 RV modelling and injection/retrieval tests

Given the results of the frequency analysis presented in Section 3.6.1, we performed a `PyDE+emcee` RV fit with `PyORBIT`, following the methodology as described in Section 3.5, and assuming the model

Table B.1 Best-fitting parameters from the five-planet RV fit, assuming period boundaries of 2-100 days for the outermost planet.

Parameter	TOI-561.02	TOI-561.01	TOI-561.03	TOI-561.04	TOI-561.05
P (d)	0.44658 ± 0.00001	10.778 ± 0.004	16.294 ± 0.008	$25.64^{+0.21}_{-0.18}$	77.9 ± 1.9
T_0^a (d)	1517.4983 ± 0.0008	1527.061 ± 0.003	1521.883 ± 0.004	1521^{+3}_{-5}	1535^{+9}_{-10}
e	0 (fixed)	$0.069^{+0.068}_{-0.048}$	$0.069^{+0.074}_{-0.048}$	$0.073^{+0.078}_{-0.051}$	$0.061^{+0.068}_{-0.043}$
ω (deg)	90 (fixed)	178 ± 75	235^{+135}_{-100}	275^{+60}_{-80}	100^{+93}_{-113}
K (m s^{-1})	1.41 ± 0.33	1.73 ± 0.36	< 0.37	3.12 ± 0.36	2.78 ± 0.44
M_p ($M_\oplus$)	1.43 ± 0.33	5.1 ± 1.0	< 1.27	12.2 ± 1.4	15.7 ± 2.5
Common parameter					
σ_{jitter}^b (m s^{-1})	1.32 ± 0.23				
γ^c (m s^{-1})	79702.58 ± 0.30				

[a] BJD$_{\text{TDB}}$-2457000. [b] Uncorrelated jitter term. [c] RV offset.

Table B.2 Best-fitting parameters from the five-planet RV fit, assuming period boundaries of 100-200 days for the outermost planet.

Parameter	TOI-561.02	TOI-561.01	TOI-561.03	TOI-561.04	TOI-561.05
P (d)	0.44658 ± 0.00001	10.779 ± 0.004	16.294 ± 0.007	25.82 ± 0.19	$179.5^{+8.3}_{-7.4}$
T_0^a (d)	1517.4983 ± 0.0009	1527.061 ± 0.003	1521.883 ± 0.004	1518 ± 3	1633^{+13}_{-15}
e	0 (fixed)	$0.067^{+0.072}_{-0.047}$	$0.064^{+0.070}_{-0.045}$	$0.072^{+0.071}_{-0.051}$	$0.058^{+0.064}_{-0.041}$
ω (deg)	90 (fixed)	148^{+118}_{-107}	189^{+118}_{-127}	287^{+67}_{-73}	128^{+98}_{-113}
K (m s^{-1})	1.57 ± 0.32	$0.69^{+0.41}_{-0.46}$	< 0.54	3.10 ± 0.36	3.17 ± 0.49
M_p ($M_\oplus$)	1.59 ± 0.33	$2.01^{+1.20}_{-1.35}$	< 1.91	12.1 ± 1.4	23.7 ± 3.7
Common parameter					
σ_{jitter}^b (m s^{-1})	1.34 ± 0.23				
γ^c (m s^{-1})	79703.86 ± 0.25				

[a] BJD$_{\text{TDB}}$-2457000. [b] Uncorrelated jitter term. [c] RV offset.

suggested by the Bayesian evidence computed in Section 3.6.1 (see Table 3.4), i.e. a model with the three transiting candidates plus two additional ones. We performed two independent fits, constraining the period of the outer signal to be shorter or longer than 100 days, in order to disentangle the 78 periodicity from its alias at 180 respectively. We ran the chains for 150 000 steps, discarding the first 50 000 as burn-in. The results of this analysis are reported in Tables B.1 and B.2.

In all our RV fits, regardless of the assumed period of the outermost planet, TOI-561.03 (i.e., the candidate with period of $\sim$ 16.3 d) remains undetected with an upper limit of $K \lesssim 0.5$ m s^{-1}, corresponding to a rather nonphysical mass of $\lesssim 2$ $M_\oplus$ (at 1σ) for a planet with $R_p \simeq 2.7$ $R_\oplus$. We thus performed a series of injection/retrieval simulations in order to assess the influence of the observational sampling and of the precision in the mass measurements of the other planets. In a first run, the synthetic datasets were simulated by assuming the orbital parameters as previously determined in the RV fits for the candidate planets .01, .02, and the non-transiting candidates, while the RV semi-amplitude

of the candidate planet at 16 d was varied between 0.0 m s^{-1} and 1.5 m s^{-1} in steps of 0.5 m s^{-1}. For computational reasons, we performed this analysis only with the 78-d solution for the outer planet. We projected the model onto the real epochs of observation and then we added a Gaussian noise corresponding to the measured error plus an RV jitter of 1.0 m s^{-1} added in quadrature, while preserving the original value in the analysis. We built 50 different noise realisations and analysed each of them with the same methodology as before, i. e., `PyDE+emcee` through `PyORBIT`, but for a shorter chain length[1] to reduce computing time. The posteriors of each parameter were then obtained by putting together the individual posterior distributions from each noise realisation. We finally repeated the same analysis but varying the RV semi-amplitude of the candidate planet .01, i. e., the closest signal in frequency space and the one with the most uncertain RV semi-amplitude measurement other than the USP candidate, by $\pm$0.5 m s^{-1} with respect to the value of 1.7 m s^{-1} used in the previous analysis. See Section 3.6.1 for the discussion on the results of this analysis.

---

[1] 10 000 steps after convergence, reached at approximately 15 000 steps.

Appendix C

TOI-561: CHEOPS light curves and telegraphic pixel treatment

As described in Section 4.3.2, the three *CHEOPS* visits of TOI-561 were reduced via the standard DRP processing. The light curves presented in this study, obtained using the RINF aperture size (RINF = $0.9 \times$ DEFAULT, where DEFAULT = 25 px; see also Section 4.3.2) are shown in Figure C.1. While for the two initial visits the automatic DRP processes was performed, the appearance of some telegraphic pixels during the third visit required a more in-depth analysis.

In addition to the large number of known hot pixels present in the *CHEOPS* CCD (some of them visible in Figure 4.2), some normal pixels can change their behaviour during the duration of a visit, for example becoming 'hot' after a SAA (South Atlantic Anomaly) crossing. These pixels, called 'telegraphic' for their abnormal behaviour, can affect the photometry if located within the photometric aperture (see for example Leleu et al. 2021a). During the third *CHEOPS* visit, we identified an unusual flux bump before the ingress of TOI-561 d transit, at BJD $\sim$ 2459318.75 (top panel, Figure C.2). After analyzing the statistics of each pixel light curve within the photometric aperture, we detected a telegraphic pixel with a large flux variation (second panel, Figure C.2) located within the *CHEOPS* PSF. The exact position of this pixel on the *CHEOPS* CCD is shown in Figure 4.2. We masked the pixel flux and repeated the photometric extraction of the visit using the RINF aperture, so removing the flux jump in the light curve (bottom panel, Figure C.2). During this analysis, we detected two additional telegraphic pixels within the photometric aperture, inducing smaller, but still significant variations in the light curve flux (third panel, Figure C.2). We corrected for the effect of these pixels as described above.

While investigating the nature of the flux bump happening during the third visit, we also extracted the light curve using a PSF-photometry approach exploiting the `PIPE` (PSF Imagette Photometric Extraction) software[1]. `PIPE` is a photometric extraction package specifically developed to extract *CHEOPS* light curves by applying PSF photometry on the 60-pixel imagettes, complementing the offical DRP extraction. The use of PSF photometry makes usually easier to filter out the impact of hot pixels and


[1]https://pipe-cheops.readthedocs.io/en/latest/index.html

cosmic rays, by either giving them a lower weight or masking them entirely in the fitting process. However, in this case the telegraphic pixel was located inside the *CHEOPS* PSF, requiring a careful manual masking. As for the DRP light curve, the flux bump in the PIPE photometry is reduced after masking the telegraphic pixel (bottom panel, Figure C.3). The PIPE-extracted light curve resulted in a slightly lower mean absolute deviation (MAD) with respect to the DRP photometry (top panel, Figure C.3), mainly due to the lower number of outliers present in the PSF photometry. For a more detailed comparison between PIPE and DRP photometries, see Morris et al. (2021b). We performed the same global analysis described in Section 4.5 using the PIPE light curve instead of the DRP one, obtaining consistent results and comparable uncertainties on the transit parameters of both planets b and d. We therefore decided to use the light curve obtained with the official DRP extraction in our final analysis.
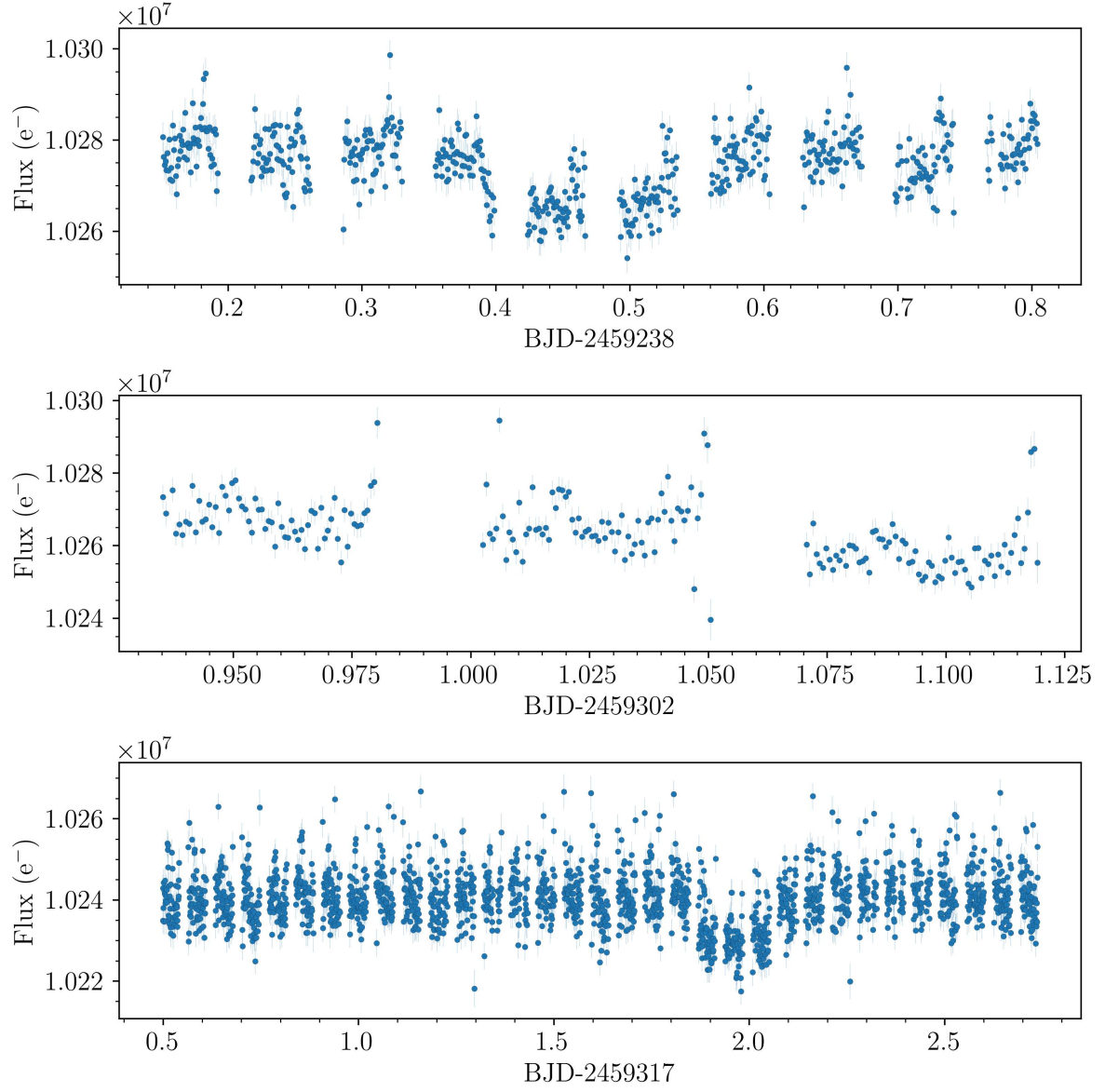
Figure C.1 *CHEOPS* RINF light curves of TOI-561 as extracted from the DRP, with 4σ-clipping for outliers removal. Visits 1, 2 and 3 are shown from top to bottom.
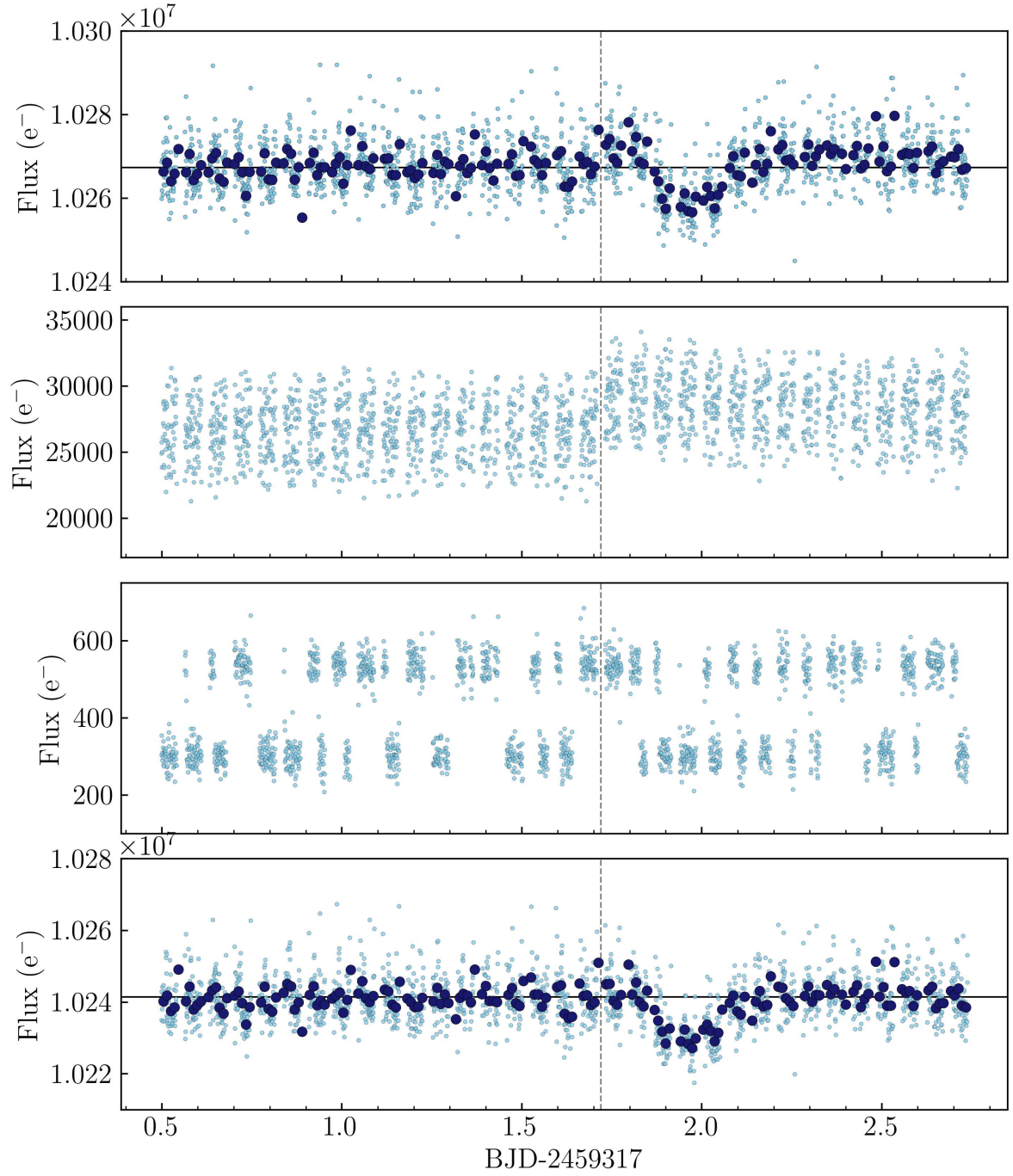
Figure C.2 Top panel: TOI-561 RINF original light curve of the third visit (light blue dots) after the removal of 4σ outliers, with over-plotted the 15-minute binned light curve (dark blue dots). The start of the flux jump due to the telegraphic pixel is marked with the dashed vertical line. Second panel: light curve of the telegraphic pixel located within the *CHEOPS* PSF. Third panel: light curve of the two additional telegraphic pixels located within the RINF aperture. Bottom panel: corrected light curve after masking the three telegraphic pixels.
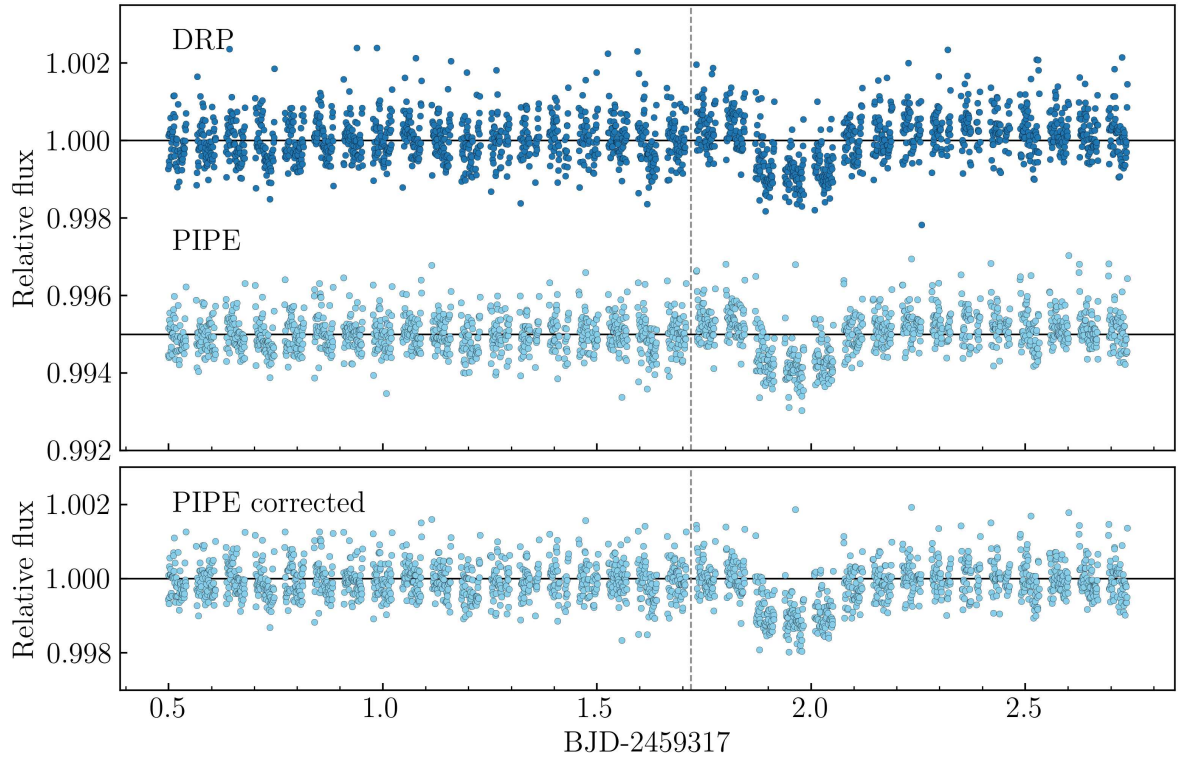
Figure C.3 Top panel: comparison between DRP and `PIPE`-extracted light curve of TOI-561 third visit, before the telegraphic pixel correction and with 4σ outliers removal. The DRP has a MAD of 371 ppm over the whole light visit, while `PIPE` of 325 ppm. Bottom panel: `PIPE` light curve after the telegraphic pixel correction. The light curve gets slightly noisier (MAD = 331 ppm) because one less pixel is considered in the reduction, but more reliable thanks to the exclusion of the telegraphic pixel flux. In both panels, the beginning of the flux jump is highlighted with a vertical dashed line.

Appendix D

Floating Chunk Offset method on TOI-561 b

In order to investigate the literature discrepancy on the mass of TOI-561 b (Section 4.2.2), we adopted a specific observing strategy with HARPS-N targeting the USP planet (Section 4.3.3), obtaining multiple observations during the same night for 22 nights. Multiple nightly observations can be used to precisely infer the mass of USP planets using the Floating Chunk Offset method (FCO; Hatzes 2014), which consists in applying a nightly offset to remove all the other signals present in the system, both of planetary and stellar origin (i.e. Howard et al. 2013, Pepe et al. 2013, Malavolta et al. 2018, Frustagli et al. 2020). The FCO method is only applicable when the separation between the USP period and the period of all the other signals is large enough, and the RV semi-amplitude has a similar or larger value with respect to the other signals. As demonstrated in L21, these conditions apply to TOI-561 b, for which the authors derived an FCO semi-amplitude of $K_{\rm b,FCO} = 1.80 \pm 0.38$ m s^{-1} ($M_{\rm b,FCO} = 1.83 \pm 0.39$ $M_{\oplus}$) exploiting multiple observations collected over ten nights.

Here, we applied the FCO method to TOI-561 b on a total of 22 HARPS-N nights, adding 12 novel nights to the 10 nights already presented in L21. Out of the total set, four nights have six multiple observations extending over more than 40 per cent of the orbital period of the planet, and span opposite orbital phases to provide an optimal phase coverage. We performed a `PyDE + emcee` fit with `PyORBIT`, assuming a fixed zero eccentricity and Gaussian priors on period and T_0 coming from the global fit, and we added a jitter term to account for possible additional white noise. We derived a semi-amplitude of $K_{\rm b} = 1.81 \pm 0.31$ m s^{-1}, corresponding to a mass of $M_{\rm b} = 1.86 \pm 0.33$ $M_{\oplus}$, with a jitter of $0.96^{+0.25}_{-0.23}$ m s^{-1}. Figure D.1 shows the resulting phase-folded RVs. The derived mass and semi-amplitude are nicely in agreement with the L21 values, and they support the values inferred from our joint photometric and RV modelling (Section 4.5), being consistent within 1σ. Given the higher number of RVs included in the joint fit, which led to smaller uncertainties on the derived parameters, we decided to adopt as final values for TOI-561 b the ones obtained from the global modelling, i.e. $K_{\rm b} = 1.93 \pm 0.21$ m s^{-1}, $M_{\rm b} = 1.99 \pm 0.22$ $M_{\oplus}$.
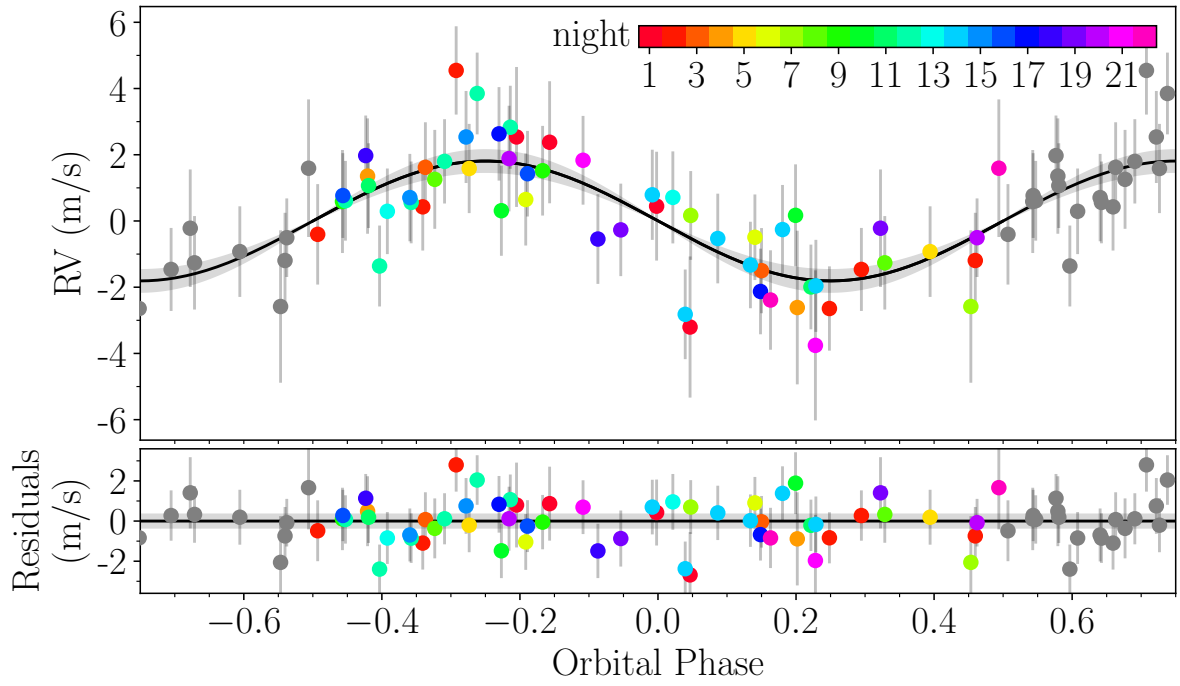
Figure D.1 Phase-folded RVs of the 22 HARPS-N nights used to model TOI-561 b with the FCO method. The error bars include the jitter term added in quadrature.